Interactions and Evolution of the Greenland Ice Sheet Surface Mass Balance with the Global Climate

Sellevold, R.

DOI
10.4233/uuid:b442ec3c-75f3-491f-99af-3843b19fcb92

Publication date
2021

Document Version
Final published version

Citation (APA)
Sellevold, R. (2021). *Interactions and Evolution of the Greenland Ice Sheet Surface Mass Balance with the Global Climate*. [Dissertation (TU Delft), Delft University of Technology].
https://doi.org/10.4233/uuid:b442ec3c-75f3-491f-99af-3843b19fcb92

Interactions and Evolution of the Greenland Ice Sheet Surface Mass Balance with the Global Climate

Interactions and Evolution of the Greenland Ice Sheet Surface Mass Balance with the Global Climate

Dissertation

for the purpose of obtaining the degree of doctor
at Delft University of Technology
by the authority of the Rector Magnificus Prof. dr. ir. T.H.J.J. van der Hagen,
chair of the Board for Doctorates,
to be defended publicly on
Wednesday 3 March 2021 at 15:00 o'clock

by

Raymond SELLEVOLD

Master of Science in Meteorology and Oceanography,
University of Bergen, Norway
born in Bergen, Norway.

This dissertation has been approved by the promotors.

Composition of the doctoral committee:

Rector Magnificus,	chairperson
Prof. dr.-ing.habil. R. Klees,	Delft University of Technology, promotor
Dr. M. Vizcaino,	Delft University of Technology, copromotor
Independent members:	
Prof. dr. ir. B.J.H. van de Wiel,	Delft University of Technology
Prof. dr. E. Hanna,	University of Lincoln, United Kingdom
Prof. dr. M.R. van den Broeke,	University of Utrecht, the Netherlands
Dr. X. Fettweis,	University of Liège, Belgium
Dr. R. Mottram,	Danmarks Meteorologiske Institut, Denmark
Prof. dr. ir. H.W.J. Russchenberg,	Delft University of Technology, reserve member

This research was funded by the Nederlandse Organisatie voor Wetenschappelijk Onderzoek (NWO).

Keywords: Greenland ice sheet, surface mass balance, climate modeling, climate change

Printed by: Guus Gijben, Proefschrift (AIO)

Cover by: Raymond Sellevold

ISBN 978-94-6384-201-3

An electronic version of this dissertation is available at
http://repository.tudelft.nl/.

Greenland is not for sale!

Mette Fredriksen

Contents

Preface

The thesis at hand would not have been written without the help of several people. Therefore, this section will be dedicated to them.

When starting my studies in meteorology and oceanography, I did not foresee pursuing a Ph.D. after completing my studies. As I was writing my master's thesis, the idea of starting a Ph.D. after my studies emerged. Luckily, I was given a chance to get a short taste of what doing A Ph.D. would be like when I continued for three months at the University of Bergen, turning my master thesis into a manuscript. Thank you, Camille and Stefan, for giving me that opportunity; it made it easy to choose to pursue a Ph.D. after I was finished.

Six months later, I was at work on a meteorological station on a deserted Arctic island, browsing for what to do next. There I came over an advertised position on "Coupled Global Modeling of the Greenland Ice Sheet." I was drawn to the topic and decided to apply. After an interview and some time, I got invited to take on this project as a Ph.D. candidate. For this, I need to thank Miren. Thank you for taking a chance on me and for the many hours of discussion, correction of manuscripts, figures, and presentations.

I also want to thank the coupled-ice-climate group I enjoyed working with: Laura, Carol, Michele, and Sarah.

One of the primary tools for completing this thesis was the Community Earth System Model, developed and maintained by the National Center for Atmospheric Research. I want to thank them and, in particular, the Land Ice Working Group for support and their annual workshops and working group meetings, which I learned a lot from.

During my Ph.D., I was lucky to have a research stay at the University of Boulder, hosted by my co-supervisor Jan, where Chapter 5 of this thesis was born. Thank you, Jan, for this great stay.

Further, I would like to thank Roland for being my promotor and taking the time to improve this thesis. Also, thanks to the PSG group for the monthly meetings.

The papers that make the foundation of this thesis would not have been published without co-authors' help and contributions; thank you!

Last, I thank my family and friends for your patience with me while I have worked on this Ph.D.

Raymond Sellevold
Delft, September 2020

Summary

One of the major consequences of ongoing global warming is the melting of the Greenland ice sheet (GrIS). The GrIS, as the world's second-largest freshwater reservoir, has the potential to raise sea levels by 7.4 m (Bamber et al., 2018a,b). Such a sea-level rise would have a devastating effect on coastal societies, where a large fraction of the world's population lives. Therefore, constraining the GrIS' contribution to sea-level rise is an important and vital task to plan for the future efficiently.

Since the 1990s, the GrIS has been losing mass at an accelerated rate (Enderlin et al., 2014; Bamber et al., 2018a; Shepherd et al., 2019; Oppenheimer et al., 2019). We can separate GrIS mass loss into the contribution from the surface mass balance (SMB) and ice discharge. The SMB is the primary contributor to recent GrIS mass loss (van den Broeke et al., 2016); thus, there is a need for accurate projections of GrIS SMB, and a thorough understanding of physical processes governing the surface mass loss under global warming. Further, the GrIS also interacts with the climate system (Fyke et al., 2018), highlighting the need for coupled global climate projections.

This thesis' primary targets are to

1. Investigate the co-evolution of the GrIS SMB and the global climate under increased greenhouse gases.

2. Examine the impact of reduced Arctic sea ice on GrIS SMB

3. Make projections of future GrIS surface melt.

This is achieved by using the Community Earth System Model (CESM) version 2.1 (Danabasoglu et al., 2020). CESM2 is a newly developed coupled earth system model that features an online downscaling of the SMB through elevation classes (ECs), advanced snow physics (van Kampenhout et al., 2017), and a prognostic calculation of snow albedo (Flanner and Zender, 2006). Also, the EC simulated SMB is interactive; that is, modification of surface fluxes of mass and energy is communicated to the earth system's other components.

The present-day CESM1 SMB simulation with ECs was shown to be realistic (Vizcaíno et al., 2013). However, the EC downscaling itself and its effects on the downscaled SMB and SEB components were not analyzed or evaluated. To evaluate this original EC implementation, simulations with CESM1 were run. The EC method aims to tackle the challenge of a too low resolution in the CESM1 global climate model to capture the steep topographic gradients of the GrIS accurately. Capturing these steep topographic gradients is necessary for a realistic representation of SMB, which can be provided as forcing to a coupled (or standalone) ice sheet model(s).

The EC method in CESM1 applies elevation corrections (lapse rates) to the near-surface temperature and specific humidity.

We find that the elevation gradients of SMB in CESM1 are very similar to those of the Regional Atmospheric Climate Model version 2.3 (Noël et al., 2015), partly due to compensating biases or lack of downscaling in the individual gradient of snowfall, surface melt and refreezing. Sensitivity experiments using different lapse rates for the near-surface temperature reveal that a lower than default (6 K km^{-1}) lapse rate unrealistically expands the ablation area due to little redistribution of energy with elevation. Also, lower lapse rates do not adequately capture the strong melting at the margins of the GrIS. A higher lapse rate than the default gives the opposite effect.

This thesis also assesses how the implementation of ECs in the land component modifies the regional climate simulation. The EC method compensates for a warm bias associated with topographic smoothing and leads to downwind cooling. The topographic smoothing is due to the inability of representing complex topography at the relatively low resolution of the climate model. Further, the downwind cooling leads to growth of sea-ice on the eastern side of Greenland and in the Barents Sea. Finally, several recommendations based on the results are made towards the future development of the EC method to improve the SMB simulation in CESM.

To investigate the coupled global climate and SMB evolution under elevated greenhouse gas forcing, this thesis analyzes a CESM2 simulation with idealized CO_2 forcing and a fixed present-day GrIS topography. A simulation with idealized CO_2 forcing was chosen because it permits a clearer separation of the effect of the CO_2 from other forcings and feedbacks. In the 150-year-long simulation, CO_2 increases with 1% per year, compared to pre-industrial levels, until 4× stabilization in the last 10 years. We find that a GrIS surface mass loss signal emerges from natural variability for global warming of 2.7 K, with respect to the pre-industrial climate, whereafter the surface mass loss accelerates. Much increased surface melt and loss of refreezing capacity cause the fast loss of surface mass. Increased net longwave radiation is the primary contributor to melt energy increase before acceleration. As the ablation areas expand, and the surface temperature of the GrIS approaches the melting point, melt-albedo feedbacks and increased energy from the turbulent heat fluxes accelerate the surface mass loss. CO_2 forced atmospheric circulation changes in the North Atlantic Oscillation (towards more persistent positive phase) and Greenland Blocking Index (towards more persistent negative phase) partially reduce surface melt.

To address the question of the SMB evolution with an evolving and dynamical ice sheet, this thesis analyzes a similar, but longer (350 years) simulation with bi-directional coupling between CESM2 and the Community Ice Sheet Model version 2.1 (CISM2). We find that mass loss accelerates for global warming of 4.2 K due to the processes described above. The incorporation of an evolving ice sheet allows for the SMB-elevation feedback. The SMB-elevation feedback accounts for an additional 44% decrease of GrIS SMB. Locally, for areas below the equilibrium line altitude, the SMB-elevation feedback accounts for as much as 50% of the SMB decrease. These results highlight the importance of a fully coupled (that is, including an evolving ice

sheet model) for SMB projections on longer timescales.

Attributing the influences of different earth system components on the GrIS SMB is complex in coupled climate simulations of global warming. For this reason, this thesis investigates the influence of Arctic sea ice loss on the GrIS SMB. This is done by analyzing a CESM2 simulation under present-day atmospheric CO_2 concentrations with prescribed monthly Arctic sea ice concentration and sea surface temperatures, corresponding to a +2 K global warming. Results show that Arctic sea ice loss enhances the hydrological cycle over the GrIS, through increases in winter precipitation and summer melt. The wintertime increase in GrIS precipitation is caused by higher Arctic moisture availability and increased cyclone activity. In summer, a warmer and wetter Arctic increases the sensible and latent heat fluxes over the GrIS, leading to increased melt and associated melt-albedo feedback. Further, strong vertical winds at the upwind side (over Baffin Bay) of the GrIS results in deep warming, which causes regional enhancement of the 500 hPa geopotential heights and consequent increases in blocking over the GrIS.

Future projections of GrIS surface melt, the primary contributor to present-day surface mass loss, are limited due to the computational expense of making such projections. To address this challenge, we build artificial neural networks (ANNs) and train them with climate and melt data from CESM2 to project 21st-century surface melt from the suite of climate models participating in the Coupled Model Intercomparison Project phase 6 (CMIP6). The ANNs predict an end of the century surface melt increase by 414$\pm$276, 724$\pm$371, 1,031$\pm$436, and 1,378$\pm$555 Gt yr^{-1}, for the Socioeconomic Pathways (SSP) 1-2.6, SSP2-4.5, SSP3-7.0, and SSP5-8.5, respectively with respect to 1979–1998. The ANNs predict similar melt trajectories for five global climate models when compared to the Modèle Atmosphérique Régionale version 3.11 (MAR; Hanna et al., 2020). The primary source of projection uncertainty throughout the 21st century is due to the spread in the models' climate sensitivity, as well as their spread in the regional simulation around Greenland.

This thesis presents analysis of some of the first simulations of Greenland ice sheet climate and SMB with the newly developed CESM2 and CESM2-CISM2. While many questions regarding the future of the GrIS remain, the results presented here contribute towards a better understanding of the coupled global climate and GrIS SMB evolution, and processes leading GrIS surface mass loss. The first steps towards making computationally efficient and robust projections of GrIS surface melt through machine learning are also taken.

1

Introduction

Du kan tenke dig seks bitte små mygg
marsjerende over et forferdelig stort laken.

Fridtjof Nansen

1

1.1. Greenland on a Warming Earth

The Earth is warming in response to increased anthropogenic greenhouse gas emissions, a phenomenon called global warming. The 2010–2019 global mean temperature is 0.8 K higher than the 1951-1980 mean (Fig. 1.1) and has increased at a rate of 0.1 K decade^{-1} since 1950. Global warming is spatially heterogeneous. Generally, the land warms faster than ocean areas, with some ocean areas even having a non-significant trend. The most rapid warming occurs in the Arctic.

The potential consequences of global warming are dramatic. Amongst many other damaging effects (Monirul Qader Mirza, 2002; Emanuel, 2011), global warming leads to higher sea levels. The global mean sea level increased with 0.16 (0.12-0.21) m between 1902 and 2010 (Oppenheimer et al., 2019). The main contributors to the sea level rise are thermal expansion of the ocean water, melting of glaciers, changes in terrestrial water storage, and the melting and ice discharge from the Antarctic and Greenland ice sheets. In recent years, the Greenland ice sheet (GrIS) contributed to around 21% of the global mean sea-level rise (Oppenheimer et al., 2019). Due to this substantial contribution, processes governing the mass loss of the GrIS require extensive investigation.

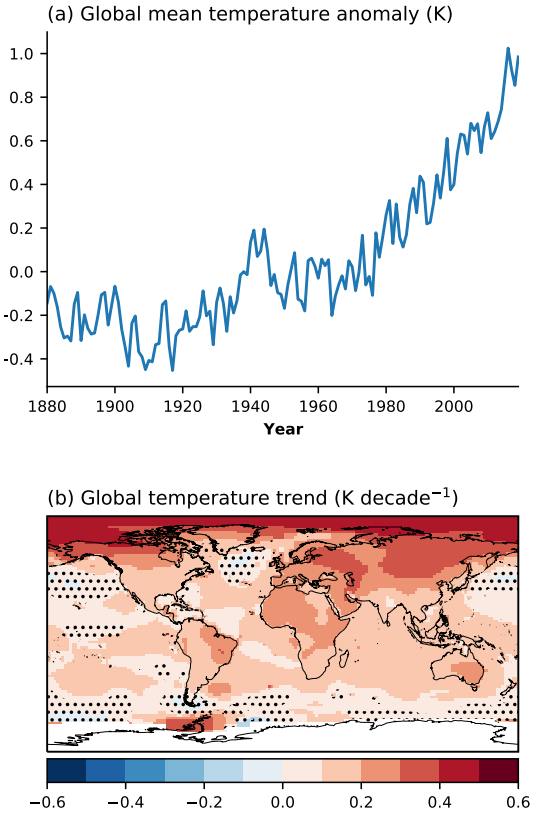

Figure 1.1: Observed a) global mean temperature anomaly (K) relative to the 1950–1950 global mean, and b) 1950–2019 global temperature trends (K decade^{-1}). Dots represent areas with no significant (p>0.01) trend. Data from GISTEMP (Lenssen et al., 2019)

Greenland is a large island located at the intersection of the Arctic and the North Atlantic oceans. The island is 2,166,086 km^2 with a peak elevation of 3,673 m (Fig. 1.2a). The island consists of the world's second-largest (after Antarctica) freshwater reservoir, stored as ice. This ice comprises the GrIS (Fig. 1.2b) and is up to 3,435 m thick. If all the ice were to melt instantaneously, this would raise the global mean sea level by 7.4 m (Bamber et al., 2018b), assuming no glacial isostatic adjustment. The bedrock of Greenland has a highly spatially varying elevation (Fig. 1.2c). With-

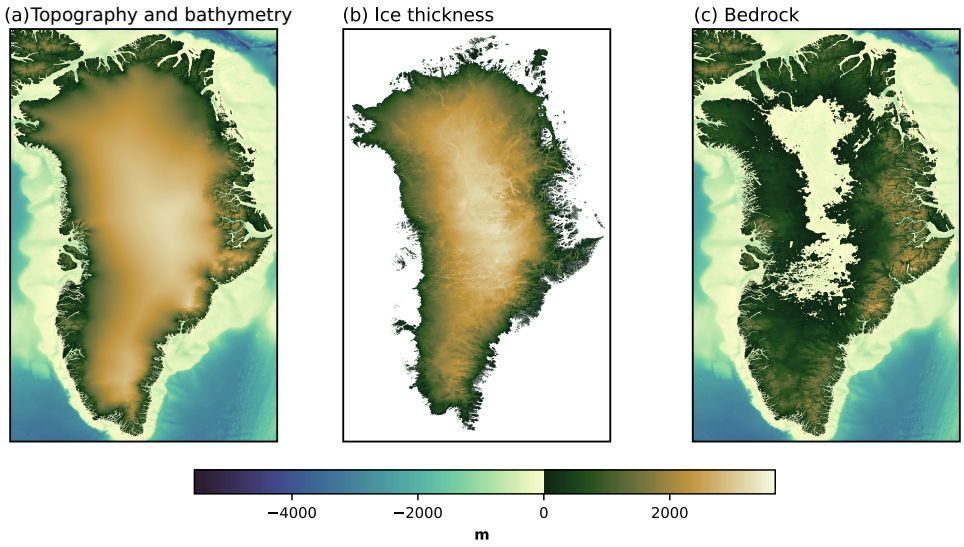

Figure 1.2: Present-day observed (a) surface elevation and ocean bathymetry (m), (b) ice thickness (m), and (c) bedrock elevation (m). Data from BedMachine v3 (Morlighem et al., 2017).

out the ice, and ignoring glacial isostatic adjustment (Whitehouse, 2018), central Greenland is a large lake, barred by mountainous regions. However, in the south-west, northwest, and northeast, there are some relatively flat regions.

The mass budget of the GrIS can be expressed through the mass balance (MB; Gt yr^{-1}),

$$\mathrm{MB} = \mathrm{SMB} - \mathrm{ID}, \tag{1.1}$$

where SMB is the surface mass balance, and ID is the ice discharge. A distinction between the two terms on the r.h.s. is that the SMB is the balance of mass where the ice meets the atmosphere, while the ID occurs where the ice meets the ocean. Atmospheric processes, such as precipitation, cloud cover, and heat advection, are primary influences on the SMB. The SMB can be either positive or negative (or zero). The ID is mainly influenced by ocean temperatures and the glacier velocities, and can only be positive (or zero).

The GrIS has been losing mass since the 1990s and has lost 3,902 $\pm$ 342 Gt (10.8 $\pm$ 0.9 mm sea-level equivalent) between 1992 and 2018 (Shepherd et al., 2019). So far, both SMB and ID have contributed about 50% to the mass loss. However, since the 2000s, the SMB decrease has accelerated and is the primary contributor to the recent acceleration of mass loss (Enderlin et al., 2014; van den Broeke et al., 2016). Thus, it is crucial to improve projections of the future SMB to constrain projections of future sea-level rise.

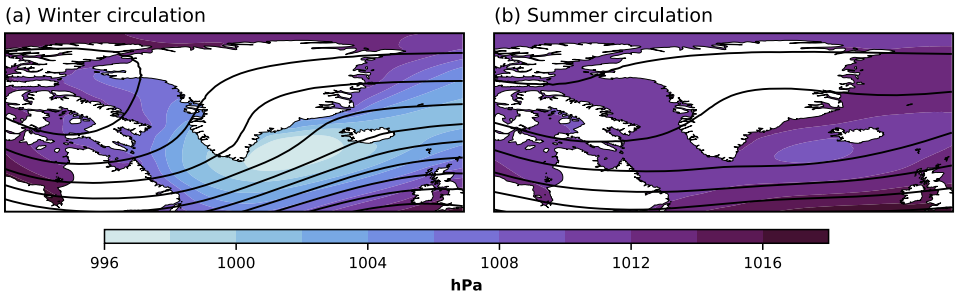

Figure 1.3: Seasonal mean 1979–2019 500 hPa geopotential heights [contours] and sea level pressure [hPa; colors] in (a) winter and (b) summer. Data from ERA5 (Hersbach et al., 2020)

1.2. Present-day Greenland Surface Mass Balance

In this section, we will explore the GrIS SMB and climate to provide an overview of processes relevant to shaping the SMB. This is vital to understand the challenges scientists are facing when making projections of SMB.

The GrIS is located at the northern flank of the North Atlantic storm tracks. The upper-level winds over Greenland are predominantly westward, with a more south-westerly direction in winter (Fig. 1.3). Just southeast of the GrIS, in the Irminger Sea, there is a local minimum in sea-level pressure, known as the Icelandic Low. The Icelandic Low is deeper and placed further west in winter than in summer. The cause for this climatic low is the high occurance of cyclones. Westward propagating cyclones are steered to this region, as the GrIS acts as a barrier to flow preventing synoptic systems to pass over it (Ettema et al., 2010). Further, about 10%-15% of the cyclones appearing in this region (Serreze et al., 1997) are generated by lee-side cyclogenesis (Tsukernik et al., 2007).

The map of present-day GrIS SMB consists of low-elevation ablation areas, where the GrIS loses mass, and high-elevation accumulation areas, where the GrIS gains mass (Fig. 1.4a). The equilibrium line altitude (ELA), where SMB=0, separates the accumulation and ablation areas. The ELA ranges from about 1500 m in the south to about 1000 m in the north. The lower ELA in the north is due to a generally colder and drier climate. Two prominent features of the GrIS SMB are its strong topographic gradients and the very high spatial variability. To understand the cause of these characteristics, we need to separate the SMB into components. We can write the SMB components:

$$\mathrm{SMB} = \mathrm{PRECIPITATION} - \mathrm{RUNOFF} - \mathrm{SUBLIMATION}, \tag{1.2}$$

which can again be rewritten, by substituting PRECIPITATION = SNOWFALL + RAINFALL and RUNOFF = RAINFALL + MELT - REFREEZING, to

$$\mathrm{SMB} = \mathrm{SNOWFALL} - \mathrm{MELT} + \mathrm{REFREEZING} - \mathrm{SUBLIMATION}. \tag{1.3}$$

Snowfall is the leading source for mass gain at the surface (Noël et al., 2015; Fettweis et al., 2017). In the accumulation areas, the signature of snow is visible

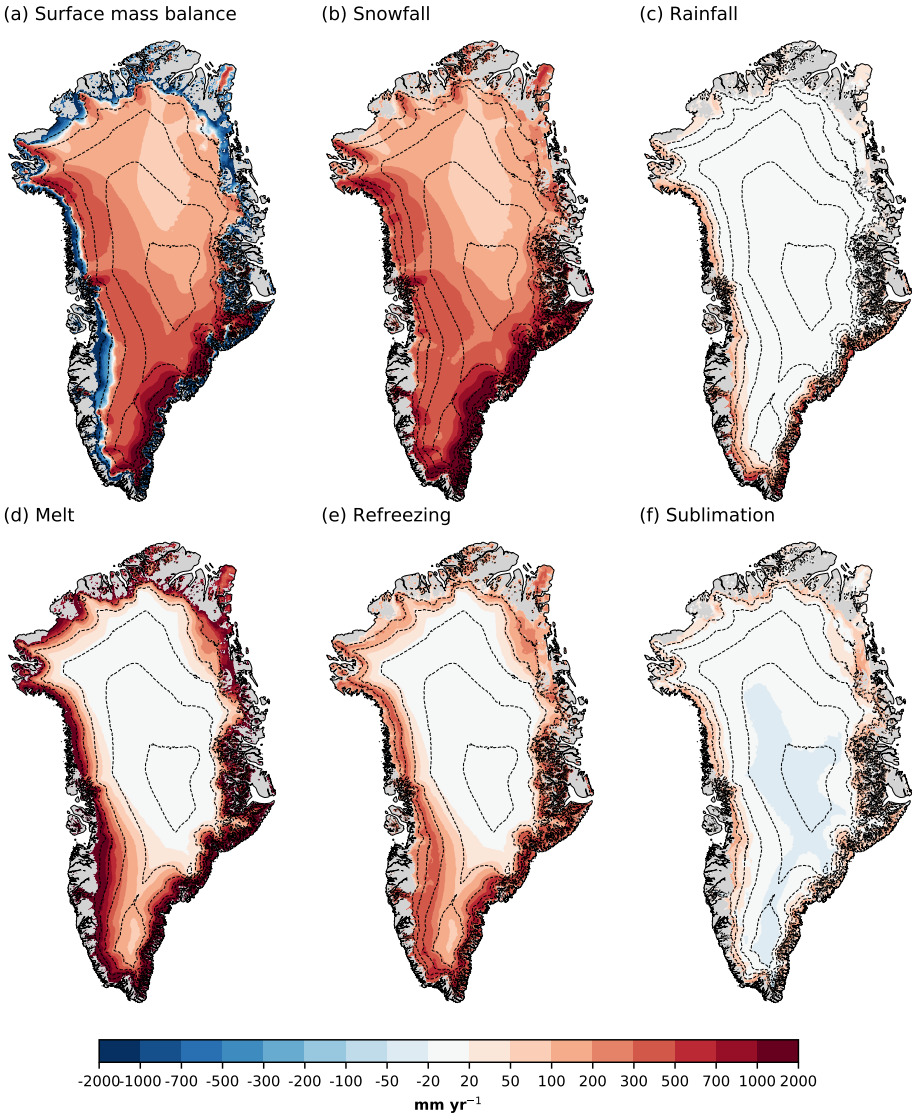

Figure 1.4: Annual mean 1979–2019 GrIS SMB and SMB components [mm yr^{-1}]. (a) SMB, (b) snowfall, (c) rainfall, (d) melt, (e) refreezing, and (f) sublimation. Dotted contours show surface elevation (m), starting from 1000 m with 500 m intervals. Data from MAR v3.9.6 (Delhasse et al., 2020).

(Fig. 1.4a,b). Around the ice sheet, there are many local snowfall maxima caused by mesoscale weather systems (Ettema et al., 2009). The highest snowfall rates are in the southeast, because of the high occurrences of storms in this region. There is also a considerable amount of snowfall on the western side of the ice sheet. Most of the snowfall comes from cyclones steered northward (rather than steered to the southwest), and upper-level moisture advection into this region (Ettema et al., 2010).

Further downwind, into the ice sheet interior, snowfall is meager. As the air is lifted into the cold high-elevation areas of the interior, moisture evaporates and leaves little precipitable water left to cause snowfall. Only about 10% of the precipitation on the ice sheet falls as rain (Steger et al., 2017), and the rainfall is confined to lower elevation areas (Fig. 1.4c).

Melt on the ice sheet surface is currently the primary source of surface mass loss (van den Broeke et al., 2016; Fettweis et al., 2017). Surface melt is highly correlated to elevation (Noël et al., 2016), with the highest melt rates at low elevations. Surface melt occurs over a fairly large area of the ice sheet, including the southern dome (Fig. 1.4d). In the extreme year of 2012, surface melt was even recorded at the summit of Greenland (Nghiem et al., 2012).

Despite the extensive melt, the GrIS only loses mass through runoff at a relatively narrow (10-100 km; van Angelen et al., 2013) band around the ice sheet. This is in large part because of refreezing. When surface melt occurs over a snowy surface, the melt will percolate in the snow, and if there is enough pore space and the snow is below freezing point, the water will refreeze (Parry et al., 2007; Cox et al., 2015). In this way, the refreezing acts as a sponge to the meltwater and restrict runoff to occur only at lower elevations. Refreezing maxima are located along the ELA. Below the ELA, the melt rates are so high that the snow disappears during the melt season. When there is no snow, meltwater cannot refreeze. Above the ELA, there is generally more snow, but the melt rates are lower than at the ELA.

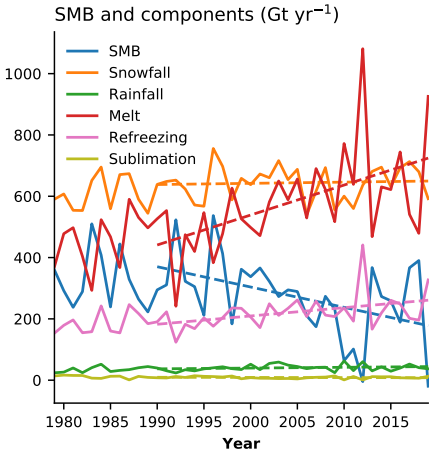

Figure 1.5: 1979–2019 GrIS annual integrated SMB and SMB components [Gt yr^{-1}]. SMB, snowfall, rainfall, melt, refreezing, and sublimatation is represented by the blue, orange, green, red, pink, and olive lines, respectively. Dotted lines show the 1990–2019 linear trend. Data from MAR v3.9.6 (Delhasse et al., 2020).

Some of the mass loss at the margins is due to sublimation. Sublimation occurs when ice is directly converted to gas, skipping its liquid phase (Box and Steffen, 2001). The opposite of sublimation is riming/deposition, which occurs in the interior when relatively humid air is advected over the cold surface.

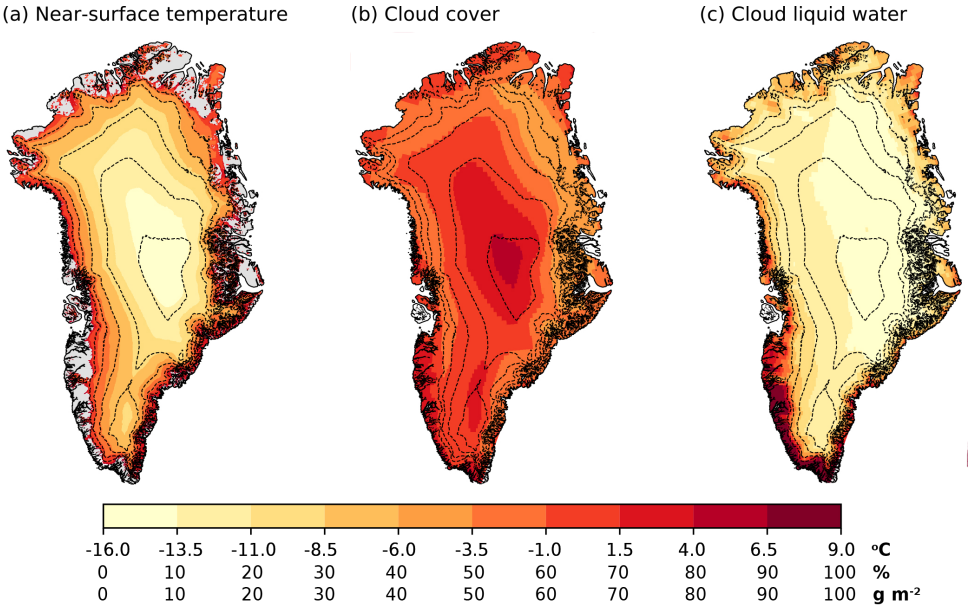

Figure 1.6: 1979–2019 summer (JJA) averaged a) near-surface temperature [°C], b) cloud cover [%], and c) cloud liquid water [g m^{-2}]. Dotted contours show surface elevation (m), starting from 1000 m with 500 m intervals. Data from MAR v3.9.6 (Delhasse et al., 2020).

The main contributor to the increasing surface mass loss is increased surface melt (Fig. 1.5), part of which is buffered in the snow, causing increased refreezing. The other components of the SMB are currently not changing significantly (Fettweis et al., 2017; Noël et al., 2020b).

Most of the ice sheet surface melt takes place in the summer months (JJA; June-July-August). In these months, lower elevation areas have a near-surface temperature that is, on average, above 0°C (Fig. 1.6a). The near-surface temperature of the ice sheet decreases with elevation, at a rate of approximately 4.7 K km^{-1} (Fausto et al., 2009).

Clouds have a profound impact on surface climate, through its influence on the amount of solar (shortwave) radiation that can reach the Earth's surface, and through how much longwave (infrared/terrestrial) radiation that can escape to space (Bintanja and van den Broeke, 1996; Cawkwell and Bamber, 2002; van den Broeke et al., 2008). Cloud cover generally increases with elevation over the GrIS (Fig. 1.6b). However, the clouds over high-elevated colder surfaces contain less liquid water than clouds over lower elevations (Fig. 1.6c and Ettema et al., 2010).

The amount of melt on the GrIS surface depends on how much energy is available. The surface energy balance [W m^{-2}] can be written as

$$\mathrm{M} = \mathrm{SW}_{net} + \mathrm{LW}_{net} + \mathrm{SHF} + \mathrm{LHF} + \mathrm{GHF}, \tag{1.4}$$

where M is the melt energy, SW_{net} is the net shortwave radiation, LW_{net} is the

net longwave radiation, SHF is the sensible heat flux, LHF is the latent heat flux, and GHF is the ground heat flux. When M=0, all the energy is used to raise the temperature of the surface. When M>0, melt occurs.

We can also express the surface energy balance (Eq. 1.4) as

$$\mathrm{M} = \mathrm{SW}_{in} \cdot (1 - \alpha) + \mathrm{LW}_{in} - \epsilon\sigma \mathrm{T}_s^4 + \mathrm{SHF} + \mathrm{LHF} + \mathrm{GHF}, \tag{1.5}$$

where SW_{in} is the incoming shortwave, α is the albedo, ϵ is the surface emissivity, σ is the Stefan-Boltzmann constant, and T_s is the surface temperature (in Kelvin).

The SW_{in} and LW_{in} have opposite gradients with elevation, where SW_{in} increases with elevation (Fig. 1.7a). Although the cloud cover is higher at higher elevations, clouds are more transparent to shortwave radiation due to the lack of liquid water (van den Broeke et al., 2008; Ettema et al., 2010). The LW_{in} gradient is a product of many factors. First of all, the surface temperature of the GrIS is higher at lower elevations, allowing for higher longwave radiation emission from the surface. This outgoing longwave radiation gets re-emitted to the surface, and the atmospheric emission is proportional to atmospheric temperatures, which are higher at lower elevations. Further, clouds act as greenhouse gases, as they trap the longwave radiation and re-emits it to the surface. The more liquid water the clouds contain, the higher the trapping effect is (Bennartz et al., 2013).

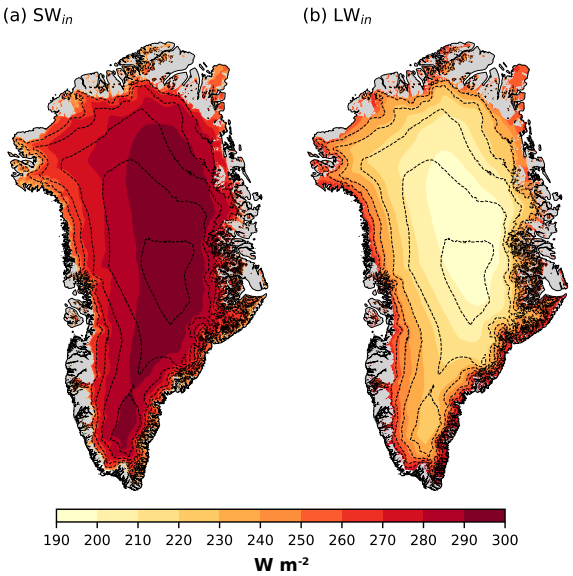

Figure 1.7: As Fig. 1.6 but for a) SW_{in} and b) LW_{in}, both in W m^{-2}.

As described by eq. 1.4, it is the net radiation that contributes to the energy used for melt. Although SW_{in} decreases with lower elevations, the SW_{net} increases with lower elevations, leaving more energy for melt (Fig. 1.8a). This can be explained through the albedo (Fig. 1.8b). The albedo is a measurement of how well a surface absorbs solar radiation. Relatively dark surfaces, like bare ice, present at the margins of the GrIS during summer, reflect about 0.55 of the solar radiation (Box et al., 2012; Alexander et al., 2014). The wet snow around the ELA reflects around 65 - 75% of the solar radiation. The dry snow in the interior reflects almost all (80 - 90%) of the solar radiation. The distribution of SW_{net} is dominated by albedo over SW_{in}. LW_{net} contributes negatively to the melt energy everywhere (Fig. 1.8c). The spatial variability of LW_{net} is much smaller than that of SW_{net}.

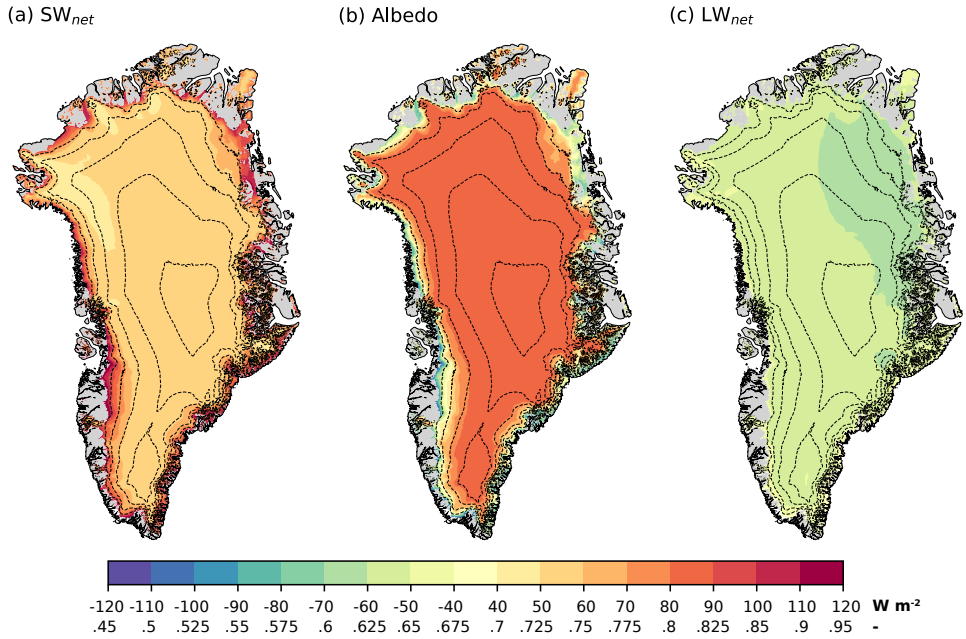

Figure 1.8: As Fig. 1.6 but for a) SW$_{net}$ [W m^{-2}], b) albedo [-], and c) LW$_{net}$ [W m^{-2}].

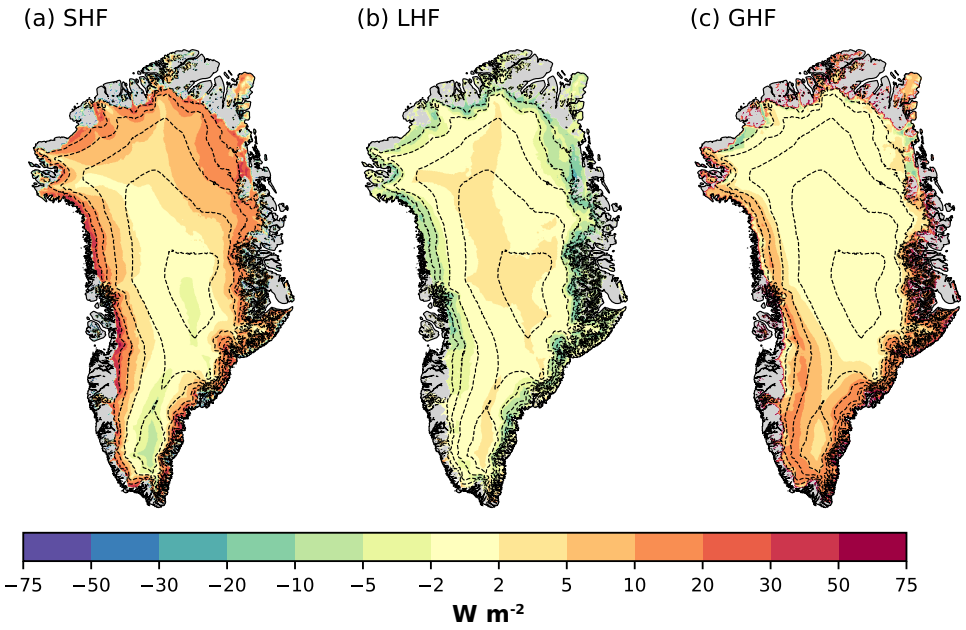

Figure 1.9: As Fig. 1.6 but for a) SHF, b) LHF, and c) GHF, all in W m^{-2}.

The SHF is proportional to the difference in near-surface (air) and surface temperature. The amount of turbulence in the boundary layer, where more turbulence is typically associated with higher wind speeds and/or rougher surfaces, also influence SHF. In summer, the SHF is positive at low elevations, which indicate heat transfer from the air to the surface (Fig. 1.9a). The elevation gradient is negative so that SHF reduces with increasing elevation and even becoming negative at the very high elevations at the summit and the southern dome. In these high elevation areas, the air is so cold that it transfers heat (from, e.g., radiation) away from the surface. The LHF has similar patterns, but with an opposite gradient (Fig. 1.9b). At low elevations, sublimation occurs, which reduces the energy available for melt through the LHF. In the interior, where deposition dominates, the LHF is positive as the water vapor that gets deposited contains a certain amount of energy. The GHF maxima are co-located with the refreezing maxima. When water percolates and refreezes in the snow, there is heat release (Charalampidis et al., 2016). Part of the heat release is conducted to the surface and contributes to melt energy through the GHF (Ettema et al., 2010).

The temperature over the GrIS has increased due to global warming, and the near-surface air is warming slightly faster than the surface (Fig. 1.10a). Also, the radiative forcing over the GrIS has increased, with the SW_{in} increasing faster than the LW_{in} (Fig. 1.10b). The main reason for increased SW_{in} is a reduced summer cloud cover over the GrIS (Hofer et al., 2017). Despite the reduced cloud cover, LW_{in} also increases as a consequence of the trapping effect of greenhouse gases and atmospheric warming, allowing for more re-emission of longwave radiation to the surface. The surface albedo has declined over the last decades (Fig. 1.10c). As seen, the albedo is powerful in modulating the SW_{net}, the largest contributor to melt energy. Expansion of bare-ice areas due to continued melting causes the albedo decline (Alexander et al., 2014).

The increase in radiative forcing, accompanied by a declining albedo, has led to more surface melt of the GrIS. SW_{net} is the main contributor to the melt increase (Fig. 1.10d). SHF and GHF have also slightly increased. On the other hand, LW_{net} has decreased as the increased surface temperature has caused the GrIS to emit more longwave radiation.

Changes in atmospheric circulation may have contributed to about 50% of the melt increase (Delhasse et al., 2018), with global warming accounting for the other 50%. The most noticeable change in atmospheric circulation is increased blocking over the GrIS (Hanna et al., 2016). Blocking events are long-lived (five days or longer) and slow-moving high-pressure systems that prevent the westerly flow (Kennedy et al., 2016). They are typically associated with warm-air advection and reduced cloudiness. The warm air advection leads to the onset of melting at the GrIS surface. In response, the albedo lowers (Box et al., 2012). Together with increased solar radiation, due to reduced clouds, melt amplifies. The post-2010 increase in blocking is unprecedented in the observational record. The mechanisms behind this circulation anomaly are debated, as well as whether it is an anthropogenically-forced response or caused by natural variability (Hahn et al., 2018).

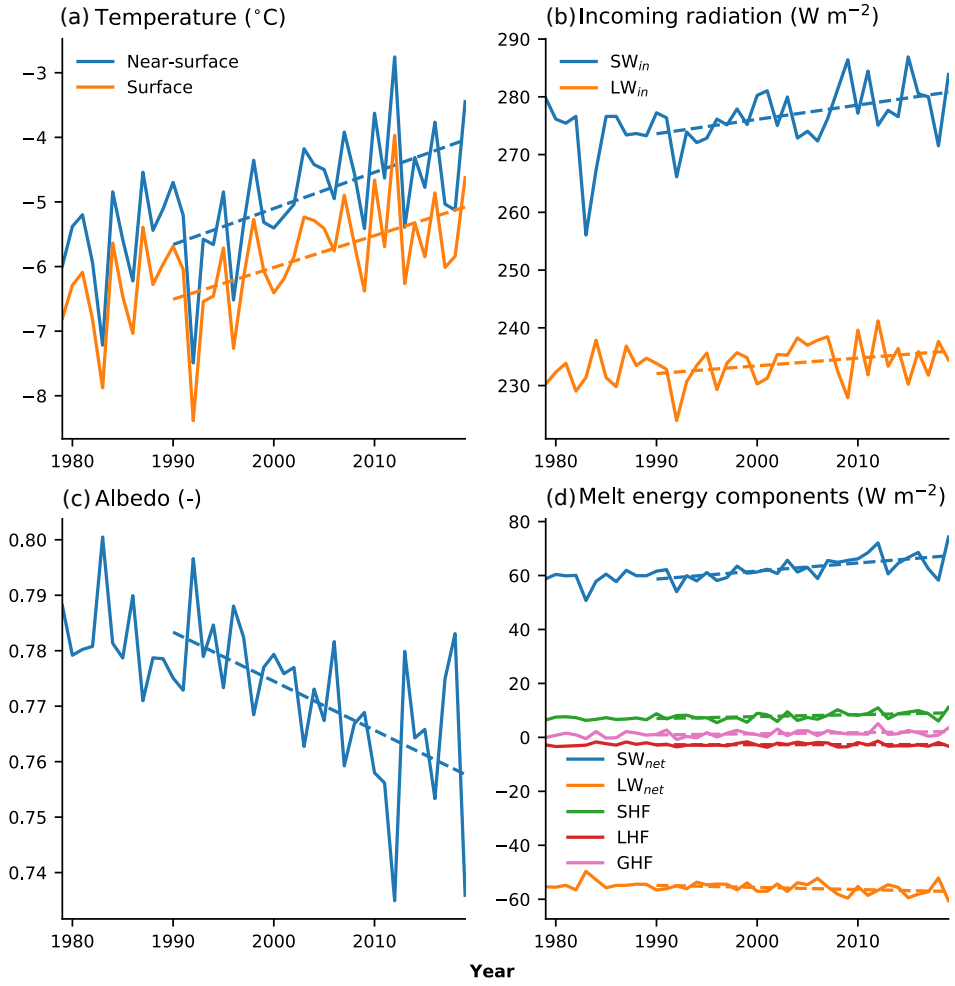

Figure 1.10: 1979–2019 GrIS summer mean averages of selected energy influential variables. a) Temperature (near-surface in blue and surface in orange) [°C], b) incoming radiation (SW_{in} in blue, LW_{in} in orange) [W m^{-2}], c) albedo [-], and d) melt energy components (SW_{net} in blue, LW_{net} in orange, SHF in green, LHF in red, and GHF in pink) [W m^{-2}]. Dotted lines show the 1990–2019 linear trend.

1

1.3. Open Research Questions

1.3.1. How will the SMB evolve under global warming?

According to current global warming projections, the SMB will likely continue to decrease (Oppenheimer et al., 2019). However, the evolution of SMB is uncertain. The surface mass loss has accelerated in the previous decades, and the acceleration is expected to continue. The physical mechanisms behind future acceleration are hypothesized to be loss of refreezing capacity (van Angelen et al., 2013), melt-albedo feedback, and the SMB-elevation feedback (Vizcaino et al., 2015; Pattyn et al., 2018), among others. The relative importance of these mechanisms is not yet evident. Also, between 2013 and 2018, there is a hiatus in melt increase due to regional atmospheric cooling relative to the previous years (Bevis et al., 2019; Khazendar et al., 2019; Mouginot et al., 2019). The extent to which pauses in warming affects the evolution of the SMB is still an open question.

Clouds are essential regulators of the surface energy balance of the GrIS. Cloud projections are one of the main contributors to climate sensitivity uncertainties (Bony et al., 2015). Further understanding of high-latitude cloud response to global warming is necessary in order to more reliably make projections of future GrIS SMB.

Regional climate models (RCMs) simulate the state-of-the-art projections of GrIS SMB. They have the advantage of explicitly simulating the GrIS surface climate and SMB processes at high-resolution. On the other hand, they are dependent on external climate forcing provided by a global climate model. As the global climate models cannot realistically simulate GrIS SMB, and given all the possible interactions between the GrIS and other components of the climate system (Fyke et al., 2018), it is uncertain how this affects the projections of RCMs.

This thesis provides answer to certain aspects of these questions in Chapter 3 and 4.

1.3.2. Is there a threshold for an irreversible mass loss?

The existence of a threshold for irreversible mass loss of the GrIS is well embedded in literature. The most widely used indicator for this threshold is a negative SMB (Gregory and Huybrechts, 2006; Robinson et al., 2012; van den Broeke et al., 2016). As the ID can never be positive, a negative SMB leads to a negative MB. Gregory and Huybrechts (2006) find this threshold to happen for a global warming of 3.1 K. However, such a threshold is likely more dependent on the time-integrated warming than the instantaneous warming. Taking this into account, Robinson et al. (2012) find a warming threshold of 1.6 K for irreversible mass loss.

van den Broeke et al. (2016) find that the SMB turns negative somewhere between 2024 and 2043 by extrapolating the current SMB trend. Non-linear feedbacks may change this estimation drastically. An example of such a non-linear feedback is the melt-elevation feedback. When the surface of the GrIS melts, its elevation becomes lower and warmer, giving way for more melt. This feedback may be so strong that it could drive irreversible mass loss for a global warming between 1.5 K - 2.0 K (Pattyn et al., 2018).

Gregory et al. (2004) propose that surface melt higher than snowfall is a threshold for irreversible mass loss. When more surface melt than snowfall occurs on the GrIS, this will ultimately lead to a negative SMB and irreversible mass loss. They find this threshold to be crossed for a 2.7 K warming of the GrIS.

The required global warming to give way for irreversible mass loss is uncertain. Much of this uncertainty is due to the lack of understanding of non-linear feedbacks. Further, knowledge on the timing of activations of these feedbacks may help to reduce this uncertainty.

Gregory et al. (2020) argue there is no threshold for irreversible mass loss, and that the GrIS will persist in a reduced state. They claim this is due to negative feedbacks, such as increased precipitation along the GrIS margin due to changes in atmospheric circulation. A full examination of this question would require detailed and physically based simulations of the GrIS over multi-century timescales, and possibly even multi-millennial timescales.

This question is partially adressed in Chapter 3 and 4.

1.3.3. How will the GrIS respond to contrasting Arctic and North Atlantic temperature trends?

Currently, the Arctic is warming twice as fast as the global average (Serreze and Francis, 2006; Serreze and Barry, 2011). This trend is to continue with the declining sea ice cover (Barnes and Polvani, 2015b). On the other hand, the North Atlantic has weakly cooled (Fig. 1.1b). The cooling of the North Atlantic may continue with warming temperatures, increased Arctic precipitation, and melting of land ice slowing down the North Atlantic Meridional Overturning Circulation (Sgubin et al., 2017). As the GrIS borders both regions, it is unclear how this will influence the GrIS SMB. Will one influence dominate the other? Will specific areas of the GrIS follow Arctic warming, while others follow North Atlantic cooling? Will global warming overwhelm both influences?

In Chapter 5, this thesis adresses the impact of a declining Arctic sea-ice on the GrIS SMB.

1.3.4. Can we extrapolate current trends in atmospheric circulation to the future?

Recent changes in atmospheric circulation have contributed about 50% to the GrIS surface melt increase (Delhasse et al., 2018). The most pronounced change is increased blocking events and/or duration near the GrIS, detected by the Greenland Blocking Index (GBI) metric. Simulations from the Coupled Model Intercomparison Project phase 5 (CMIP5; Taylor et al., 2012) project a decrease in the GBI with global warming (Hanna et al., 2018). However, the skill of the CMIP5 models to accurately project this circulation anomaly is questionable, as none of them are capable of representing the currently observed changes.

This thesis provide projections of atmospheric circulation changes in Chapter 3.

1

1.4. Translating Global Warming Projections to Surface Mass Balance Projections

Global climate models are the primary tool for simulating the future climate response to increasing greenhouse gases. To run efficient simulations, the horizontal resolution of global climate models is limited to ~1° (~ 100 km). At this resolution, the topography is smoothed (Fig. 1.11), leaving the global climate models unable to resolve the steep climate gradients over the GrIS and the narrow ablation zones (Cullather et al., 2014). The resolution required to represent them over the GrIS accurately is less than 10 km (van den Broeke et al., 2008). Projections of future SMB are also important for the projections of ice dynamics, and consequently sea levels, as ice sheet models require SMB as a boundary condition.

The classical approach to calculate SMB from global climate models is through positive-degree-day models (Braithwaite, 1995; Wilton et al., 2017). These models take precipitation and temperature data from global climate models and use simple parameterizations to estimate the SMB and SMB components. For example, the surface melt is parameterized by the number of days with a positive temperature (in Celsius) scaled by an ice or snow specific degree-day factor. These models perform poorly in conditions with high ablation, which is the expected result of global warming (van de Wal, 1996; Bougamont et al., 2007; Fettweis et al., 2020).

Regional climate models give state-of-the-art SMB projections. Their high-resolution and ability to explicitly calculate the SMB components and the surface energy balance makes them capable of realistically represent present-day SMB, which gives confidence in their future projections. With global warming, it is expected that the surface melt of the GrIS will increase (Fettweis et al., 2013a). Two significant (longer-term) consequences are topographic changes and a large amount of freshwater runoff to the ocean. These two consequences can potentially impact on the global circulation, that the regional climate models do not simulate. Also, regional climate models are computationally expensive, so they can only downscale a limited set of global climate projections for the 21st century.

Efforts to include a realistic representation of GrIS SMB into global climate models have resulted in state-of-the-art global climate models with elevation-class downscaling of SMB (Lipscomb et al., 2013; Alexander et al., 2019; Smith et al., 2020). Elevation classes divide each of the ~1° grid-cells into elevation bins, making it possible to account for sub-grid variations in atmospheric forcing associated with elevation variability. GrIS SMB downscaled through elevation classes can simulate a present-day SMB comparable to regional climate models (Vizcaíno et al., 2013; van Kampenhout et al., 2020).

Another promising approach is to use a variable resolution global climate model (Rhoades et al., 2016, 2018). Global climate models with variable resolution employ a high-resolution grid in areas of interest. A current present-day SMB reconstruction by van Kampenhout et al. (2019) employed such a model with a 25 km resolution over the GrIS.

To summarize, making fully-coupled projections of GrIS SMB is challenging. One of the main challenges is the relatively low resolution of global climate models

Table 1.1: Range of projected mean annual integrated GrIS SMB and SMB components for three Representative Consentration Pathways (RCPs). Values show the anomalies for the end of the 21st century (2081–2100) with respect to present-day values. Data from Fettweis et al. (2013a); van Angelen et al. (2013); Vizcaíno et al. (2014a); Oppenheimer et al. (2019).

Component	RCP2.6 (Gt yr^{-1})	RCP4.5 (Gt yr^{-1})	RCP8.5 (Gt yr^{-1})
SMB	-265 to 24	-527 to -35	-1059 to -114
Runoff	116 to 228	159 to 589	458 to 1150
Melt		648	634
Refreeze		133	78
Snowfall	17 to 115	18 to 94	52 to 136
Rainfall		74	174
Sublimation		-3 to 3	6

with respect to the required resolution for modeling SMB. Advances since the latest Intergovernal Panel on Climate Change report now allow for coupled projections of GrIS SMB in state-of-the-art global climate models.

1.5. Current projections of Greenland Surface Mass Balance

SMB is projected to decrease with higher atmospheric greenhouse gases (Table 1.1) and associated increasing radiative forcing. The uncertainty in how much the SMB will reduce is high. The main contributor to the SMB decrease is increasing runoff due to more surface melt. In response to increasing surface melt, the refreezing increases as more meltwater can be stored in the snow. However, the refreezing capacity (ratio of surface water to refreezing) over the GrIS is projected to decrease (van Angelen et al., 2013) as snow saturates.

With higher air temperatures, the atmosphere can hold more water, which results in more precipitation over the GrIS. Increased precipitation with global warming dampens the effect of increased meltwater somewhat. While snowfall and rainfall will increase, the percentage increase in rainfall is much higher than that of snow. On the one hand, increasing rainfall can add mass to the surface through refreezing (or zero contribution if it runs off). On the other hand, when rainfall refreezes, it releases latent heat to the snowpack, adding energy to raise snow temperature or adding energy for melt.

Projections of GrIS cloud cover show an increasing trend with global warming (Franco et al., 2013). The growing cloud cover traps more longwave radiation, which, together with higher atmospheric emission rates of longwave radiation, leads to more incoming longwave radiation. More cloudiness has a blocking effect on incoming solar radiation, which dampens the increasing melt-albedo-feedback. At the margins of the GrIS, SHF becomes a major contributor to melt energy through more heat advection.

1

1.6. Research questions

This thesis aims to gain further understanding of the coupled climate and SMB evolution, processes contributing to surface mass loss and the influence of atmospheric variability on SMB. To obtain these insights, we use the Community Earth System Model (CESM; Hurrell et al., 2013; Danabasoglu et al., 2020). CESM features an SMB calculation with downscaling via elevation classes (Lipscomb et al., 2013; Sellevold et al., 2019) and a snow model fit for polar applications (van Kampenhout et al., 2017), making it a state-of-the-art framework to answer the following questions:

1. **Does the elevation class method generate realistic sub-grid surface mass balance gradients?**
   The implementation of elevation classes in global climate models enables coupled SMB/global climate simulations, and elevation classes simulated SMB compares reasonably well against observations (Vizcaíno et al., 2013). So far, the simulation at the sub-grid scale has not been evaluated. Given the simple parameterizations the elevation class method uses (Vizcaíno et al., 2013; Lipscomb et al., 2013), it is not clear which relevant processes are accurately captured, or if the sub-grid SMB gradients are realistic. More knowledge about the inner workings of elevation classes is fundamental to interpret SMB projections from global climate models, particularly with a dynamic ice sheet model, and guiding future development.

2. **How much global warming leads to accelerated surface mass loss?**
   Acceleration of surface mass loss, possibly leading to irreversible GrIS mass loss, is expected as non-linear feedback to global warming is triggered. The most relevant feedback for accelerated surface mass loss is the melt-albedo feedback. However, the timing and magnitude of feedbacks in relatively long-term projections is not known. There is also potential for not yet discovered feedbacks, as coupled modeling of SMB with the global climate is a fairly new research area.

   This research question contributes towards open research questions 1.3.1 and 1.3.2.

3. **How do changes in atmospheric circulation influence the SMB with global warming?**
   Anthropogenic-forced changes in circulation are likely to occur with global warming. For the GrIS surface melt, the most relevant changes are in the GBI and the NAO. The GBI and the NAO are expected to decrease and increase, respectively (Hanna et al., 2018). A decrease in GBI and an increase in NAO are linked to cooling of the GrIS and reduced surface melt. As these projections were made without interactive calculation of SMB, new projections with updated global climate models with an interactive SMB calculation are necessary to provide knowledge of the coupled atmosphere-GrIS surface evolution. Also, previous generation global climate models were unable to

accurately represent the GBI, warranting new investigations with newer models.

Changes in atmospheric circulation can also influence precipitation. The North Atlantic storm tracks are essential contributors to precipitation over the GrIS. The physical link between changes in storm tracks, e.g., through North Atlantic cooling through a reduced North Atlantic meridional overturning circulation, is not yet fully understood.

This research question contributes towards open research questions 1.3.4.

4. **Does Arctic sea ice loss impact the GrIS SMB?**
   A rapidly warming Arctic may impact on the GrIS by increasing heat and moisture advection over the ice sheet. Arctic sea ice loss may also have an indirect effect on the GrIS SMB by forcing atmospheric circulation changes (Francis and Vavrus, 2012). As these latter changes are not possible to study using regional climate models, an investigation using global climate models with interactive SMB simulation is warranted.

   This research question contributes towards open research questions 1.3.3.

5. **Can we infer surface melt from global climate models through machine learning?**
   Recent advances in utilizing graphics processing units have increased the popularity of advanced machine learning techniques, due to their computational efficiency. Artificial neural networks, a machine learning technique, are attractive due to their ability to learn complex non-linear relations. As CESM2 includes interactive calculation of surface melt, is it possible for a neural network to determine the relationship between global climate evolution and surface melt evolution? And if so, could a neural network apply this artificial knowledge to infer melt from other global climate models?

1.7. Outline

The thesis will provide answers to the questions of Section 1.6.

Chapter 2 explores research objective 1. Here, the elevation classes implementation in the Community Earth System Model (CESM) version 1.0 is evaluated (Sellevold et al., 2019). This is done by comparing the energy and mass fluxes downscaled through elevation classes with a regional climate model. Several experiments are conducted to explore the elevation classes method's sensitivity to parameterizations. We find that CESM1.0 yields realistic sub-grid SMB gradients.

We find that while sub-grid scale SMB variation with elevation is realistically captured by the elevation classes downscaling, not all relevant processes show a realistic variation with elevation. We also find that the implementation of elevation classes in a global climate model partially compensates for a warm bias associated with topographic smoothing.

Chapter 3 deals with research questions 2 and 3. Here we use CESM2.1 and an idealized CO_2 scenario (Sellevold and Vizcaino, 2020). The motivation for using an

idealized CO_2 scenario is that it permits to more clearly separate the effect of the CO_2 forcing from the feedbacks and a lagged response. The idealized scenario ends up with an atmospheric CO_2 which is four times higher than pre-industrial levels, a concentration identical to a high emission scenario (SSP5-8.5). The higher CO_2 forcing causes atmospheric warming, which leads to accelerated SMB decrease for a global mean temperature increase of 2.7 K. The leading causes of the accelerated SMB decrease is a loss of refreezing capacity and acceleration of surface melt. Increased LW_{in} due to higher atmospheric temperatures is the primary contributor to increased melt energy before acceleration. At and after acceleration, increasing SW_{net} due to albedo decrease is the main contributor to increased melt energy. Reduced SW_{in} by thickening of clouds delays the melt-albedo feedback. We also find that the sensible heat flux accelerates after SMB acceleration, as the ice sheet ablation areas are limited to a warming up to melting point. At the same time, the atmosphere continues to warm, which increases the surface-to-air temperature gradient. This chapter also studies atmospheric circulation changes, and quantify their impact on GrIS melt and precipitation. CESM2.1 simulates GBI anomalies comparable to present-day with a trend towards negative GBI, which, together with a positive trend in the NAO, acts to reduce surface melt partially.

Research question 2 is also inspected in Chapter 4. This chapter has a similar experimental setup as in Chapter 3, but with a coupled ice sheet model; moreover, the experiment is run for 200 more years (Muntjewerf et al., 2020b). We find that for this experimental setup, the accelerated decrease in SMB requires an additional 1.5 K of global warming. Moreover, we see a strong influence of the SMB-elevation feedback on the acceleration of SMB. For areas close to or below the ELA, the SMB-elevation feedback doubles the ablation rate.

In Chapter 5 we explore the sensitivity of the SMB to Arctic sea ice loss (research question 4). We use idealized simulations with CESM2.1, with Arctic sea ice loss and SST increase representative of a 2 K warmer world (Sellevold et al., in review). In response to this forcing, SMB increases in winter due to more precipitation. The higher precipitation is caused by a moister atmosphere, together with increased occurrence of Arctic cyclones. In summer, surface melt increases. The increase in the surface melt is caused by higher sensible heat fluxes and associated melt-albedo feedback. The sea ice loss imposes increased 500 hPa geopotential heights over the GrIS, which enhances heat advection to the ice sheet and increases atmospheric blocking.

Research question 5 is dealt with in Chapter 6. Artificial neural networks are trained with CESM2 climate and melt data to translate global climate model projections to projections of GrIS surface melt (Sellevold and Vizcaino, in review). The neural network is used to predict surface melt from the full suite of CMIP6 climate models. The climate patterns the neural networks emphasize to predict surface melt, and points of surface melt acceleration are discussed.

Finally, concluding remarks and suggestions for future research are presented in Chapter 7.

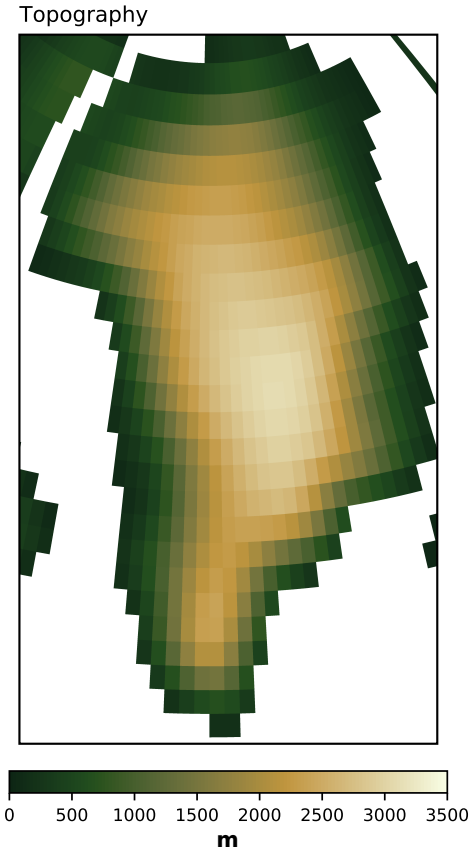

Figure 1.11: Topography (m) from the Community Earth System Model version 2.1 for the ~1° horizontal resolution.

2

Surface mass balance downscaling through elevation classes in an Earth System Model: application to the Greenland ice sheet

Big whirls have little whirls,
That feed on their velocity;
And little whirls have lesser whirls,
And so on to viscosity.

Lewis Fry Richardson

The modeling of ice sheets in Earth System Models (ESMs) is an active area of research with applications to future sea level rise projections and paleoclimate studies. A major challenge for surface mass balance (SMB) modeling with ESMs arises from their coarse resolution. This paper evaluates the elevation classes (EC) method as an SMB downscaling alternative to the dynamical downscaling of regional climate models. To this end, we compare EC-simulated elevation-dependent surface energy and mass balance gradients from the Community Earth System Model 1.0 (CESM1.0) with those from the regional climate model RACMO2.3. The EC implementation in CESM1.0

Parts of this chapter have been published in The Cryosphere **13**, 3193 (2019) (Sellevold et al., 2019).

combines prognostic snow albedo, a multi-layer snow model, and elevation corrections for two atmospheric forcing variables: temperature and humidity. Despite making no corrections for incoming radiation and precipitation, we find that the EC method in CESM1.0 yields similar SMB gradients as RACMO2.3, in part due to compensating biases in snowfall, surface melt and refreezing gradients. We discuss the sensitivity of the results to the lapse rate used for the temperature correction. We also evaluate the impact of the EC method on the climate simulated by the ESM and find minor cooling over the Greenland ice sheet and Barents and Greenland Seas, which compensates for a warm bias in the ESM due to topographic smoothing. Based on our diagnostic procedure to evaluate the EC method, we make several recommendations for future implementations.

2.1. Introduction

During the 20th century, the Arctic has warmed much faster than the rest of the world (e.g., Serreze and Francis, 2006; Screen and Simmonds, 2010; Hartmann et al., 2013; Overland et al., 2018) due to shrinking sea ice cover Serreze and Stroeve (2015), associated positive albedo-temperature feedbacks (Pithan and Mauritsen, 2014), and increased moisture and heat transport from the mid-latitudes (Screen et al., 2012). The Greenland ice sheet (GrIS) lies within this fragile and rapidly changing environment. The GrIS is the world's second largest ice sheet, after the Antarctic ice sheet, and has an estimated volume of 2.96×10^6 km^3 of ice, which would lead to an increase in global mean sea level by 7.36 m if it were all melted (Bamber et al., 2013). Since the 1990s, the GrIS has lost mass at an accelerated rate (Shepherd et al., 2012; Kjeldsen et al., 2015; Hanna et al., 2013a; Bamber et al., 2018a; Mouginot et al., 2019). This mass loss is projected to be sustained and contribute 0.04-0.21 m sea level rise by the end of the 21st century, depending on the climate scenario (Church et al., 2013). This broad range of estimates is due to uncertainties in climate scenarios, climate sensitivity and simulated mass balance of the GrIS by ice sheet models (ISMs). This latter uncertainty is currently being targeted by the Ice Sheet Model Intercomparison for CMIP6 (ISMIP6; Nowicki et al., 2016), a major international effort to investigate future ice sheet evolution, constrain estimates of future global mean sea level and explore ice sheet sensitivity to climate forcing.

State-of-the-art Earth System Models (ESMs; coupled climate models capable of simulating the Earth's chemical and biological processes, in addition to the physical processes, Flato, 2011) typically operate at a resolution of 1° (~ 100 km), which poses a challenge for studies with a regional interest, such as GrIS surface mass balance (SMB). For instance, the extent of GrIS ablation areas may be underestimated (Cullather et al., 2014). Also, there is a significant disparity between different model estimates of GrIS SMB even for models with higher resolution (Fettweis, 2018). Downscaling techniques are likely required to capture realistically the sharp gradients of SMB with elevation in the GrIS ablation zone (Lenaerts et al., 2019). Most common downscaling techniques for the GrIS SMB are

1. Dynamical downscaling, as is done in regional climate models (RCMs, e.g., Box and Rinke, 2003; Noël et al., 2018; Fettweis et al., 2017) and recently as regional grid refinement within ESMs (van Kampenhout et al., 2019). This type of downscaling allows for explicit modeling of the climate at relatively high resolution for a region of interest. Physical parameterizations need to be readjusted over the fine grid (Hourdin et al., 2017; Schmidt et al., 2017), and in some cases, the model physics can be better tuned for this region. A major disadvantage of this downscaling method is the computational cost and the dependency on another global model for lateral forcing in the case of RCMs.

2. Statistical downscaling (Hanna et al., 2005, 2011; Wilton et al., 2017) uses elevation corrections on either SMB or components of SMB (e.g., runoff). This type of downscaling is successful when realistic topographic gradients of SMB or melt are captured in the model (Helsen et al., 2012; Noël et al., 2016). However, in an ESM these gradients are typically not well-captured (Cullather et al., 2014), making this technique unsuitable.

3. Hybrid downscaling, where elevation corrections are applied to components of SMB or surface energy balance (SEB), and the full SEB and/or SMB are explicitly calculated offline at a higher resolution. This method was used by Vizcaíno et al. (2010) to construct a SMB field from a global climate model for coupling to an ice sheet model.

A variant of the hybrid approach with ”online” (that is, within the ESM) implementation has been developed recently. This method is based on the use of elevation classes (ECs) (Fyke et al., 2011; Lipscomb et al., 2013; Fischer et al., 2014; Alexander et al., 2019). It simulates the SEB and SMB over glaciated surfaces, with specific albedo and snowpack evolution for each EC. A benefit of this ”online” approach is that it is able to capture feedbacks between the downscaled surface simulation and the atmospheric component of the ESM. This method has been successfully applied to the simulation of historical and RCP8.5-scenario projections of the GrIS SMB and mass balance evolution (Vizcaíno et al., 2013; Lipscomb et al., 2013; Vizcaíno et al., 2014a; Fyke et al., 2014a,b) with the Community Earth System Model version 1.0 (CESM 1.0). However, the EC downscaling in itself and its effects on the downscaled SMB and SEB components in CESM1.0 or other models have not been analyzed or evaluated before. Our study aims to fill this gap in three steps. First, we compare the simulated EC gradients of SMB and SEB components with gradients simulated by an RCM. Second, we investigate the sensitivity of the GrIS surface mass balance simulation to the main EC downscaling parameter, i.e., the temperature forcing lapse rate. It must be noted that our model does not downscale precipitation. Third, as the downscaling of SMB in the ECs takes place online within the climate model, we investigate how the EC implementation impacts the regional climate.

Although we analyze the particular EC implementation in a specific ESM (CESM1.0), we aim to provide an evaluation and diagnostic framework to guide future implementation of EC downscaling in other climate models, for offline SMB estimates, and/or forcing of ice sheet models.

The paper is structured as follows: Section 2 describes the modeling setup as well as the regional model used for evaluation. In Section 3 we present the results. The discussion (Section 4) addresses the strengths and limitations of the EC implementation in CESM1.0. Section 5 gives the main conclusions and the outlook.

2.2. Methods

2.2.1. CESM1.0 and EC downscaling scheme

The model used for this study is the Community Earth System Model 1.0.5 (CESM1.0) (Hurrell et al., 2013) with all components active. The atmospheric model is the Community Atmosphere Model 4 (CAM4; Neale et al., 2013) which is run at a horizontal resolution of 0.9° × 1.25° and has a finite volume dynamical core. The land model is the Community Land Model 4.0 (CLM4.0; Lawrence et al., 2011) which is run at the same horizontal resolution as CAM4. Within a CLM4.0 grid cell, different land cover types can exist. The grid cell average passed to the atmosphere is calculated with an area-weighted average of the fluxes. The ocean is simulated with the Parallel Ocean Program 2 (POP2; Smith et al., 2010) with a nominal resolution of 1°. The ocean model grid is a dipole with its northern pole centered over Greenland to prevent numerical instabilities, implying a higher effective resolution around Greenland. Sea ice is modeled with the Los Alamos Sea Ice Model 4 (CICE4; Hunke et al., 2010; Jahn et al., 2012) which runs on the same grid as the ocean. The ice sheet model in CESM1.0 is the Glimmer Community Ice Sheet Model 1.0 (CISM1.0; Rutt et al., 2009; Lipscomb et al., 2013), with a default resolution of 5 km. For the simulations performed in this study, the GrIS ice thickness and extent does not evolve, i.e. it is static. A static ice sheet surface that corresponds to present-day observations (Bamber et al., 2013) is used to downscale SMB, energy fluxes and other quantities at the land/atmosphere interface through the EC scheme.

The main steps for the EC calculation in an ESM are as follows

1. A set of elevation classes are defined for each (partially) glaciated grid cell in the land model.
2. A selected set of atmospheric variables are downscaled by applying simple elevation corrections (typically, prescribed lapse rates).
3. The land model calculates the SEB and SMB per EC.
4. EC outputs are area-averaged per grid cell, and these averages are coupled to the atmospheric component.

In the following, the EC calculation is described in more detail. SMB calculations in CESM1.0 are done in CLM4.0 through ECs using the CLM4.0 snowpack mass balance scheme. EC downscaling accounts for sub-grid elevation variability. SMB is explicitly calculated at multiple surface elevations to force the higher resolution ice sheet model. The EC calculation is activated in the glaciated fraction of any grid cell with total or partial glacier coverage within a pre-defined region of interest (e.g., Greenland for the present study).

The EC method takes sub-grid surface elevation data from the ice sheet model and bins them into n ECs. In this study, n is 10 and the $n+1$ boundaries are fixed at 0, 200, 400, 700, 1000, 1300, 1600, 2000, 2500, 3000 and 10000 m elevation a.s.l. The choice of n=10 was motivated by a compromise between computing time and increased (vertical) resolution. Offline test showed this number to be appropriate, and is the default for CESM1.0. After this binning, CLM4.0 calculates the relative weight of each EC within a given grid cell, as well as the mean topography for each EC. The weight of each EC within a grid cell is determined by the area of the high-resolution topography dataset that lies within an EC. These weights are used to calculate the grid cell average that will be output of CLM4.0 and coupled to CAM4, as well as for the interpolation of SMB and ice sheet surface temperature (which is equivalent to the temperature at the bottom snow/ice layer in CLM), which are standard forcings for ice sheet models (Goelzer et al., 2013).

Through the coupling with the atmosphere model, CLM4.0 receives surface incoming shortwave and longwave radiation, precipitation, 10-m wind, relative and specific humidity, surface pressure, and 2-m air temperature. Incoming radiation, precipitation (which has a complex variation with elevation; Noël et al., 2016), and wind are kept constant across all ECs within a grid cell. In contrast, the method downscales near-surface (2m) air temperature to the ECs with a default lapse rate of 6 K km^{-1}, and specific humidity is downscaled by assuming the relative humidity to be constant with elevation (Lipscomb et al., 2013). At each EC, an energy balance model is used to calculate the surface energy balance every 30 minutes (SEB; W m^{-2}) as

$$M = SW_{in}(1-\alpha) + LW_{in} - \epsilon\sigma T^4 + SHF + LHF + GHF, \tag{2.1}$$

where M is the melt energy [W m^{-2}], SW_{in} is the incoming solar radiation [W m^{-2}], α is the surface albedo [-], LW_{in} is incoming longwave radiation [W m^{-2}], ϵ is surface emissivity [-], σ is the Stefan-Boltzmann constant [W m^{-2} K^{-4}], T is the surface temperature [K], SHF is the sensible heat flux [W m^{-2}], LHF is the latent heat flux [W m^{-2}], and GHF is the subsurface heat flux into the snow or ice [W m^{-2}]. For these surface fluxes, positive values indicate energy transfer from the atmosphere to the land surface, and from the subsurface to surface for GHF. Snow albedo is calculated based on snow grain size, depth, density, and other properties (Flanner and Zender, 2006). The first term on the right-hand side of Eq. (2.1) is the net solar radiation, and the sum of the second and third term on the right-hand side is the net longwave radiation. As a result of the SEB calculation, CLM4.0 calculates prognostic temperature, wind, relative humidity, and other quantities, taking into account the simulated exchanges of heat and moisture and surface roughness.

Additionally, the SMB (mm water equivalent yr^{-1}, referred to as mm yr^{-1} in this paper) is calculated at each EC, with the same frequency as the SEB calculation, as

$$SMB = SNOW + REFR - MELT - SUBL, \tag{2.2}$$

where $SNOW$ refers to the snowfall rate, $REFR$ is the refreezing rate of snowmelt and rainfall, $MELT$ is the sum of snow and ice melt rates, and $SUBL$ is the rate of sublimation/evaporation minus deposition/condensation. Rain and meltwater that

do not refreeze are routed to runoff. For further details on the calculation of SEB and SMB, see Vizcaíno et al. (2013). Total snow mass is limited to 1 m water equivalent, so that any precipitation falling on 1 m of snow will be routed to the ocean. This is to avoid snowmass to grow infinitely, as the model does not include snow-to-ice compaction physics.

The resulting SMB is interpolated onto the ice sheet grid, in two steps: first, with a bilinear horizontal interpolation per EC, and second with a vertical linear interpolation between two ECs (above and below), based on the ice sheet model high-resolution topography.

2.2.2. Simulations design

We perform four CESM1.0 simulations with an identical setup, except for a different temperature lapse rate forcing to the ECs. The lapse rate forcing is the same across all ECs and varies only between simulations. These four lapse rates are 1 K km^{-1}, 4 K km^{-1}, 6 K km^{-1} (default) and 9.8 K km^{-1}, and we refer to the corresponding simulations as EC-1K, EC-4K, EC-6K, and EC-9.8K, respectively. EC-1K is chosen to represent minimal activation of the EC calculation. EC-4K is chosen as a lapse rate forcing between EC-1K and EC-6K that is close to the summer lapse rate over the Greenland ice sheet as estimated from observations (e.g., Fausto et al., 2009). As the upper limit of the magnitude of the lapse rate, 9.8 K km^{-1} (dry adiabatic lapse rate) is used.

All simulations start in 1955 from a CMIP5 historical run that is evaluated in detail in Vizcaíno et al. (2013) (which also describes the spinup procedure and the setup for the EC-6K) and run to 2005. All CESM1.0 model components are allowed to vary freely. The first 10 years are used for model adjustment to the new lapse rate, leaving the period 1965-2005 for analysis.

2.2.3. RACMO2.3 and the evaluation procedure

For evaluation of the EC downscaled simulation of SEB and SMB, we compare with the dynamical downscaling in the Regional Atmospheric Climate Model version 2.3 (RACMO2.3; Noël et al., 2015) with a horizontal resolution of $\sim$ 11 km, and forced by the ERA-Interim reanalysis (Dee et al., 2011). We analyze the period between 1965 and 2005 for both RACMO2.3 and CESM1.0. As we are only comparing CESM1.0 simulations with identical initial conditions, we are likely to sample a different realization of climate variability than the reanalysis forced RACMO2.3. RACMO2.3 has been successfully evaluated in multiple studies by comparison with in-situ and remote sensing observations (Ettema et al., 2009, 2010; Ran et al., 2018). Version 2.3 includes updates in cloud microphysics, surface and boundary layer microphysics, radiation and precipitation (Noël et al., 2015). For the latter, precipitation falls exclusively as snow when near-surface temperatures are between -7°C and -1°C.

For the comparison, we use SEB and SMB components simulated at each EC with those simulated at the native grid of RACMO2.3. For CESM1.0, this results in between 1 and 10 values per CLM4.0 grid cell, depending on sub-grid elevation heterogeneity. We subtract each EC value of SEB or SMB component from the grid cell average, as well as the corresponding EC topographic height from the CLM4.0

mean height. We subtract these averages to only capture gradients within each grid cell, and to reduce the effect of internal climate variability. With these differences, we calculate a linear function with elevation. The slope term of the linear function will be referred to as the gradient. To generate these gradients for RACMO2.3, we first cluster RACMO2.3 model output from the 11 km native grid onto the CLM4.0 grid ($\sim$ 100 km). We then calculate averages for each RACMO2.3 SEB/SMB component and surface elevation over the coarse CLM4.0 grid cells. We subtract these averages from the native original values, and we construct the gradients via a linear fit. In this way, up to 56 RACMO2.3 grid cells are mapped into each CLM4.0 grid cell giving a total of 13,311 points for evaluation. For CLM4.0, the resulting number of points is 1,551.

For comparison of the overall downscaled SMB in CESM1.0 to a previous RACMO version (2.1), and an evaluation of the simulation at the mean elevation, see Vizcaíno et al. (2013).

2.3. Results

2.3.1. Process-based comparison of EC and dynamical downscaling

We use CESM1.0 output from a simulation using the default lapse rate forcing of 6 K km^{-1} (EC-6K). Figure 2.1 illustrates the comparison of the downscaled SEB component gradients for CESM1.0 ECs and RACMO2.3 RCM. Regression slopes m (gradients) and r-values (correlation with elevation) are given in Table 1.

In CESM1.0, incoming solar radiation is not downscaled. As a result, all ECs within a grid cell receive the same amount as simulated by the atmospheric component. In reality, however, incoming shortwave radiation generally increases with elevation as a result of thinner clouds (van den Broeke et al., 2008; Ettema et al., 2010). RACMO2.3 simulates the incoming shortwave elevation gradient as 15.1 W m^{-2} km^{-1} (Table 2.1, Fig. 2.2a), giving less energy with decreasing elevation. On the other hand, for the absorbed solar radiation (Eq. 2.1), albedo variations generally dominate over the variations in incoming solar radiation. The albedo gradient (Fig. 2.1a) is underestimated in CESM1.0 (0.019 km^{-1}, lower albedo with decreasing elevation) when compared to RACMO2.3 (0.081 km^{-1}). Part of this difference may be explained through CESM1.0 not being able to capture the anomalies (-0.35 to -0.20, Fig. 2.1a) corresponding to very low albedos in RACMO2.3. These differences in the models arise from the treatment of albedo during bare ice exposure. Both models treat snow albedo in a sophisticated fashion (Flanner and Zender, 2006). On the other hand, CESM1.0 and RACMO2.3 treat bare ice albedo quite differently. CESM1.0 uses a fixed value of 0.50 (0.60 for visible light and 0.40 for near-infrared radiation) while RACMO2.3 uses albedo from satellite observations (Noël et al., 2015), which can be as low as 0.30 for the simulated period. The albedo in RACMO2.3 is better correlated with elevation (r=0.60) than CESM1.0 (r=0.35). As a result of the underestimated gradients in both downwelling shortwave and albedo in CESM1.0, the net solar radiation gradient is also underestimated: -3.5 W m^{-2} km^{-1} (CESM1.0) compared to -19.6 W m^{-2} km^{-1} (RACMO2.3), as illustrated

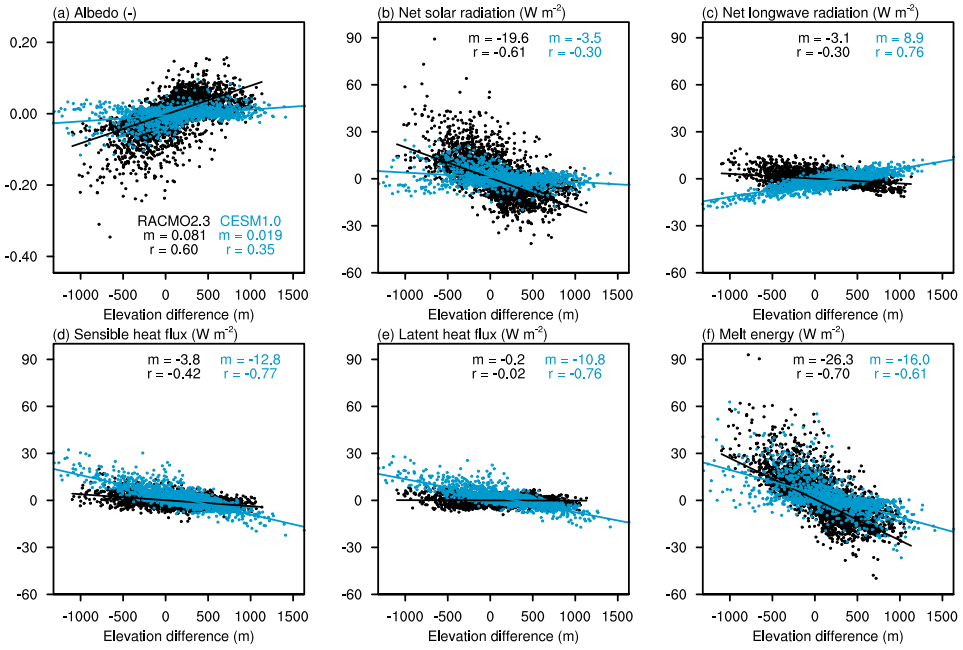

Figure 2.1: Comparison of EC downscaling (simulation EC-6K, blue) versus dynamical downscaling in a RCM (RACMO2.3, black) for several summer (JJA) SEB components and near-surface climate, a) albedo, b) net solar radiation (W m^{-2}), c) net longwave radiation (W m^{-2}), d) sensible heat flux (W m^{-2}), e) latent heat flux (W m^{-2}) and f) melt energy (W m^{-2}). The x values show deviation of surface elevation (m) from the coarse grid cell ($\sim$ 100 km) mean, and the y values show deviation of the physical quantity from the grid cell mean. In plots (b) through (f), positive y values indicate more energy available for melting. Melt energy (f) is the sum of the radiation and turbulent flux in terms in (b) through (e), plus the ground heat flux (not shown). The lines represent least-squares linear regression. The annotated m is the least-squares linear regression gradient (W m^{-2} km^{-1} or km^{-1} for albedo), r is the correlation coefficient.

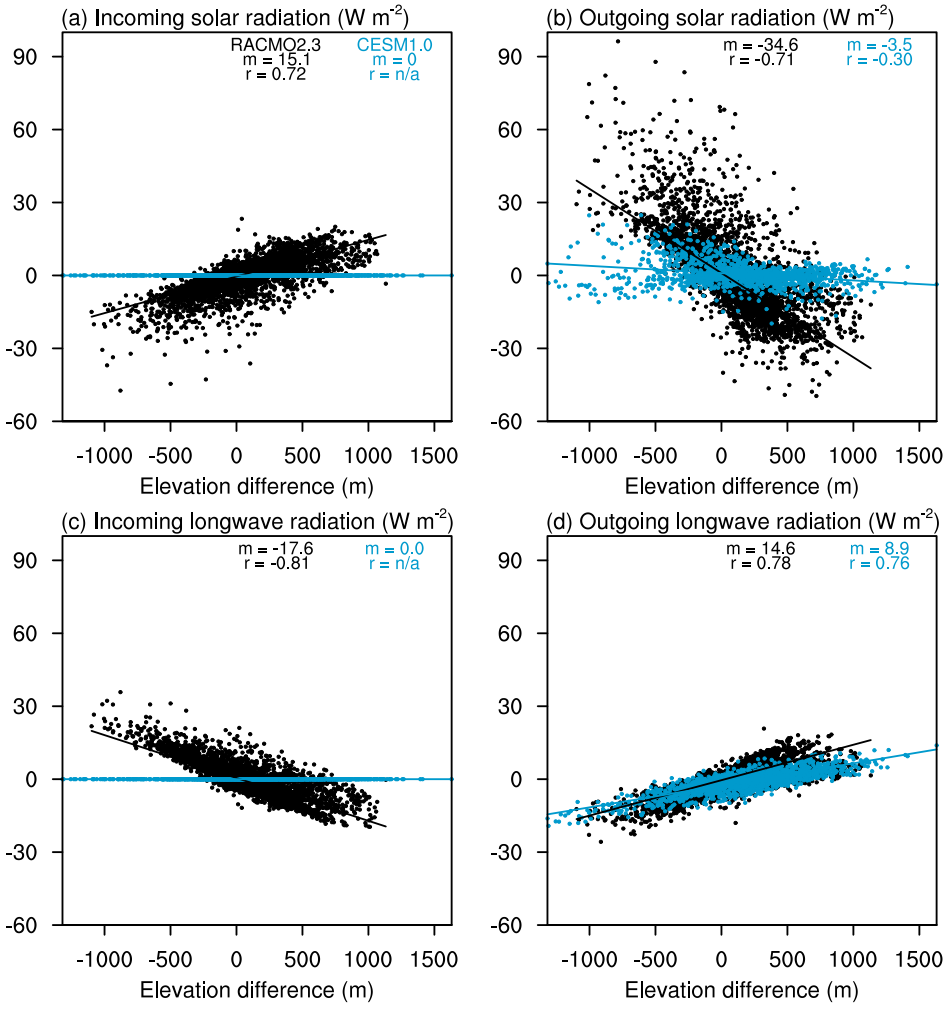

Figure 2.2: Same as figure 1, for summer SEB components from EC-6K (blue) and RACMO2.3 (black). a) Incoming solar radiation (W m^{-2}), b) outgoing solar radiation (W m^{-2}), c) incoming longwave radiation (W m^{-2}) and d) outgoing longwave radiation (W m^{-2}). The lines represent least-squares linear regressions. The annotated m is the least-squares linear regression gradient (mm yr^{-1} km^{-1}, r is the correlation coefficient.

Table 2.1: Gradients (m) and correlation with elevation (r; unitless) of surface energy and mass balance components as simulated through EC downscaling in CESM1.0. Values correspond to JJA (energy) and annual (mass) averages for the period 1965-2005. Melt energy is the sum of the net shortwave and longwave radiation and the heat fluxes. Surface mass balance is the sum of snowfall and refreezing, minus melt and sublimation.

	RACMO2.3		CESM1.0	
	m	r	m	r
Surface energy balance components				
Incoming solar radiation (W m^{-2} km^{-1})	15.1	0.72	0.0	-
Albedo (km^{-1})	0.081	0.60	0.019	0.35
Net solar radiation (W m^{-2} km^{-1})	-19.6	-0.61	-3.5	-0.30
Incoming longwave radiation (W m^{-2} km^{-1})	-17.6	-0.81	0.0	-
Net longwave radiation (W m^{-2} km^{-1})	-3.1	-0.30	8.9	0.76
Sensible heat flux (W m^{-2} km^{-1})	-3.8	-0.42	-12.8	-0.77
Latent heat flux (W m^{-2} km^{-1})	-0.2	-0.02	-10.8	-0.76
Ground heat flux (W m^{-2} km^{-1})	0.4	0.05	2.1	0.46
Melt energy (W m^{-2} km^{-1})	-26.3	-0.70	-16.0	-0.61
Surface mass balance components				
Snowfall (mm yr^{-1} km^{-1})	-218	-0.26	0	-
Melt (mm yr^{-1} km^{-1})	-717	-0.70	-425	-0.58
Refreezing (mm yr^{-1} km^{-1})	-129	-0.45	62	0.49
Sublimation (mm yr^{-1} km^{-1})	13	0.27	47	0.75
Surface mass balance (mm yr^{-1} km^{-1})	369	0.28	439	0.58

in Fig. 2.1b. In other words, the absorbed solar energy increases strongly with decreasing elevation for RACMO2.3, but only weakly for CESM1.0.

The downscaled net longwave radiation (difference between incoming and outgoing longwave radiation, Eq. 2.1) in CESM1.0 has an opposite elevation gradient (8.9 W m^{-2} km^{-1}) compared to RACMO2.3 (-3.1 W m^{-2} km^{-1}) as shown in Fig. 2.1c. That is, the net longwave energy available for melting increases with lower elevation for RACMO2.3, but decreases with lower elevation for CESM1.0. The reason for this difference is that CESM1.0 does not downscale the incoming longwave radiation, while RACMO2.3 simulates a gradient of -17.6 W m^{-2} km^{-1} with a relatively high correlation with elevation (r=-0.81, Fig. 2.2c, Table 2.1). This negative correlation in RACMO2.3 is caused by thicker clouds as well as higher water vapor and atmospheric temperatures at lower elevations (van den Broeke et al., 2008; Ettema et al., 2010). As the outgoing thermal radiation depends on the surface temperature, both models simulate negative gradients (Fig. 2.2d). The result is a positive gradient for the net longwave in CESM1.0. In RACMO2.3, the magnitude of the outgoing longwave gradient is smaller than the incoming longwave gradient, resulting in a net negative gradient. Due to the complex relationship between the different components of the longwave radiation, the net longwave has a low correlation with elevation in RACMO2.3 (r=-0.30). In contrast, CESM1.0 simulates a high correlation (r=0.76) as the surface temperature gradient directly controls the net longwave gradient. The net radiation gradient in CESM1.0 is 5.4 W m^{-2} km^{-1} and in RACMO2.3 is -22.6 W m^{-2} km^{-1} (Table 2.1).

In summary, biases in the downscaling of net radiation in CESM1.0 are due to null gradients of incoming radiation in the model, and weaker albedo gradients. As a result, the gradient is dominated by the outgoing longwave gradient in CESM1.0, whereas by the albedo and incoming longwave gradients in RACMO2.3.

Next, turbulent fluxes of latent and sensible heat are examined, as well as their contribution to the available melt energy with respect to radiation. The gradients of sensible and latent heat fluxes are negative in both models (Table 2.1); more energy is available for melting at lower elevation. The sensible heat flux gradient is stronger than the latent heat flux gradient and shows a larger spread of values (Fig. 2.1d,e.). In CESM1.0, this is a result of the elevation correction applied to the near-surface temperature (lapse rate). This correction increases atmospheric temperature and specific humidity at lower ECs and decreases them at higher ECs within each coarse grid cell. In RACMO2.3, these heat flux gradients are smaller and less correlated with elevation (r=-0.42 and r=-0.02, for sensible and latent heat fluxes, respectively) than in CESM1.0 (r=-0.77 and r=-0.76). Stronger sensible and latent heat gradients in CESM1.0 appear to compensate for most of the underestimation of the radiation gradients (Fig. 2.1c,d,e.), resulting in a melt energy gradient (-16.0 W m^{-2} km^{-1}) which is similar in magnitude and sign as RACMO2.3 (-26.1 W m^{-2} km^{-1}; Fig. 2.1f, Table 2.1).

Figure 2.3 compares snowfall, surface melt, refreezing, and SMB gradients between the two models. While CESM1.0 does not downscale snowfall, RACMO2.3 simulates an elevation gradient of -218 mm yr^{-1} km^{-1} that has little correlation with elevation (r=0.26), possibly due to the competition of the dominant effect of height-desertification (less snowfall at higher elevations due to colder and drier air), orographic forcing of snowfall, and small scale atmospheric circulation features (Ettema et al., 2009). Consistent with the melt energy gradients, the surface melt gradient in RACMO2.3 is -717 mm yr^{-1} km^{-1} while for CESM1.0 it is -425 mm yr^{-1} km^{-1} (Table 2.1).

The CESM1.0 refreezing gradient (62 mm yr^{-1} km^{-1}) is in disagreement with RACMO2.3 (-129 mm yr^{-1} km^{-1} and Fig. 2.3c). CESM1.0 simulates a positive gradient, implying increasing refreezing at higher ECs despite reduced melt rates. We hypothesize that at low elevation ECs, this is due to limited refreezing capacity in CLM4.0, as a result of the limited snow depth (Section 2.2.1). On the contrary, at the higher ECs, where the melt is lower, refreezing is favored due to lower snow temperatures, more available pore space and thicker snowpacks. The overestimation of rainfall at higher elevation (Vizcaíno et al., 2013) may also be an important factor. In contrast to CESM1.0, RACMO2.3 simulates a negative gradient of -129 mm yr^{-1} km^{-1} (Table 2.1), suggesting a dominant control from the increased melting at lower elevation. As the refreezing gradient results from the combination of opposite gradients, i.e., available meltwater and available refreezing capacity, the correlation with elevation is low in RACMO2.3 (r=-0.45, Table 2.1). It is similarly low in CESM1.0, in part due to lower correlation for the melt gradient than in RACMO2.3.

Regardless of substantial differences in melt gradients in both models, the SMB gradient is relatively close (Fig. 2.3d; CESM1.0: 439 mm yr^{-1} km^{-1} and RACMO2.3:

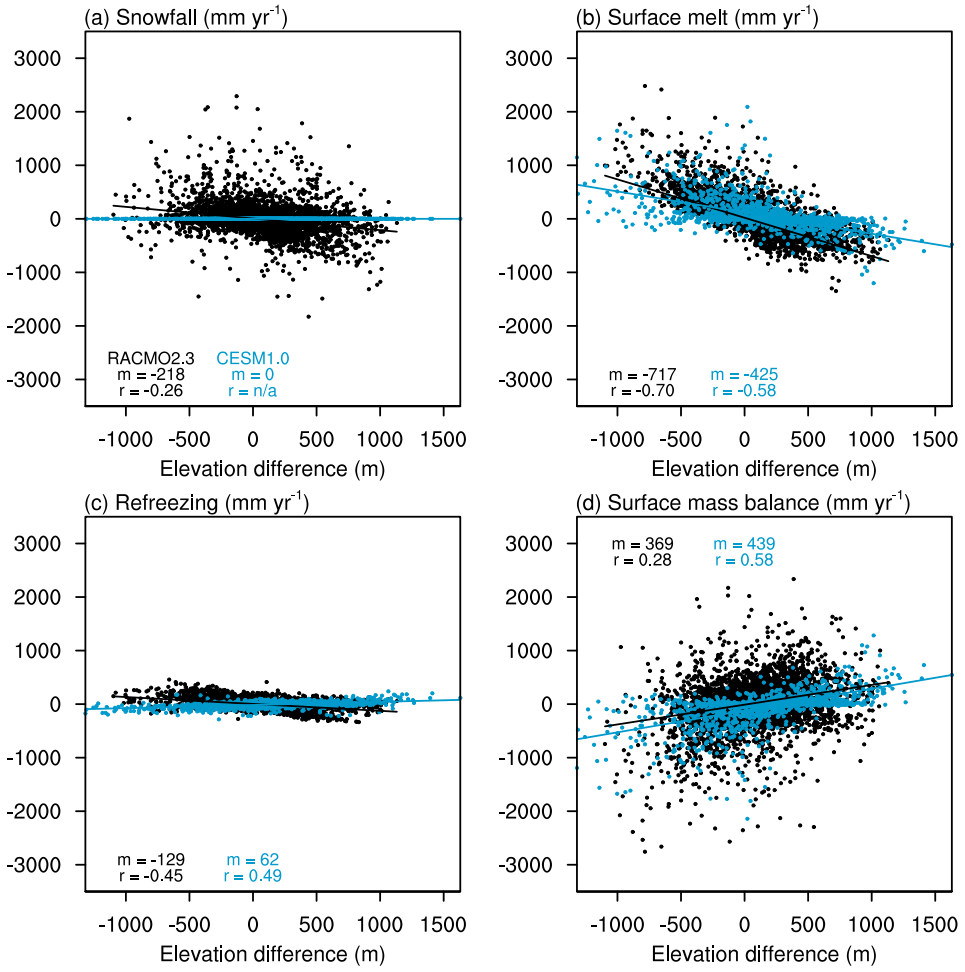

Figure 2.3: Same as figure 1, for annual SMB components from EC-6K (blue) and RACMO2.3 (black). a) Snowfall (mm yr^{-1}), b) Surface melt (mm yr^{-1}), c) refreezing (mm yr^{-1}) and d) surface mass balance (mm yr^{-1}). Surface mass balance is the sum of snowfall (a) and refreezing (c), minus the surface melt (b) and sublimation (not shown). The lines represent least-squares linear regressions. The annotated m is the least-squares linear regression gradient (mm yr^{-1} km^{-1}), r is the correlation coefficient.

369 mm yr^{-1} km^{-1}, Table 2.1). CESM1.0 compensates for underestimation of the melt gradient with the snowfall and refreezing gradients (in order of importance, see Table 2.1). In addition to the snowfall contribution of +218 mm yr^{-1} km^{-1} to the CESM1.0 SMB gradient difference with RACMO2.3, the difference in the refreezing gradient contributes with +191 mm yr^{-1} km^{-1}. The higher elevation correlation of SMB with elevation in CESM1.0 (r=0.58) compared to RACMO2.3 (r=0.27) is due to the null precipitation gradient in CESM1.0.

In summary, the EC method in CESM1.0 with the default lapse rate of 6 K km^{-1} (EC-6K) is approximately reproducing SMB gradients of RCM RACMO2.3. The EC method partially compensates for the biases in radiation downscaling with an overestimated turbulent heat flux gradient. The resulting melt energy gradients, however, are still lower than in RACMO2.3. However, the EC method compensates for this in the net SMB gradient due to lack of snowfall downscaling (leading to a more positive gradient relative to RACMO) and a positive bias in the refreezing gradient.

2.3.2. EC downscaling sensitivity to lapse rate of temperature forcing

Figure 2.4 shows how the most relevant energy fluxes and SMB respond to different lapse rate forcings. With a larger lapse rate forcing, the simulated sensible heat flux gradient is stronger, from -3.2 W m^{-2} km^{-1} in EC-1K to -20.0 W m^{-2} km^{-1} in EC-9.8K (Fig. 2.4 a-d). This implies that the stronger the lapse rate forcing, the more heat is redistributed from upper to lower elevations. The correlation with elevation only increases marginally when increasing the lapse rate forcing (Fig. 2.4 a-d).

Albedo gradients are sensitive to lapse rate forcing, from close to zero gradients in EC-1K to 0.029 km^{-1} in EC-9.8K (Fig. 2.4 e-h). Even with the maximum lapse rate forcing, CESM1.0 is only able to produce an albedo gradient that is 35% of the RACMO2.3 gradient. Albedo gradients are triggered by surface temperature and melt gradients resulting from turbulent heat flux gradients. In the case of EC-1K, the turbulent heat flux gradient is not sufficient to trigger substantial albedo-melt feedback. Downscaled albedos have a variation range of similar magnitude in EC-4K and EC-6K, however more points in EC-6K have non-null variations.

The combined effects of the turbulent heat flux gradients and the associated albedo gradients result in higher melt energy gradients with higher lapse rate forcing (Fig. 2.4 i-l). The melt energy gradient in EC-1K is -3.5 W m^{-2} km^{-1} which is very similar to the sensible heat flux gradient (-3.2 W m^{-2}). With higher lapse rate forcings, the difference between melt energy and sensible heat gradients becomes larger, which is interpreted as an effect of the albedo-melt feedback.

The melt energy gradient as simulated by RACMO2.3 is best matched with EC-9.8K (Figure 2.4, Table 2.1). However, EC-6K matches the SMB gradient best (SMB gradients for EC-1K, EC-4K, and EC-9.8K are 110, 310 and 711 mm yr^{-1} km^{-1}, Fig. 2.4, compare with Table 2.1). This is explained by compensation from the snowfall and refreezing gradients.

Figure 2.5 compares the downscaled SMB maps on the ice sheet model grid (5 km resolution) for the four lapse rates and RACMO2.3 (11 km resolution). Spatially,

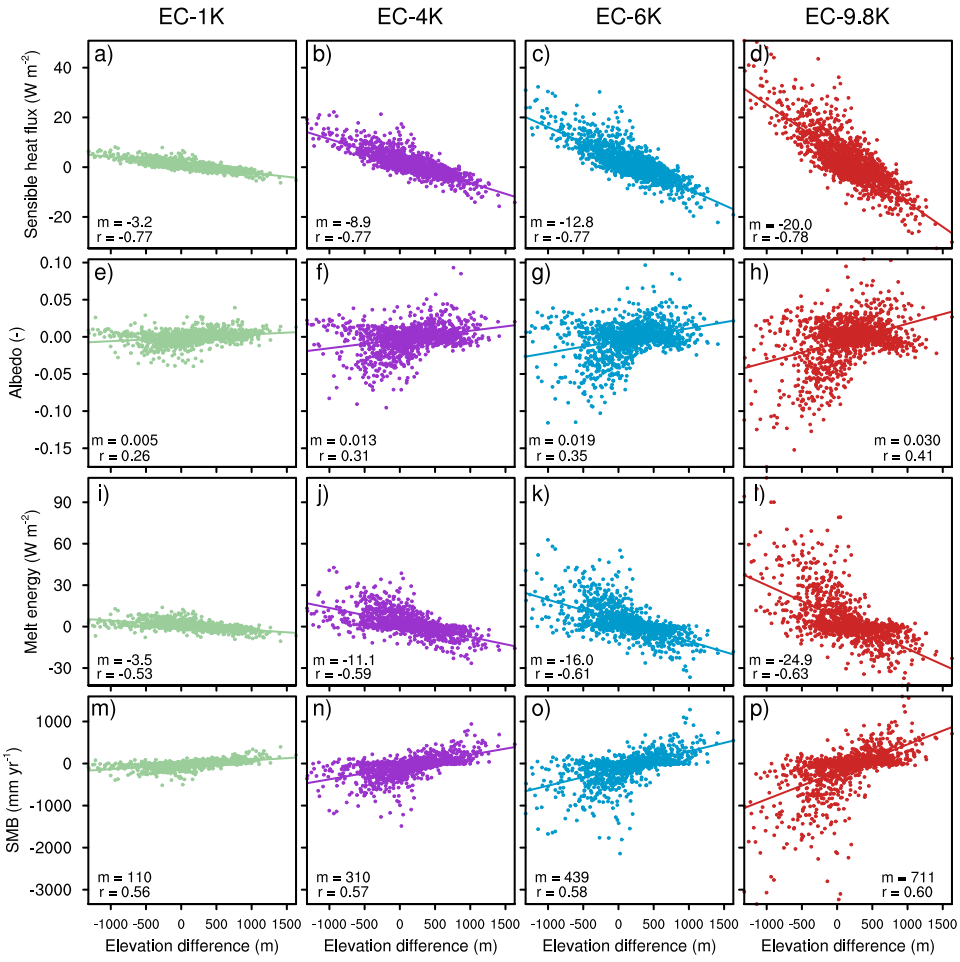

Figure 2.4: Comparison of 1965-2005 summer (JJA) downscaled energy fluxes among four simulations with different elevation corrections for the atmospheric temperature forcing. The first column corresponds to EC-1K, the second to EC-4K, the third to EC-6K and the last to EC-9.8K for a-d) sensible heat flux (W m^{-2}), e-h) albedo (-), i-l) melt energy (W m^{-2}), and m-p) surface mass balance (mm yr^{-1}). The x- and y-value represent deviation of surface elevation and energy component for each data point with respect to the climate model grid (~ 100 km) mean. The lines represent least-squares linear regressions. The annotated m is the least-squares linear regression gradient (W m^{-2} km^{-1} or km^{-1} for albedo), r is the correlation coefficient.

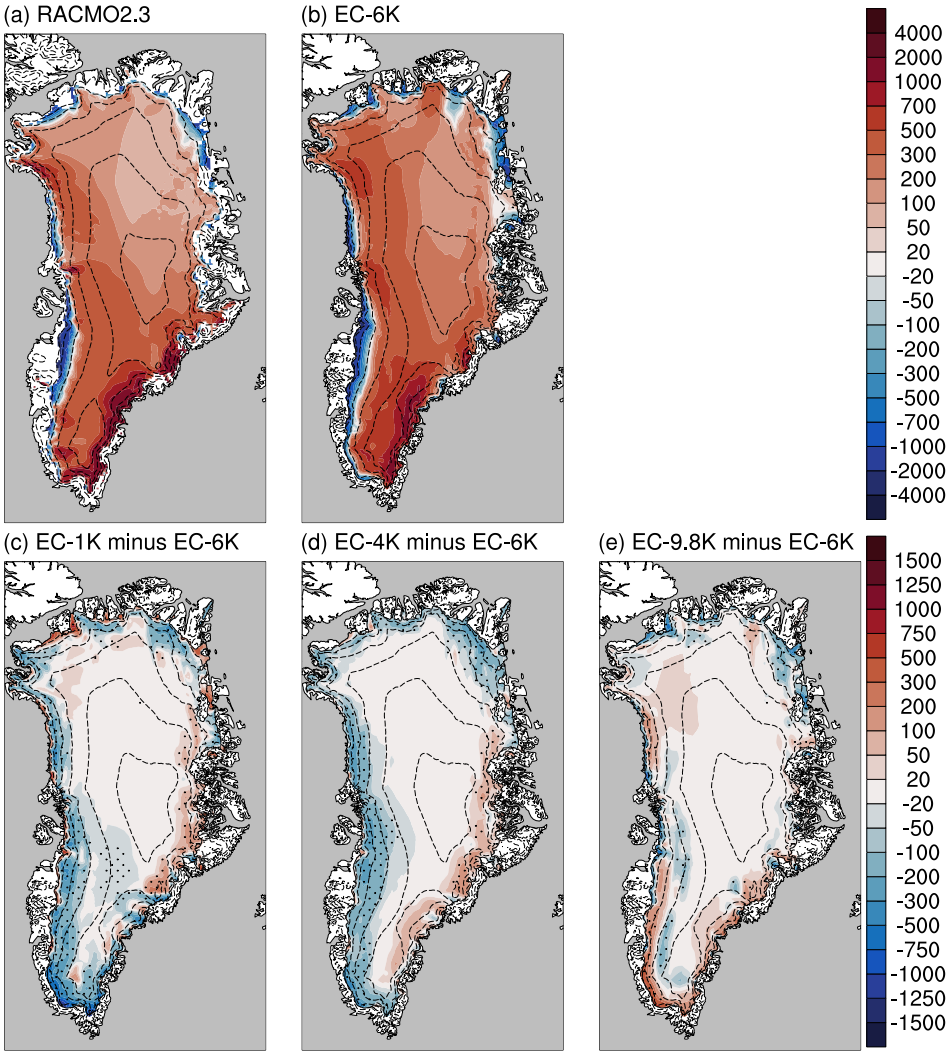

Figure 2.5: Climatological (1965-2005) SMB for RACMO2.3 (a), CESM1.0 downscaled to 5 km (b), and SMB anomalies (c, d, e) (mm yr^{-1}) using lapse rates c) 1 K km^{-1}, d) 4 K km^{-1} and e) 9.8 K km^{-1}. Anomalies are with respect to the default lapse rate of 6K km^{-1}. Solid black contour shows the ice sheet margin. Elevation contours (dashed) are plotted every 500 m. The black line shows the ice sheet margin. Black dots show where differences are significant at the 95% level according to a student t-test.

the largest responses to a varying lapse rate occur along the margin of the ice sheet, and close to the equilibrium line (Fig. 2.5c,d,e). At the margins, a low lapse rate leads to a higher SMB with respect to EC-6K in a very narrow band of only 10-20 km, due to the aforementioned relatively low turbulent fluxes and weak albedo-temperature feedbacks. In the EC-9.8K, this effect becomes opposite resulting in a similarly narrow band of lowered SMB (blue rim). Further inland, this extreme lapse rate leads to larger areas with higher SMB, as higher melt energy gradients reduce melt at high elevation ECs.

Larger lapse rates result in reduced ablation area, from 16.4% of the GrIS in EC-1K to 13.0% in EC-9.8K (Table 2.2. This reduction is due to an enhanced melt gradient (Fig. 2.4 i-l), reducing melt at higher ECs and resulting in a lower equilibrium line altitude (ELA, where SMB equals zero), and reduces interannual variability (although only mildly, from 4.0% to 3.0%). Due to this expansion of the accumulation area with higher lapse rates, the total SMB of the accumulation area increases (Table 2.2), although within the standard deviations. For the SMB of the ablation area, the area reduction is partially compensated with higher specific (local) ablation rates for higher lapse rates, resulting in the most negative SMB in the ablation area for EC-4K. The total SMB is the sum of the SMB for ablation and accumulation areas, and it is maximum for EC-6K. The SMB for EC-6K is at the same time the closest to RACMO2.3, also for the standard deviation. However, the range of variation of the mean total SMB across the four simulations is not large and is within the standard deviations. As an additional note of caution, the values in Table 2.2 result from four simulations with independent atmospheric simulation, perhaps sampling different segments of, e.g., multidecadal precipitation variability (Bromwich et al., 2001), and therefore reflect more than just the effect of the lapse rate choice.

To summarize, lapse rates lower than EC-6K result in larger ablation areas and lower integrated SMB. These results indicate a dominant effect on the CESM1.0 ELA simulation of higher melt rates at high elevation ECs versus reduced melt rates at low elevation ECs.

To complete this sensitivity investigation, we compare "prognostic" near-surface temperature gradients across the four simulations (Table 2.2). This prognostic temperature is calculated per EC within each CLM4.0 time step and is a result of heat and moisture exchange between surface and atmosphere. Therefore it differs from the prescribed lapse rate forcing. The prognostic temperature gradients are lower in magnitude than the respective lapse rate forcing for all CESM1.0 simulations. The magnitude of the June-August (JJA) gradient is also less than for December-February (DJF) and is approximately half of the forcing lapse rate. The former is also the case for RACMO2.3. The simulation EC-9.8K gives the prognostic temperature gradient closest to RACMO2.3, which is in between the EC-6K and EC-9.8K gradients. It is remarkable that the simulation EC-4K with the lapse rate forcing that is closest to the observational summer gradient (4.7 K km^{-1}, Fausto et al. (2009)) and RACMO2.3 (4.3 K km^{-1}) is however not the simulation with the closest prognostic gradient.

Table 2.2: Simulated whole-ice-sheet SMB, ablation area, total SMB in the ablation and accumulation areas, and prognostic near-surface temperature gradients for the four simulations performed in this study with varying lapse rates, and for the reference regional model RACMO2.3. Values correspond to the climatological (1965-2005) average with the standard deviation in parentheses.

	RACMO2.3	EC-1K	EC-4K	EC-6K	EC-9.8K
Surface mass balance (Gt yr^{-1})	382 (102)	326 (122)	326 (128)	372 (101)	367 (125)
Ablation area (% of total GrIS area)	10.9 (2.4)	16.4 (4.0)	15.6 (4.1)	13.4 (3.0)	13.0 (3.0)
SMB in ablation area (Gt yr^{-1})	-138 (45)	-142 (68)	-153 (75)	-128 (50)	-142 (48)
SMB in accumulation area (Gt yr^{-1})	520 (71)	468 (68)	480 (78)	500 (63)	509 (92)
Prognostic temperature lapse rate [JJA] (K km^{-1})	4.3 (0.2)	0.5 (0.0)	2.0 (0.1)	3.0 (0.1)	5.0 (0.2)
Prognostic temperature lapse rate [DJF] (K km^{-1})	4.6 (0.2)	0.8 (0.0)	2.5 (0.0)	3.6 (0.0)	5.8 (0.0)

2.3.3. Impact of the EC calculation on regional climate simulation

Next, we examine how the EC calculation in the land component (CLM4.0) affects the simulation of Arctic climate in CESM1.0. If the EC method is active in CLM4.0, sub-grid gradients in the ice sheet surface budget are coupled to the atmosphere model (and via the atmosphere to other components) during runtime. We compare two simulations for this analysis. The EC-1K simulation serves as the control as it represents the simulation closest to non-active EC downscaling, which is the standard for most CMIP5 ESMs. The EC-6K is used to assess the climatic effect of using the EC method. Figure 2.6 shows differences in selected climate variables between EC-6K and EC-1K.

Near-surface temperatures decrease over large parts of the GrIS and on average by 0.9 K in EC-6K with respect to EC-1K (Fig. 2.6a,b and Table 2.3). This relative cooling in EC-6K is due to two factors. First, because the atmospheric topography (the topography used by the atmospheric component) is more smoothed than the topography in the ice-sheet covered land grid cell, the atmospheric mean elevation per grid cell is lower than the land model mean elevation per grid cell. This gives higher ECs a higher areal weight per grid cell. Second, the characteristic quasi-parabolic shape of the ice sheet contributes to this areal effect. This results in the dominance of the net (negative) energy anomalies from high elevation ECs. Maximal cooling coincides with areas of rapid change in slope in the SE and NW. Downwind advection of colder air masses from the eastern side of the ice sheet causes mild cooling in the Greenland and the Barents Sea, which is amplified by the growth of sea-ice (Fig. 2.6h).

Turbulent heat fluxes respond most strongly over the Greenland ice sheet, the Labrador Sea and along the sea ice edges in Greenland and Barents Sea (Fig. 2.6c,d, and Table 2.3). Significant differences over the Greenland ice sheet are collocated with areas showing a significant decrease in air temperature. In these simulations, the atmosphere transfers turbulent heat to the surface on average (Fig. 2.6c). The reduction in air temperature, and consequently air humidity (not shown), results in decreased turbulent heat transfer. Over the Barents Sea, larger sea-ice covered areas cause a reduction in the heat transfer from the ocean to the atmosphere.

Net surface longwave radiation increases over the Greenland ice sheet where the near-surface temperature decreases (Fig. 2.6f). Over these areas, incoming longwave radiation decreases; however, this is overcompensated for by a reduction in emitted longwave radiation due to surface cooling.

Figure 2.7 compares near-surface temperature, turbulent heat fluxes, net longwave radiation and sea ice extent in EC-1K and EC-6K with ERA-Interim over the entire area in Fig. 2.6, with the tentative goal of assessing whether the EC method improves or deteriorates the climate simulation. However, the differences between EC-1K and EC-6K are small compared to the difference between these simulations and ERA-Interim, likely due to different realizations of internal climate variability. This precludes a robust conclusion. For Greenland, on the other hand, an assessment is more reliable as the differences between the EC-1K and EC-6K simulations are of the same magnitude as differences with RACMO2.3. The simulation of the

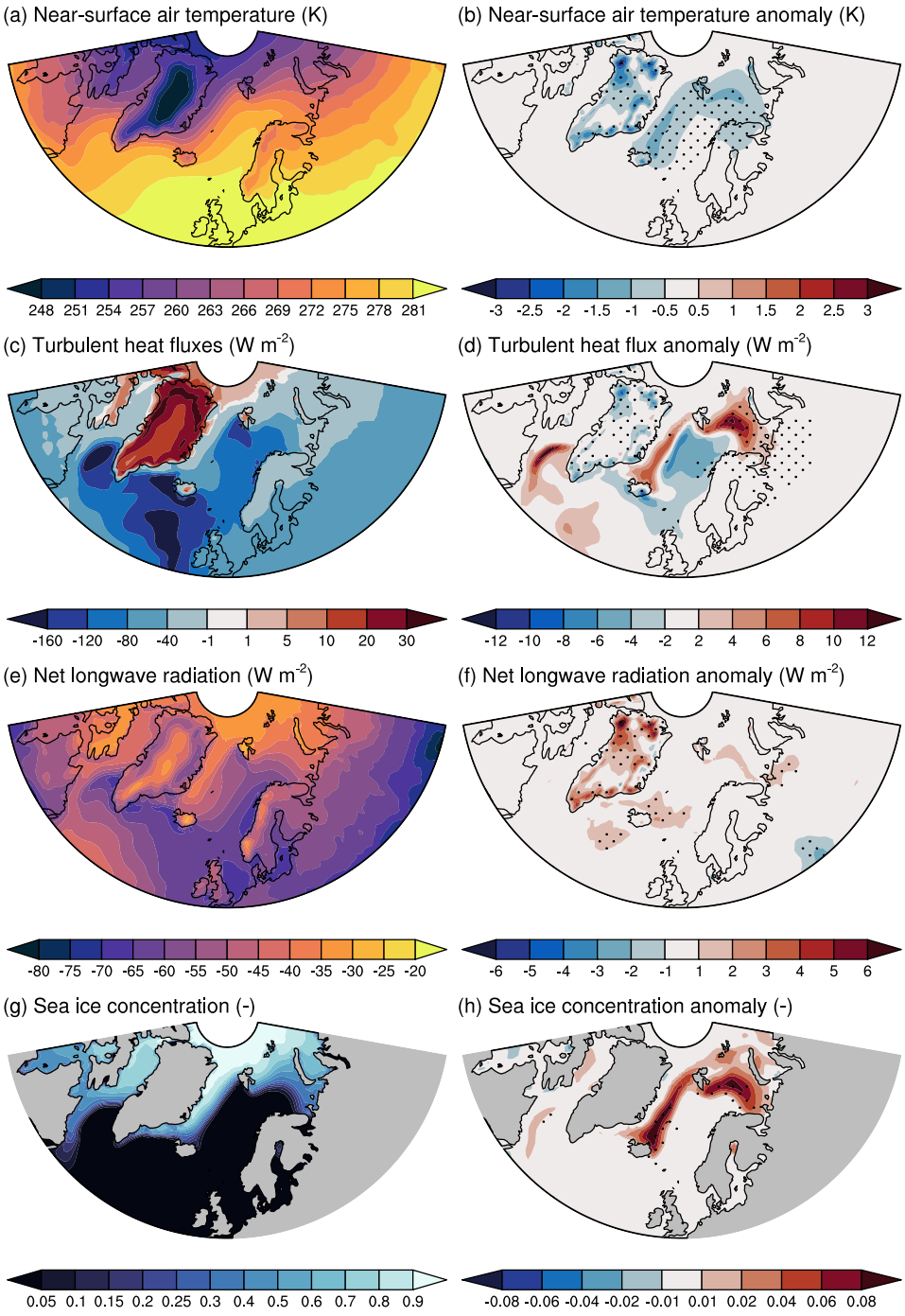

Figure 2.6: Annual climatology (1965-2005) of EC-1K (left column) and anomalies of EC-6K with respect to EC-1K, which approximate the EC imprint (right column). a,b) near-surface air temperature (K), c,d) turbulent (sensible+latent) heat fluxes (W m^{-2}), e,f) net longwave radiation (W m^{-2}) and g,h) sea ice concentration (-). Black dots indicate significance at the 95% level according to a students t-test. Positive signs for a-f indicate energy transfer from atmosphere to the surface.

Table 2.3: Simulated annual (ANN) and summer (JJA) GrIS averaged components of the surface energy with the standard deviation in parentheses. The period considered is 1965 to 2005. Closest values to RACMO2.3 are given in bold.

	RACMO2.3		EC-1K		EC-6K	
	ANN	JJA	ANN	JJA	ANN	JJA
Albedo (-)		0.81 (0.01)		0.78 (0.02)		0.78 (0.01)
Near-surface air temperature (K)	252.0 (0.8)	265.6 (0.8)	252.9 (0.8)	266.5 (0.9)	**252.0** (0.8)	**265.9** (0.8)
Turbulent heat flux (W m^{-2})	19.1 (0.5)	2.7 (0.7)	23.2 (0.8)	**3.0** (1.3)	**21.1** (0.6)	0.5 (1.0)
Net longwave radiation (W m^{-2})	-43.9 (0.9)	-52.4 (2.0)	-45.9 (1.2)	**-47.5** (3.4)	**-43.9** (1.0)	-44.9 (2.7)
Melt energy (W m^{-2})	2.8 (0.5)	10.2 (1.9)	3.5 (0.8)	12.4 (3.1)	**3.2** (0.6)	**11.6** (2.4)

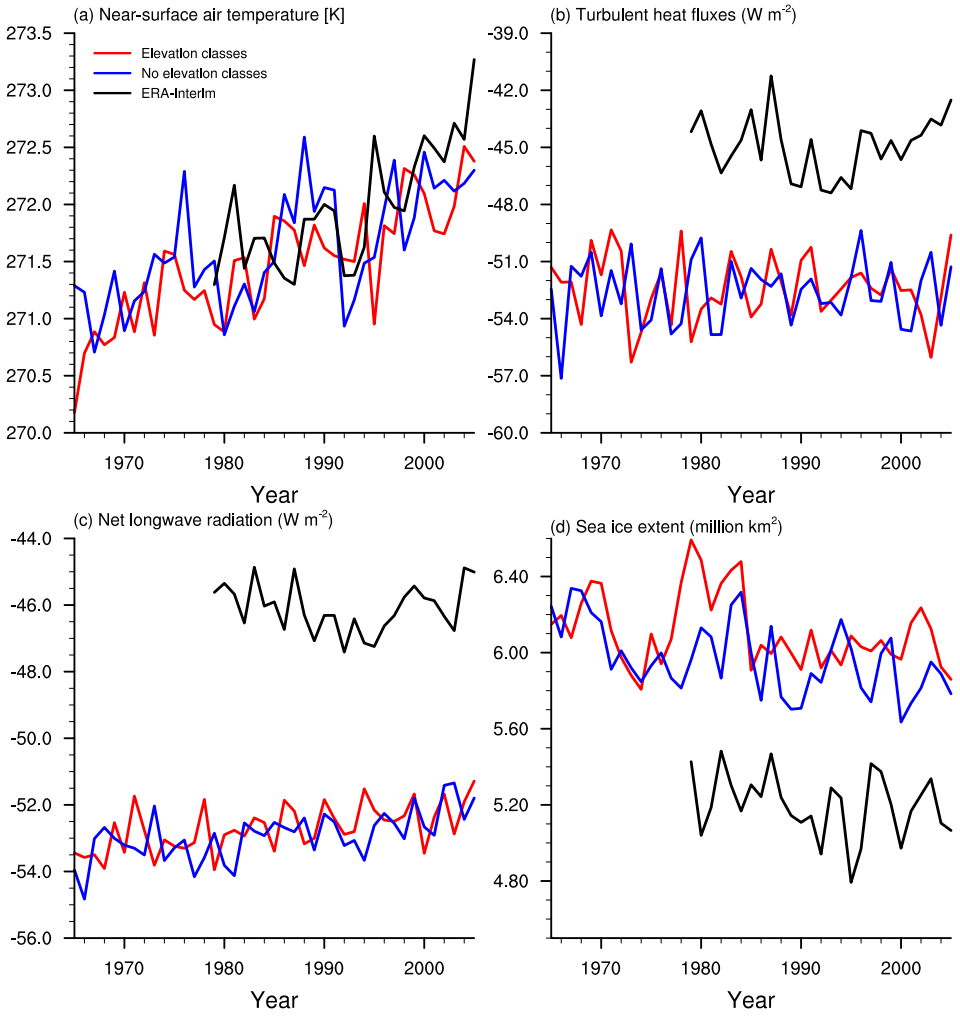

Figure 2.7: Annual means of selected climate variables in the simulations EC-1K ("No elevation classes", blue) and EC-6K ("elevation classes", red), and ERA-Interim (only 1979-2005, black) for reference. The data are area-weighted averages (integrated for sea-ice) for the region in Fig. 2.6.

GrIS-averaged annual and summer near-surface air temperature is improved in EC-6K, using RACMO2.3 as a reference, as well as the net longwave radiation, melt energy, and (only annual) turbulent heat flux (see bold values in Table 2.3). The simulated cooling partially counteracts the temperature overestimation in the ESM due to topographic smoothing, resulting in a close fit to RACMO2.3.

2.4. Discussion

This study has evaluated for the first time the EC method for SMB downscaling from a global climate model of ~ 100 km resolution to the much higher resolution (5 km) of an ice sheet model. Other studies (e.g., Alexander et al., 2019) have evaluated the effect of implementing ECs on the coarse grid cell, but not at the sub-grid resolution as done here. This evaluation uses gradients of SEB and SMB components as the primary metric. These gradients are obtained by linear regression of the components on sub-grid elevations in all GrIS grid cells. While this provides a systematic framework of comparison, it does not account for relevant non-linear elevation variations for SMB gradients (e.g., Helsen et al., 2012; Noël et al., 2016) and SMB components (e.g., precipitation); or heterogeneity arising from different Greenland climate sub-regions, local influences on climate (e.g. proximity of tundra, valleys, fjords), or proximity to the ELA.

We justify our comparison with the RCM as dynamical downscaling is the most advanced downscaling technique as shown in numerous evaluations (e.g., Ettema et al., 2010; Noël et al., 2015). However, one of the limitations of comparing with a RCM is that unlike an ESM, the RCM is laterally forced with reanalysis. Also, there are fundamental differences in the physical schemes and simulated climate components between the ESM and RCM compared here. Additionally, RACMO2.3 has some well-documented biases, e.g., an underestimation of net longwave radiation, which is compensated by the sensible heat flux (Ettema et al., 2010; Noël et al., 2015). Further, the RACMO2.3 model was forced at its lateral boundaries by ERA-Interim reanalysis (Dee et al., 2011), which limits the "intrinsic" or "natural" climate variability compared to an ESM. Therefore, a more systematic comparison could be made by forcing a RCM with the same ESM where the EC method is implemented.

As a result of the combination of EC downscaling and advanced snow physics (Lipscomb et al., 2013), CESM1.0 shows high skill in simulating GrIS climate compared to same-generation global climate models/earth system models (Cullather et al., 2014). The ability to realistically represent GrIS SMB in ESMs has been utilized for projections of future SMB change (Vizcaíno et al., 2014a; Fyke et al., 2014a,b), without a RCM for additional dynamical downscaling. Reliable simulation of the GrIS surface climate at ESM resolution enables exploration of the interaction between the high-resolution surface simulation and other climate components (e.g., atmosphere, ocean, sea-ice).

While the EC method in CESM1.0 realistically simulates SMB gradients, we have shown here major deficiencies in the simulation of individual gradients of surface energy and mass balance components compared to RACMO2.3. This is an important caveat for modelers who may need to calculate the SMB from individual components of the energy or mass balance, e.g., to perform corrections for one atmospheric

forcing field. It also limits the possibility to investigate individual processes at a higher resolution. In the following, we discuss the relative importance and possible fixes of the biases in these individual processes as identified for CESM1.0.

1. CESM1.0 does not capture low enough albedo values due to the use of a single fixed ice albedo, while bare ice has a broader range of albedos (Alexander et al., 2014). We recommend therefore the use of spatially varying ice albedos, e.g., to simulate the impacts of impurities on ice "darkening" (Wientjes et al., 2011; Ryan et al., 2018).

2. The EC scheme in CESM1.0 does not downscale incoming radiation, despite the fact that it varies over small scales at the GrIS surface (van den Broeke et al., 2008; Van Tricht et al., 2016a). The lack of downward longwave downscaling leads to an underestimation of net radiative energy at low elevation ECs and an overestimation at high elevation ECs. We recommend downscaling of incoming radiation to reduce over-compensation from the turbulent heat fluxes gradients and more realistically capture radiation-snow-ice interactions such as shortwave-generated subsurface snowmelt.

3. Since snowfall has no elevation corrections in CESM1.0, small-scale orographically induced precipitation, height-desertification effects, and small scale variations in the rain to precipitation ratio are not captured. Designing realistic and effective elevation corrections for precipitation is a challenging task as the precipitation's correlation with elevation is spatially highly variable over the GrIS (Noël et al., 2016). To account for fine-scale variations in the rain to precipitation ratio with a simple parameterization, we propose the implementation of a scheme relating the phase of precipitation with atmospheric near-surface temperature, similarly as in Noël et al. (2015).

4. CESM1.0 does not realistically simulate the refreezing gradient, mainly due to limited snow mass in the CLM4.0 snowpack and biased high rainfall rates at high elevations. A realistic simulation of refreezing is key in modeling the response time of an ice sheet to a changing climate (van Angelen et al., 2014) as it acts as a buffer for meltwater to run off the ice sheet surface. A more physically based treatment of snow could be used with a snow densification scheme that does not impose a maximum allowed snow depth. An intermediate approach is using relatively large snow and firn depths. As an example along this line, the maximum snow depth can be increased, as in the version 5.0 of CLM, with respect to CLM4.0 due to the further development of the snow scheme to allow for realistic firn simulation (van Kampenhout et al., 2017).

Assessing the optimal choice of lapse rate forcing proves challenging. In this study, the EC-1K results in the turbulent heat flux gradients closest to RACMO2.3 (Fig. 2.4a), but almost null melt energy and SMB gradients. EC-4K does not stand out in any way. EC-6K results in the most realistic SMB gradients, despite EC-9.8K comparing the best with RACMO2.3 for the melt gradient. This discrepancy

is because CESM1.0 does not downscale snowfall which has an opposite slope to the melt gradient. For the downscaled SMB, EC-6K and EC-9.8K give fairly similar results, making it hard to distinguish one or the other as the best choice. Further improvements of the physical representation of SMB processes at the EC scale might allow for a better identification of an observationally constrained optimal lapse rate.

Global climate models often have warm biases over high areas like the ice sheets, due to topographic smoothing. Here we showed that the EC implementation in CESM1.0 results in moderate cooling over Greenland, which fully compensates for the warm bias in CESM1.0 when compared to the RCM. The cooling pattern from the EC method is similar to that of Franco et al. (2012) who explored the sensitivity of the simulated GrIS surface climate to horizontal resolution with a RCM.

2.5. Conclusions

The EC downscaling as implemented in CESM1.0 results in realistic GrIS SMB gradients as shown through comparison with a state-of-the-art RCM. In CESM1.0, high turbulent heat flux gradients compensate for absence of incoming radiation downscaling. Explicit simulation of snow albedo enables the albedo-melt feedback which is shown to contribute to realistic melt gradients and consequently realistic SMB gradients. Therefore, we conclude that the EC classes method in CESM1.0 efficiently generates a realistic downscaled SMB, despite the fact that only temperature and humidity are downscaled.

Our sensitivity experiments show that a larger lapse rate for the temperature correction results in higher melt energy gradients, as expected. As a consequence of these gradients, ablation areas narrow in CESM1.0, although this result may be different for other models or ice sheet topographies. In turn, this leads to a general cooling downwind of Greenland and an increase in sea ice cover over the Greenland Sea and the Barents Sea. For future implementations of the EC classes within ESMs, we recommend evaluation of the effects on regional climate simulation.

Future improvements of the EC method could be headed towards realistic downscaling of the individual surface energy and mass budget components. Some concrete examples include, (1) a lower and/or spatially varying albedo; (2) downscaling of incoming radiation; (3) downscaling of precipitation phase; and (4) development of more adequate snowpack parametrizations for realistic representation of e.g., snow compaction, firn, and refreezing, fit for polar conditions. Some of these improvements are implemented in CESM2, where a lower albedo of 0.4 for bare ice is prescribed, downscaling of downwelling longwave radiation with a fixed lapse rate of 32 W m^{-2} km^{-1}, a rain-snow repartition based on near-surface temperature and improved snow representation for ice sheets (van Kampenhout et al., 2017). The effect of these changes in CESM2 on the GrIS SMB is evaluated in van Kampenhout et al. (2020).

This study aims to guide future implementation of the EC method, providing diagnostic metrics and evaluation methodology. We recommend in any case that these metrics are adapted to the particular targets of scientific research to be conducted with each model.

3

Global Warming Threshold and Mechanisms for Accelerated Greenland Ice Sheet Surface Mass Loss

Like there's actually need for Greenland.
You can get ice at 7-eleven.

Steve Kluger

The Community Earth System Model version 2.1 (CESM2.1) is used to investigate the evolution of the Greenland ice sheet (GrIS) surface mass balance (SMB) under an idealized CO_2 forcing scenario of 1% increase until stabilization at 4 × pre-industrial at model year 140. In this simulation, the SMB calculation is coupled with the atmospheric model, using a physically-based surface energy balance scheme for melt, explicit calculation of snow albedo, and a realistic treatment of polar snow and firn compaction. By the end of the simulation (years 131-150), the SMB decreases with 994 Gt yr^{-1} with respect to the pre-industrial SMB, which represents a sea-level rise contribution of 2.8 mm yr^{-1}. For a threshold of 2.7 K global temperature increase with respect to pre-industrial, the rate of expansion of the ablation area increases, the mass loss accelerates due to loss of refreezing capacity and

Parts of this chapter have been published in Journal of Advances in Modeling Earth Systems **12**, e2019MS002029 (2020) (Sellevold and Vizcaino, 2020).

accelerated melt, and the SMB becomes negative 6 years later. Before acceleration, longwave radiation is the most important contributor to increasing energy for melt. After acceleration, the large expansion of the ablation area strongly reduces surface albedo. This and much increased turbulent heat fluxes as the GrIS-integrated summer surface temperature approaches melt point, become the major sources of energy for melt.

3.1. Introduction

Since the 1990s, the Greenland ice sheet (GrIS) has lost mass (Shepherd et al., 2012; Bamber et al., 2018a; King et al., 2018). This mass loss has further accelerated since around 2000 (Bamber et al., 2018a). The cumulative mass loss from Greenland since the 2000s is equivalent to ~ 11 mm of sea-level rise (Bamber et al., 2018a). Both increasing ice discharge and a decreased surface mass balance (SMB) contribute to the mass loss. Of these, the SMB is the dominant contributor (van den Broeke et al., 2016; Fettweis et al., 2017), and the acceleration in mass loss is attributed to accelerated SMB decline (Enderlin et al., 2014). Proposed driving mechanisms behind the accelerated surface mass loss are changes in North Atlantic circulation (Fettweis et al., 2013b; Hanna et al., 2018; Delhasse et al., 2018), albedo-melt feedback (Box et al., 2012), depletion of firn refreezing capacity (Vandecrux et al., 2019), and the hypsometric geometry of the GrIS (van As et al., 2017).

State of the art models project reductions of GrIS SMB. These projections are made with either simple positive degree day calculations (Yoshimori and Abe-Ouchi, 2012; Golledge et al., 2019), using regional climate models (RCM) (Rae et al., 2012; van Angelen et al., 2013; Fettweis et al., 2013a; Franco et al., 2013; Mottram et al., 2017) or earth system models (Vizcaíno et al., 2014a). There is a consensus among these studies that future SMB decline is due to increased surface melt and runoff, with a small offset due to increased snow accumulation in the interior. However, the magnitude of the SMB decline varies greatly. Scenario uncertainty and model sensitivity to CO_2 are the greatest contributors to this uncertainty (Fettweis et al., 2013a).

Here we present projections of GrIS SMB with the Community Earth System Model version 2.1 (CESM2.1) under an idealized high CO_2 scenario. CESM2.1 produces realistic present-day GrIS SMB, both through its interactive calculation (van Kampenhout et al., 2019) and as a driving model of RCM downscaling (Noël et al., 2020a). The SMB is calculated in the land component and is downscaled through elevation classes (Sellevold et al., 2019), with a prognostic albedo, and an advanced snow-model fit for applications to polar ice sheets (van Kampenhout et al., 2017). This paper seeks to answer the following scientific questions: What is the modeled SMB evolution in response to CO_2? What are the mechanisms involved in the surface mass change? What is the impact of future changes in atmospheric circulation on the SMB?

The model, experimental setup, and analysis methods are described in section 2. Section 3 shows an overview of projected global and Arctic changes. GrIS SMB

projections and processes are described in section 4, with linkages to atmospheric circulation metrics in section 5. We make a summary, discussion, and conclusions in section 6.

3.2. Methods

3.2.1. Model

The model used for this study is CESM2.1 (Danabasoglu et al., 2020). This model features a fully coupled atmosphere, ocean, sea ice, land, and ice sheet components. The atmospheric model is the Community Atmosphere Model version 6. This model uses a finite-volume dynamical core at 0.9 (latitude) x 1.25 (longitude) degrees horizontal resolution, with 32 vertical levels where the model top is at 3.6 hPa. This model features a new subgrid orographic drag parameterization (Beljaars et al., 2004), new cloud microphysics (Gettelman and Morrison, 2015), and a new subgrid cloud parameterization (Bogenschutz and Krueger, 2013). The ocean component is the Parallel Ocean Program version 2 (Smith et al., 2010; Danabasoglu et al., 2012) with a nominal resolution of 1 degree. The ocean model uses 60 vertical levels, with a maximum depth of 5,500 m. The sea ice is simulated with the Los Alamos Sea Ice model version 5 (Hunke et al., 2017) at the same grid as the ocean model.

The land model is the Community Land Model version 5 (Lawrence et al., 2019). This model now features a realistic representation of polar snow (van Kampenhout et al., 2017), which allows for an explicit and realistic calculation of snow refreezing and extending the snow cap from 1 m water equivalent in the previous generation CESM model to 10 m water equivalent. The simulation of melt over glaciated surfaces is done through the use of elevation classes to account for sub-grid topographical variations (Sellevold et al., 2019). For each of the 10 elevation classes, the near-surface atmospheric temperature is downscaled using a fixed lapse rate of 6 K km^{-1}, the near-surface humidity is downscaled by assuming fixed relative humidity, and the incoming longwave radiation is downscaled with a fixed lapse rate of 32 W m^{-2} km^{-1}. The phase of precipitation is also downscaled to the elevation classes based on near-surface air temperature. At temperatures lower than -2°C, precipitation falls purely as snow, at temperatures higher than 0°C precipitation falls exclusively as rain.

The melt is calculated at each elevation class independently with a surface energy balance (SEB) scheme. The scheme computes melt energy M (in W m^{-2}) from the sum of radiative, turbulent, and conductive fluxes at the ice sheet surface:

$$M = SW_{net} + LW_{net} + SHF + LHF + GHF, \tag{3.1}$$

where SW_{net} is net shortwave radiation, LW_{net} is longwave radiation, SHF is the sensible heat flux, LHF the latent heat flux, and GHF the ground heat flux.

This equation can be rewritten more specifically as

$$M = SW_{in}(1-\alpha) + LW_{in} - \sigma_{sb}\epsilon T_{sfc}^4 + SHF + LHF + GHF, \tag{3.2}$$

where SW_{in} is the incoming shortwave (solar) radiation, α is the albedo, LW_{in} is the incoming longwave radiation, σ_{sb} is the Stefan Boltzman constant, ϵ is the surface

emissivity, and T_{sfc} is the surface temperature. For bare ice, the albedo is fixed to 0.5 in the visible spectrum and 0.3 in the near-infrared spectrum. The snow albedo is prognostically simulated (Flanner and Zender, 2006).

The SMB (in mm of water equivalent) is calculated at each elevation class as

$$SMB = SNOW + REFREEZING - MELT - SUBLIMATION. \quad (3.3)$$

The SMB, and its components, is then represented by the area-weighted average across the elevation classes at the lower resolution (same as atmospheric component) grid cell of the land model.

The land ice model is the Community Ice Sheet Model (CISM) version 2.1 (Lipscomb et al., 2019). This model has a default horizontal resolution of 4 km for the Greenland domain. In this study, ice sheet evolution is turned off, so CISM2.1 is used purely as a diagnostic model to output downscaled SMB. The SMB downscaling from elevation classes to CISM is done through a bilinear horizontal interpolation and vertical linear interpolation. SMB in CISM does not account for snowmass variations, as in the land model, but only variations in ice mass.

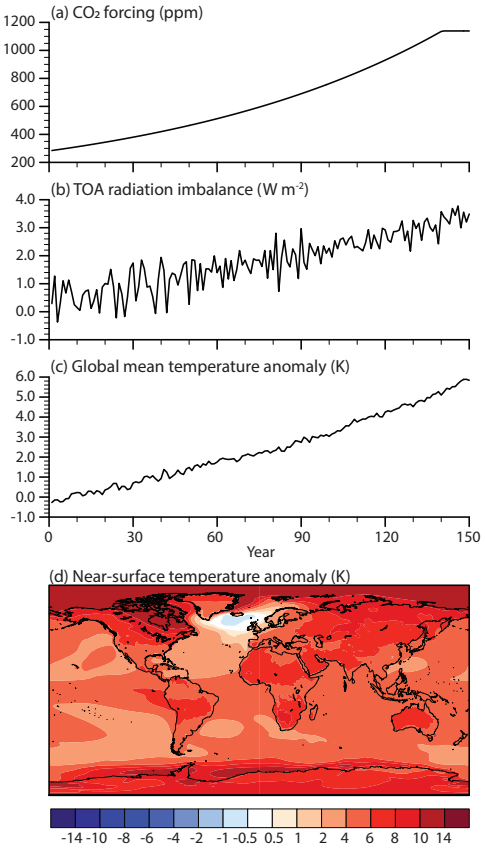

Figure 3.1: Global responses in the 1PCT simulation. Annual average time-series of (a) CO_2 forcing (ppm), (b) cumulative top-of-the-atmosphere radiation imbalance (W m^{-2}), (c) global mean temperature anomaly (K), and (d) map of change in global temperatures (K) for years 131-150 of 1PCT with respect to CTRL. Note the non-linear color scale.

3.2.2. Simulations

The control simulation (CTRL) is a pre-industrial simulation with a fixed atmospheric CO_2 concentration of 284.7 ppm (Danabasoglu et al., 2019a). This simulation participates in the Tier 1 simulations of the Coupled Model Intercomparison Project (CMIP) 6 Diagnostic, Evaluation and Characterization of Klima (DECK) experiments (Eyring et al., 2016). It is $\sim$ 1200 years long. Here we only use the years 501-650 from the CTRL simulation, as our sensitivity simulation is branched off at year 501 and run for 150 years. As the pre-industrial simulation is at steady-state, 150 years are sufficient to sample the unforced climate variability.

To assess the response of the GrIS SMB to CO_2 forcing, we use a 1% increase in CO_2 concentration per year, until 4 × pre-industrial CO_2 concentration (1PCT; Danabasoglu, 2019b). After reaching stabilization at 1,140 ppm of CO_2 concentration, the CO_2 forcing is kept constant. The simulation is 150 years long. This simulation is also participating as a Tier 1 CMIP6 DECK simulation.

A longer simulation with the same greenhouse gas forcing and a dynamical GrIS is analyzed in (Muntjewerf et al., 2020b). In the current study, the main focus is on the coupling between the atmosphere and the GrIS SMB, with detailed analysis of SMB and SEB components.

3.2.3. Analysis

Oceanic and Atmospheric Circulation Metrics

The North Atlantic Meridional Overturning Circulation (NAMOC) index is calculated from annual values as the maximum of the overturning stream function north of 28°N to 90°N and below 500 m depth.

The North Atlantic Oscillation (NAO) is calculated as the leading empirical orthogonal function (EOF) of the seasonal mean (December-February: DJF, and June-August: JJA) sea-level pressure in the North Atlantic region (20°N to 80°N, and 90°W 40°E (Hurrell, 1995; Hurrell and Deser, 2010). The NAO index is calculated from the resulting principal component (PC) time-series and standardized with respect to the index from CTRL.

To calculate the Greenland blocking index (GBI), we use the revised index from Hanna et al. (2018). The procedure to calculate this index is as follows:

1. We make seasonal means (DJF and JJA) of 500 hPa geopotential heights (Z_{500}). The next steps are applied to the seasonal averages independently.
2. Calculate the area-averaged Z_{500} over the Greenland region (60°N to 80°N, and 80°W to 20°W)
3. Calculate the area-averaged Z_{500} over the Arctic region (60°N to 80°N)
4. Subtract the Arctic averaged Z_{500} from the Greenland Z_{500}.
5. The resulting time-series is standardized with respect to the CTRL.

The North Atlantic jet latitude is calculated with the formula from Woollings et al. (2010). The calculation is as follows:

1. Daily zonal winds at 700 hPa, 775 hPa, 850 hPa, and 925 hPa are vertically averaged
2. We extract data in the region 15°N to 75°N and 60°W to 0°W based on the resulting profile from (1)
3. The resulting profile is zonally averaged
4. We then apply a Lanczos low-pass filter with 61 weights and a 10-day cut-off frequency to remove winds associated with individual synoptic systems

5. The jet latitude is the latitude where we find the maximum zonal wind speed

The NAO, GBI, and jet latitude are further decomposed into a sub-decadal and decadal component. To extract sub-decadal variations, we use a Lanczos high-pass filter with 21 weights and a cut-off frequency of 10 years. For the decadal component, we use a 10 to 30 year Lanczos band-pass filter with 21 weights.

Composite and Trend Analysis

For maps illustrating responses to greenhouse gas forcing, we compare the last 20 years of the 1PCT simulation with the entire CTRL simulation. We use a Wilcoxon t-test with a threshold of $p < 0.01$ to test the significance of responses. The choice of using the Wilcoxon t-test instead of the more common student's t-test is our expectation of a change in variability and the different sample sizes of our CTRL and the last 20 years of the 1PCT simulation.

To assess trends, we use linear least-squares regression fits, and consider trends as significant when $p < 0.01$. Wherever the trends are non-linear due to, e.g., acceleration, we use piecewise linear regression fits and report on the slope and length of each of these.

To address the question of whether a CO_2 forced signal has emerged or not from internal variability, we apply a similar metric as outlined by Fyke et al. (2014a). We consider a signal emerged, if the 20-year backward running mean is lower or higher than the mean $\pm$ 2 standard deviations of the corresponding quantity from the CTRL. Also, we apply the condition that the running mean needs to stay lower or higher than this threshold for the rest of the simulation.

3.3. Global and Arctic Climate Change

The response to the increased CO_2 forcing (Fig. 3.1a) is an increase in the amount of radiation in the earth system (Fig. 3.1b). This leads to a rise in global mean surface air temperatures (T_{2m}; Fig. 3.1c,d). The radiation imbalance, defined as LW_{net} + SW_{net} at the top of the atmosphere, is increasing with time. In the last 20 years of the simulation, the imbalance is 3.2 $\pm$ 0.3 W m^{-2}. Part of this excess energy increase is used to raise atmospheric temperatures. The global mean near-surface temperature trend in the simulation is 0.04 K yr^{-1}. The annual global mean temperature increase (ΔT_{global}) by the end of the simulation (years 131-150) compared to CTRL is 5.3 $\pm$ 0.4 K. The Arctic region (north of 60°N) warms the most (Fig. 3.1d), by 8.7 $\pm$ 1.0 K, or 1.6 times the global mean. Within the Arctic, the highest warming occurs over the ocean. Northern Canada, the Weddell Sea, and the Bellingshausen Sea are areas with high warming. The North Atlantic stands out, as it is the only region with cooling (of up to -1 K), in connection with a large slowdown in the NAMOC (Fig. S1) (Drijfhout et al., 2012; Bryden et al., 2020). This NAMOC slowdown is a common feature in CESM2.1 (Muntjewerf et al., 2020a).

A CO_2 forced signal in September sea ice decline emerges by year 31, for a ΔT_{global} = 0.8 K (Fig. 3.2a). Further, the Arctic becomes seasonally ice-free (< 1 x 10^6 km^2 sea ice extent) in year 72 at ΔT_{global} = 2.1 K. Despite this large reduction, the turbulent heat fluxes from the now sea ice free ocean do not significantly

change (Fig. 3.2b). Rather, the temperature and humidity increase of the atmosphere inhibits the turbulent transfer of heat and moisture from the ocean to the atmosphere over the Arctic ocean in September. In the North Atlantic, less turbulent heat is transferred from the ocean to the atmosphere. The largest reduction is collocated with the region of cooling in the North Atlantic (Fig. 1d).

The yearly maximum (March) sea ice extent in the Arctic decreases with -2.9 $\pm$ 1.1 x 10^6 km^2 by years 131-150 with respect to CTRL. The anthropogenic signal can be separated from natural variability in year 89, when ΔT_{global} = 2.8 K. The sea ice is less sensitive to winter warming than summer warming. The ice edge retreats everywhere except for the Baffin Bay. Outside of the CTRL ice edge, the turbulent heat fluxes increase (i.e., there is less surface-to-atmosphere energy transfer) as in September, but the response is stronger. The strongest positive responses are located close to the GrIS. On the other hand, the turbulent heat fluxes decrease (i.e., more surface-to-atmosphere transfer) everywhere inside of the CTRL ice edge, due to reduced pan-Arctic sea ice and snow thickness. Strongest responses are co-located with the 1PCT ice edge and the Beaufort Gyre. The areas co-located with the 1PCT ice edge experience a large decrease as the surface becomes ice-free.

Increases in Arctic summer temperature by the end of 1PCT are strongest over land (Fig. 3.3a), in connection with large snow cover decrease. Additionally, the cloud cover over the Arctic land is reduced (Fig. 3.3b), increasing incoming solar radiation at the surface. The Arctic ocean warms less, likely due to the additional energy being used to melt sea ice and raise ocean temperatures. Summer precipitation increases over the Arctic, including the GrIS, and decreases over land towards midlatitudes (Fig. 3.3c).

In winter, the warming over the Arctic ocean is strongest (Fig. 3.3d), in connection with sea ice reduction and increased turbulent fluxes as already shown. The strongest local warming is over the Beaufort Gyre. This area also sees the strongest increase in cloud cover during winter (Fig. 3.3e). As clouds increase the incoming longwave radiation, this contributes to generating the strongest warming here. Winter precipitation decreases along the southern Greenland margin and in the Greenland sea (Fig. 3.3f). This precipitation decrease is co-located with the lowering of near-surface temperatures. It is likely that the decreased ocean-to-atmosphere fluxes of heat and moisture act to stabilize the atmosphere, resulting in fewer or weaker storms and less precipitation here.

3.4. GrIS Surface Mass Balance and Surface Energy Balance Evolution

3.4.1. SMB evolution

The SMB of the GrIS decreases with $\sim$ 994 Gt yr^{-1} in the 1PCT simulation (Fig. 3.4a, Table 3.1). According to the criteria in section 3.2.3, we consider the CO_2 forced SMB signal emerged from variability in year 90 (ΔT_{global} = 2.7 K). The SMB becomes negative in year 96 (ΔT_{global} = 3.0 K). In the first 90 years of the simulation, the trend is -2.5 $\pm$ 0.4 Gt yr^{-2}. Around year 90, this trend transitions to -15.9 $\pm$ 1.1 Gt yr^{-2}, which represent a six-fold increase, i.e., a strong acceleration.

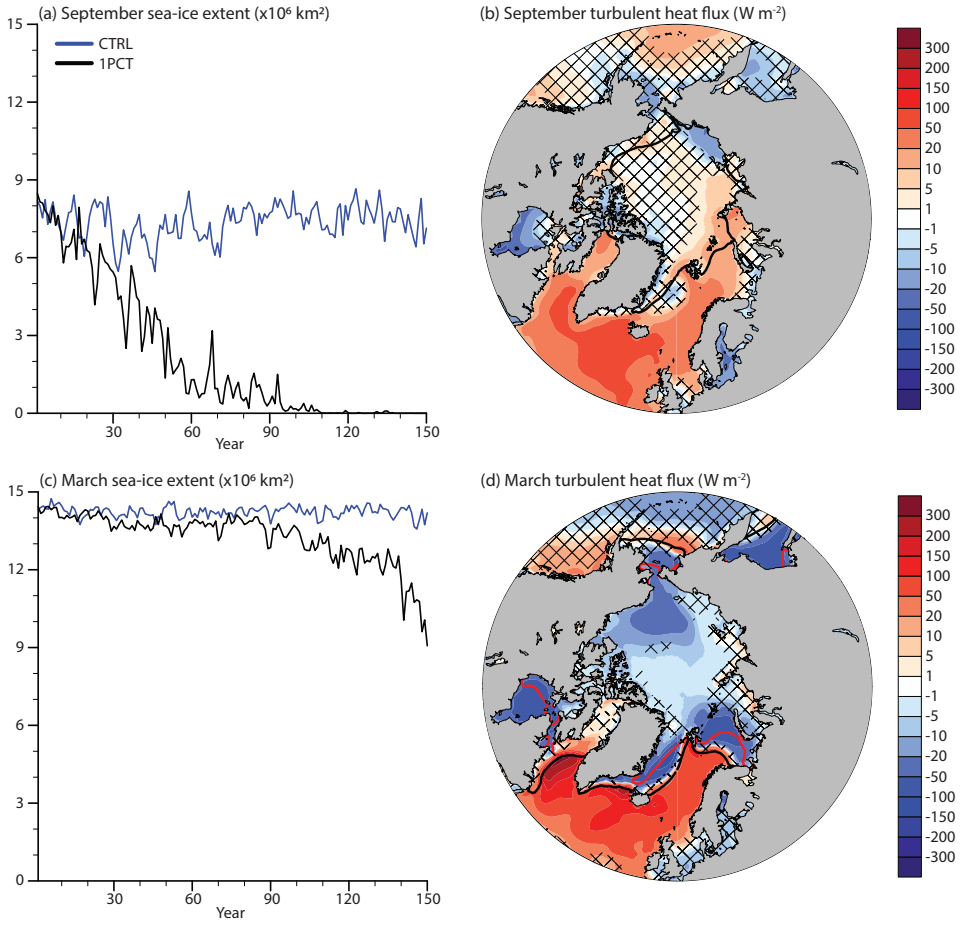

Figure 3.2: Sea ice responses to the CO_2 forcing for (top) September and (bottom) March. (a,c) Sea ice extent (x 10^6 km^2) and (b,d) turbulent heat flux anomaly (W m^{-2}) for the years 131-150 compared to CTRL. Note the non-linear color scales. For the time series (a,c) the blue line shows the CTRL, while the black line shows the 1PCT simulation. The sea ice extent is defined as the area north of 60°N where sea ice concentration is greater than 15%. For (b,d) the black line shows the sea ice extent from CTRL, and the red line shows the sea ice extent from the 1PCT. Positive turbulent heat flux means energy gain at the surface. Areas with non-significant changes are patched.

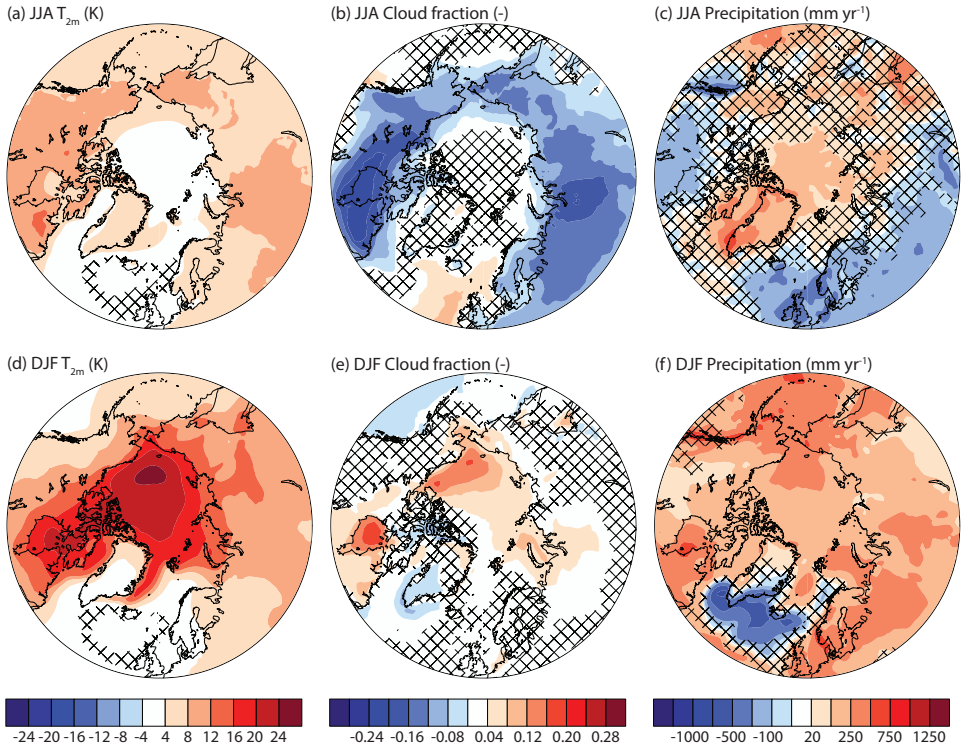

Figure 3.3: Overview of Arctic climate change in the last 20 years of the 1PCT simulation compared to CTRL for JJA (top) and DJF (bottom). (a,d) Near-surface temperature (K), (b,e) cloud fraction (-), and (c,f) precipitation (mm yr^{-1}). Areas with non-significant changes are patched. Note the non-linear color scale for (c) and (f).

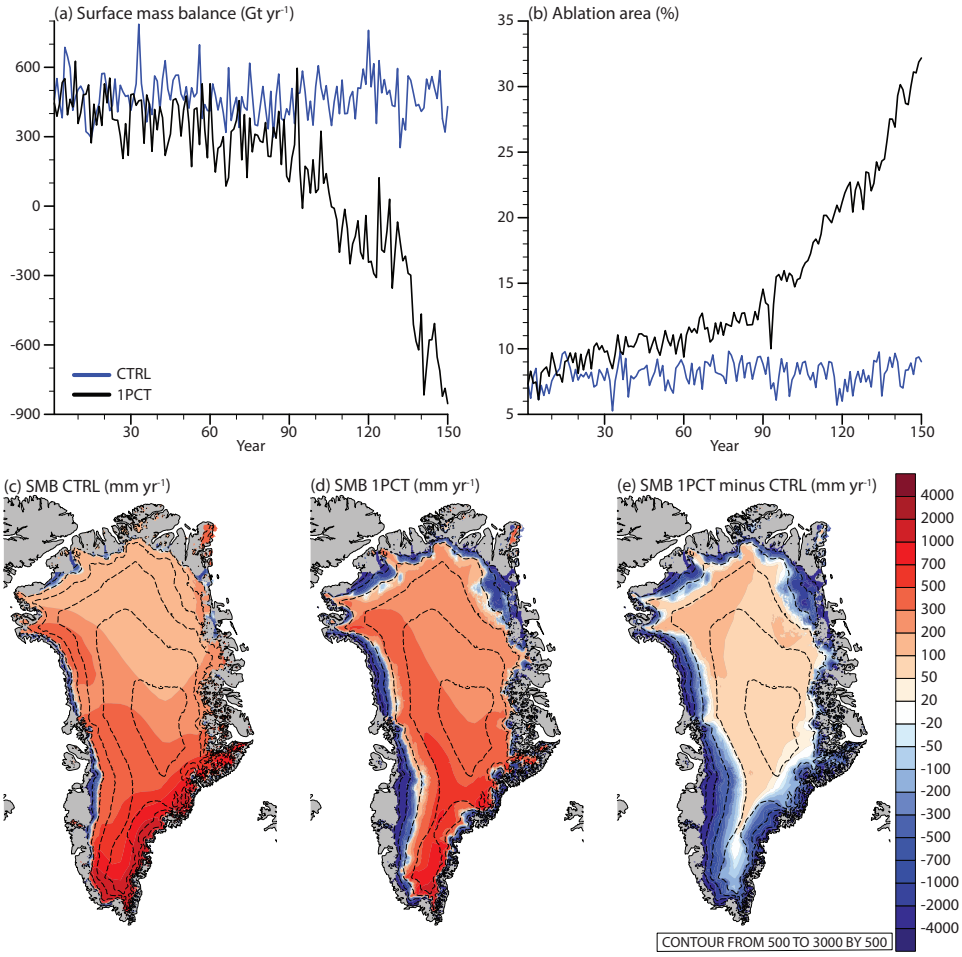

Figure 3.4: Annual ice sheet integrated (a) SMB (Gt yr^{-1}) and (b) ablation area (%; as a percentage of total ice sheet area) for CTRL (blue) and 1PCT (black). Maps of annually-averaged SMB (mm yr^{-1}) at the ice sheet model grid (4 km) in (a) CTRL, (b) year 131-150 of 1PCT, and (c) SMB anomalies of year 131-150 of 1PCT with respect to CTRL. Note the non-linear color scale. Dashed lines show surface elevation contours, starting with 500 m up to 3,000 m by 500 m.

The ablation area expands from 8.1% (pre-industrial) to 27.6% (years 131-150) during the 1PCT (Fig. 3.4b). The CO_2 forced signal emerges already in year 44 (ΔT_{global} = 1.0 K), 46 years before the anthropogenic SMB signal emerges. This is due to much lower interannual variability in the ablation area.

The lower row of Fig. 3.4 shows the SMB as simulated by CTRL, 1PCT, and their difference. The CTRL simulation (Fig. 3.4c) shows SMB patterns comparable to present-day SMB (Noël et al., 2016; Fettweis et al., 2017). There are two local accumulation maxima, one located in the South-East and one in the North-West. Ablation areas are along the margins, in western and northern parts of the ice sheet. The regionally heterogenous equilibrium line altitude is in the range 500 - 1500 m.

The most striking SMB feature of the last 20 years of the 1PCT is the large expansion of the ablation areas (Fig. 3.4d). This raises the equilibrium line with ~ 500 m. The high accumulation area in the South-East remains the area with the highest accumulation.

The anomaly map (Fig. 3.4e) reveals that SMB is decreased along the margin, and up to approximately 2,000 m. On the other hand, SMB increases in the interior. This result is in line with 21st-century projections of GrIS SMB (Vizcaíno et al., 2014a; Mottram et al., 2017).

3.4.2. SMB components evolution

To understand the processes contributing to the large and rapid decline in SMB, particularly after year 90, we investigate individual SMB components. Precipitation increases over most parts of the ice sheet (Fig. 3.5c). The highest increases are in the high accumulation area in the North-West, in the South-West, and at the northern margin. Precipitation decreases along the high accumulation area in the South-East, likely due to reduced cyclogenesis in the Greenland sea.

Snowfall, the largest SMB component in the CTRL simulation (Table 3.1), shows a non-significant decrease of -6 $\pm$ 78 Gt yr^{-1} (Fig. 3.5a, Table 3.1). This decrease is likely related to (multi-)decadal variations in the snowfall. This result is in contrast to other studies (Rae et al., 2012; van Angelen et al., 2013; Fettweis et al., 2013a; Vizcaíno et al., 2014a; Mottram et al., 2017) which show increased snowfall over the GrIS in 21st century projections. Although the integrated snowfall does not significantly change during the simulation, significant local changes in snowfall are apparent in Fig. 3.5d. In the interior and the north, snowfall increases. The map of increased snowfall corresponds well to the map of where SMB increases (Fig. 3.4e). At the South-West margin, snowfall decreases due to higher temperatures causing the precipitation to fall as rain. At the South-East margin, less snowfall is caused both by a higher fraction of rainfall and less total precipitation (Fig. 3.5c).

Rainfall increases significantly with 180 $\pm$ 33 Gt yr^{-1} (Fig. 3.5a, Table 3.1) by 131-150, which is a three-fold increase. The time series reveals that the trend in rainfall is small (Table 3.1) before year 90. After year 90, the trend becomes positive. Part of the explanation of this positive trend is the general precipitation increase from a warmer and moister atmosphere. Additionally, due to the warmer atmosphere over the ice sheet, a higher fraction of precipitation falls as rain (Figure 3.5b). The fraction of precipitation falling as rain on the GrIS increases from 8%

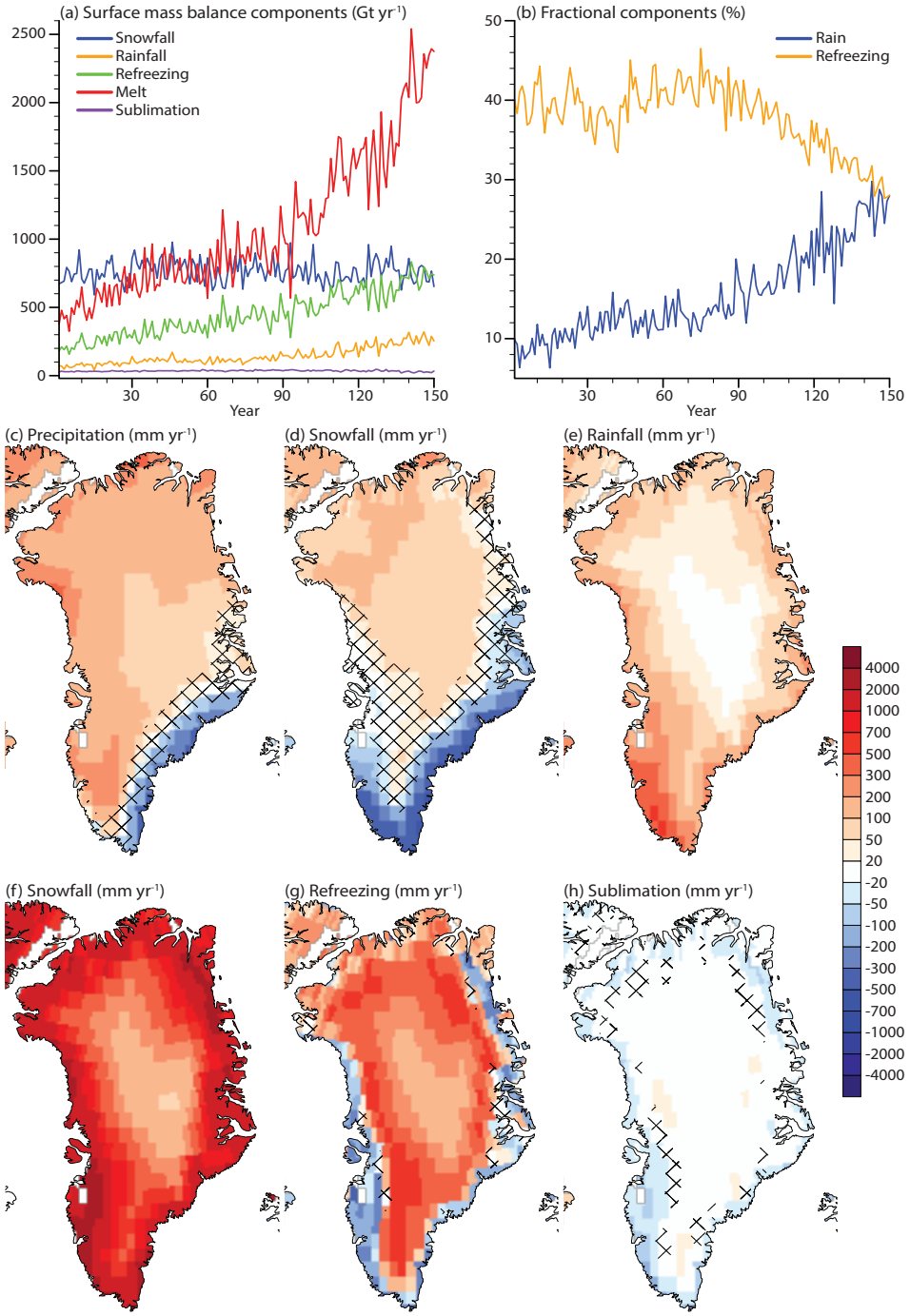

Figure 3.5: Annual ice sheet integrated (a) SMB components (Gt yr^{-1}) and (b) fractional components (%). In (a) we show snowfall (blue), rainfall (yellow), refreezing (green), melt (red), and sublimation (purple). In (b) we show rain fraction (blue; defined as the fraction of rain to total precipitation) and refreezing fraction (yellow; the ratio of refreezing to melt and rainfall). Annual anomaly maps of the last 20 years of 1PCT compared to CTRL for selected SMB components (mm yr^{-1}). (c) Precipitation, (d) snowfall, (e) rainfall, (f) surface melt, (g) refreezing, and (h) sublimation. Note the non-linear color scale. Only values corresponding to the glaciated part of the grid cell are shown. Areas showing non-significant changes are patched.

to 27%. More rainfall is robust among projections of future GrIS SMB. Spatially, rainfall increases everywhere on the ice sheet (Fig. 3.5e). The largest increase in rainfall is in the South-West.

Melt production at the surface of the GrIS increases significantly with 1540 $\pm$ 317 Gt yr^{-1} (Fig. 3.5a and Table 3.1) and thereby melt becomes the largest SMB component around year 90 (ΔT_{global} = 2.7 K). After year 90, the positive melt trend increases (Table 3.1). Melt increases significantly over the entire ice sheet (Figure 3.5f). The increase in the melt is topographically dependent, with the largest increases at the margins (low elevation) and the smallest increases in the interior (high elevation).

Refreezing, the amount of available water at the surface from surface melt and rain that is being refrozen in the snow mass significantly increases with 466 $\pm$ 83 Gt yr^{-1}. The rate of refreezing increase is positive and significant (Table 3.1) in the first 90 years of the simulation. After year 90, the refreezing increase accelerates (Table 3.1). The refreezing capacity (the fraction of refrozen water to available water at the surface) decreases at the start of the 1PCT simulation up to year 40 (Figure 3.5b), whereafter the refreezing capacity recovers for a period of $\sim$ 40-50 years. After this period, the refreezing capacity continuously declines until the end of the simulation. The reason for this latter rapid loss of refreezing capacity is that the melt generation and rainfall increases are largest in areas experiencing larger loss of snow mass. As a result, refreezing decreases in areas where the melt increase is highest (Figure 3.5g).

The integrated sublimation change in the 1PCT is -1 $\pm$ 7 Gt yr^{-1} (not significant). However, the anomaly map of sublimation reveals significant local changes (Figure 3.5h). Along the margins, the sublimation decreases, while in the accumulation area, sublimation increases. These changes can be explained through changes in LHF, which will be addressed in the next subsection.

3.4.3. Surface energy balance evolution

Figure 3.6 shows the evolution of summer SEB components. With the exception of GHF, all SEB components significantly increase in the ablation area (Fig. 3.6, Table 3.2). This results in a 69.8 $\pm$ 12.4 W m^{-2} increase in melt energy by 131-150. Until year 100, SW_{net} only increases slightly and after that stabilizes. This is due to the compensation of a decreased SW_{in} due to thicker clouds, and a decreased albedo (Figure 3.7a,c, Table 3.2). After year 100, SW_{net} increases as the SW_{in} stabilizes while the albedo continues to decrease. LW_{net} is the largest contributor to the melt energy increase (Table 3.2). This is caused by increased LW_{in} (Figure 3.7b, Table 3.2), caused by more emission of longwave radiation from the atmosphere to the surface as the atmosphere warms. SHF increase (Table 3.2) is caused by atmospheric warming, more heat advected over the ice sheet, and the difference between T_{2m} and T_{sfc} becoming larger (Figure 3.8) as the ice sheet surface has an upper limit of warming to 0 °C. LHF increases (Table 3.2). There is a regime shift around year 80, where LHF goes from being negative during the summer to positive, likely due to the higher amount of moisture held by the atmosphere together with lengthened bare ice exposure. GHF decreases as the refreezing is much lower in

Table 3.1: SMB and SMB components in the CTRL, the last 20 years of 1PCT, and their difference (diff). Trend 1 is the linear regression slope between years 1-89, trend 2 is the slope in year 90-150. Differences and trends in bold are significant. SMB (4 km) only accounts for ice mass variations, while SMB also includes snowmass variations. The ± indicates the one standard deviation.

Component	CTRL (Gt yr^{-1})	1PCT (Gt yr^{-1})	Diff (Gt yr^{-1})	Trend 1 (Gt yr^{-2})	Trend 2 (Gt yr^{-2})
SMB (4 km)	472 ± 91	-522 ± 239	**-994**	**-2.5 ± 0.4**	**-15.9 ± 1.1**
SMB	464 ± 99	-615 ± 285	**-1,081**	**-2.6 ± 0.5**	**-17.1 ± 1.4**
Snowfall	763 ± 75	757 ± 78	-6	0.3 ± 0.3	-0.1 ± 0.6
Rainfall	77 ± 14	257 ± 33	**180**	**0.6 ± 0.1**	**2.5 ± 0.2**
Refreezing	227 ± 36	692 ± 83	**466**	**2.0 ± 0.2**	**4.8 ± 0.5**
Melt	496 ± 81	2,036 ± 317	**1,540**	**5.9 ± 0.5**	**22.0 ± 1.5**
Sublimation	30 ± 2	30 ± 7	-1	**0.1 ± 0.0**	**-0.2 ± 0.0**

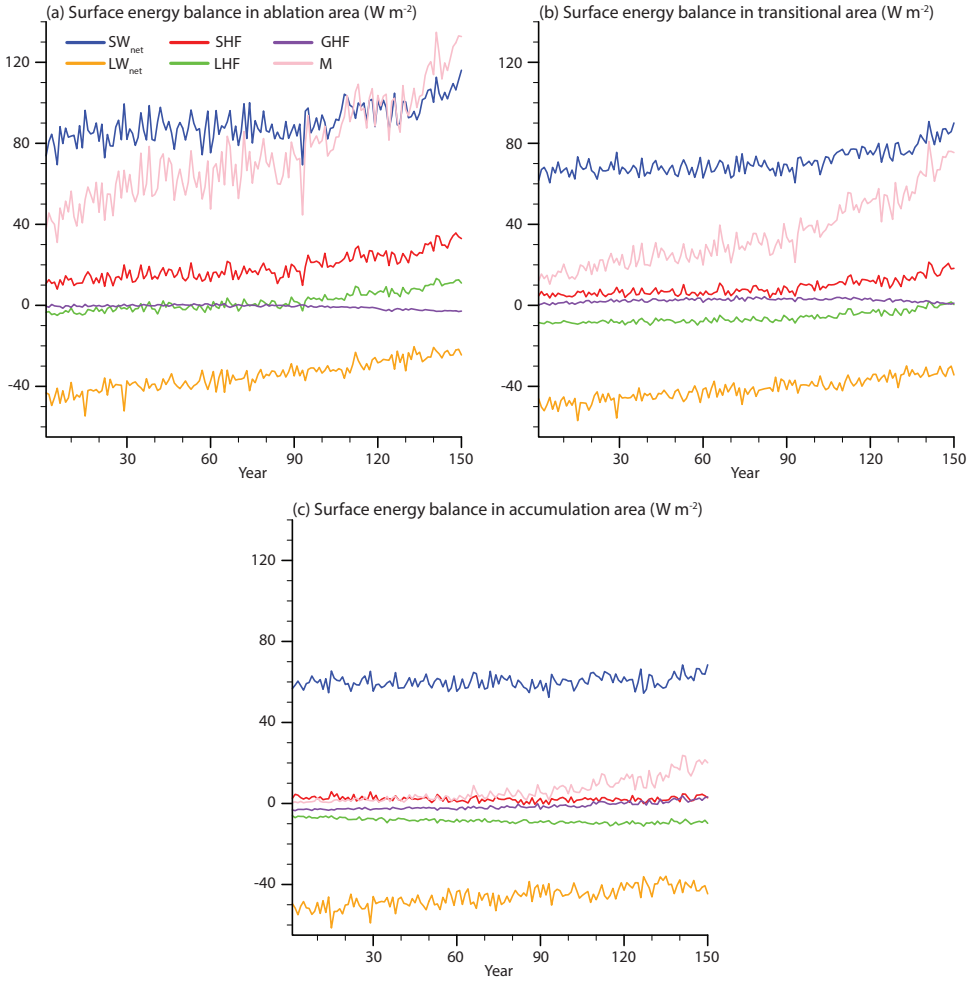

Figure 3.6: Summer (JJA) ice sheet averaged surface energy balance components (W m^{-2}) in (a) ablation area, (b) transitional area, and (c) accumulation area. The ablation area is defined as the ablation area in the CTRL simulation. The transitional area is defined as the area that is accumulation area in the CTRL simulation, but transition into ablation area during the 1PCT. The accumulation area is the area of the ice sheet that is an accumulation area in the CTRL and remains an accumulation area through the 1PCT simulation. The components shown are SW_{net} (blue), LW_{net} (yellow), SHF (red), LHF (green), GHF (purple), and melt energy (pink) (all in units of W m^{-2}. Positive values mean increased energy at the ice sheet surface.

the ablation area (Table 3.2).

In the transitional area, the melt energy increases with 51.0 $\pm$ 9.3 W m^{-2} (Fig. 3.6b, Table 3.2), somewhat less than in the ablation area. The largest contributor to this increase is the SW_{net}. Also here, the compensation between SW_{in} and albedo maintains a stable SW_{net} in the first decades. Albedo decrease accelerates after year 90 as snow mass decreases, and there is more bare ice exposure, leading to increased SW_{net}. In the last 30 years, SW_{in} does not further decrease. LW_{net} increases (Table 3.2) for the same reason as in the ablation area. However, the increase in LW_{net} is less, due to the compensation of increasing LW_{out} as the surface temperature increases. As in the ablation area, SHF is stable in the first 90 years, whereafter it increases for the same reasons. However, the increase is less than in the ablation area (Table 3.2), likely due to the T_{sfc} being at the melting point for a shorter period than in the ablation area during the summer. The same mechanism leading to increased LHF in the ablation area leads to an LHF increase in the transitional area. With this increase, the 20-year summer mean indicates this area has not transitioned from being dominated by sublimation to condensation. GHF shows no significant change, likely due to a competition between increased water available for refreezing and reduced refreezing capacity.

Also, the melt energy increases in the accumulation area (16.6 $\pm$ 4.3 W m^{-2}, Table 3.2, and Fig. 3.6c) by 131-150. The SW_{net} only increases slightly in the last 30 years of the simulation, for the same reasons as the SW_{net} showing a late response in the other areas. As the albedo change in this area is rather small (Fig. 3.7c), the SW_{net} increase is also smaller than in the other areas. LW_{net} is the largest contributor to increased melt energy for the accumulation area (Table 3.2). This increase is caused by enhanced LW_{in} due to increased cloud thickness and higher atmospheric temperatures. SHF shows no significant change, due to a very small change in the difference between T_{2m} and T_{sfc}. On the other hand, the LHF decreases and becomes more negative, indicating more energy is used for sublimation. GHF increases due to more melting in the accumulation area, allowing for more refreezing, which releases heat in the snowpack.

Figure 3.7 shows spatial maps of SW_{in}, LW_{in}, albedo, and cloud water path (CWP) anomalies. SW_{in} decreases the most in the north due to increased cloud fraction (Fig. 3.3b) and increased CWP (Fig. 3.7d). Over large parts of the ice sheet, the decrease in SW_{in} is between 20-30 W m^{-2}. This smaller change is due to no change in cloud fraction, and a smaller increase in cloud thickness. Increases in LW_{in} show a different pattern than decreases in SW_{in}. Except for the north, the LW_{in} increase shows a topographically and latitudinal dependent pattern. The topographically dependent pattern is caused by summer atmospheric warming being stronger at higher elevations. A positive south-to-north gradient causes the latitudinal pattern in cloud fraction and thickness change. Albedo decreases significantly over the entire ice sheet (Fig. 3.7c). The largest increases are found along the margins, particularly in regions covered permanently by snow now has bare ice exposure. Also, we expect in areas with seasonal snow cover at the margins, that the bare ice exposure is prolonged.

We showed that the melt energy accelerates after year 90, causing larger amounts

Table 3.2: Surface energy balance components in the CTRL, the last 20 years of 1PCT, and their difference for the ablation area, transitional area, and the accumulation area. The ± indicates the one standard deviation.

Component	CTRL (W m^{-2})	1PCT (W m^{-2})	Difference (W m^{-2})
Ablation area			
SW_{in}	251.7 ± 6.9	226.1 ± 8.0	**-25.6**
SW_{net}	82.7 ± 5.8	102.7 ± 6.9	**20.2**
LW_{in}	260.2 ± 3.1	289.4 ± 2.4	**29.2**
LW_{net}	-44.3 ± 2.7	-23.9 ± 2.0	**20.4**
SHF	11.8 ± 2.1	29.7 ± 4.0	**17.9**
LHF	-3.6 ± 1.2	10.0 ± 2.0	**13.6**
GHF	-0.2 ± 0.5	-2.5 ± 0.4	**-2.3**
Melt energy	46.4 ± 7.1	116.2 ± 12.4	**69.8**
Transitional area			
SW_{in}	279.6 ± 4.6	253.0 ± 5.2	**-26.5**
SW_{net}	66.5 ± 2.7	82.8 ± 5.4	**16.3**
LW_{in}	245.6 ± 3.4	277.5 ± 2.7	**31.9**
LW_{net}	-48.0 ± 2.5	-32.7 ± 2.0	**15.4**
SHF	5.1 ± 1.0	16.2 ± 3.1	**11.2**
LHF	-8.7 ± 0.6	-0.4 ± 1.8	**8.2**
GHF	1.5 ± 0.6	1.4 ± 0.6	-0.1
Melt energy	16.4 ± 2.7	67.4 ± 9.3	**51.0**
Accumulation area			
SW_{in}	300.1 ± 4.6	276.6 ± 4.3	**-23.5**
SW_{net}	59.5 ± 2.2	62.5 ± 3.5	**3.0**
LW_{in}	220.0 ± 4.9	260.7 ± 3.4	**40.7**
LW_{net}	-51.7 ± 2.8	-40.4 ± 2.5	**11.2**
SHF	2.9 ± 1.0	3.0 ± 1.4	0.1
LHF	-6.8 ± 0.5	-0.4 ± 1.8	**-2.3**
GHF	-2.9 ± 0.3	1.7 ± 1.1	**4.6**
Melt energy	1.0 ± 0.5	17.6 ± 4.3	**16.6**

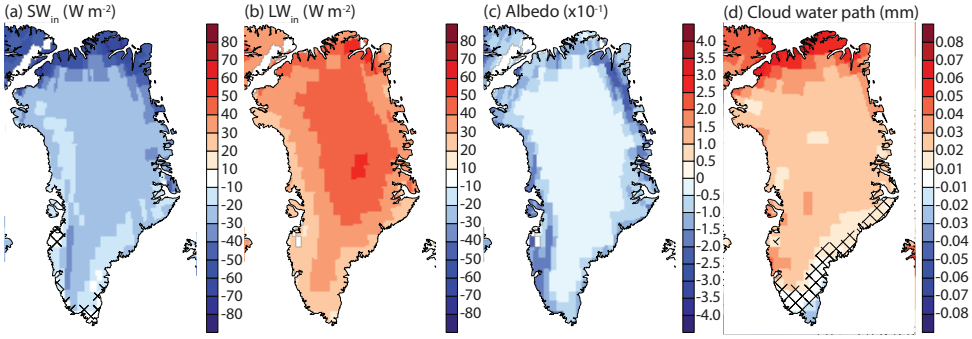

Figure 3.7: Summer (JJA) anomaly maps of the last 20 years of 1PCT compared to CTRL for selected radiation influent quantities. (a) Incoming solar radiation (W m^{-2}), (b) incoming longwave radiation (W m^{-2}), (c) albedo (-), and (d) cloud water path (mm). Only values corresponding to the glaciated part of the grid cell are shown. Areas showing no significant change are patched.

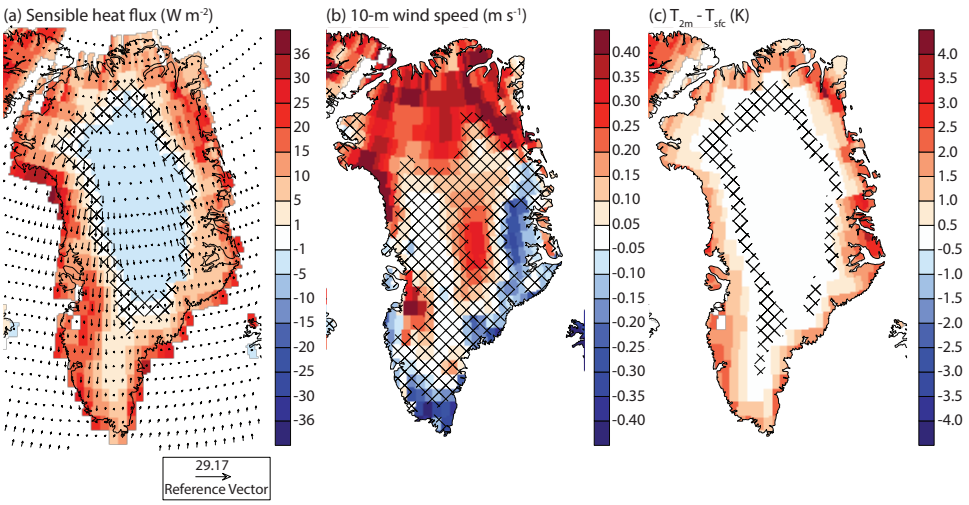

Figure 3.8: Summer (JJA) anomaly maps of the last 20 years of 1PCT compared to CTRL for selected sensible heat flux influential quantities. (a) Sensible heat flux (W m^{-2}), (b) 10-m wind speed (m s^{-1}), and (c) T2m – Tsfc (K). Note the non-linear color scale for (a). Only values corresponding to the glaciated part of the grid cell are shown. Arrows on (a) indicate wind speed and direction at 850 hPa. Areas showing no significant change are patched.

of surface melt and results in an accelerated SMB decrease. SHF contributes to this acceleration over the regions of the GrIS, producing the largest amounts of melt. The SHF increases the most at the margins (Fig. 3.8a). In the interior, the SHF slightly decreases. The 850 hPa winds over Greenland are cyclonic, which is the pattern associated with a positive phase of NAO.

The 10-m wind speed (Fig. 3.8b), a proxy for the strength of turbulent transfer between atmosphere and surface, only changes significantly in the north, at the summit, locally in the southwest and along the southeastern margin. Over large parts of the northern ice sheet, wind speeds increase. Also, in the west, wind speeds increase locally. On the other hand, in the South-East, wind speed decreases of up to the same magnitude appear.

The temperature difference between the near-surface atmosphere and the surface increases the most in the ablation and transitional area. In this area, the surface reaches the melting point and cannot further increase its temperature while the T_{2m} continues to increase in response to the CO_2 forcing. This increase in the difference between T_{2m} and T_{sfc} increases the SHF.

3.5. Effects of North Atlantic Atmospheric Circulation Change on GrIS SMB

The aim of this section is 1) to explore variability and trends in North Atlantic circulation, and 2) investigate its potential impact on GrIS precipitation and melt. For the first part, we examine the evolution of the indices for the NAO, GBI,

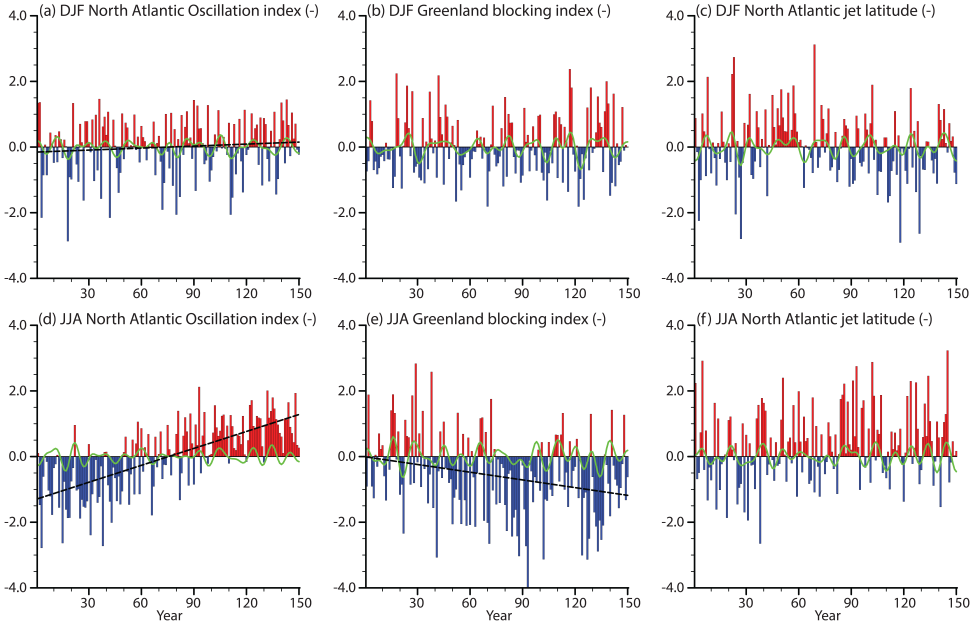

Figure 3.9: Indices of North Atlantic circulation metrics in red (positive) and blue (negative) bars. The upper row shows DJF means, and the lower row shows JJA means of (a,d) North Atlantic Oscillation, (b,e) Greenland blocking index, and (c,f) jet latitude. All indices are standardized with respect to CTRL. Significant trends are indicated with a dashed black line. The green line shows 10 to 30 years band-pass filtered time series.

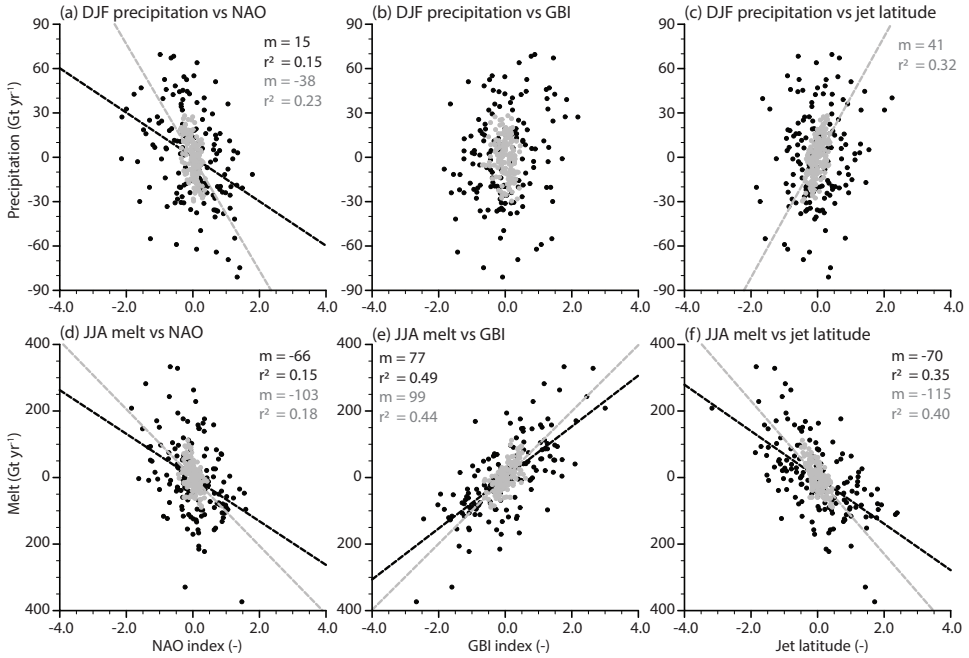

Figure 3.10: DJF GrIS integrated filtered precipitation (Gt yr^{-1}) regressed onto DJF North Atlantic circulation filtered indices (upper row) and JJA GrIS integrated filtered surface melt (Gt yr^{-1}) regressed onto JJA North Atlantic circulation filtered indices (lower row). Circulation indices used are (a,d) NAO, (b,e) GBI, and (c,f) jet latitude. Black dots represent 10-year high-pass filtered quantities, and grey dots represent 10 to 30-year band-pass filtered quantities. The time-scale of the filtered quantities effectively removes both the mean and the trend of each time series. Black (grey) lines are drawn where the regression is significant, with an annotated m (slope), and r^2 for the explained variance.

and latitudinal position of the North Atlantic jet, with the metrics outlined in section 3.2.3 and separately for winter and summer (Fig. 3.9).

The winter NAO exhibits a small, but a significant trend towards its positive phase during years 1 to 150 of the 1PCT simulation. On the contrary, the winter GBI index does not exhibit a significant trend. As the winter GBI, the winter jet latitudinal position does not have a significant trend.

The summer NAO exhibits a strong significant trend towards its positive phase in response to CO_2 forcing. As seen in Fig. 3.8a, we do see a circulation anomaly related to this phase of the NAO. The GBI exhibits a significant negative trend towards its negative phase. The jet stream, on the other hand, does not significantly change its position.

Figure 3.10 shows linear regressions between GrIS-integrated, summer melt, and winter precipitation and the corresponding seasonal NAO, GBI, and jet latitude indices.

The NAO and the jet position modulate the amount of winter precipitation falling on the GrIS (Fig. 3.10a,c). A more positive NAO results in less precipitation. This

relationship is robust through the timescales investigated here, where sub-decadal variations in NAO explain 15% of the precipitation variability, while decadal oscillations explain 23% of the variability. For the jet stream, only its decadal component seems to have an impact on GrIS precipitation variability. On this timescale, a more northern displaced jet stream results in higher precipitation rates over the GrIS. Changes in the jet stream position account for 32% of the precipitation variability. Variations in GBI does not show any significant relationship to GrIS precipitation (Fig. 3.10b).

The relationship between melt and NAO is significant, both on sub-decadal and decadal timescales. A more negative NAO implies higher melt rates. The change in the melt due to decadal variations in the NAO is stronger than on sub-decadal timescales. Sub-decadal variations in the NAO explain 15% of melt variability, while 18% is explained for decadal variations in melt variability. A relationship between GBI and surface melt is also shown (Fig. 3.10e). On sub-decadal timescales, the GBI explains 49% of the surface melt variability. The GBI also shows to have a strong influence on surface melt on decadal timescales, explaining around 44% of the variation. The NAO and the GBI trends towards its positive and negative phases, respectively (Fig. 3.9d), while the melt increases in response to higher CO_2 (Fig. 3.5). This result shows that the NAO and GBI are not the main drivers of increased melt. Instead, the relationship suggests that the change in NAO and GBI counteracts the effect of global warming on the surface melt. Our simulation also shows a relationship between the position of the jet stream and the GrIS surface melt (Fig. 3.10f). A more southern displaced jet stream is related to more surface melt, both on sub-decadal and decadal timescales. In contrast to the GBI, a change in jet position explains more of surface melt variability on decadal timescales (40%) than on sub-decadal timescales (35%).

3.6. Discussion

This study projects the transient climate and GrIS SMB response to increasing CO_2 forcing until quadrupled pre-industrial levels with a fully coupled Earth System Model. With respect to previous work that focuses on regional climate modeling (RCM) or simplified melt calculations from global models, the main novelty is in the detailed analysis of GrIS surface energy and mass budgets using a global climate model coupled with a realistic representation of ice sheet snow and firn processes (van Kampenhout et al., 2017).

CESM2.1 simulates a global mean temperature increase of 5.3 $\pm$ 0.4 K by the end of the simulation (years 131-150). The model has a high equilibrium climate sensitivity of 5.3 K (Gettelman et al., 2019a) to CO_2 forcing compared to models from the CMIP5 (Taylor et al., 2012), that simulate equilibrium climate sensitivities in the range of 2.1-4.7 K (Andrews et al., 2012). Generally, the CMIP6 models have a higher climate sensitivity than the CMIP5 models (Zelinka et al., 2020; Hofer et al., 2020). At the same time, CESM2.1 projects high reductions in NAMOC (Fig. 3.11). Both high climate sensitivity and NAMOC reduction are important controls on the GrIS SMB response to CO_2 forcing.

The simulated Arctic amplification (ratio between mean temperature > 60°N and global mean temperature) is 1.6 (years 131-150). Major summer contributions to Arctic warming are loss of snow over the terrestrial Arctic, associated albedo feedback, and decreased cloud cover. In winter, the main contribution is from sea ice loss. The Arctic amplification factor was found to be 1.5-4.5 in CMIP3 (Holland and Bitz, 2003). Also, a previous study with CESM version 1.0 found an amplification factor of 2.1 (Vizcaíno et al., 2014a). So the Arctic warming, compared to the global warming found here, is in the lower range. This may be due to the Arctic sea ice being biased thin in CESM2.1. Further, we find that the Arctic becomes seasonally sea ice free at a global warming of 2.1 K. A September sea ice-free Arctic is a robust response (Snape and Forster, 2014) to representative concentration pathway (RCP)8.5 forcing, which ends with a CO_2 forcing of > 1,370 ppm (which is similar to the final CO2 of 1,140 ppm in this study). The timing of seasonal sea ice-free conditions under RCP8.5 forcing is estimated at years 2040-2060 in Wang and Overland (2012); Snape and Forster (2014).

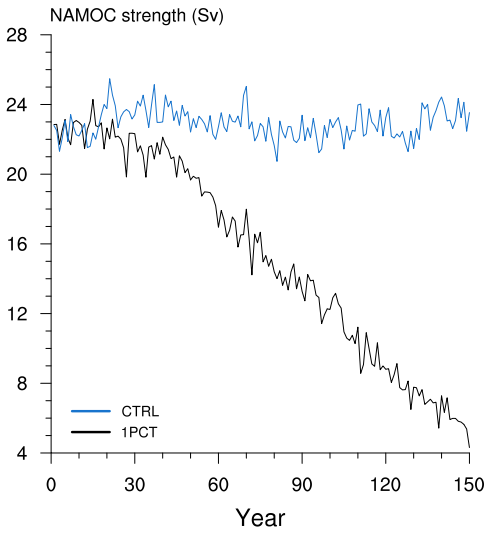

Figure 3.11: North Atlantic Meridional Overturning Circulation strength (Sv) in CTRL (blue) and 1PCT (black).

The SMB of the GrIS decreases with 994 Gt yr^{-1} in our simulation. In a similar CESM2.1 study, though with a dynamically evolving ice sheet, the SMB decreases with 952 Gt yr^{-1} by the same time (Muntjewerf et al., 2020b). This SMB decrease represents a 2.8 mm yr^{-1} contribution to global mean sea level rise, assuming the pre-industrial ice sheet SMB would give no change in sea level rise. Compared to Church et al. (2013), this contribution is at the high end, likely due to the high climate sensitivity simulated here. The main contributor of the SMB decrease is a melt increase of 1,540 Gt yr^{-1}. This melt is higher than what is projected under an RCP8.5 scenario (600-700 Gt per year; Rae et al., 2012; Fettweis et al., 2013a; Vizcaíno et al., 2014a), likely due to the higher climate sensitivity. The refreezing is here projected to increase with 466 Gt yr^{-1}, which is a factor of 0.30 to the melt increase. Rae et al. (2012) find this factor to be in the range 0.19-0.45, depending on the forcing model and RCM. Vizcaíno et al. (2014a)) find this factor to be 0.21, likely in connection with limited refreezing capacity from an absence of firn modeling as GrIS snow thickness is capped at 1 m of water equivalent.

An interesting feature of the SMB decrease is the pause in the decrease around the years 120-135 (Fig. 3.4a). Figure 3.5a shows that this timing corresponds to a time of temporarily increased snowfall, likely due to internal variability, and a pause in surface melt increase. The reason for this pause in surface melt increase

is due to a pause in the increase of SHF and SWnet in the ablation area (Fig. 3.6a). Due to the low summer GBI together with high summer NAO in these years (Fig. 3.9d,e), it is likely that reduction in warm air advection compensates for increased atmospheric warming, and temporarily prevents further albedo-melt feedback.

Increases in GrIS precipitation are projected in state-of-the-art studies (Fettweis et al., 2013a; Vizcaíno et al., 2014a; Mottram et al., 2017). These projected increases in both snow and rainfall, while CESM2.1 projects only rainfall increase of 180 $\pm$ 33 Gt yr^{-1}. Further, the spatial patterns of precipitation change modeled here differ substantially from other studies (e.g., Mottram et al., 2017) that find the maximum increase in the area where CESM2.1 projects decreased precipitation. In our simulation, this decrease is attributed to regional cooling from NAMOC reduction, which induces stabilization of the atmosphere in the North Atlantic and the Greenland Sea and reduces storminess in South-East Greenland.

At a global mean surface temperature increase of 2.7 K, we find that SMB decrease accelerates (from -2.5 $\pm$ 0.4 Gt yr^{-2} to -15.9 $\pm$ 1.1 Gt yr^{-2}). This threshold temperature may be subject to change if we considered an evolving ice sheet. Gregory et al. (2004) found this temperature to be a threshold for GrIS deglaciation, as melt becomes larger than snowfall, which is in line with our findings. The surface mass loss acceleration is due to melt acceleration, together with loss of refreezing capacity. The latter has previously been identified as a key driver to the accelerated ice sheet and ice caps surface mass loss (van Angelen et al., 2013; Noël et al., 2017). The main contributor to melt increase before acceleration is the LW_{net}. The summer LW_{net} increases due to higher atmospheric temperatures and thicker clouds over the GrIS in this season. At the time of acceleration, a large fraction of the GrIS reaches the melting point during the summer. This accelerates the SHF over the ablation areas, as the difference between the surface and air temperatures increase at the rate of the air temperature increase. This further contributes to an expansion of the ablation area, which exposes more bare ice leading to accelerated solar radiation absorption from the albedo feedback.

The simulated ablation area expansion emerges from background variability already at a global mean temperature increase of 1.0 K with respect to preindustrial, decades before SMB (decrease) emergence. Therefore, we suggest that the monitoring of ablation area expansion can be used as a precursor for the detection of an emerging anthropogenic signal in surface mass balance.

The most SMB-relevant changes in North Atlantic atmospheric circulation projected by CESM2.1 are trends towards more positive NAO in the winter and summer, and more negative Greenland Blocking Index (GBI) in summer. High GBI in recent decades has been proposed to explain a large fraction of the recent melt increase (Hanna et al., 2018; Delhasse et al., 2018). The increase in the NAO index is robust among the CMIP5 ensemble (Gillett and Fyfe, 2013). In winter, we find that a positive NAO is related to less precipitation over the GrIS. The simulated summer trends in both NAO and GBI indices are apparent in both the CMIP5 models (Hanna et al., 2018) and the CMIP6 models (Delhasse et al., 2021), and cause partial reduction of melt. From this, we suggest that care must be taken when extrapolating the current circulation anomaly to the future, as, e.g., potential NAMOC weakening

may result in future atmospheric circulation changes that reduce melt. On the other hand, there is no guarantee that the models have a correct representation of, e.g., future NAMOC weakening and the current observed anomalous circulation pattern may continue to intensify.

3.7. Conclusions

1. GrIS surface mass loss accelerates for a global warming of 2.7 K through increased surface melt and loss of refreezing capacity.
2. Longwave radiation is the main contributor to melt increase before acceleration; albedo and turbulent heat fluxes add major contributions after.
3. Anthopogenic-forced atmospheric circulation changes (NAO and GBI) partially reduce melt.

4

Greenland ice sheet surface mass loss using the coupled CESM2.1-CISM2.1

Future melting of the Greenland ice sheet (GrIS) poses a danger to coastal communities through its contribution to sea-level rise. We use the Community Earth System Model version 2.1, coupled to the dynamically evolving Community Ice Sheet Model version 2.1, to investigate the multi-century evolution of the GrIS surface mass balance (SMB) under an idealized high CO_2 scenario. For a global warming of 4.2 K, with respect to a pre-industrial control simulation, the surface mass loss accelerates. Before acceleration, longwave radiation is the primary contributor to summer melt energy increase. Due to ablation area expansion, melt-albedo feedback and turbulent heat fluxes are the main contributors to melt energy increase after acceleration. Integrated over the GrIS, the SMB-elevation feedback causes an additional 44% surface mass loss. However, locally, the SMB-elevation feedback accounts for up to 50% of the surface mass loss. The results here show the need for fully coupled projections of GrIS on multi-century timescales.

4.1. Introduction

The Greenland ice sheet (GrIS) has been losing mass since the 1990s (Bamber et al., 2018a; Shepherd et al., 2019) in response to ongoing global warming. A major immediate effect of GrIS mass loss is a contribution to global mean sea-level rise. Future sea-level rise (Oppenheimer et al., 2019) is one of the main concerns for low-lying coastal populations. Since the 2000s, decreasing surface

Parts of this chapter have been published in Journal of Advances in Modeling Earth Systems **12**, e2019MS002031 (2020) (Muntjewerf et al., 2020b) and show my contribution to the manuscript.

mass balance (SMB) due to surface runoff increase is the primary contributor to GrIS mass loss (Enderlin et al., 2014; van den Broeke et al., 2016). Because of this high relative importance of the SMB, it will be the focus of this study. On longer time-scales than a century, in addition to the sea-level rise contribution, the GrIS may impact on the regional climate through its effects on ocean and atmospheric circulation (Ridley et al., 2005; Fyke et al., 2018). These effects may impact on future SMB, e.g., through the positive SMB-elevation feedback. This warrants a realistic representation of a dynamical GrIS in global climate simulations longer than a century.

Several challenges are associated with the bi-directional coupling of an ice sheet model (ISM) to a global climate model (GCM). An ISM requires a much higher resolution to resolve ablation areas and areas of fast-flowing ice than what is computationally efficient for a GCM. Furthermore, the GCM needs to provide the surface mass balance (SMB) as forcing to the ISM. The SMB itself also demands high resolution and advanced snow physics to be calculated over the GrIS. Challenges associated with the realistic treatment of the runoff, mass conservation, and energy conservation also needs to be addressed to achieve full coupling.

Due to these challenges, most beyond century GrIS SMB simulations are run with a standalone ice sheet models (Golledge et al., 2019; Aschwanden et al., 2019) or with simplified GCM-ISM coupling (Ridley et al., 2005; Vizcaíno et al., 2010; Vizcaino et al., 2015). Under high emission scenarios, GrIS elevation changes are small and have negligible impacts on SMB and atmospheric circulation. Beyond, these impacts become larger, and a failure to capture them will lead to incorrect projections. For the SMB, the most relevant feedbacks to capture through GCM-ISM coupling on longer time-scales is the SMB-elevation feedback (Edwards et al., 2014; Pattyn et al., 2018), regional warming by exposing more vegetation at Greenland (Ridley et al., 2005), high latitude cooling by a slowdown of NAMOC (Driesschaert et al., 2007), and precipitation changes due to changes in atmospheric circulation.

This study uses a coupled Community Earth System Model version 2.1 (CESM2.1) bi-directionally coupled with the Community Ice Sheet Model version 2.1 (CISM2.1) to make a multi-century projection of GrIS SMB under high idealized CO_2 forcing. CESM2.1 features a realistic representation of SMB (van Kampenhout et al., 2020) through its downscaling via elevation classes (Sellevold et al., 2019), and advanced snow physics (Flanner and Zender, 2006) suitable for polar conditions (van Kampenhout et al., 2017). Further, the CESM2.1-CISM2.1 includes dynamic landcover (ice can become vegetation, and vice versa) and GrIS topographic updating. The experimental setup is similar to that of Sellevold and Vizcaino (2020) (Chapter 3 in this thesis), but expands on that study by making a 200 years longer projection and by including a dynamically evolving GrIS.

In Section 2, we describe the model, coupling, and simulations in more detail. We then present the resulting global and Arctic climate change from the high CO_2 forcing, as well as SMB projections in Section 3. Section 4 provides a discussion where the results obtained are contextualized with existing literature.

4.2. Methods

4.2.1. Model Description

We used CESM2.1 (Danabasoglu et al., 2020) in our simulations. CESM2.1 is a fully coupled global Earth System model with prognostic components for atmosphere, ocean, land sea-ice, and land-ice. Atmospheric processes are simulated with the Community Atmosphere Model version 6, using the finite volume dynamical core (Lin and Rood, 1997; Neale, in review), at a nominal 1° horizontal grid, and 32 levels in the vertical. Ocean processes are simulated with the Parallel Ocean Program version 2 (Smith et al., 2010), which runs on a nominal 1° displaced-pole grid with 60 levels in the vertical. Sea-ice is represented by the Los Alamos National Laboratory sea-ice model version 5 (Hunke et al., 2017), which runs on the same horizontal grid as the ocean.

Land processes are simulated by the Community Land Model version 5 (CLM5; Lawrence et al., 2019). CLM5 has the same horizontal resolution as the atmosphere model. Depending on the land surface type, there is a maximum of 15 subsurface layers with layer depth ranging from ~0.02 m near the surface to ~14 m for the deepest layer. Snow is modeled by up to 10 snow layers, with a total maximum snow mass of 10 m water equivalent. CLM5 further includes the Model for Scale Adaptive River Transport to handle land surface runoff based on topographic gradients.

The GrIS is simulated using the CISM2.1 (Lipscomb et al., 2019). For the GrIS, CISM2.1 runs on a 4 km rectangular grid with 11 terrain-following vertical levels. The velocity solver uses a depth-integrated higher-order approximation (Goldberg, 2011) of the Stokes equations for ice flow. A pseudo-plastic sliding law described by Aschwanden et al. (2016) is used to parameterize basal sliding. Calving in this study occurs immediately as ice floats into the ocean

CESM2.1 contributes to the Coupled Model Intercomparison Project phase 6 (CMIP6; Eyring et al., 2016), and the Ice Sheet Model Intercomparison Project for CMIP6 (ISMIP6; Nowicki et al., 2016).

4.2.2. Coupling Description

In the default CESM2.1 configuration, ice sheets do not evolve, but the simulations described here have a dynamic GrIS which is interactively coupled to the other Earth system components (Muntjewerf et al., submitted). The model features an SMB calculation with a surface energy balance calculation of melt. The SMB (= snowfall + refreezing - sublimation - melt) is computed in CLM5 in ten elevation classes (ECs) for each glaciated grid cell (Lipscomb et al., 2013; Sellevold et al., 2019). The EC downscaling uses a fixed near-surface temperature lapse rate of 6 K km^{-1} and downscaling of specific humidity assuming constant relative humidity with elevation. Rainfall is converted to snowfall when the near-surface temperature is lower than -2°C, and snowfall to rainfall when the near-surface is higher than 0°C. In the case of snowfall-to-rainfall conversion, the resulting rainfall is routed directly to the ocean. The EC scheme features an interactive coupling to the atmosphere and explicit modeling of albedo, refreezing, and snow and firn compaction (van Kampenhout et al., 2017, 2019). The SMB is downscaled by the coupler to the

higher resolution CISM2.1 grid using a trilinear remapping scheme and corrected to conserve global water mass. Muntjewerf et al. (submitted) describes the remapping scheme.

The GrIS freshwater budget from surface runoff, basal melt, and ice discharge (i.e., calving) is coupled to the ocean model. The freshwater flux received by the ocean from the GrIS is the sum of surface runoff from CLM5, and the basal melt and ice discharge from CISM2.1. The surface runoff and the basal melt are distributed in the ocean by an estuary box model over the 30 m upper layers of the ocean grid cell (Sun et al., 2017). Ice discharge is delivered to the nearest ocean grid cell and spread horizontally in the surface layer with a Gaussian distribution with a maximum distance of 300 km. Ice melts instantaneously.

CESM2.1-CISM2.1 further includes dynamic land-unit change from glaciated to vegetated land cover as the ice sheet retreats, or vice versa, when the ice sheet advances. The ice sheet surface topography from CISM2.1 is used to recompute the fractional glacier coverage in CLM5, affecting the albedo and soil vegetation characteristics. The evolving ice sheet topography is also coupled to the atmospheric model, which enables orographic circulation feedbacks. Surface elevation and surface roughness fields are updated every ten years in the simulations.

4.2.3. Simulations

We analyzed two simulations in this study: a 300-year control simulation with constant pre-industrial (year 1850) forcing, and a 350-year transient simulation with an idealized atmospheric CO_2 scenario. The atmospheric CO_2 concentration initially increases by 1% per year until reaching 4× pre-industrial CO_2 level (1140 ppmv; hereafter 4×CO_2) in year 140 (Fig. 4.1a). The 4×CO_2 level is then maintained for the remaining 210 years of the simulation.

Both simulations start from the spun-up pre-industrial Earth system/ice sheet state in Lofverstrom et al. (2020). A near-equilibrium state is obtained by alternating a fully coupled model configuration, and a computationally efficient (coupled) model configuration with a data atmosphere. The residual drift in the near-equilibrated GrIS volume is 0.03 mm SLE yr^{-1}, with a GrIS volume and area which are overestimated by 12% and 15%, respectively when compared to observations. Ice sheet velocities and SMB compare reasonably well with present-day observations and regional modeling reconstructions (Colgan et al., 2012; Lipscomb et al., 2019; van Kampenhout et al., 2020).

4.3. Results

4.3.1. Global, Arctic and North Atlantic Climate Change

Figure 4.1b shows the evolution of the top-of-the-atmosphere (TOA) radiation imbalance. There is increasingly more radiation trapped in the Earth System due to the CO_2 forcing; therefore, the system warms. The global annual average near-surface temperature increases at an approximately constant rate in the first 140 years. By year 131–150, the warming is 5.2 $\pm$ 0.3 K (where the $\pm$ indicate 1 standard deviation for the same period; Fig. 4.1c). In the two centuries that follow, the

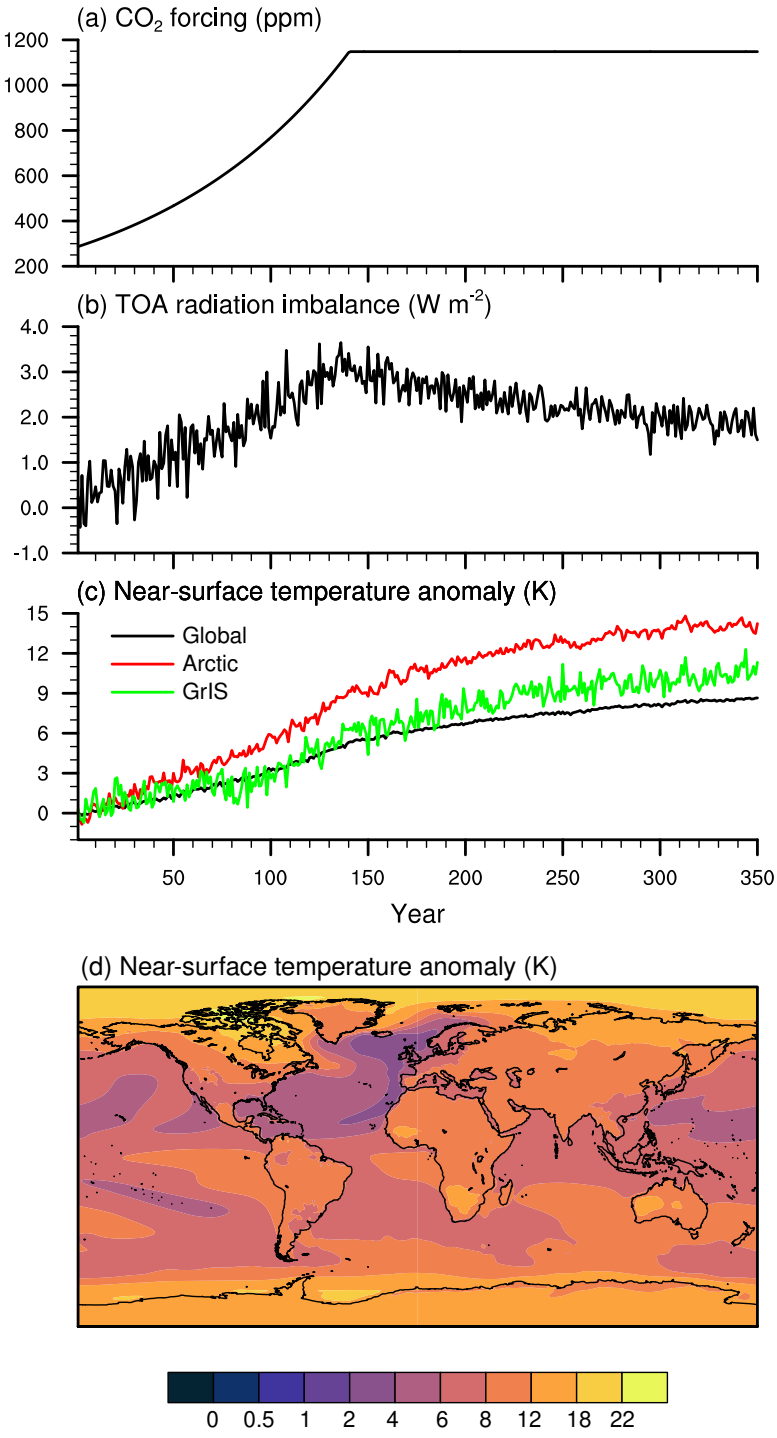

Figure 4.1: Evolution of (a) CO_2 (ppmv), (b) cumulative top-of-the-atmosphere (TOA) radiation imbalance, (c) near-surface temperature anomaly with respect to pre-industrial mean, and (d) anomaly map of near-surface temperature anomalies. The black lines show global averages, the red line shows Arctic (60°N-90°N) average, and the green line shows GrIS average. The anomaly map in (d) shows the difference between year 331–350 of the $4xCO_2$ run and the pre-industrial control.

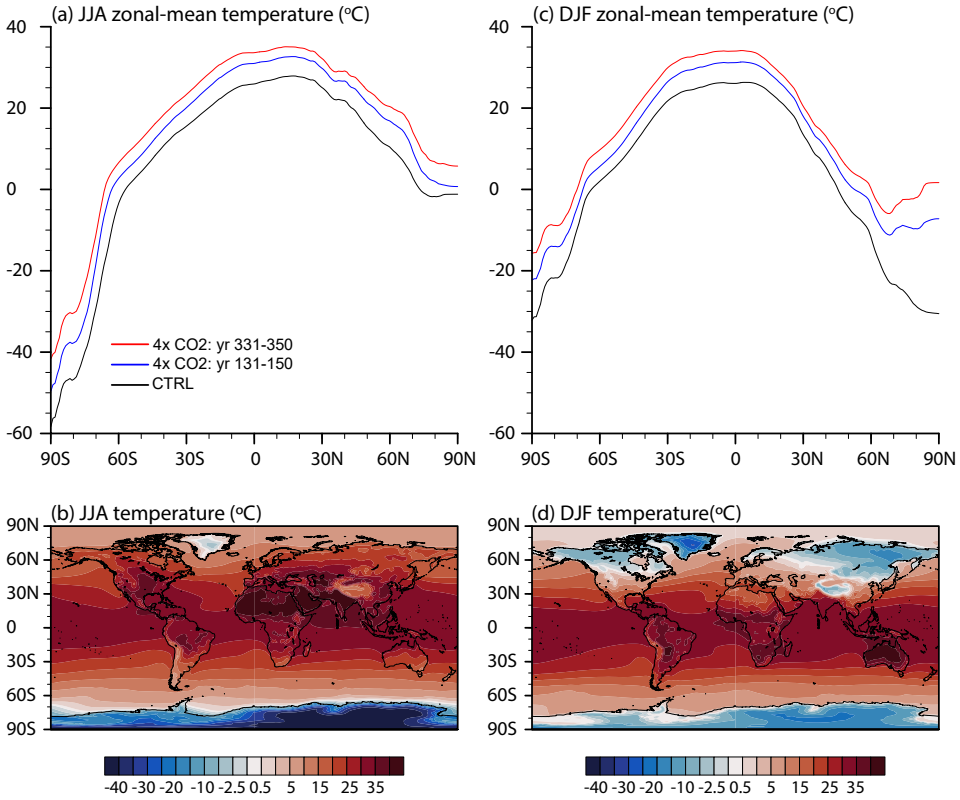

Figure 4.2: Zonal-mean (top) and maps (bottom) of summer (JJA; left) and winter (DJF; right) near-surface temperature (°C). The lines show the pre-industrial control (CTRL; black), 4× CO_2 years 131–150 (blue), and 4× CO_2 years 331–350 (red). The maps show the seasonal averages end-of-simulation (years 331–350).

temperature increases by an additional 3.3 K. The Arctic (defined as north of 60°N) warming follows a similar trajectory. The Arctic amplification factor (ratio between the Arctic and global temperature increase) is 1.6, where much of the signal comes from Arctic sea-ice loss. The GrIS amplification (ratio between GrIS and global temperature increase) with 1.2 is smaller than the Arctic amplification, as the GrIS is a terrestrial region with perennial ice/snow cover that holds the summer surface temperature below melting point.

Spatially, the annual near-surface temperature increases globally (Fig. 4.1d), with the most pronounced warming (>18 K) over the Arctic Ocean, the Canadian archipelago, and Antarctica. The North Atlantic warms the least due to the slow-down of the North Atlantic overturning circulation associated with meridional heat transport. The Arctic becomes seasonally ice-free from year 270, as the March sea-ice extent declines to less than 1×10^6 km^2.

Figure 4.2 shows the zonal means of the near-surface JJA and DJF tempera-

tures. The high Arctic (north of 80°N) warms somewhat less than lower Northern Hemisphere latitudes by years 131–150 in JJA. This is likely connected with the energy being used for melting sea ice. By years 331–350, the high Arctic warms more than other Northern Hemisphere latitudes due to lack of sea ice and a reduced snow cover. The interior of the GrIS is the only region in the Northern Hemisphere where the temperatures are below freezing.

The zonally averaged near-surface temperature in the Northern Hemisphere DJF (Fig. 4.2c) shows the Arctic amplification for years 131–150 and 331–350. The meridional temperature gradient reverses from ~70°N in both periods, though more pronounced in the second period. This reversal reflects the sea-ice thinning and retreat by 131–150, and sea-ice-free conditions by 331–350. By years 331–350, most Arctic land regions remain below freezing temperatures, while the ocean is sea ice-free (Fig. 4.2c). The GrIS is the coldest region in the Northern Hemisphere by the end of the simulation.

4.3.2. Change in Surface Mass Balance

The SMB in the pre-industrial simulation is 585 Gt yr^{-1} (Table 4.1), which is higher than present-day SMB (Noël et al., 2015, 2016; Fettweis et al., 2017), primarily due to a larger ice sheet and higher snowfall rates (Lofverstrom et al., 2020; van Kampenhout et al., 2019). In the 1% simulation, the surface mass loss increases by three distinct rates (Fig. 4.3c, black line). The SMB trend is -3.5 Gt yr^{-2} until year 119 and accelerates to -13.9 Gt yr^{-2} for the years 120–226. The global mean temperature increase is 4.2 K by year 120, with respect to the pre-industrial climate. In the years 226–350, the surface mass loss trend reduces to -5.4 Gt yr^{-2}, at the same time as the radiative forcing is reduced (Fig. 4.1b). The anthropogenic signal in the SMB emerges over background variability (20 years running mean is two standard deviations lower than the pre-industrial control mean; Fyke et al., 2014a) by year 84. At this year, the global mean temperature anomaly is 2.5 K. The SMB becomes negative by year 96, at a warming of 2.9 K.

Figure 4.3a shows the evolution of the ablation area as a percentage of the total GrIS area (note, the GrIS area is decreasing). The ablation area is the area with an annual mean SMB of < 0 Gt yr^{-1}. The anthropogenic-forced signal emerges over background variability in year 46 when the global mean temperature anomaly is 1.1 K. In a CESM2.1-only simulation (without an interactive ice sheet) under the same scenario forcing (Sellevold and Vizcaino, 2020), this ablation area signal emerges sooner than the SMB signal due to lower interannual variability. In the pre-industrial simulation, the ablation area is 5.5% (1.1×10^5 km^2). The ablation area expands rapidly in the 1% simulation, with three distinct trends whose timing of change appears sooner than those of the SMB trends. Up to year 98, the ablation area expands at a rate of 0.1% yr^{-1}. From year 99, the rate of expansion triples to 0.3% yr^{-1}; by years 131–150, the ablation area is 24.2% (4.8×10^5 km^2). Between years 193–350, the trend is again 0.1% yr^{-1}, leading to an ablation area covering 60.1% (10.1×10^5 km^2) of the total ice sheet area.

The area that is present below a certain elevation is shown in Fig. 4.3b. GrIS area increases exponentially with elevation, so a fixed increase in equilibrium line

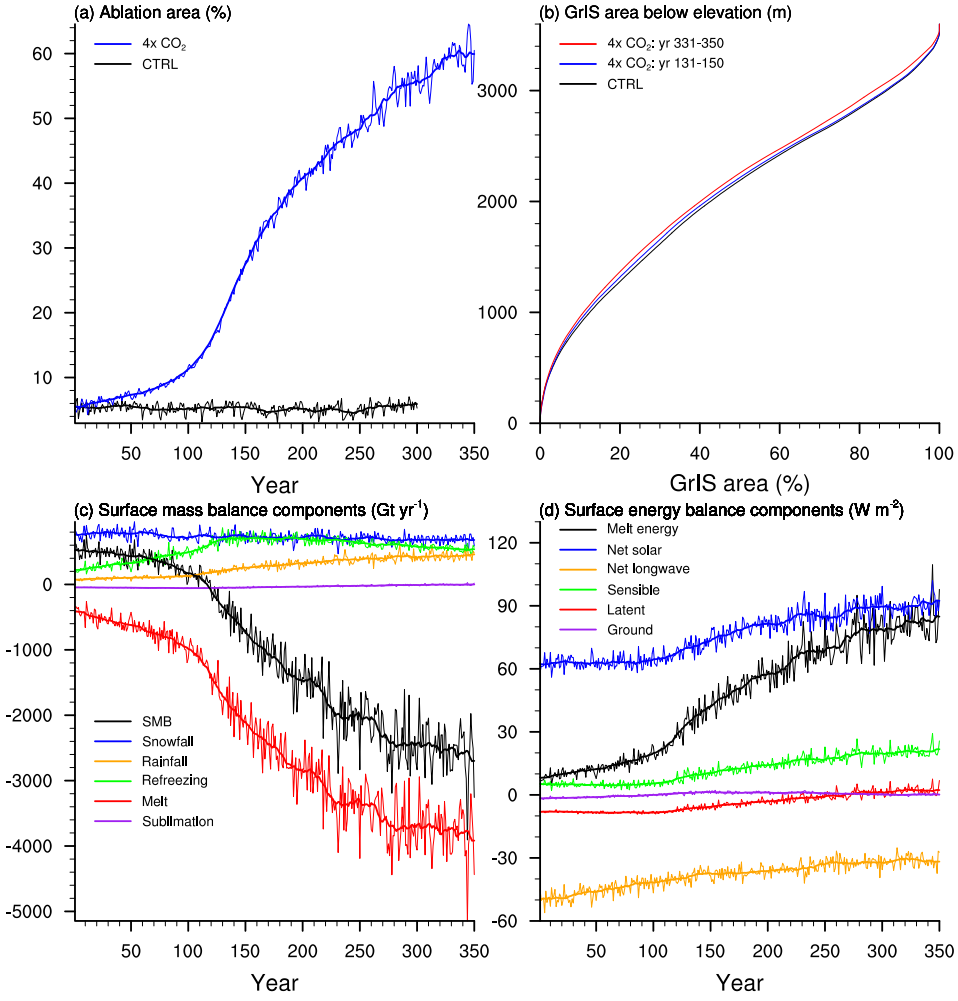

Figure 4.3: Change in annual SMB and JJA surface energy balance over the GrIS. a) Ablation area (%; as percentage of total ice sheet area), b) cumulative ice sheet area (x-axis) below a certain elevation (m; y-axis), c) Annual GrIS-integrated SMB components (Gt yr^{-1}), and d) JJA area-weigted averages of surface energy balance components (W m^{-2}). The thick lines in a), c-d) show the 20-years running means.

Table 4.1: Annual ice sheet integrated surface mass balance and components mean (standard deviation) and anomalies of the mean with respect to pre-industrial (Gt yr^{-1}). SMB (1°) values are calculated as the sum of components as calculated in CLM. SMB (4 km) values are in CISM, after downscaling and remapping. SMB (1°) = snowfall + refreezing - melt - sublimation. Rain (%) = rain * 100 / (snowfall + rain). Refreezing (%) = refreezing * 100 / (rain + melt). All changes in the mean are significant ($p < 0.05$) except snowfall by 131–150. Differences between the SMB (4 km) and SMB (1°) are because of the latter also accounting for changes in snow mass, while SMB (4 km) only accounts for changes in ice mass due to mass conservation (Vizcaíno et al., 2013)

Component	Pre-industrial	Years 131–150		Years 331–350	
		Absolute	Anomaly	Absolute	Anomaly
SMB (4 km)	585 (85)	-367 (166)	-952	-2259 (357)	-2844
SMB (1°)	544 (103)	-521 (217)	-1065	-2589 (442)	-3133
Precipitation	846 (83)	986 (97)	140	1122 (97)	276
Snowfall	780 (80)	750 (74)	-30*	683 (71)	-97
Rain	72 (12)	235 (38)	163	439 (59)	367
Refreezing	223 (54)	693 (73)	470	534 (43)	311
Melt	415 (92)	1,914 (251)	1499	3,804 (443)	3389
Sublimation	45 (4)	50 (6)	5	3 (11)	-42
Rain (%)	8 (1)	24 (3)	16	39 (4)	31
Refreezing (%)	46 (4)	32 (3)	-14	13 (1)	-33

altitude (ELA) will result in larger ablation area expansion, the higher on the ice sheet the ELA is. This can in part explain the rapid expansion of the ablation areas. The changing topography of the GrIS somewhat counteracts this effect. For example, a change in ELA from 1,000 m to 2,000 m with the pre-industrial topography (black line) will expand the ablation area with 30.2%. The corresponding ablation area expansion is 29.3% for the topography by the end of the simulation (red line).

Figure 4.3c shows the time evolution of the SMB components. Total precipitation rate increases throughout the simulation (Table 4.2), but the signal emerges relatively late (year 202, for a global mean temperature increase of 6.8 K). This is due to the combination of global warming and reduced North Atlantic meridional overturning circulation. The latter reduces the precipitation in the southern part of the ice sheet through its influence on the NAO (Peings and Magnusdottir, 2014a; Berdahl et al., 2018) and partly compensates for the moderate precipitation increases elsewhere (Sellevold and Vizcaino, 2020). Snowfall, unlike precipitation, decreases during the simulation but does not emerge over background variability. This decrease is due to an increased fraction of precipitation falling as rain, from 9% in the pre-industrial simulation to 39% by years 331–350, as a result of warming. The small decrease in snowfall rate and increased rain impact on refreezing. More rain refreezes in the snow, while the refreezing capacity is not refreshened by snowfall, causing a decrease in refreezing capacity.

Melt increases from the start of the simulation and accelerates after the first century. By years 131–150, the melt is five times greater than the pre-industrial melt (Table 4.1). Melt continues to increase until year 280 and reaches 9 times the pre-industrial values by the end of the simulation. Refreezing also increases from the beginning of the 1% simulation. This is mostly due to increased avail-

able liquid water from surface melt and rainfall, with melt representing the largest contribution (90% by the end of simulation). The refreezing capacity, defined as the fraction of refreezing to available meltwater, decreases from 46% in the pre-industrial simulation (in agreement with estimates from regional climate modeling; Noël et al., 2018) to 32% (131–150), in agreement with RCP4.5 projections (van Angelen et al., 2013). After the years 131–150, the refreezing amounts do not increase anymore, despite a further increase in available water. This is because the meltwater saturates the refreezing capacity of snow. From year 200 to the end of the simulation, the refreezing rate decreases. By the end of the simulation, the refreezing capacity is 13%. The maximum refreezing has values close to but below the total snowfall rate (93% for 131–150 and 79% for 331–350), confirming the validity of parameterizations that estimate potential refreezing as a fraction of total snowfall (Aschwanden et al., 2019).

Table 4.2: Summer GrIS-averaged albedo (-), near-surface temperature and skin temperature (°C), incoming short-wave radiation at the surface, incoming long-wave radiation at the surface, and surface energy balance components (W m^{-2}) (mean [standard deviation]). Melt energy = net short-wave radiation SW_{net} + net long-wave radiation LW_{net} + sensible heat flux SHF + latent heat flux LHF + ground heat flux GHF. All changes in the mean are significant ($p < 0.05$)

	Pre-industrial	Years 131–150	Years 331–350
Albedo	0.78 [0.01]	0.72 [0.01]	0.62 [0.01]
T_{2m}	-7.1 [0.8]	-1.5 [0.5]	0.6 [0.3]
T_{skin}	-7.6 [0.8]	-2.3 [0.4]	-0.8 [0.2]
SW_{in}	289.6 [3.7]	264.4 [5.2]	252.6 [6.2]
LW_{in}	231.3 [3.7]	266.6 [3.5]	279.7 [3.4]
Melt energy	8.2 [2.0]	38.2 [5.0]	83.1 [9.1]
SW_{net}	62.5 [2.3]	71.3 [3.4]	91.4 [4.4]
LW_{net}	-49.8 [2.0]	-37.7 [2.7]	-31.4 [2.8]
SHF	5.0 [1.0]	9.6 [1.9]	20.8 [2.9]
LHF	-7.8 [0.4]	-6.3 [1.0]	2.1 [2.1]
GHF	-1.7 [0.3]	1.2 [0.5]	0.2 [0.4]

The surface energy balance components (Fig. 4.3d) are necessary to explain the melt acceleration after year 120, and the subsequent acceleration in SLR contribution. In the first century of the 1% simulation, the primary source of additional melt energy is the increase in net longwave radiation (Table 4.2). The net shortwave radiation at the surface does not increase, because of reduced incoming shortwave radiation from enhanced cloudiness (Sellevold and Vizcaino, 2020) cancels out the effect of a reduced albedo. By years 131–150, the primary source of additional melt energy (40%) is still net longwave radiation. By the end of the simulation, albedo decrease makes net shortwave radiation the primary source (39%) followed by the turbulent heat fluxes (34%).

Melt energy reaches a threshold or tipping point close to year 120. The net shortwave and turbulent heat fluxes substantially increase, while the net longwave radiation continues a more smooth increase, as the global warming continues (Fig. 4.1). The sharp increases are the result of the combination of two processes. On the one hand, the ice-albedo feedback is a trigger and amplifies the melt increase

as the ablation area expands (Fig. 4.3a). Then, as the ablation area extends, more bare ice is exposed, which has an albedo of 0.4. This is much lower than, e.g., fresh snow and wet snow, which have albedos of 0.85-0.90 and 0.65-0.75, respectively. Further, the global mean temperature increase exceeds a certain threshold (4.2 K) that translates regionally into summer GrIS mean temperatures close to the melting point (Table 4.2). Large parts of the ice sheet surface are at melting point, while the near-surface temperatures can go above the melting point. This results in a stronger surface temperature gradient and leads to enhanced turbulent heat fluxes.

We now turn our focus towards spatial changes of the GrIS during summer (JJA). The pre-industrial ice sheet's albedo is 0.71, as most parts of the ice sheet are covered with perennial snow (Fig. 4.4a). With the CO_2 forcing, the margins retreat and reveal the low albedo vegetation under the ice sheet (Fig. 4.4b,c). Also, the ablation areas expand, and the snow in the interior gets wetter, causing a lowered albedo almost everywhere at the ice sheet. The mean ice sheet albedos are 0.72 and 0.62 by 131–150 and 331–350, respectively.

In the pre-industrial summer, the latent heat flux is negative everywhere over the ice sheet (Fig. 4.4d). A negative latent heat flux here represents energy loss from the surface to the atmosphere, due to sublimation or evaporation. With more energy available in the summer, sublimation increases at the ice sheet surface, except for at the margins (Fig. 4.4e,f). This effect causes the more negative latent heat fluxes over most of the ice sheet. However, at the margins, the latent heat flux becomes more positive with global warming. The more positive latent heat fluxes imply that moist air cools as it flows over the cold surface and reaches saturation, such that water vapor condenses or deposits on the melting ice. With time, as ice sheet surface melt increases, summer deposition becomes larger than sublimation, causing the sign change in Fig. 4.3d, red line. While deposition increases the melt energy, it has a small effect on the SMB (Fig. 4.3d, purple line).

The sensible heat flux is positive almost everywhere over the GrIS in summer (Fig. 4.4g), as the atmosphere is warmer than the surface. Over the ice sheet, the sensible heat flux increases with global warming (Fig. 4.4h,i). As the surface of the GrIS approaches the melting point, while the atmosphere continues to warm, the temperature gradient increases and causes more energy transfer to the GrIS surface.

To evaluate the effect of using a dynamically evolving ice sheet margin and topography on the SMB, we use the $4\times CO_2$ simulated elevation-dependent SMB as calculated by the elevation classes method and downscale to the pre-industrial (static) topography and ice sheet extent. It should be noted that the elevation classes calculated SMB still considers the evolving topography, such that the SMB is calculated with respect to e.g., change in precipitation patterns as the topography evolves.

The SMB on the static pre-industrial topography and ice sheet extent is 26 ± 14 Gt yr^{-1} (131–150) and 314 ± 62 Gt yr^{-1} (331–350) lower than the SMB for the evolving ice sheet topography and extent (Fig. 4.5a). This is because of the very high ablation at the ice sheet margins for the static pre-industrial ice sheet (Fig. 4.5a,b) more than compensates for the SMB-elevation feedback (Fig. 4.5c). On the

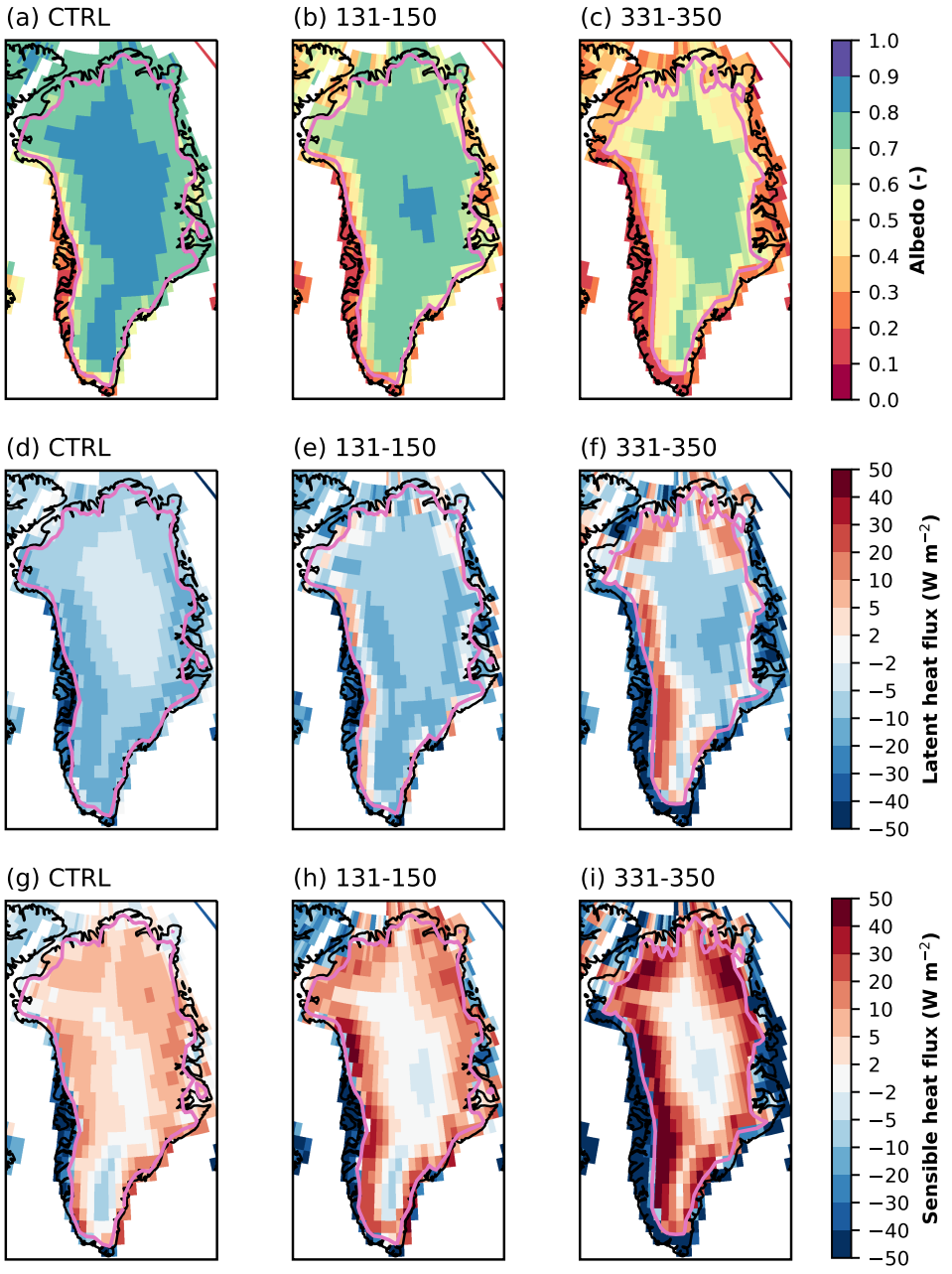

Figure 4.4: JJA Greenland climate for left row) pre-industrial (CTRL) (1-300), middle row) years 131–150 and right row) 331–350, with: a-c) albedo (-), d-f) latent heat flux (W m^{-2}), and g-i) sensible heat flux (W m^{-2}). Positive heat flux indicate heat transfer from atmosphere to land. Pink contour encloses areas with >70% glacier fraction within the grid-cell.

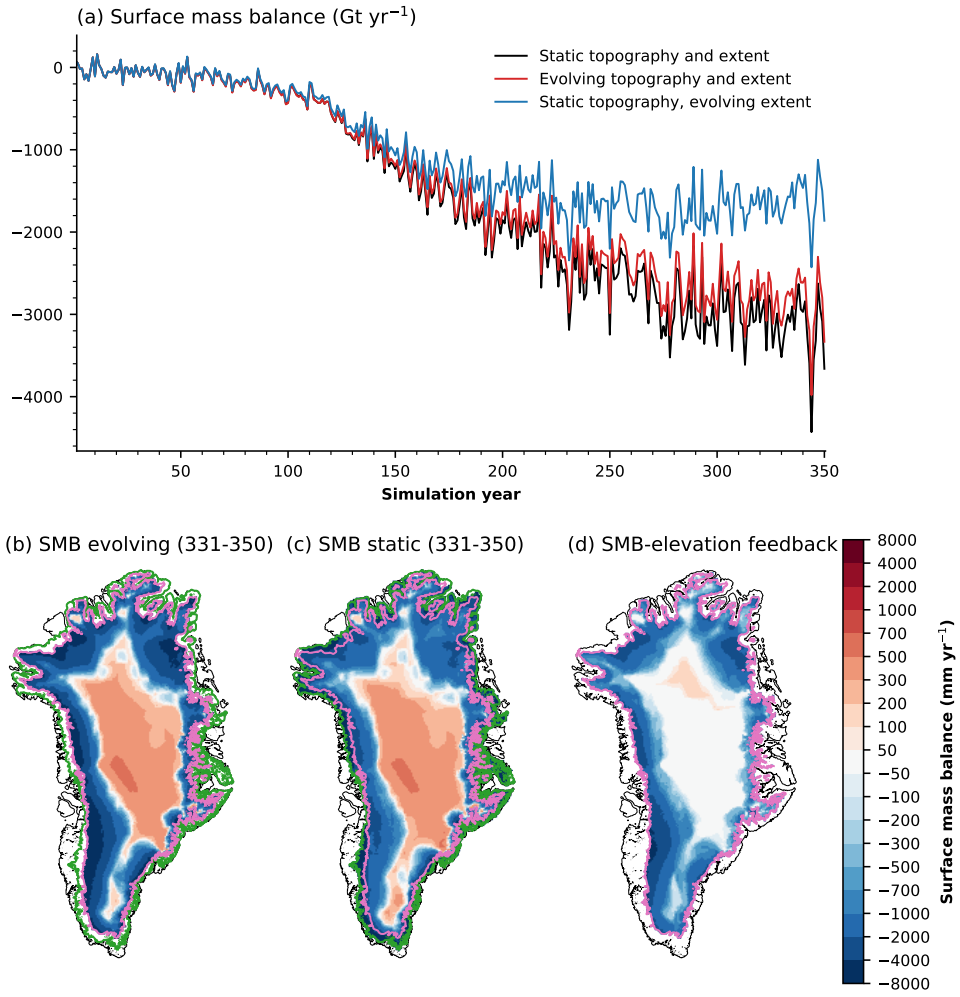

Figure 4.5: Annual mean surface mass balance anomalies with respect to the pre-industrial mean (Gt yr^{-1}; a) with a static pre-industrial topography and ice sheet extent (black line), with evolving topography and ice sheet extent (red line), and with a static topography, but evolving ice sheet extent (blue line). Annual mean 331–350 surface mass balance b) on the evolving topography (mm yr^{-1}), c) on the pre-industrial static topography (mm yr^{-1}), and d) SMB-elevation feedback (mm yr^{-1}). The SMB-elevation feedback is defined as the 331–350 SMB anomaly in the 4×CO_2 simulation, with respect to the 331–350 SMB on the pre-industrial topography(i.e., b-c). The green solid line in (b,c) shows the pre-industrial GrIS extent, while the pink (b-d) shows the 331–350 GrIS extent.

other hand, when evaluating the SMB on the pre-industrial ice sheet topography, but accounting for the retreating margin, the SMB is 112 $\pm$ 18 Gt yr^{-1} (131–150) and 1,259 $\pm$ 109 Gt yr^{-1} (331–350) higher than the SMB for the evolving ice sheet topography and extent. So, when accounting for the retreating margins, the SMB-elevation feedback decreases the SMB with an additional 12.1% by 131–150 and 44.4% by 331–350 (Fig. 4.5a,c).

An interesting feature of the SMB evolution without SMB-elevation feedback and a retreating margin is that the SMB is seemingly increasing by the end of the simulation. This may imply that the SMB-elevation feedback sustains the end of the simulation SMB decrease.

Figure 4.6 shows the time evolution of SMB and topography along three 400 km long cross-sections following the topographic gradient in the southwest (67°N), and north (Peterman and NEGIS catchments). At the start of the simulation, the equilibrium line altitude (ELA) is at 1,500 m in the SW. From year 120, the ELA starts to increase. The first 500 m increment of the ELA takes around 30 years and brings the ablation 60 km further inland. The next 500 m increment, raising the ELA to 2,500 m, takes another 90 years, and brings the ablation another 100 km inland. Another apparent feature is how the topography is lowering and steepening. For example, at the start of the simulation, the distance from the 2,000m to the 2,500m contour is ~100 km, while at the end of the simulation, this distance decreases to 80 km. Steeper topography implies faster flowing ice, and increased katabatic winds.

If we follow the change of SMB at 1,500 m (which is at x=100 km at the start of the simulation), we see that it starts at ~ 0 mm yr^{-1} and ends up at ~ -4 mm yr^{-1} after 350 years of CO_2 forcing. However, if we follow the SMB evolution at x=100 km, at year 350, the SMB is -8 mm yr^{-1}. If we assume this point would have followed the climate evolution at its original topography if it did not decrease, then locally, the SMB-elevation feedback is as important as the CO_2 forcing.

4.4. Discussion and conclusions

In this study, we forced the coupled CESM2.1-CISM2.1 by increasing CO_2 with 1% per year (compared to pre-industrial levels) until 4×CO_2 stabilization in year 140. The simulation was then continued with a fixed 4×CO_2 forcing for 210 more years. Our primary focus is on the SMB evolution, with a detailed analysis of the GrIS surface mass and surface energy evolution.

The SMB decreases by 952 Gt yr^{-1} (years 131–150) and 2844 Gt yr^{-1} (years 331–350). The SMB decrease here is comparable, though larger than the projections by Vizcaino et al. (2015), who project an SMB decrease of 601 Gt yr^{-1} at 4×CO_2 stabilization, and 2420 Gt yr^{-1} by the end of their multi-century projection. These differences are likely due to different anthropogenic emissions as they use the Representative Concentration Pathway 8.5 (RCP8.5) scenario, their lower GCM and ISM resolution, and differences in the GCM-ISM coupling. Le clec'h et al. (2019) run the regional climate model MAR coupled to an ISM, and project an SMB decrease of 918 Gt yr^{-1} by 4×CO_2 stabilization under a RCP8.5 scenario.

The main contributor to SMB decrease is surface melt increase. Before the SMB acceleration, increasing incoming longwave radiation due to atmospheric warming

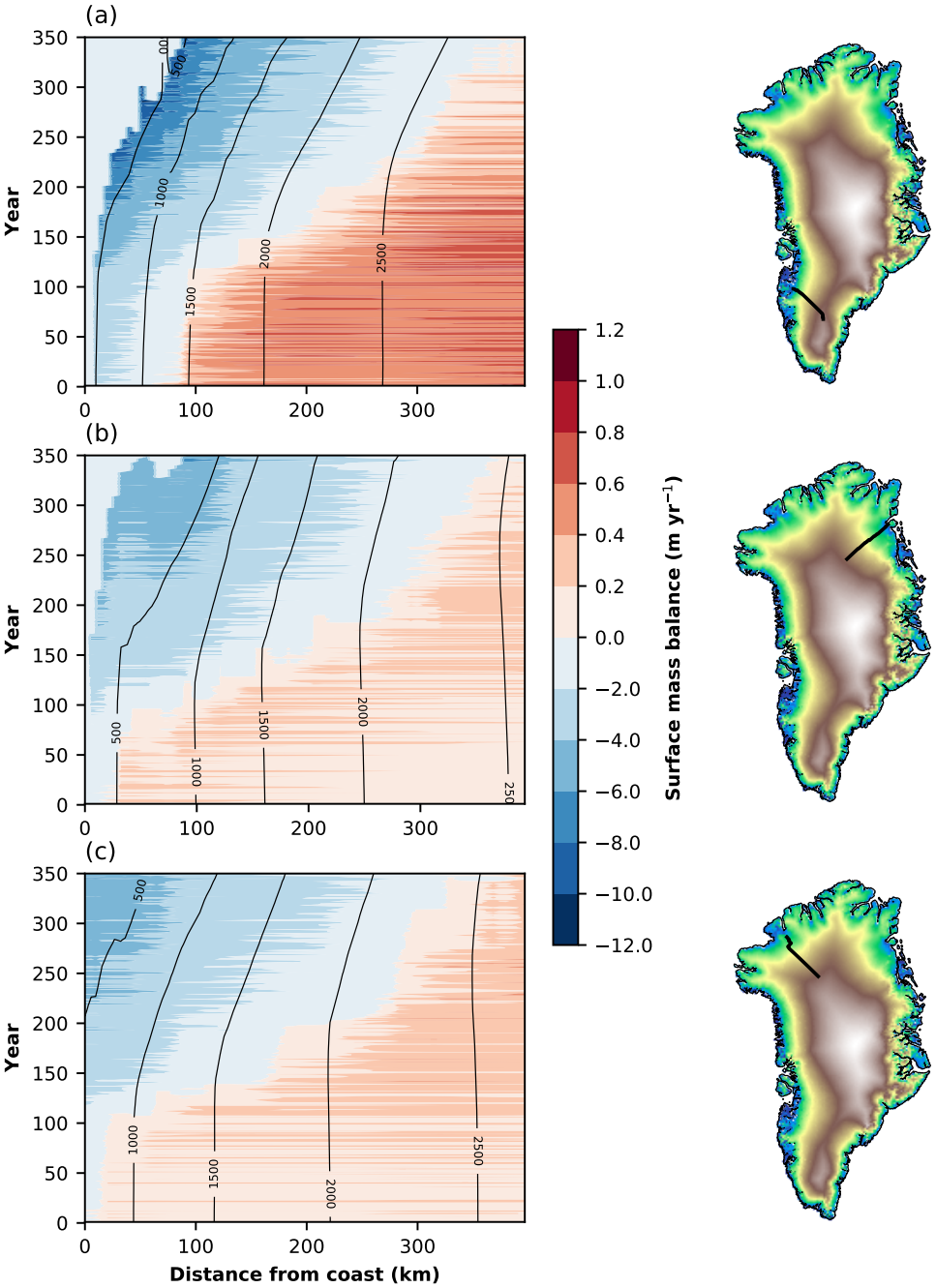

Figure 4.6: Hovmöller plots of annual mean SMB (m yr^{-1}; colors) and annual mean topography (m; contours) for three transects on the GrIS. The transects are shown in the maps to the right, where the black line corresponds to the x-axis on the left side. Note the different scaling of the positive and negative colors.

provides the energy for melt. After acceleration, melt-albedo feedback and the turbulent heat fluxes are the main contributors to melt energy increase due to the ablation area expansion exposing more bare ice during summer. These findings are in agreement with other studies (Franco et al., 2013; Sellevold and Vizcaino, 2020). However, we expand on these previous studies by providing the multi-century evolution.

We found that the SMB-elevation feedback decreases the SMB with an additional 12.1% by 131–150 and 44.4% by 331–350. For this first estimate, other studies find this number to be in the range 4.3%–11.0% (Edwards et al., 2014; Vizcaino et al., 2015; Le clec'h et al., 2019), i.e., there is considerable uncertainty. This means that the SMB-elevation feedback by the stabilization of the CO_2 forcing is somewhat stronger in our simulation. Vizcaino et al. (2015) find a contribution of the SMB-elevation feedback to be much lower (33%) than what we project here. Despite these differences, our simulations show that the SMB-elevation feedback becomes increasingly important with global warming. The SMB decrease due to global warming is more substantial than the SMB decrease due to SMB-elevation feedback, which is in agreement with other studies (Edwards et al., 2014; Vizcaino et al., 2015; Le clec'h et al., 2019; Aschwanden et al., 2019).

5

Influence of Arctic sea-ice loss on the Greenland ice sheet climate

What happens in the Arctic,
does not stay in the Arctic.

Vidar Helgesen

Arctic sea ice loss has the potential to influence the Greenland ice sheet (GrIS) surface climate. Detecting robust signals of an impact of the sea ice loss on GrIS from observations is difficult due to the short observational records. Also, signals detected using transient climate simulations may be aliases of other forcings. Here, we study the seasonal impact of reduced Arctic sea ice on GrIS surface mass balance (SMB). This is achieved by forcing the Community Earth System Model version 2.1 (CESM2), which features a coupled calculation of SMB, with pre-industrial and future monthly varying sea ice concentrations and sea surface temperatures while keeping all other forcings constant. The result is a warmer and wetter Arctic and a GrIS with an enhanced hydrological cycle. GrIS SMB increases in winter due to increased precipitation, particularly in the south, driven by the more humid atmosphere and an increase in cyclones. In summer, surface melt increases as a result of a warmer and wetter atmosphere providing increased energy transfer to the surface through the sensible and latent heat fluxes, which triggers the melt-albedo feedback. Deep warming occurs over the Baffin Bay through high (~1

Parts of this chapter are in review for Climate Dynamics

m s^{-1}) vertical winds, due to the topographical obstacle the GrIS exerts on the zonal flow. This deep warming results in regional enhancement of the 500 hPa geopotential heights over the Baffin Bay and Greenland, with increased blocking and heat advection over the GrIS' surface.

5.1. Introduction

Arctic amplification, the rapid warming of the Arctic relative to the global mean warming, is a prominent sign of contemporary climate change that has emerged in the late 1990s (Serreze and Francis, 2006; Serreze et al., 2009). A combination of many factors causes warming in the Arctic, e.g., atmospheric transport of heat from the midlatitudes (Screen et al., 2012), trapping of longwave radiation by CO_2 (Pithan and Mauritsen, 2014), increased water vapor, and albedo-temperature-feedback due to thinning and retreat of sea ice (Screen et al., 2012; Pithan and Mauritsen, 2014). Arctic amplification does not only impact the Arctic climate but may also have impacts on midlatitude atmospheric circulation and weather (Cohen et al., 2014; Overland et al., 2015; Coumou et al., 2018). However, the latter linkage is debated (Barnes, 2013; Screen and Simmonds, 2013b; Barnes and Screen, 2015a).

The GrIS is the largest body of freshwater in the northern hemisphere, and would raise the global mean sea level by 7.4 m if melted (Bamber et al., 2018a). Since 2012, the GrIS has been losing mass at a rate of 247 Gt yr^{-1} (0.69 mm yr^{-1} of global sea-level rise; Bamber et al., 2018b), after the ice sheet being in approximate mass balance before the 1990s. An increase in melt of the Greenland ice sheet (GrIS) follows the onset of Arctic warming (Trusel et al., 2018).

Surface mass balance (SMB) decline is the primary contributor (~60%) to the current GrIS mass loss, with recent increases in ice discharge as second contributor (~40%) (van den Broeke et al., 2016). The GrIS surface gains mass through snowfall, the rainfall that refreezes in the snow, and through deposition/riming (Ettema et al., 2010). On the other hand, the surface loses mass through melt that is not refrozen in the snow and sublimation. Melt occurs when the ice sheet's temperature reaches 0°C, and there is a surplus of energy (van den Broeke et al., 2008). The SMB of the GrIS has a strong seasonal cycle, with net mass gain in fall, winter, and spring, and net mass loss during the summer months.

While sea ice loss and its impacts on high latitude climate have been extensively investigated (Francis and Vavrus, 2012; Screen and Simmonds, 2013b; Barnes and Screen, 2015a; Barnes and Polvani, 2015b), little attention has been paid to the potential influence on the GrIS SMB. Observational studies suggest sea ice loss has a small impact on summer melt at the GrIS surface, restricted to western low-elevation areas (Rennermalm et al., 2009; Liu et al., 2016; Stroeve et al., 2017). When sea ice loss occurs close to the GrIS, the atmosphere becomes warmer and moister due to increased contact with the open ocean leading to increased incoming longwave radiation at the surface of the ice sheet. More incoming longwave warms the surface and leads to increased melt. The melt attributable to increased turbulent heat fluxes is small, as the onshore flow is blocked by katabatic winds over the GrIS. However, the non-zero contribution might suggest a barrier wind mechanism (van den Broeke and Gallée, 1996) mixing the onshore winds with the offshore

katabatic winds (Stroeve et al., 2017). In years with extensive melt of both sea ice and the GrIS, anomalous atmospheric ridging occurs over the GrIS (Liu et al., 2016). While this circulation pattern is likely not caused by sea ice loss, the sea ice loss may reinforce this circulation pattern. Modeling studies (Noël et al., 2014; Liu et al., 2016) corroborate the observational evidence of an impact of sea ice loss on the GrIS. Additionally, Liu et al. (2016) find that the anomalous ridging induced by sea ice loss can lead to an increase in summer atmospheric blocking events. Blocking is quasi-stationary synoptic high pressure systems that block the westerly flow. Further, Noël et al. (2014) find that annual precipitation in the southeast of the GrIS increases in response to reduced sea ice.

The short observational record makes difficult to detect robust mechanisms linking sea ice loss with increased GrIS surface melt, due to the large interannual variability and their co-relationship with global warming. Also, available modeling studies are either short (5 years) or lack a physical calculation of GrIS SMB. Motivated by this gap, we use the Community Earth System Model version 2.1 (CESM2) to simulate the climate response to Arctic sea ice and sea surface temperature (SST) perturbations with the goal of determining the response of the GrIS SMB to ongoing and future sea ice loss, and understand the underlying processes. CESM2 features a physically based calculation of SMB, making it a state-of-the-art framework for studying this possible connection. Also, we will use many ensembles (100 members per experiment) to detect robust signals of changes of the GrIS SMB induced by sea ice loss.

5.2. Methods

5.2.1. Model

We use the Community Earth System Model 2.1 (CESM2; Danabasoglu et al., 2020). This model is a participant in the climate model intercomparison project (CMIP) phase 6 (Eyring et al., 2016). The model is run with active atmosphere, sea ice, land, and ice sheet components and with prescribed ocean sea surface temperatures (SSTs). The atmospheric model is the Community Atmosphere Model version 6 (Gettelman et al., 2019b), run with a horizontal resolution of 1.25° (longitude) × 0.9° (latitude) and 32 vertical levels. The sea ice model is the Los Alamos Sea Ice Model version 5 (Hunke et al., 2017), run at a nominal 1° resolution with prescribed sea ice concentrations. The land model is the Community Land Model version 5 (CLM5; Lawrence et al., 2019), run at the same horizontal resolution as the atmosphere. CESM2 also features an ice sheet component, the Community Ice Sheet Model version 2.1 (Lipscomb et al., 2019), at 4 km resolution. In this study, the ice sheet evolution is turned off (fixed topography), so the ice sheet model is a purely diagnostic model providing high-resolution sub-grid topography for the SMB calculation in CLM5. CESM2 successfully simulates present-day GrIS SMB (van Kampenhout et al., 2020), and reproduces the SMB response to global warming as simulated by high resolution regional climate models (Sellevold and Vizcaino, 2020).

5.2.2. Surface mass balance calculation

For the calculation of GrIS SMB, CESM2 uses an elevation class scheme (Sellevold et al., 2019). This calculation is carried out by CLM5 at every grid cell over Greenland containing non-zero glacier cover. The EC method downscales the near-surface temperature with a lapse rate of 6 K km^{-1}, the incoming longwave radiation with 32 W m^{-2} km^{-1}, and specific humidity assuming constant relative humidity, using 10 elevation bins. For the calculation of surface melt, the surface energy balance [W m^{-2}] is calculated at every EC as

$$M = SW_{in}(1-\alpha) + LW_{in} - \epsilon\sigma T_{sfc}^4 + SHF + LHF + GHF, \quad (5.1)$$

where M is the melt energy, SW_{in} is the incoming shortwave, α is the surface albedo, LW_{in} is the incoming longwave, ϵ the surface emissivity, σ the Stefan-Boltzmann constant, and T_{sfc} the surface temperature. SHF is the sensible heat flux, LHF is the latent heat flux, and GHF is the ground heat flux.

At every EC, the SMB [Gt yr^{-1}] is calculated as

$$SMB = SNOW + REFRZ - MELT - SUBL, \quad (5.2)$$

where SNOW is the snowfall, REFRZ is the amount of refreezing of rainfall or melt, MELT is the surface melt, and SUBL is the sublimation (deposition if negative). Phase partitioning of rain and snowfall occurs at each EC based on near-surface temperature. At temperatures lower than -2°C, precipitation falls exclusively as snow, while at temperatures higher than 0°C, precipitation falls exclusively as rain. In between this range it appears as mixed phase precipitation.

5.2.3. Simulations

The simulations analyzed here are contributions to the polar amplification model intercomparison project (PAMIP; Smith et al., 2019). Two experimental setups are used, both starting in April 2000 and running through May 2001. The first two months are discarded as spinup, leaving a full year for analysis. Each of the two experiments consist of 100 one-year simulations, each with slightly different initial condition. The difference between the two experiments are only in the sea ice and within-Arctic SST prescription, one corresponding to pre-industrial conditions (CTRL; Danabasoglu, 2019e) and the other to a 2°C warmer climate (FUT; Danabasoglu, 2019f) as illustrated in Fig. 5.1.

We obtain monthly varying sea ice concentrations and SST's from the historical and RCP8.5 scenario simulations from the CMIP5 (Taylor et al., 2012). Three distinct periods are defined: Pre-industrial, present-day, and future, with global mean temperatures of 13.7°C, 14.2°C, and 15.7°C, respectively. For each CMIP5 model, the 30-year running mean global mean temperature is calculated. When this global mean temperature matches those defined above, a 30 year average of SIC and SST is taken to represent the period. At each grid point, linear regression between present-day values and pre-industrial (or future) values of SIC and SST across the the 30 year averages from each model are computed. Then, the required pre-industrial (or future) estimate is taken as the point where this regression relationship intersects the observed (1979-2008 climatology from the Hadley Centre

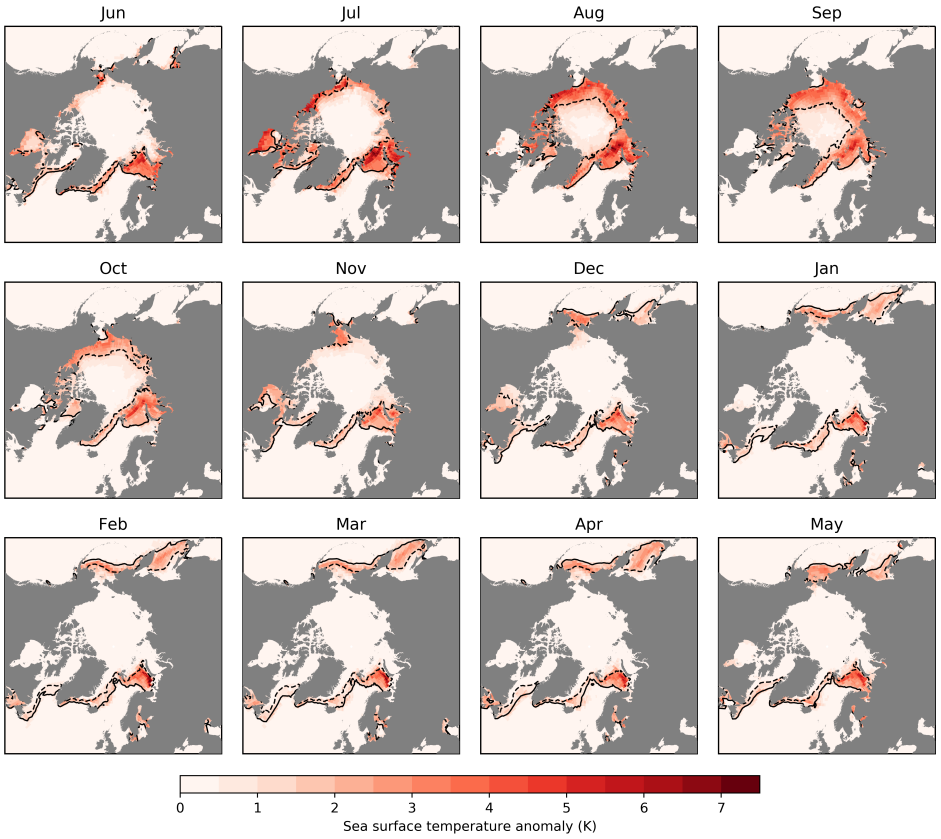

Figure 5.1: Sea-ice extent and sea surface temperature differences between future (FUT) and control (CTRL) experiments for the months of the year. The solid black line corresponds to the CTRL sea ice edge (>0.15 SIC), while the black dashed line corresponds to the FUT sea ice edge. The color corresponds to the difference in prescribed SST between FUT and CTRL.

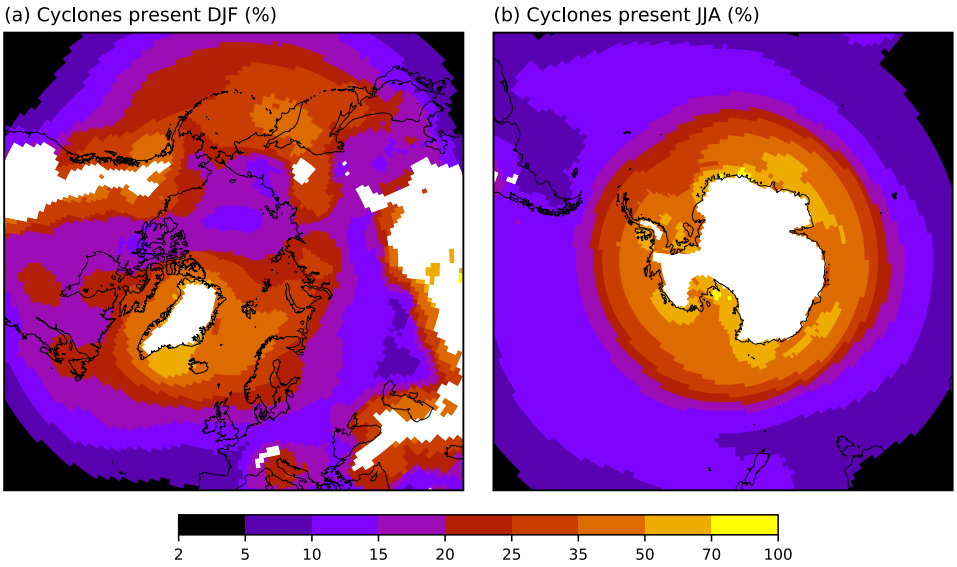

Figure 5.2: The amount of time where a cyclone is present in a grid cell (%) in a) DJF and b) JJA.

Sea Ice and Sea Surface Temperature dataset; Rayner et al., 2003) values in order to constrain the estimates of SIC and SST. In the regression to obtain SIC and SST, quartile regression (Waldmann, 2018) is used instead of the more common least square regression to reduce the influence of outliers. For the pre-industrial (future), the upper (lower) quartile of the regression is used to give higher weight to models with more (less) sea ice and colder (warmer) SST's. Following the method of Screen et al. (2013a), in any grid cell where the pre-industrial or future SIC deviates with more than 10% from the present-day value, SST's derived using the method described above are prescribed.

5.2.4. Analysis

To assess the response to Arctic sea ice loss and increased SSTs, we make use of some specific circulation metrics.

To identify individual cyclones, we use a modified version of the method presented in Zhang et al. (2004). The method applies these steps on 6 hourly averaged sea level pressure (SLP) data:

1. Remove SLP values where the topography surface elevation is higher or equal to 1,000 m.

2. Any grid point with SLP lower than its eight surrounding neighbors is considered a cyclone candidate.

3. The minimum SLP gradient between the cyclone candidate and its eight surrounding grid points is required to be 1.5×10^{-6} hPa m^{-1}. The SLP values

at the eight surrounding grid points are representative of the spatial average using their nine adjacent grid points.

4. The minimum SLP gradient between the four surrounding points of the cyclone candidate and their outside adjacent grid points must be negative inward.

5. We add a radius of 600 km to each cyclone center.

6. The daily average over the 6 hourly cyclones is calculated, to obtain the fraction of a day when a cyclone influences a grid point.

Different cyclone detection algorithms do give different results. The cyclone climatology produced with the method presented here (Fig. 5.2) compares well with those of other methods (Neu et al., 2013).

To identify dynamic blocking events, we use the modified two-dimensional method described by Kennedy et al. (2016). We take the 5-day running mean of daily averaged 500 hPa geopotential heights (Z_{500}) to enforce a 5-day criterion on the duration of a blocking event. At every grid point within 35°N and 80°N, we calculate the northern (G_N) and southern (G_S) gradients through the formula

$$G_S = \frac{Z_{500}(\phi_0) - Z_{500}(\phi_S)}{\phi_0 - \phi_S}, \quad G_N = \frac{Z_{500}(\phi_N) - Z_{500}(\phi_0)}{\phi_N - \phi_0}, \tag{5.3}$$

where ϕ_0 corresponds to the latitude of the grid cell, $\phi_N = \phi_0 + 10°N$, and $\phi_S = \phi_0 - 10°N$. Whenever $G_S > 0$ and $G_N < -10$ m degree^{-1}, we consider the grid cell blocked. The difference of our method compared to the original method, is that we calculate gradients with a distance of 10°N rather than 15°N. This allows us to extend to 80°N, while the original method can calculate up to 75°N. However, the two methods give similar results within the overlapping area (not shown).

5.3. Results

5.3.1. Large-scale climate response

In this section, we explore the Arctic response in CESM2 to the monthly varying SIC and SST perturbations shown in Fig. 5.1. Sea ice is reduced in every month of the year and is accompanied by a co-located increase in SST. The most widespread loss of sea ice occurs in summer and late fall. In the other months, the largest sea ice losses occur in the Barents Sea, the Greenland Sea, the Bering Sea, and the Sea of Okhotsk. In the seas surrounding Greenland, there is a year-round loss of sea ice. The sea ice reductions in the Arctic (>60°) are 4.1×10^6 km^2 and 3.8×10^6 km^2 for winter and summer, respectively. The corresponding SST increases are 0.4 K and 1.4 K.

In response to this forcing, the Arctic experiences summer and winter warming (Fig. 5.3a,c). In winter, there is widespread warming over both the Arctic ocean and Arctic land (Fig. 5.3a). Three local warming maxima can be found in the Barents-Kara Seas, the Hudson Bay, and the Chukchi Sea. The warming imprint is evident over the entire Greenland ice sheet, with the strongest warming occurring in the South. The Arctic surface warming extends to a depth of ~600 hPa (Fig. 5.3b).

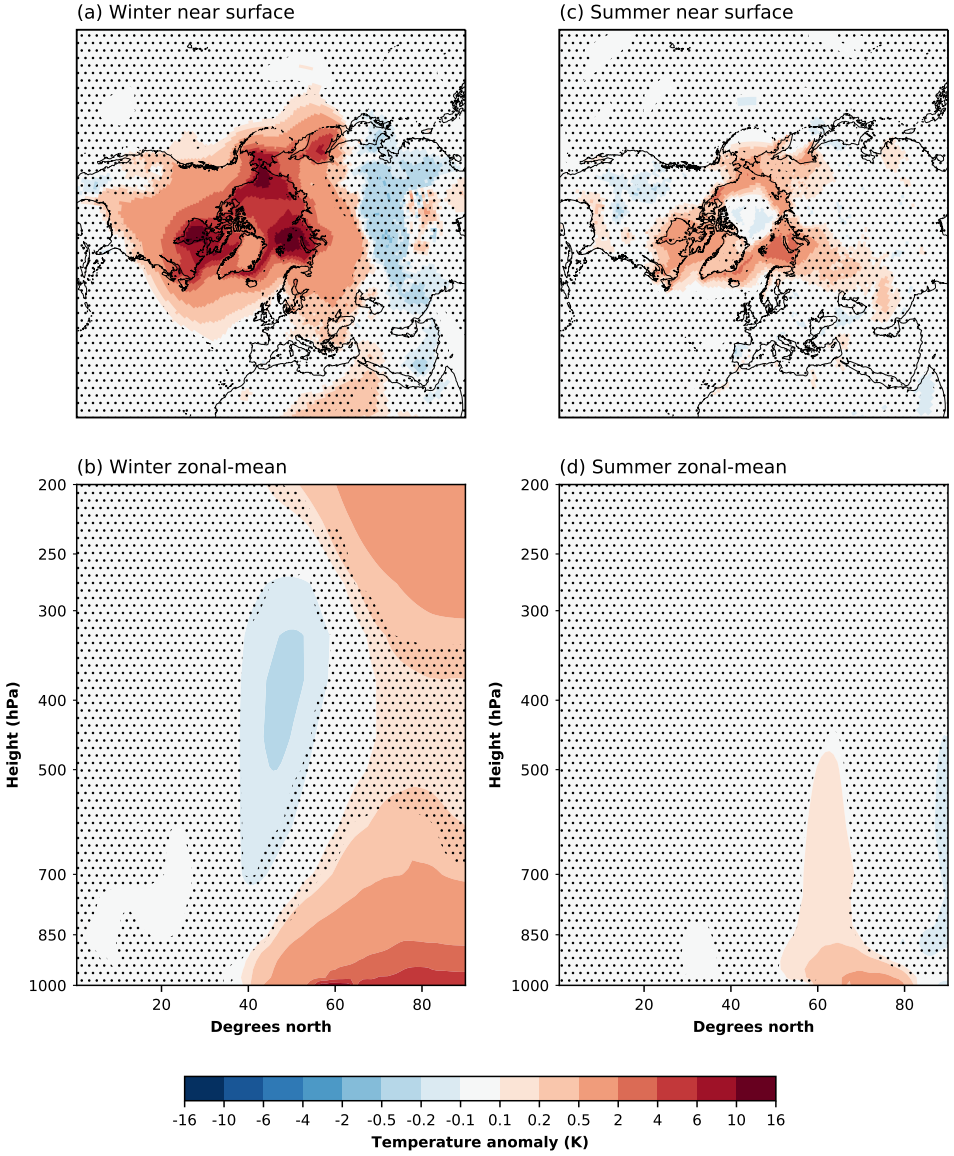

Figure 5.3: Simulated Arctic amplification as a response to the forcing. (a) Winter near surface [K], (b) winter zonal-mean [K], (c) summer near surface [K], and (d) summer zonal-mean [K] temperature anomalies. Dots indicate non-significant response at 95 % level, according to a student's t-test.

There is also warming occurring in the upper troposphere in response to the sea ice and SST forcing. There is some mid-tropospheric cooling around 40°N, associated with a weak (not significant) surface signature in central Asia.

During summer, the warming is primarily confined to the ocean in a latitudinal band of 50°N-80°N (Fig. 5.3c). Also, the southern part of Greenland warms. Central parts of the Arctic Ocean show a small (0.1 K) yet significant cooling. In the zonal-mean, the Arctic surface warms, and this warming extends into the troposphere (up to ~ 450 hPa; Fig. 5.3d).

Figure 5.4 shows different components of the Arctic surface energy budget. In winter, there is a decrease in SW_{in} over the Hudson Bay and the Sea of Okhotsk (Fig. 5.4a), indicative of increased cloud cover. The decrease in SW_{in} is more than compensated for by a decrease in albedo leading to increased SW_{net} (Fig. 5.4b). There is a pan-Arctic increase in LW_{in} (Fig. 5.4c) caused by increased atmospheric re-emittance of LW radiation as the atmosphere warms and moistens. The patterns follow the near-surface air temperature response pattern closely (Fig. 5.3a). However, in these areas the LW_{out} increases more than the LW_{in} due to high warming of the surface, leading to decreased LW_{net} (Fig. 5.4d). In central Arctic Ocean, and over Arctic landmasses in Siberia and Canada, the LW_{net} increases as a result of increasing LW_{in}. In these areas, the snow or ice-covered surfaces does not warm enough to compensate for the increased LW_{in}. Where sea ice is lost in FUT, SHF+LHF increases substantially in the Barents-Kara Seas, Hudson Bay, the Chukchi Sea, and in the Sea of Okhotsk (Fig. 5.4e). The SHF+LHF increase is due to the strong SST warming prescribed with the sea ice loss, at the boundary of a relatively cold atmosphere. Where sea ice is perturbed, more heat and moisture are entering the atmosphere, which is advected over the North Atlantic and the Pacific Ocean, where there is no change in surface conditions. This leads to a decrease in SHF+LHF in these areas. The decrease means less heat and moisture transfer from the ocean to the atmosphere, rather than an increased atmosphere to ocean transfer.

In summer, large parts of the Arctic Ocean experience more cloud cover, leading to a reduction in SW_{in} (Fig. 5.4f). As in winter, in areas with sea ice loss, the SW_{net} increases (Fig. 5.4g) despite the reduction in SW_{in} due to reduction in surface albedo. This effect is larger in summer as the background solar insolation is higher in summer. Due to the increased cloud cover and higher atmospheric temperatures, the LW_{in} increases. This increase is much smaller in summer than in winter, as the atmospheric temperature response is smaller in summer. The patterns of LW_{net} largely correspond to those of winter (Fig. 5.4i). The Arctic SHF+LHF is much smaller in summer than in winter (Fig. 5.4j). This is mostly due to the reduced temperature contrast between the atmosphere and the ocean. There is a reduction in SHF+LHF in the central Arctic, both due to longwave radiative heating of the surface and lower near-surface air temperatures (Fig. 5.3c).

5.3.2. GrIS surface mass balance response

Sea ice loss and ocean warming increase the winter SMB over the GrIS by 23 Gt yr^{-1} (Table 5.1). SMB increases everywhere except in the northwest, the mid-East, and

Figure 5.4: Arctic surface energy components' anomalies in FUT with respect to CTRL. (a)+(f) SW_{in} [W m^{-2}], (b)+(g) SW_{net} [W m^{-2}], (c)+(h) LW_{in} [W m^{-2}], (d)+(i) LW_{net} [W m^{-2}], and (e)+(j) SHF+LHF [W m^{-2}]. The convention for SHF+LHF is that positive means increased energy transfer to the atmosphere. The upper two rows contains winter (DJF) averaged quantities, the lower two rows summer (JJA) averaged. Dots indicate non-significant response at 95 % level, according to a student's t-test.

Table 5.1: GrIS integrated mass components in winter (DJF) and summer (JJA), all in Gt yr^{-1}. The standard deviation is given by $\pm$, and bold values indicate a significant response at the 95% level according to a student's t-test.

Simulation	SMB	Precipitation	Melt
DJF			
CTRL	177 $\pm$ 34	164 $\pm$ 33	0 $\pm$ 0
FUT	**200** $\pm$ **32**	**186** $\pm$ **32**	0 $\pm$ 0
JJA			
CTRL	-123 $\pm$ 64	231 $\pm$ 36	454 $\pm$ 75
FUT	**-156** $\pm$ **63**	226 $\pm$ 36	**490** $\pm$ **77**

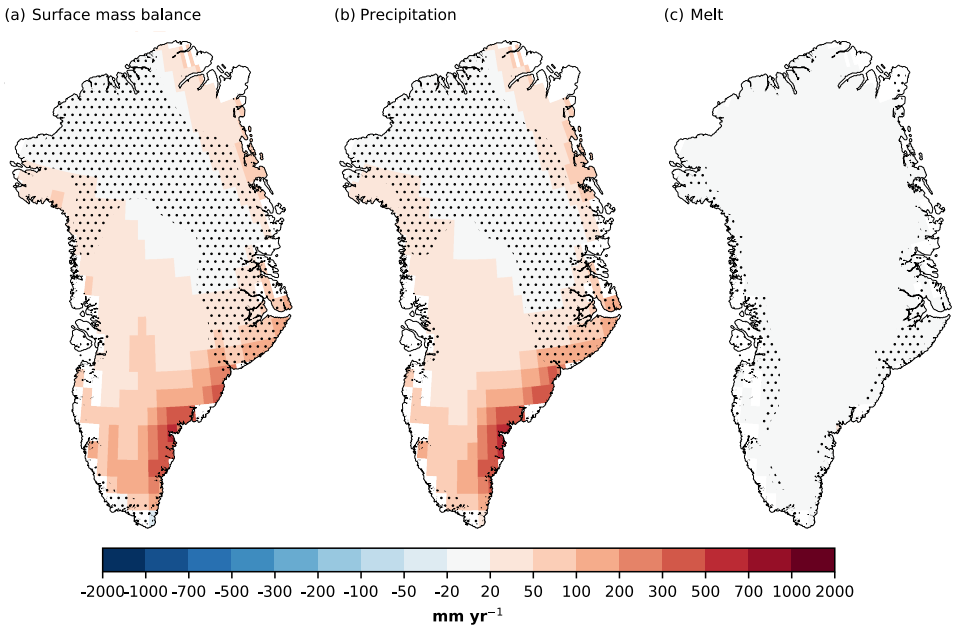

Figure 5.5: GrIS mass anomalies in FUT with respect to CTRL during winter (DJF). (a) Surface mass balance, (b) precipitation, and (c) melt, all in mm yr^{-1}. Dots indicate non-significant responses at the 95% level according to a student's t-test.

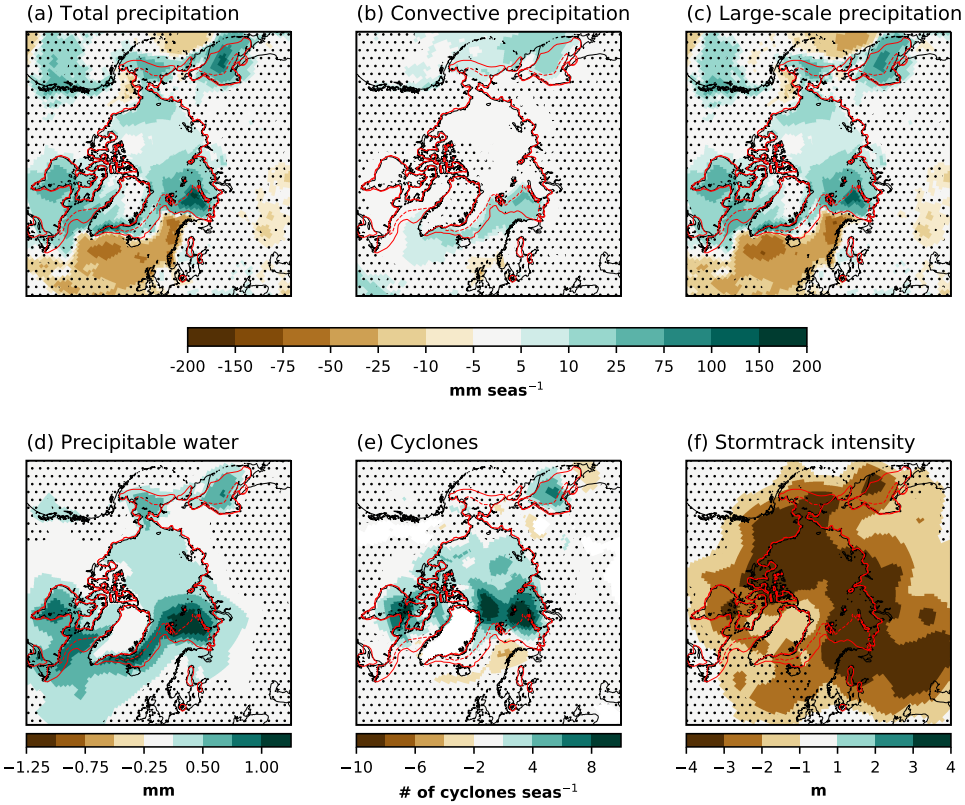

Figure 5.6: Precipitation and storm responses in FUT with respect to CTRL in winter. (a) Total precipitation [mm seas^{-1}], (b) convective precipitation [mm seas^{-1}], (c) large-scale precipitation [mm seas^{-1}], (d) column-integrated precipitable water [mm], (e) number of cyclones per season, and (f) storm track intensity [m]. The storm track intensity is calculated as the standard deviation of the 2-6 days band-pass filtered Z_{500}. The solid (dotted) red line is the sea ice extent from CTRL (FUT). Dots indicate non-significant responses at the 95% level.

at the summit (Fig. 5.5a). The largest increase in SMB is in the high accumulation area in the southeast. The main cause of this SMB increase is a 22 Gt yr^{-1} increase in precipitation (Table 5.1, Fig. 5.5b). Despite ice-sheet-wide winter warming over the GrIS, melt does not increase (Fig. 5.5c) because temperatures remain below freezing.

To understand the increased winter precipitation over Greenland, we explore the atmospheric dynamics in the Arctic and the North Atlantic. The total amount of precipitation increases in the Arctic (Fig. 5.6a), where the largest increases are in areas with sea ice loss. A smaller part of the total precipitation increase can be attributed to increased convection (Fig. 5.6b). Increased convection mainly occurs in areas with sea ice loss. Large-scale precipitation is the main contributor to Arctic precipitation increase (Fig. 5.6c), and the anomalies highly resemble the total precipitation anomalies. The precipitable water increases everywhere in

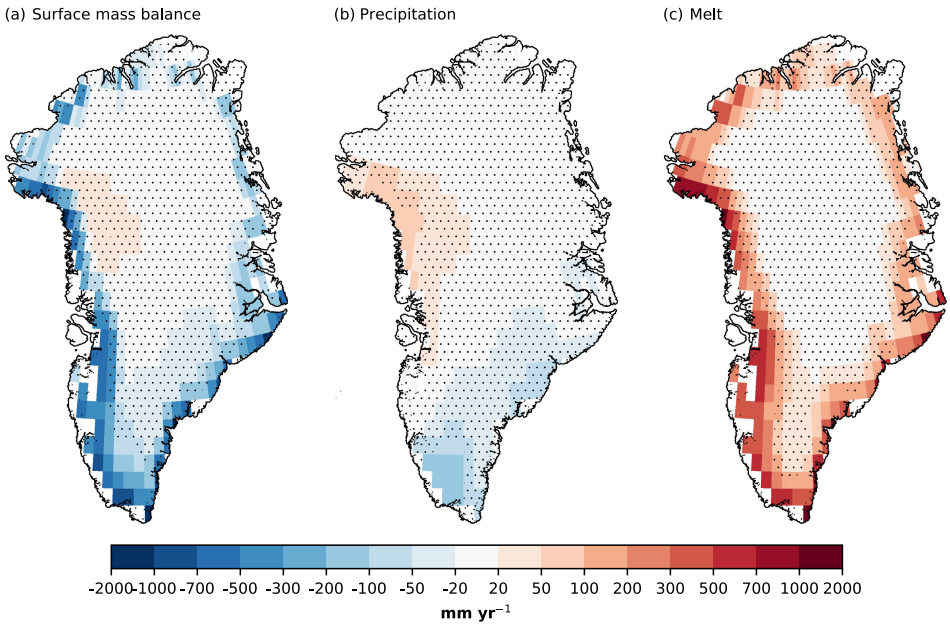

Figure 5.7: Same as Fig. 5.5, but for summer (JJA).

the Arctic (Fig. 5.6d). The largest increases in precipitable water are consistent with positive SHF+LHF anomalies (Fig. 5.4e), as these are the locations where more water enters the atmosphere. Further, this moisture is advected to the central Arctic and southward to, e.g., the North Atlantic. There are more cyclones (Fig. 5.6e) in the Arctic, likely due to destabilization of the atmosphere through increased SHF+LHF. Together with relatively much increased atmospheric moisture, precipitation increases even though the storm intensity is reduced (Fig. 5.6f).

An interesting feature of the large-scale precipitation response, is the contrast between the Arctic and the North Atlantic, with reduced precipitation in the North Atlantic. There are fewer cyclones (Fig. 5.6e) and weaker storm tracks (Fig. 5.6f), which is consistent with reduced large-scale precipitation, despite the increase in atmospheric moisture. A plausible explanation for the storm response is that ocean temperatures in the North Atlantic are identical in the runs, leading to increased atmospheric heat and moisture (Fig. 5.3a, 5.6d) in the North Atlantic reducing the climatological ocean-to-atmosphere SHF+LHF (Fig. 5.4e). This may stabilize the atmosphere, and together with a weaker equator-to-pole SST gradient, reduce the baroclinicity in the North Atlantic (Fig. 5.6e).

SMB decreases along coastal, low elevation areas of the GrIS in summer (Fig. 5.7a). The total SMB decrease is 33 Gt yr^{-1} (Table 5.1). The main component of this decreased SMB is melt increase (Fig. 5.7f), which increases by 36 Gt yr^{-1} (Table 5.1). The summer precipitation response shows a dipole structure, with increased precipitation in the high accumulation area in the northwest, and decreased precip-

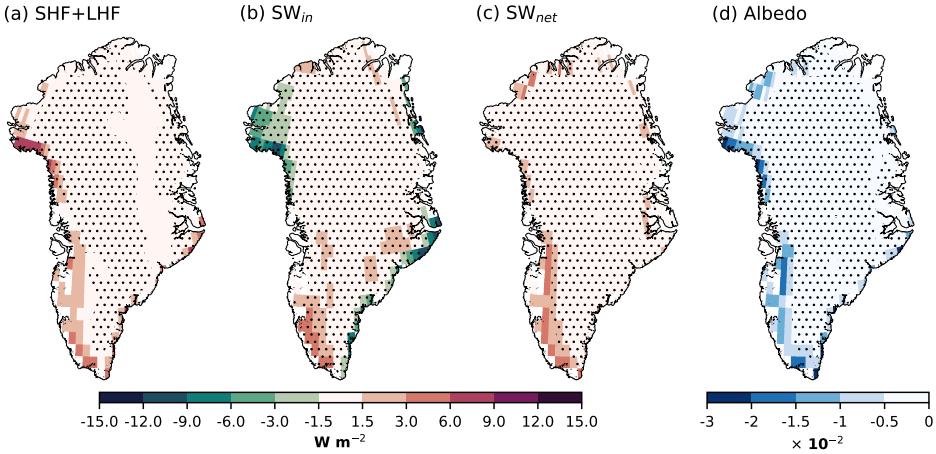

Figure 5.8: Summer GrIS surface energy balance response to the sea ice forcing. (a) SHF+LHF [W m^{-2}], (b) SW$_{in}$ [W m^{-2}], (c) SW$_{net}$ [W m^{-2}], and (d) albedo [-]. Dots indicate non-significant responses at the 95% level.

5

itation in the South. These two precipitation anomalies approximately cancel each other in the total mass budget, leading to a small, non-significant decrease in the integrated summer SMB.

The summer melt increase, leading to a lower summer SMB, can be explained through changes in the surface energy balance. Along the margins of GrIS, there is increased SHF+LHF (i.e., more energy transfer from the atmosphere to the ice sheet surface). Increased SHF+LHF (Fig. 5.8a) occurs as the atmosphere warms (Fig. 5.3a) and moistens. The largest responses are found in the western part of the GrIS, which can be explained by two factors. First, this is an area where the ice sheet experiences the highest melt during the summer, so the surface temperature is at 0°C for a long time in the summer, also in the absence of sea ice forcing. When the surface is at 0°C, any additional atmospheric warming increases the surface-to-atmosphere temperature contrast leading to higher SHF+LHF, as opposed to when the surface also warms. Second, Baffin Bay is one of the areas warming the most during summer. The positive south-to-north SHF+LHF anomaly gradient in the West is caused by anomalous faster winds in the north and anomalous slower winds in the South (Fig. 5.9b,c). Despite the SW$_{in}$ not showing a statistically significant response (Fig. 5.8b) to the sea ice forcing, the SW$_{net}$ increases along the margins (Fig. 5.8c). The increased absorption of SW energy is due to a lower albedo (Fig. 5.8d). The higher SHF+LHF likely provides the energy for initial melt, leading to triggering of the melt-albedo feedback (Box et al., 2012).

Summer sea ice loss influences the atmospheric circulation over the GrIS. A robust, highly localized increase in blocking events can be detected over the north-western GrIS (Fig. 5.9a). There is an increase in 2-3 days (~25%) with blocked atmospheric circulation in this region. Increased blocking is related to melt by sustained warm air advection over the ice sheet. Further, the increased blocking in this

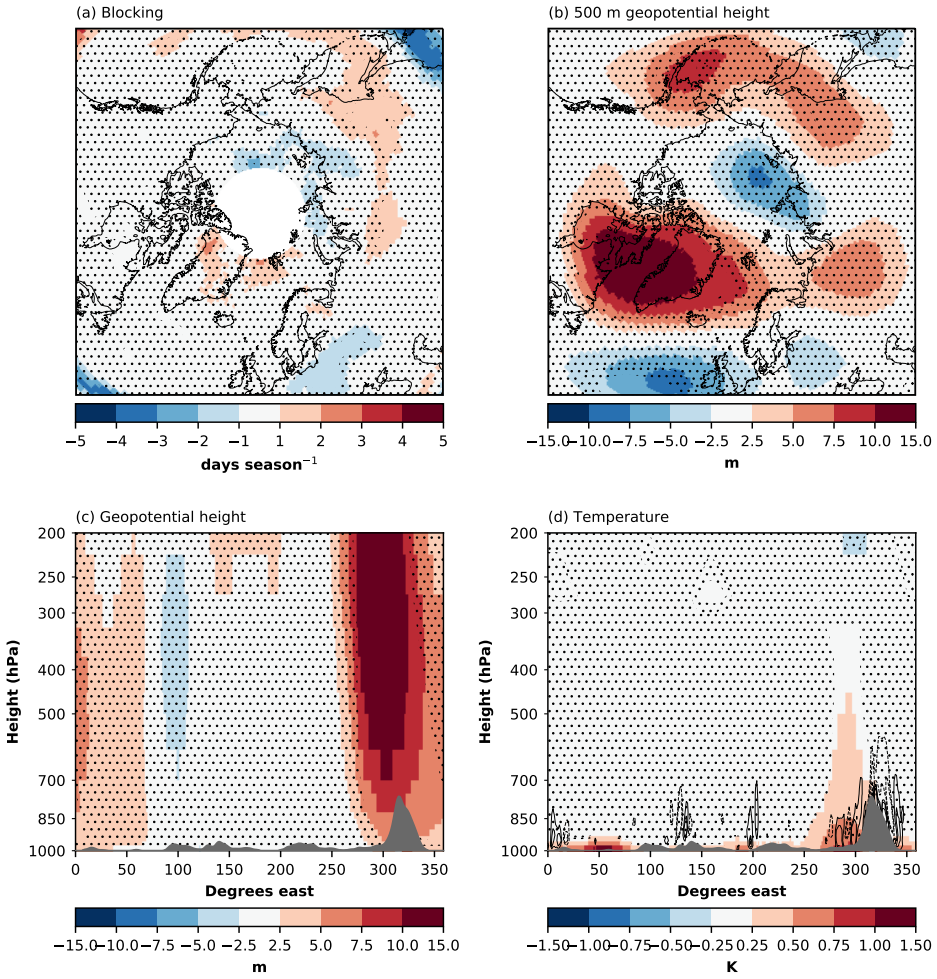

Figure 5.9: Summer atmospheric circulation responses to sea ice forcing. (a) Blocking days [days seas^{-1}], (b) 500 hPa geopotential height [m], (c) meridional-mean geopotential height [m], and (d) meridional-mean temperature [m]. For (c) and (d), the meridional-mean is taken between 60°N and 80°N. The contours in (d) is the vertical velocities, scaled by the horizontal wind speed. The contour levels are 0.25, 0.5, 0.75, 1, and 1.5, and are symmetric around zero. Solid lines show positive values, while dashed lines show negative values. Dots indicate non-significant responses at the 95% level.

region is consistent with the higher SHF+LHF's (Fig. 5.8a). This increase in blocking is accompanied by a larger-scale increase in Z_{500} centralized over Baffin Bay (Fig. 5.9b). This anomalous circulation pattern acts to increase wind speeds in the northwestern part of the ice sheet, and slows down winds in the southwestern part. This explains the dipole precipitation pattern (Fig. 5.7b), as the winds affect the amount of moisture transfer over the ice sheet. Further, this circulation anomaly is similar to the circulation anomaly associated with the Greenland blocking index (Davini et al., 2012; Hanna et al., 2015, 2018). However, the present-day GBI-related anomaly is approximately 6× stronger than the circulation anomaly found here (Hanna et al., 2016). Still, this indicates that sea-ice loss modulate the strength of the GBI. The geopotential height anomaly is deep, with an equivalent barotropic structure (Fig. 5.9c). This deep anomaly occurs only over the Baffin Bay/Greenland, although the strongest surface forcing is not located there (Fig. 5.1a-c).

The Baffin Bay/Greenland region is the region where also the temperature response is deepest (Fig. 5.9d). Deeper heating of the atmosphere has been related to a stronger upper-level response (Sellevold et al., 2016). We hypothesize that this deep atmospheric heating is due to the strong vertical winds at the coast of the GrIS. The free-atmosphere wind flow in the polar/extratropical northern hemisphere is predominantly westerly. The GrIS acts as a barrier to this flow, forcing vertical motion and enhancing turbulent mixing of air (Fig. 5.9d). This way, the high elevation of the GrIS, together with sea ice loss, contributes to generate an anomalous circulation pattern that increases the ice sheet's surface melt.

5.4. Discussion

The impact of reduced Arctic sea ice on GrIS SMB was investigated by forcing CESM2 with pre-industrial and future (corresponding to +2°C global mean temperature) monthly varying SIC and SST. We found ice-sheet wide significant increase in precipitation during winter months. Future summer increases in melt were only simulated at lower elevations, yet present around the entire margin, with the strongest responses in the West of the ice sheet.

The results presented here rely on idealized SIC and SST perturbations in an attempt to isolate the impact of sea ice loss on the GrIS. However, some indirect effects are not captured with this experimental setup. For example, sea ice loss may cause warming over lower latitude oceans (Blackport and Kushner, 2017) altering the North Atlantic responses reported here. In turn, these changes in North Atlantic responses may affect the simulated response of the GrIS.

In our study, the Arctic becomes warmer and more humid in response to sea ice reductions. In winter, the driving processes are increased surface-to-atmosphere SHF+LHF and more LW_{in}. In summer, increased SW_{net} through reduced albedo where sea ice transitions to open ocean, adds to the warming. These Arctic responses are robust among climate simulations with a similar setup (e.g., Deser et al., 2010; Screen et al., 2013a; Peings and Magnusdottir, 2014b). The negative SHF+LHF response south of the sea ice edge is likely overestimated due to the lack of ocean coupling. Still, it is present in coupled simulations of global warming (Sellevold and Vizcaino, 2020) as the atmosphere warms faster than the ocean.

Precipitation over the GrIS increases in winter. This response was also identified by Noël et al. (2014). However, the response they found was confined to the southeast, while here we found widespread precipitation increase over the GrIS. One possible explanation for this discrepancy could be the difference in model resolution, as they use a regional climate model. The lower resolution here, with associated smoothed topography over the GrIS, may allow for moisture to travel further into the ice sheet.

Enhanced summer melting at low elevation areas of the GrIS, as found here, is also a robust response to reduced Arctic sea ice cover (Rennermalm et al., 2009; Noël et al., 2014; Stroeve et al., 2017; Pedersen and Christensen, 2019). The main mechanism for increased surface melt is argued to be increased LW_{in} due to sea ice loss induced atmospheric warming (Liu et al., 2016) over the GrIS. Here we find a that LW_{in} only significantly increases for a limited area in the northwest, due to the limited warming of the GrIS in the summer. We find the primary mechanisms for increased melt to be a triggering of the albedo-melt feedback by increased SHF+LHF. The effect of increased SHF+LHF due to sea ice loss on increased surface melt is debated, due to the katabatic winds blocking onshore flow (Noël et al., 2014). The results found here indicate mixing of the katabatic winds with the anomalous warm onshore flow. It is important to acknowledge that the melt response may be highly dependent on the background state of the GrIS. For a warmer GrIS (e.g., due to global warming) the impact of sea ice loss on GrIS melting through SHF+LHF might be higher (Franco et al., 2013; Sellevold and Vizcaino, 2020).

Regional enhancement of the Z_{500} over Baffin bay and Greenland occurs in response to the sea ice forcing. A similar, but stronger, circulation pattern is connected to present-day high surface melt of the GrIS (Hanna et al., 2016; Delhasse et al., 2018). We find that this circulation pattern increases onshore advection of heat and moisture in the northwest of GrIS, and reduces it in the southwest. This has an effect on precipitation, with increase in the northwest and decrease in the southwest. Further, this increase in Z_{500} is connected with an increase in blocking in northwest Greenland. The increased blocking in this region was also reported by Liu et al. (2016), albeit with a different blocking metric. We hypothesize that the increase in Z_{500} is triggered by deep warming over the Baffin Bay through high vertical winds (compared to horizontal winds), and high turbulent flow around the GrIS.

On the other hand, the regional enhancement of the Z_{500} over Greenland is not supported by fully coupled climate models in response to anthropogenic climate change (Sellevold and Vizcaino, 2020; Delhasse et al., 2021). This suggest that other influences (e.g., North Atlantic Meridional Overturning Circulation weakening) are more important than Arctic sea ice loss to future circulation changes over Greenland.

5.5. Conclusions

Sea ice loss, together with increasing SSTs, warms the Arctic surface and atmosphere in both winter and summer. This Arctic amplification intensifies the hydrological cycle over the GrIS, with 23 Gt yr^{-1} of increased accumulation during the

accumulation season and 33 Gt yr^{-1} of increased ablation in the ablation season.

The loss of sea ice also causes up to 15 m of regional enhancement of the 500 hPa geopotential heights over the GrIS. Regional enhancement of the 500 hPa geopotential heights over the GrIS is linked to recent unprecedented GrIS melt increased, by promoting atmospheric blocking, anomalous warm wind, and clearer skies.

The interest of applying a global climate model to address the question of the impact of Arctic sea ice loss on the GrIS SMB, is due to its capabilities to capture large-scale general circulation changes, which is not possible with a regional climate model (Noël et al., 2014).

6

Projecting 21st century Greenland ice sheet surface melt using artificial neural networks

If you torture the data long enough,
it will confess to anything.

Ronald H. Coase

Increased surface melt is the primary contributor to the current sea level contribution of the Greenland ice sheet (GrIS). Projections of future GrIS melt are limited by the lack of explicit melt calculations within most global climate models and the high computational cost of dynamical downscaling with regional climate models. Here, we train artificial neural networks (ANNs) to obtain relationships between global climate model simulations and GrIS surface melt. To this end, we use model output from the Community Earth System Model 2.1, which features interactively calculated surface melt based on a downscaled surface energy balance. We find that ANNs can accurately predict surface melt based on input from an independent CESM2.1 simulation and five regional climate simulations. The ANNs using climate data from CMIP6 project a melt increase for 2081-2100 ranging from 414±275 Gt yr^{-1} (SSP1-2.5) and 1,378±555 Gt yr^{-1} (SSP5-8.5), with 724±371 Gt yr^{-1} and

Parts of this chapter are in review for Geophysical Research Letters

1,031±436 Gt yr^{-1} for the intermediate scenarios SSP2-4.5 and SSP3-7.0, respectively. The primary source of projection uncertainty throughout the 21st century is due to the spread in the models' climate sensitivity.

6.1. Introducion

Greenland is losing mass at an accelerating rate since the 1990s (Bamber et al., 2018b; Mouginot et al., 2019; Shepherd et al., 2019) in response to global warming. This is alarming, as the freshwater stored on the Greenland ice sheet (GrIS) has the potential of raising the global mean sea level with 7.34 m if fully melted (Bamber et al., 2018b). The mass loss of the GrIS is the sum of increased ice discharge and a decreased surface mass balance (SMB). The dominant contributor is identified as the decreasing surface mass balance (van den Broeke et al., 2016; Fettweis et al., 2017), which is also causing the accelerating rate of mass loss (Enderlin et al., 2014; Shepherd et al., 2019). The main component of contemporary GrIS surface mass loss is increased surface melt (Fettweis et al., 2017; Noël et al., 2020b).

Projections of future GrIS surface melt are scarce, as a realistic calculation does not default in current global climate models (Lenaerts et al., 2019). To run efficient global climate projections, global climate models' horizontal resolution is too low to capture the spatially heterogeneous GrIS surface melt accurately.

The classical approach to translating climate model projections to GrIS surface melt is through positive-degree-day schemes (Braithwaite, 1995; Wake and Marshall, 2015). While these schemes are often used for computational efficiency, their performance is poor when surface melt/ablation is high (Bauer and Ganopolski, 2017), which we expect during global warming. Current state-of-the-art 21st century projections of GrIS surface melt come from regional climate models (RCMs; Fettweis et al., 2013a; van Angelen et al., 2013; Mottram et al., 2017). These models are run at high resolution and with a surface energy balance based calculation of melt, making them ideal for surface melt projections. However, they are computationally expensive and require external forcing by a global climate model.

Here, we investigate the performance of artificial neural networks (ANNs) in translating global climate model projections to GrIS surface melt projections. ANNs are computationally efficient, and able to learn complex, non-linear relationships. The ANNs can learn the relationship between global climate model simulation and simulated melt by using climate data from the Community Earth System Model version 2.1 (CESM2; Danabasoglu et al., 2020), as it features an interactive calculation of the GrIS surface melt based on downscaling of the surface energy balance (Sellevold et al., 2019). This paper aims to take the first steps towards taking advantage of the full climate data archive provided by the Coupled Model Intercomparison Project phase 6 (CMIP6; Eyring et al., 2016) by using ANNs for making projections of surface melt which is currently only explicitly simulated by few global climate models.

Table 6.1: Hyperparameters for the training of the artificial neural network. The scaling is the scaling applied to the input data, where X corresponds to the variable values. λ is the regularization parameter applied to the hidden layer, and the learning rate is the learning rate of the optimizer.

Variable	Number of epochs	Scaling	λ	Learning rate
T_{2m} [K]	19757	(X-180.0) / 160.0	10^{-2}	10^{-4}
Z_{500} [m]	5837	(X-4250.0) / 2000.0	10^{-1}	10^{-4}
CC [-]	630		10^{-2}	10^{-3}
RAD_{in} [W m^{-2}]	5000	X / 7000.0	10^{-1}	10^{-4}
SNOW [mm yr^{-1}]	1048	X / 7000.0	1	10^{-3}

6.2. Methods

6.2.1. Artificial neural network

To project future melt, we use an ANNs trained with CESM2 data. The ANNs are set up to predict annual melt based on summer (JJA) averages of near-surface temperature (T_{2m}), 500 hPa geopotential heights (Z_{500}), cloud cover (CC), incoming radiation (RAD_{in}; the sum of incoming shortwave and longwave radiation), and snowfall (SNOW), independently. These variables were chosen as they have been identified to be connected to melt increase. The ANNs consists of an input layer, one hidden layer, and an output layer. A detailed description of each layer can be found in Text S1. CESM2 is chosen for training as it features an explicit and realistic melt calculation (van Kampenhout et al., 2020).

Training of the network is done through a feedforward and backpropagation algorithm. The data is sent through the network in batches of 30 samples in the feedforward, where one sample is equal to one summer average with its corresponding annual melt. This generates a melt prediction, and the mean squared error between the predicted melt and the melt as simulated by CESM2 is calculated. To minimize the error, backpropagation and gradient descent is performed. Backpropagation computes the gradient of the loss function (mean squared error) with respect to the weights efficiently. To minimize the loss function, we use the adaptive moment estimation (ADAM) gradient descent algorithm to optimize the ANNs' weights. ADAM is a stochastic gradient descent algorithm with exponential decay of the learning rate (Kingma and Ba, 2014). Here we use the learning rates of Table S1, 0.9 for the first moment exponential decay rate, and 0.999 for the second raw moment exponential decay rate. When all available samples are through the network, an epoch has ended. Before starting a new epoch, the samples are randomly shuffled and divided into new batches.

Input layer

The input layer is the first layer of the ANN, which scales and vectorize the data. An overview of the scaling parameters is given in Table 6.1. The scaling makes the network find the optimal combination of weights more efficiently. After scaling the data, which is two-dimensional in nlat rows, and nlon columns, where nlat is the number of latitude points (192), and nlon is the number of longitude points (288), the data is vectorized into $\vec{X}$ of size n, where n = nlat x nlon = 55,296.

Hidden layer (feature maps)

The input is then passed to each of the units in the hidden layer. The hidden layer consists of 4 units. We chose 4 units, as adding additional units did not enhance the performance. Each unit (i) holds its unique weight vector $\vec{W}_i$ of same size as $\vec{X}$. These weights are randomly initialized (Glorot and Bengio, 2010). For each unit, we calculate a scalar F_i:

$$F_i(\vec{W}_i, \vec{X}) = B_i + \vec{W}_i^T \cdot \vec{X}, \tag{6.1}$$

where B_i is the bias. We then apply an activation function, which transforms F_i to zero if $F_i < 0$, and does nothing if $F_i \geq 0$ (also known as rectified linear unit activation; Xu et al., 2015).

When optimizing these weights, we use simple ridge regression (also known as Tikhonov regularization with units regularization matrix or L2 regularization). Ridge regression applies a penalty for large weights during optimization to ensure that weights do not grow too large. This is a common technique to avoid overfitting and to derive physically coherent patterns (Barnes et al., 2019). The regularization parameter is unique to each of the variables used for training and is given in Table 6.1. We use the parameters that minimize the loss of a validation simulation.

The weights of each unit can be restructured into the gridded format of the training data. Later, weights restructured in this way will be referred to as feature maps.

Output layer

The output layer is responsible for giving the predicted melt rates. It predicts the melt through

$$MELT = b + \sum_{i=1}^{4} F_i \cdot w_i \tag{6.2}$$

where b is a bias term, and w_i are the weights in the output layer.

6.2.2. Climate data for training

To train the neural network, we use data from CESM2. CESM2 is a fully coupled Earth system model with components for atmosphere, ocean, sea-ice, land, and land ice. It is run with a nominal 1° hortizontal resolution. Further, it features a coupled elevation classes downscaling (Sellevold et al., 2019) of the GrIS surface melt calculation. The model mean melt rates, used in the training of the neural networks are shown in Fig. 6.1.

6.2.3. Climate data for melt projection

When we have trained our ANNs, we can make use of the output from other global climate models to make GrIS surface melt projections for four Shared Socioeconomic Pathways (SSPs; O'Neill et al., 2016). The models used in this study are shown in Table 6.2; all participate in the CMIP6. We bilinearly interpolate the global climate model output to the CESM2 ~1° horizontal grid, to coerce with the

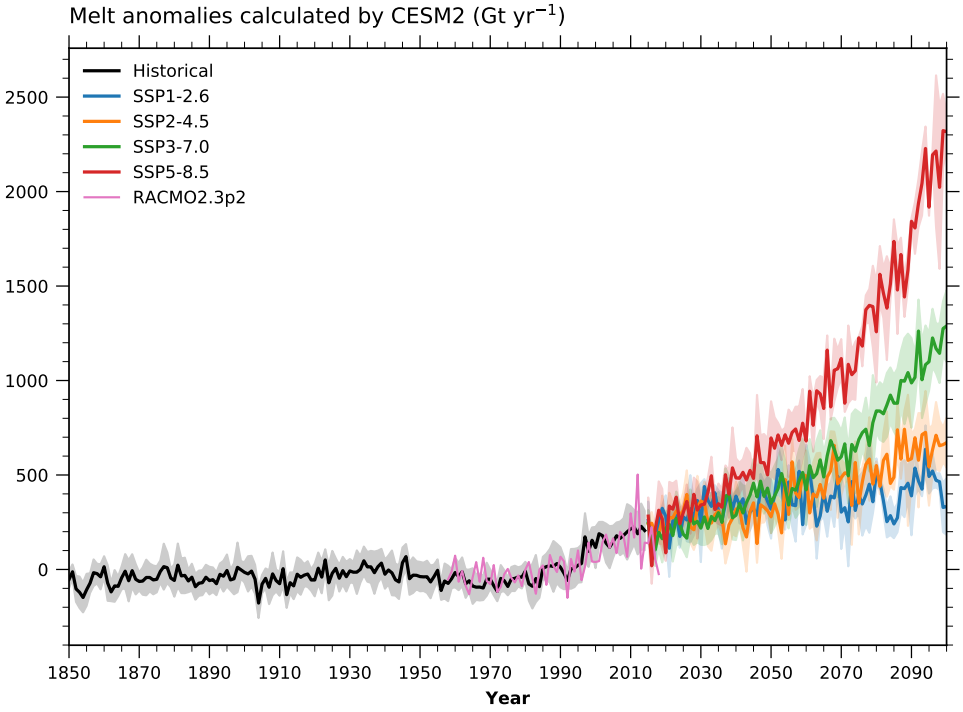

Figure 6.1: CESM2 ensemble mean melt anomalies (Gt yr^{-1}) in the years 1850–2100. The lines shown are for the historical period (black; 10 ensembles), SSP1-2.6 (blue; 3 ensembles), SSP2-4.5 (orange; 3 ensembles), SSP3-7.0 (green; 10 ensembles), and SSP5-8.5 (red; 3 ensembles). The pink line represents the RACMO2.3p2-simulated melt (1958–2018) (Noël et al., 2019). Shading represents the ensemble spread at $\pm$ 1 standard deviation.

ANNs' input layers. Further, we use climate anomalies as input, by subtracting the 1979–1998 mean climatology, and applying the anomalies to the CESM2 1979–1998 ensemble-mean climatology. This avoids potential artifacts in the projections due to a different baseline climatology than the ANNs were trained with. We did not discard simulations where some variables were missing. A full overview of the CMIP6 models used is shown in Table 6.2.

6.3. Results

6.3.1. Evaluation of neural networks

To evaluate our method, we predict melt from five atmospheric variables obtained from an independent CESM2 SSP5-8.5 simulation not used for training, and compare to the explicit melt calculation in this simulation. All the variables have high predicitive skill (Fig. 6.2, Table 6.3) when compared to CESM2. The detrended melt prediction using T_{2m} correlates very strongly (r=0.95) with the simulated melt, the other variables have a strong correlation ($r \geq$0.75). Further, predicting melt with T_{2m} and Z_{500} give an overestimation of melt, while predicting melt based on CC, RAD_{in} and SNOW underestimates melt.

A major advantage of the ANNs are their ability to represent trends or nonlinearities in the melt evolution, even if they are not present in the input data. This is achieved by applying activation functions to the hidden layer units. For Z_{500} (green line), CC (red line), and RAD_{in} (green line), such activation takes place around year 2000 (Fig. 6.2b-d). Further, these activated functions, or melt contributions, increase around the year 2020. These two timings correspond well to the melt increases simulated around these periods. Around 2040, T_{2m} (red line) activates and sharply increases around years 2060-2065. This increase coincides with the activation and increase of another unit for Z_{500}. The timing of the 2060-2065 corresponds to when the simulated melt accelerates (year 2017, according to a breakpoint analysis; Muntjewerf et al., 2020b).

The physical interpretation of the activation is not necessarily straightforward. One interpretation can be that the melt accelerates when they are activated, which is visible for T_{2m} and Z_{500} (Fig. 6.2a,b). However, this also depends on the input variable. If the input data follow a similar evolution as melt, it should be possible to predict surface melt without activating additional functions. So another interpretation of the activation functions can be that they represent feedback mechanisms, such as the melt-albedo feedback, which accelerates melt (Box et al., 2012; Sellevold and Vizcaino, 2020).

To understand how the ANNs work to predict melt, we show the feature maps (the weights learned by the model in the hidden layer) in Fig. 6.3. For T_{2m}, the highest weights are over the GrIS (Fig. 6.3a, orange), particularly at the southern dome. Also, temperatures over the adjacent ocean are weighted. All these weights are positive, meaning that increasing temperatures are related to increased melt. The feature map representing the year 2060 acceleration weighs (Fig. 6.3a, green) the temperatures in the interior and over the oceans more strongly. This is due to the interior of the ice sheet warming more than the margins during summer

Table 6.2: Number of ensemble members for each model and scenario for the CMIP6 models used for the melt prediction.

Model	Institution	Historical	SSP1-2.6	SSP2-4.5	SSP3-7.0	SSP5-8.5
ACCESS-CM2	CSIRO-ARCCSS	2	1	1	1	1
ACCESS-ESM1-5	CSIRO	3	3	3	3	3
AWI-CM-1-1-MR	AWI	1	1	1	5	1
BCC-CSM2-MR	BCC	3	1	1	1	1
BCC-ESM1	BCC	3				
CAMS-CSM1-0	CAMS	2				
CAS-ESM2-0	CAS	4				
CESM2	NCAR	10	3	3	10	3
CESM2-FV2	NCAR	3				
CESM2-WACCM	NCAR	3	1	5	1	5
CESM2-WACCM-FV2	NCAR	3				
CNRM-CM6-1	CNRM-CERFACS	30	6	6	6	6
CNRM-CM6-1-HR	CNRM-CERFACS	1	1	1	1	1
CNRM-ESM2-1	CNRM-CERFACS	9	5	5	5	5
CanESM5	CCCma	50	50	50	50	50
CanESM5-CanOE	CCCma	3	3	3	3	3
E3SM-1-0	E3SM-Project	3				
E3SM-1-1	E3SM-Project	1				
E3SM-1-1-ECA	E3SM-Project	1				
EC-Earth3	EC-Earth Consortium	4	1	3	1	1
EC-Earth3-Veg	EC-Earth Consortium	4	3	4	3	3
FGOALS-f3-L	CAS	3	1	1	1	1
FGOALS-g3	CAS	5	1	1	1	1
FIO-ESM-2-0	FIO-QLNM	3	3	3		3
GFDL-CM4	NOAA-GFDL	1		1		1
GFDL-ESM4	NOAA-GFDL	2	1	3	1	1
GISS-E2-1-G	NASA-GISS	39	1	10	1	1
GISS-E2-1-G-CC	NASA-GISS	1				
GISS-E2-1-H	NASA-GISS	23				
HadGEM3-GC31-LL	MOHC	4	1	1		3
HadGEM3-GC31-MM	MOHC	2				
INM-CM4-8	INM	1	1	1	1	1
INM-CM5-0	INM	10	1	1	5	1
IPSL-CM6A-LR	IPSL	32	6	11	11	6
MIROC-ES2L	MIROC	10	3	1	1	1
MIROC6	MIROC	10	3	3	3	3
MPI-ESM-1-2-HAM	HAMMOZ-Consortium	2				
MPI-ESM1-2-HR	MPI-M	10	2	2	10	2
MPI-ESM1-2-LR	MPI-M	10	10	10	10	10
MRI-ESM2-0	MRI	6	1	1	5	2
NESM3	NUIST	5	2	2		2
NorESM2-LM	NCC	3	1	3	1	1
NorESM2-MM	NCC	1	1	1	1	1
SAM0-UNICON	SNU	1				
TaiESM1	AS-RCEC	1				
UKESM1-0-LL	MOHC	17	5	5	5	5
Total		345	123	147	147	129

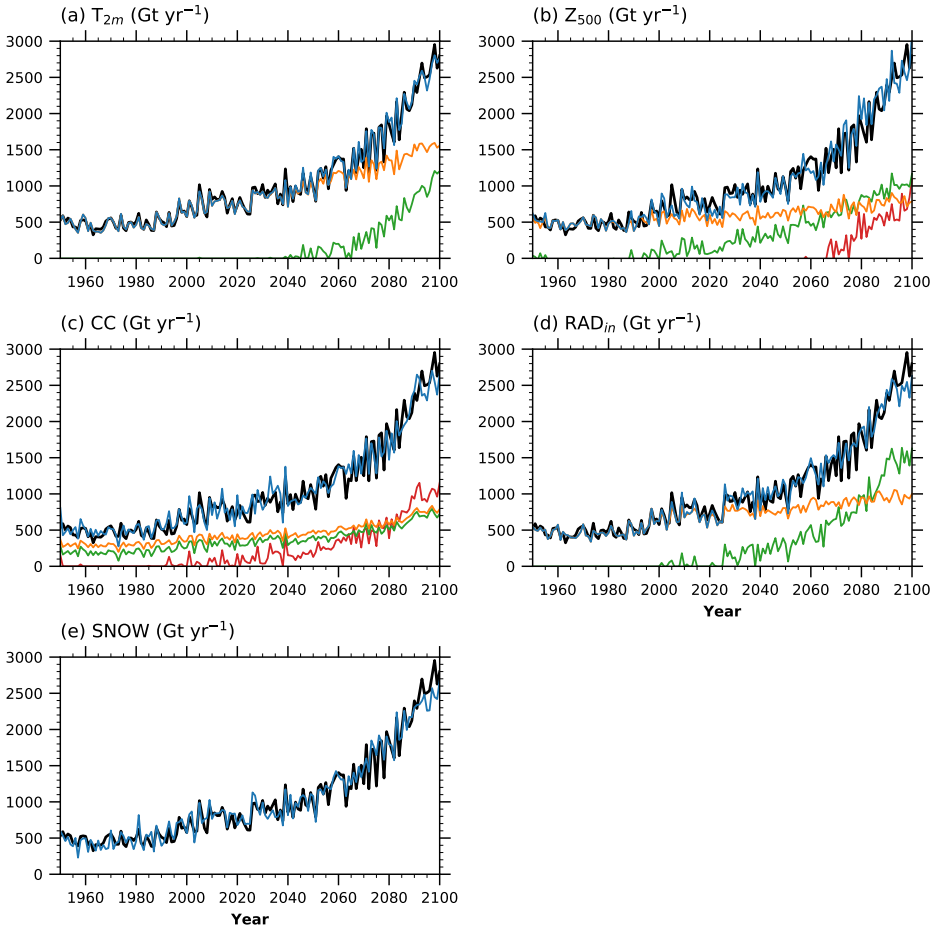

Figure 6.2: Melt predicted with the ANN compared with melt explicitly simulated by CESM2 from the independent SSP5-8.5 climate simulation. (a) melt predicted by near-surface temperature, (b) melt predicted by 500 hpa geopotential heights, (c) melt predicted by cloud cover, (d) melt predicted by incoming radiation, and (e) melt predicted by snowfall, all in Gt yr^{-1}. The black line in all the plots show the CESM2 simulated melt. Blue line shows the melt predicted by the ANN. The orange, green, and red lines correspond to the melt contribution from each feature map, with the corresponding color framed around the map in Fig. 6.3. The sum of them are equal to the predicted melt (blue line).

Table 6.3: Evaluation statistics for the melt prediction by the ANNs trained with different variables. The comparison against CESM2 is for the independent CESM2 simulation, for MAR we show the average statistics for five simulations. The r-value is the detrended correlation, where the detrending is done by subtracting the 20 year running mean. The root mean squared error (RMSE) is given, and the bias for the last 20 years (2081–2100). The bias provides an estimate of the error of the prediction by the end of the century.

	CESM2			MAR		
Variable	R-value	RMSE	Bias	R-value	RMSE	Bias
T_{2m}	0.95	62	2	0.81	257	203
Z_{500}	0.77	145	61	0.68	300	-615
CC	0.75	140	-57	0.52	345	-696
RAD_{in}	0.85	113	-55	0.67	391	-835
SNOW	0.82	120	-87	0.63	227	-145

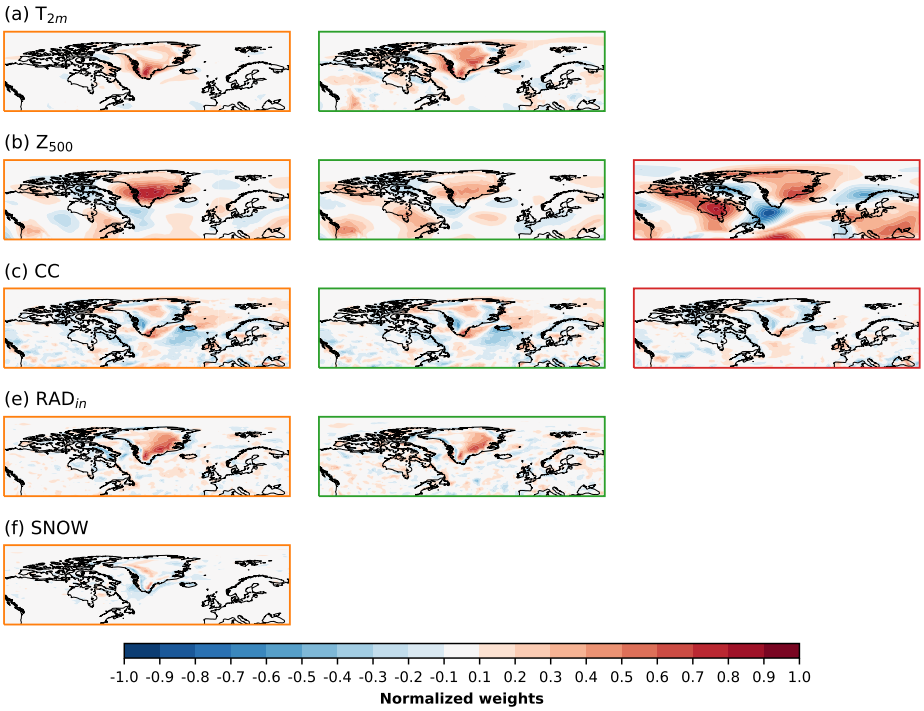

Figure 6.3: Feature maps showing how the units in the hidden layer weighs for the input of (a) T_{2m}, (b) Z_{500}, (c) CC, (d) RAD_{in}, and (e) SNOW. All the weights in the feature maps are normalized by dividing with its respective global maximum absolute value. The colors of the frames around the maps correspond to the color of the time series they represent in Fig. 6.2.

with global warming (Fettweis et al., 2013a). As the margins of the ice sheet are at melting point in summer, they cannot warm any further which limits further temperature increase (Vizcaíno et al., 2014a). Also, ocean temperatures close to the northeastern part are positively weighted, likely in connection with sea-ice retreat.

The connection between Z_{500} and melt is well established (Box et al., 2012; Hanna et al., 2016; Delhasse et al., 2018; Sellevold and Vizcaino, 2020). Increased Z_{500} promotes more heat advection, clearsky occurances and blocking. Also, negative Z_{500} anomalies, indicative of more cyclones, are linked to melt by increasing rainfall over the GrIS (Oltmanns et al., 2019). The melt prediction strongly weights Z_{500} over the GrIS (Fig. 6.3b). Z_{500} is also negatively weighted over the Labrador Sea. For the post-2000 activation (Fig. 6.3b, green) similar, though less strong, patterns appear. A third activation happens around the year 2065, with the associated patterns in Fig. 6.3b, red. In contrast to the previous feature maps, the center of the positive weights over the GrIS moves from central Greenland to the eastern coast and a weaker center in the northwest. Further, the negative weights at the southern tip for GrIS intensify.

The CC maps that are active from the beginning of the ANN prediction are very similar (Fig. 6.3, orange, green). They predict more melt if cloud cover decreases around the margins or more melt if cloud cover increases in the interior. This is likely due to the competing effects of increased incoming shortwave and decreased incoming longwave radiation with decreasing cloud cover, and vice versa (Wang et al., 2019; Izeboud et al., 2020). For high albedo surfaces, such as the snow-covered interior, decreasing the cloud cover will increase the incoming shortwave radiation. However, since a high amount of this radiation is reflected, this has minimal impact on the surface energy balance. If cloud cover increases, incoming longwave radiation increases, resulting in more energy at the surface. For a low albedo surface, such as the bare ice exposed margins, the effect is opposite, and thus decreasing the cloud cover increases the energy at the surface more than if cloud cover increases. From around year 2000, a third feature map is activated (Fig. 6.2c, red line and 6.3d, red) which is also similar to the previously activated feature maps.

The two feature maps for RAD_{in} are very similar (Fig. 6.3e). They show that increasing RAD_{in} over the GrIS surface increases the projected melt. Interestingly, the weights show that increased RAD_{in} in the south - southeast is the strongest indicator for increasing the melt prediction. The melt prediction based on SNOW shows that more melt is predicted with reduced SNOW at the margins and increased snow in the interior. Less summer snowfall at the margins is linked to higher melt rates (Noël et al., 2015; Tedesco and Fettweis, 2020), by not temporarily increasing the albedo and interrupting bare ice exposure. For the interior, this pattern is likely aliasing of the evolution due to a warming world: increasing the global temperatures leads to more snowfall in the interior (Mottram et al., 2017).

The evaluation against the regional climate model MAR (Hanna et al., 2020) shows that the melt predicted using T_{2m} and SNOW performed the best (Table 6.3). Therefore, we base our melt projections of the 21st century on the ANNs using these two variables.

Table 6.4: Surface melt projections from CESM2, ANNs, MAR. The historical represent the 1979–1998 model mean. For the SSP's, the numbers reported are the 2081–2100 anomalies with respect to the historical period. The ± denotes the 1 standard deviation model spread. The ANNs show the full range of CMIP6 models. The selected ANNs are ANNs that corresponds to the model simulations used as lateral forcing for the MAR projections. With the exception of the global mean T_{2m} (K), all numbers are of GrIS surface melt (Gt yr^{-1}).

Scenario	Global mean T_{2m}	CESM2	ANNs	Selected ANNs[1]	MAR
Historical	16.0±0.1	447±90	521±63	521±97	405±80
SSP1-2.6	1.6±0.5	413±95	414±276	371	244
SSP2-4.5	2.5±0.6	619±140	724±371		
SSP3-7.0	3.5±0.8	1,040±170	1,031±436		
SSP5-8.5	4.4±1.0	1,834±152	1,378±555	1,787±381	1,758±468

[1]Selected models are CNRM-CM6-1 for SSP1-2.6. For historical and SSP5-8.5, CNRM-CM6-1, CNRM-ESM2-1, MRI-ESM2-0, UKESM1-0-LL, and CESM2 are used.

6.3.2. Surface melt projections

The global mean T_{2m} evolution for the CMIP6 model ensemble (Table 6.2) using 1979–1998 as baseline is shown in Fig. 6.4a. The ensemble mean shows increasing temperatures since the 1960s (Fig. 6.4a). All the scenarios show anomalous warming in the last 20 years of the simulation (Table 6.4). The low warming scenario (SSP1-2.6) shows no significant trend in the last 20 years of the simulation. The other scenarios show a significant positive warming trend by the end of the century.

The low warming scenario SSP1-2.6 shows warming of 1.6 ± 0.5 K in the last 20 years of the simulation (Table 6.4). Also, by the end of the simulation, the T_{2m} trend is not significant for this scenario. The mean global warming is 2.5 ± 0.6, 3.5 ± 0.8, and 4.4 ± 1.0 for the SSP2-4.5, SSP3-7.0, and SSP5-8.5, respectively at the end of the century. They all have a significant positive trend by the end of the century.

Using the ANNs with the learned feature maps, global warming can be translated into GrIS surface melt (Fig. 6.4b). For the historical period, surface melt starts to increase around 1975 and continues to increase by the end of the historical ensemble mean. The melt projections show that melt increases in the range of 79% (SSP1-2.6) to 264% (SSP5-8.5) (Table 6.4) with respect to the 1979–1998 mean. Surface melt diverges between the years 2030-2050 for the different scenarios. By the end of the century, all SSP scenarios except for SSP1-2.6 show a significant positive trend, meaning they will likely continue to increase beyond the 21st century. SSP1-2.6 shows a non significant (p=0.017) decrease. Generally, the ANNs project higher surface melt increase for models with higher increase in T_{2m} (Fig. 6.5).

The projected surface melt increase by the ANNs agrees well with the explicitly simulated melt increase by CESM2 (Table 6.4) for all scenarios except for SSP5-8.5. This is likely due to the different regional simulation for a given global mean temperature increase. Compared to MAR, the ANNs project a higher melt increase for SSP1-2.6 and lower melt increase for SSP5-8.5 (Table 6.4). The ANNs and MAR's agreement becomes closer when comparing the selected ANNs (Table 6.4),

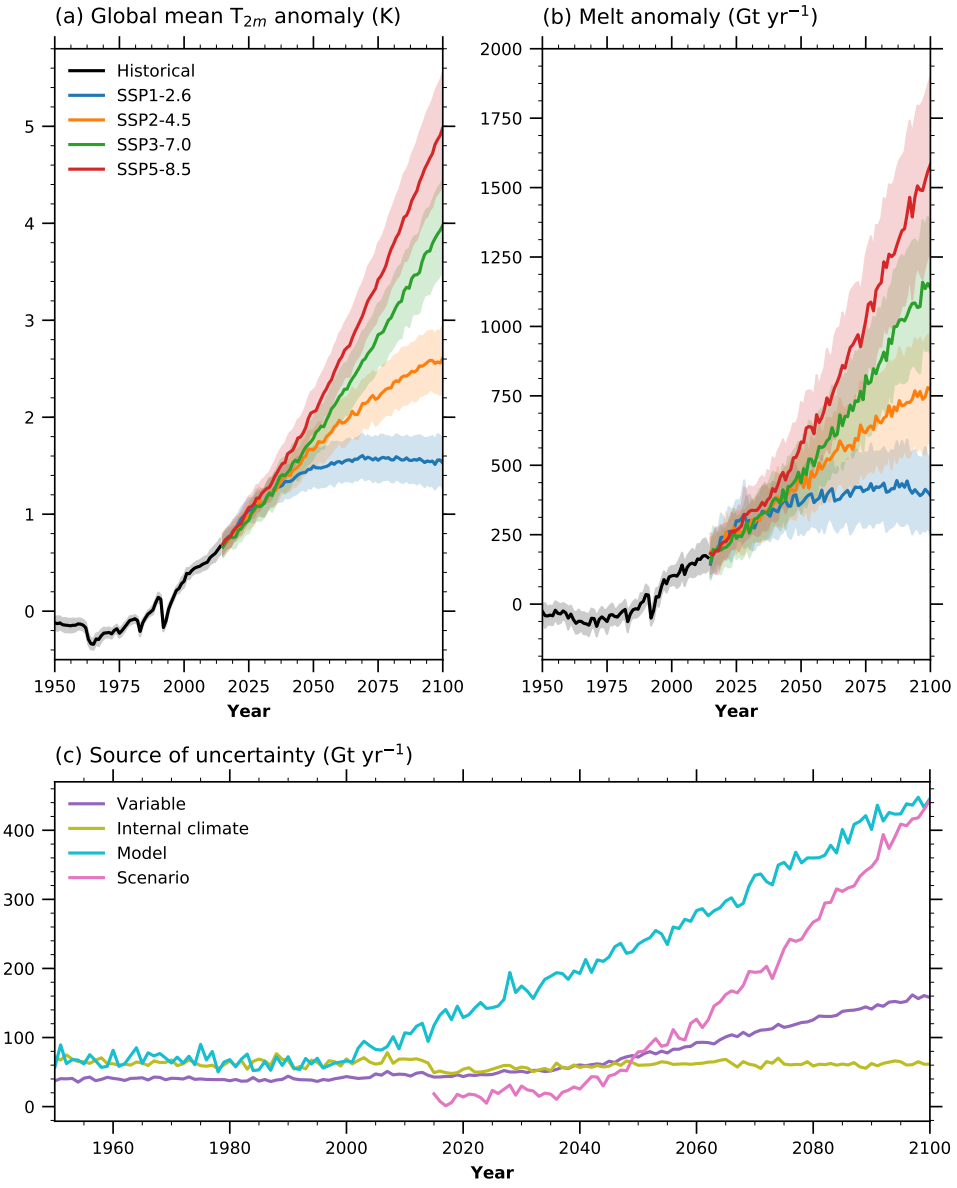

Figure 6.4: The models mean global mean temperature and GrIS surface melt evolution in the historical period and the four SSPs for (a) T_{2m} anomalies (K) and (b) GrIS surface melt anomalies (Gt yr^{-1}) with respect to the 1979–1998 mean. (c) Sources of uncertainty in the projections. For (a,b), black lines show the historical period, blue lines show SSP1-2.6, orange lines show SSP2-4.5, green lines show SSP3-7.0, and red lines show SSP5-8.5. The shading represents the model spread at $\pm$ 0.5 standard deviation (instead of 1 standard deviation to avoid heavy overlapping). In (c), the purple line corresponds to the variable spread, olive line to internal climate spread, cyan line to model spread, and pink line to scenario spread. The spread is given by the 1 standard deviation.

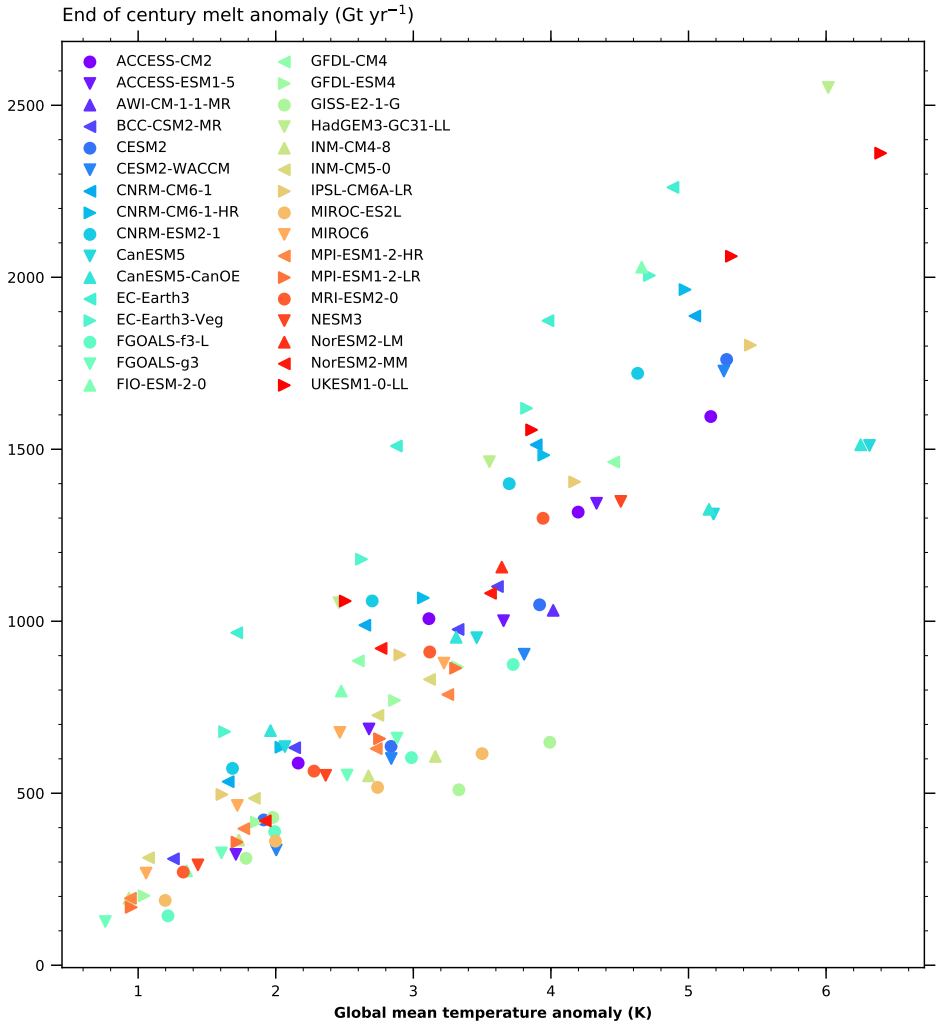

Figure 6.5: 2081–2100 surface melt anomalies (Gt yr^{-1}) and global mean temperature anomalies (K), compared to a 1979–1998 climatology, for all the SSPs.

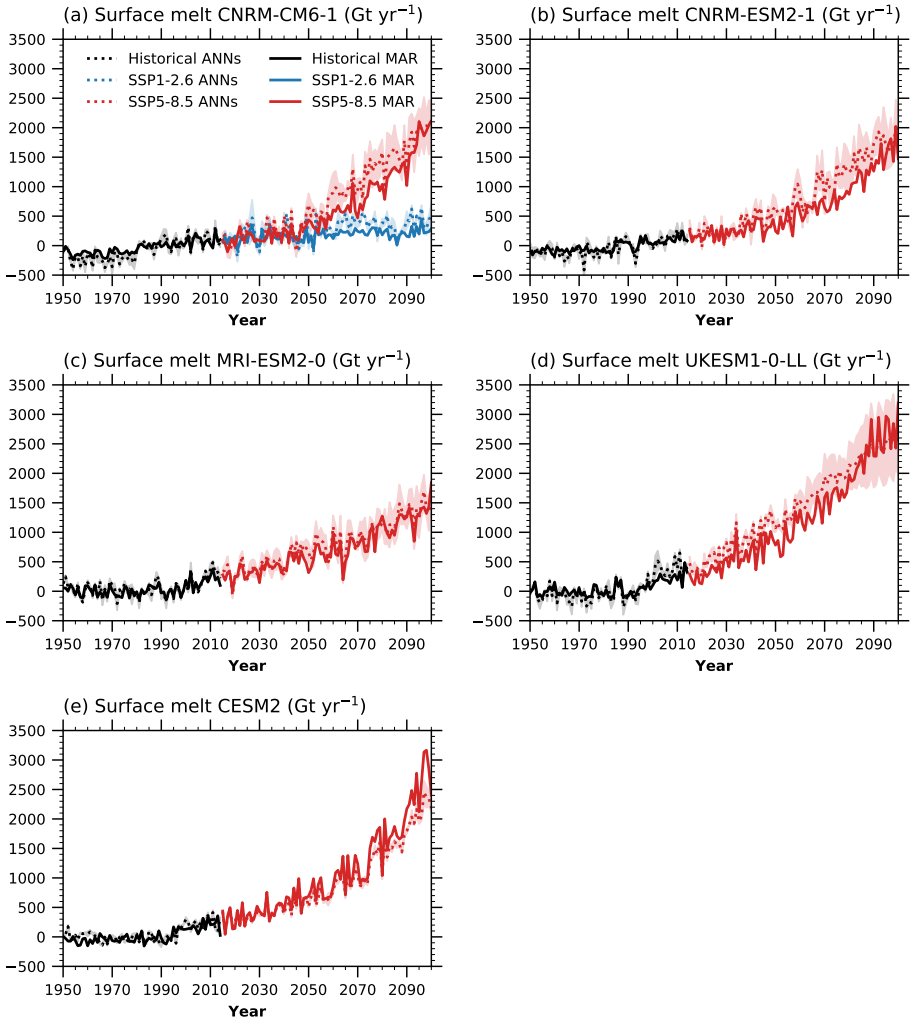

Figure 6.6: Time series of surface melt anomalies (Gt yr^{-1}) in MAR and the ANNs with respect to the 1979–1998 mean for a) CNRM-CM6-1, b) CNRM-ESM2-1, c) MRI-ESM2-0, d) UKESM1-0-LL, and e) CESM2. Black, blue, and red dotted (solid) lines correspond to the historical, SSP1-2.6, and SSP5-8.5, respectively, as projected by the ANNs (MAR).

which bases the ANNs projection on the same models and ensembles used as lateral forcing for MAR. Also, the melt evolutions for the ANNs and the MAR simulations are in large agreement (Fig. 6.6).

The main source of projection uncertainty is the model spread (Fig. 6.4c). This large spread is largely caused by the models' different climate sensitivity. The various regional simulation over the GrIS for a given change in global mean temperature further adds to this uncertainty. The uncertainty related to scenario spread is smaller than the model spread throughout the 21st century but becomes similar in the last years. The uncertainties associated with internal climate variability and variable selection are smaller than the sources mentioned above. While the spread due to internal climate variability remains relatively constant, the spread due to variable selection increases from the year 2040.

6.4. Discussion

In this study, we have trained ANNs with data from CESM2 to make projections of the 21st century GrIS surface melt. The ANNs show good performance in predicting melt when compared to an independent CESM2 simulation and five MAR simulations. This study expands on previous results by enabling melt projections from the full CMIP6 suite of models. By using the fill suite of CMIP6 models, we are well suited to assess the uncertainty related to future projections of GrIS surface melt. Our results suggest that the uncertainty related to the SSP5-8.5 scenario is 87 Gt yr^{-1} higher than the uncertainty obtained from regional climate simulations (Hanna et al., 2020).

The ANNs project GrIS surface melt increase by 414 $\pm$ 276, 724 $\pm$ 371, 1,031 $\pm$ 436, and 1,378 $\pm$ 555 Gt yr^{-1} for SSP1-2.6, SSP2-4.5, SSP3-7.0, and SSP5-8.5, respectively. These projected increases here are higher than previous estimates, which shows melt increases of 648 Gt yr^{-1} (van Angelen et al., 2013) for Representative Concentration Pathway (RCP) 4.5 and 634 Gt yr^{-1} for RCP8.5 (Vizcaíno et al., 2014a). The higher melt increases projected here are likely due to the higher climate sensitivity of the CMIP6 models when compared to the CMIP5 models (Zelinka et al., 2020; Meehl et al., 2020).

We find that the model spread is the primary source of uncertainty in the projections. Only by the end of the century, uncertainty due to scenario spread becomes an equal contributor to projection uncertainty.

We opted for a simple ANN structure in this study, as it allows us to easily explore the the feature maps and activations. More advanced ANN structures, like multichannel deep convolutional neural networks (Barros et al., 2014), which can draw connections between variables, could be applied in a follow-up for this study for comparison of projections.

6.5. Conclusions

1. We use neural networks, trained with a global climate model with explicit melt calculation, to project Greenland ice sheet surface melt from the range of CMIP6 models.

2. We project surface melt to increase by 414±276, 724±371, 1,031±436, and 1,378±555 Gt yr^{-1} for SSP1-2.6, SSP2-4.5, SSP3-7.0, and SSP5-8.5, respectively.

3. The model spread is the main source of uncertainty in our projections.

7

Conclusions and recommendations

In Chapter 1, we formulated several research questions which are to be addressed with this thesis. Here, I will conclude and provide recommendations for future research.

7.1. Conclusions

1. **Does the elevation class method generate realistic sub-grid surface mass balance gradients?**

   This question is addressed in Chapter 2.

   The elevation classes implemented in the Community Earth System Model (CESM) version 1.0 simulate realistic sub-grid gradients of surface mass balance (SMB) compared to a regional climate model, by redistributing energy and mass with elevation in a realistically. This good result is partly due to compensating biases. Strong turbulent heat flux gradients with elevation compensate for not applying any downscaling to the incoming radiation. Advanced simulation of snow albedo allows for summer triggering of the melt-albedo feedback, which contributes towards yielding realistic melt gradients with elevation. These results are important for guiding future developments and improvements to the elevation classes method.

   The overall SMB simulation is not very sensitive to the temperature lapse rate. Still, the chosen lapse rate has profound effects on the spatial distribution of the SMB. A higher lapse rate leads to more cooling at higher elevations, limiting the equilibrium line altitude from increasing. A higher lapse rate gives stronger ablation at the margins of the Greenland ice sheet (GrIS).

   Implementation of elevation classes in CESM1.0 leads to cooling of the GrIS, partially compensating for a warm bias due to low-resolution related smooth-

ing of the ice sheet topography. The cold air is also advected to the lee-side ocean, leading to more sea ice.

2. **How much global warming leads to accelerated surface mass loss?**

   This question is addressed in Chapters 3 and 4.

   In CESM2.1, we find that for a global temperature increase of 2.7 K, with respect to the pre-industrial climate, the GrIS SMB decrease accelerates when the ice sheet topography is frozen to the present-day state. For an evolving, larger than present-day ice sheet, the same global warming threshold is increased to 4.1 K when simulated by the coupled CESM2.1-Community Ice Sheet Model 2.1.

   The first indicator for the accelerated SMB decrease is a fast increase in the ablation area. After the fast increase in ablation area, the surface melt becomes as large as the snowfall, which was the largest SMB component until that point. The high melt rates saturate the refreezing capacity, so the refreezing capacity decreases swiftly. With less meltwater retained in the snow, the ablation areas expand more rapidly.

   Before the accelerated surface mass loss, longwave radiation is the primary contributor to the melt energy. At acceleration, melt-albedo feedback becomes the main contributor to increased melt energy. As the ice sheet approaches the melting point and the atmosphere keeps warming, the temperature gradient between the surface and the air increases, causing an acceleration of turbulent heat transfer to the surface.

   The SMB-elevation feedback becomes an important source of surface mass loss. The SMB decrease in regions at and below the initial equilibrium line is about twice compared to the SMB decrease if the elevation would not decrease.

3. **How do changes in atmospheric circulation influence the SMB with increasing CO_2?**

   This question is addressed in Chapters 3 and 5.

   Using CESM2.1 we find that the North Atlantic Oscillation (NAO), Greenland blocking index (GBI), and the polar jet stream position influence the integrated precipitation and surface melt of the GrIS in response to an idealized CO_2 forcing. In winter, a more positive NAO and a more southward displaced jet stream reduce precipitation. The melt increases in years with a more negative NAO, a more positive GBI, and a more southward displaced jet.

   The summer NAO is forced to a positive phase, while the GBI is forced to a more negative phase in response to increasing CO_2. This result is in line with CMIP5 projections. However, we are able to capture this response as well as the modern observed GBI anomaly, which increases the confidence in the global climate model's ability to represent atmospheric circulation changes over Greenland correctly.

Sea ice loss on the upwind side of the GrIS induces a deep thermal forcing, due to the strong turbulence of the wind flow. This deep thermal forcing regionally enhances the geopotential heights, increasing the GBI.

4. **How does Arctic sea ice loss impact the GrIS SMB?**

   This question is addressed in Chapter 5.

   By forcing CESM2.1 with monthly varying sea-ice conditions corresponding to pre-industrial sea ice cover and future sea ice cover, we find that Arctic sea ice loss enhances the hydrological cycle of the GrIS, with increased precipitation in winter and increased surface melt in the summer. Winter precipitation increases over almost all of the GrIS, with the most substantial increases in the South East. The precipitation increase is caused by a combination of higher moisture availability and an increased number of cyclones in the Arctic.

   Summer surface melt increases as the Arctic warms. Additional heat and moisture generated with sea ice loss are advected over the GrIS, causing increased incoming longwave radiation to warm the ice sheet surface and increased turbulent heat flux contribution to the melt energy. Furthermore, the melt-albedo feedback is triggered, enhancing the melt.

5. **Can we infer surface melt from global climate models through machine learning?**

   This question is addressed in Chapter 6.

   We evaluate the performance of artificial neural networks, trained with CESM2.1 climate and surface melt data, in predicting GrIS surface melt. The activation functions in the neural networks enables the prediction of the non-linear evolution of surface melt with global warming. The projected 2081–2100 surface melt from the range of CMIP6 models is an increase by 414 ± 276 Gt yr^{-1} (SSP1-2.6) to $1{,}378 \pm 555$ Gt yr^{-1} (SSP5-8.5), with respect to 1979–1998. The projection for the intermediate scenarios is an increase by 724 ± 371 Gt yr^{-1} (SSP2-4.5) and $1{,}031 \pm 436$ Gt yr^{-1} (SSP3-7.0).

7.2. Recommendations

(a) In Chapter 2, we made several recommendations for guiding the future development of the elevation classes scheme, based on results from CESM1.0. These were a lower and/or spatially varying ice albedo, downscaling of incoming radiation, downscaling of precipitation phase, and development of more adequate snowpack parameterizations. Many of these are already included in the CESM2.1. With these improvements, a similar evaluation as done in Chapter 2 should be made.

(b) We found that before SMB decrease starts accelerating in response to increased CO_2, longwave radiation was the primary contributor to melt energy increase. It is still unclear whether or not increased incoming radiation is a necessary condition for ultimately triggering the melt-albedo

feedback and accelerated turbulent heat fluxes. Idealized modeling with fixed incoming longwave radiation could investigate the importance of this preconditioning versus, e.g., turbulent heat fluxes, and the different timing of the SMB decrease acceleration without increased incoming longwave radiation.

(c) From the simulations in this study, it is still not clear if the accelerated surface mass loss relates to surface melt becoming larger than snowfall, SMB becoming negative (runoff and sublimation exceeding accumulation through snowfall and refreezing of rain), or the continued CO_2 increase. To gain further insight, we recommend similar simulations as in Chapter 3 and Chapter 4, but to stop the further rise of CO_2 at (1) the time when the surface melt is equal to snowfall and (2) when SMB is negative for the first time. Knowledge about this threshold could improve the present-day estimate of when GrIS mass balance will quickly decline and cause a rapid sea-level rise.

(d) In addition to CO_2, anthropogenic emissions also consist of the emission of aerosols. Here, we only separated the response of the GrIS to increased CO_2. Similar simulations with aerosol emission would be interesting to assess the response of the GrIS SMB to aerosols alone. Aerosols can have a cooling effect on climate, but emission of, e.g., soot may reduce the ice sheet albedo. Understanding the impact of aerosol emissions on the GrIS SMB could help in advancing our understanding of historical and future SMB evolution.

(e) Having global climate models, coupled with a realistic GrIS SMB calculation, opens many research ventures. Some examples of idealized studies include a change of the sea surface temperatures in the North Atlantic and the tropical Pacific to mimic the phases of Atlantic Multidecadal Oscillation and El Nino-Southern Oscillation, respectively. This could help in guiding the attribution of, e.g., extreme melt events.

(f) In our study of Arctic sea ice loss, we used the same GrIS surface climatology in our control and future experiments. However, Chapter 3 shows that SMB processes change over time. Another approach could be to use a GrIS surface climatology representing a pre-industrial and a surface climatology representing +2°C global warming, while keeping the rest of the experimental setup the same. While this would not isolate the sea ice forcing, it would make a more realistic estimate of the impact of sea ice loss on the future SMB.

(g) We predict the surface melt evolution of the GrIS using simple neural networks in Chapter 6. A more advanced neural network, including, e.g., convolutions, could potentially be used to predict the full SMB with all its components. Also, neural networks are not limited to representing time series, so the future spatial distribution of SMB and SMB components could also be predicted.

(h) The current high computational cost with dynamical downscaling of the SMB through a regional climate model, is due to the atmospheric component. A neural network, responsible for the atmospheric downscaling, could be bi-directionally coupled to a physically-based surface snow model to predict SMB evolution. An advantage of such an approach, compared to predicting SMB solely on learned patterns of SMB from previous simulations, would be that the neural network could draw information on the evolution of the explicitly calculated snow evolution. Having an evolving snowpack could also help by providing memory to the neural network.

References

P. M. Alexander, M. Tedesco, X. Fettweis, R. S. W. van de Wal, C. J. P. P. Smeets, and M. R. van den Broeke. Assessing spatio-temporal variability and trends in modelled and measured Greenland Ice Sheet albedo (2000–2013). *The Cryosphere*, 8(6):2293–2312, 2014. doi: 10.5194/tc-8-2293-2014.

P. M. Alexander, A. N. LeGrande, E. Fischer, M. Tedesco, X. Fettweis, M. Kelley, S. M. J. Nowicki, and G. A. Schmidt. Simulated Greenland Surface Mass Balance in the GISS ModelE2 GCM: Role of the Ice Sheet Surface. *Journal of Geophysical Research: Earth Surface*, 124(3):750–765, 2019. doi: 10.1029/2018JF004772.

T. Andrews, J. M. Gregory, M. J. Webb, and K. E. Taylor. Forcing, feedbacks and climate sensitivity in CMIP5 coupled atmosphere-ocean climate models. *Geophysical Research Letters*, 39(9), 2012. doi: 10.1029/2012GL051607.

A. Aschwanden, M. A. Fahnestock, and M. Truffer. Complex Greenland outlet glacier flow captured. *Nature Communications*, 7:10524, 2016. doi: 10.1038/ncomms10524.

A. Aschwanden, M. A. Fahnestock, M. Truffer, D. J. Brinkerhoff, R. Hock, C. Khroulev, R. Mottram, and S. A. Khan. Contribution of the Greenland ice sheet to sea level over the next millennium. *Science Advances*, 5 (6), 2019. doi: 10.1126/sciadv.aav9396.

J. L. Bamber, J. A. Griggs, R. T. W. L. Hurkmans, J. A. Dowdeswell, S. P. Gogineni, I. Howat, J. Mouginot, J. Paden, S. Palmer, E. Rignot, and D. Steinhage. A new bed elevation dataset for Greenland. *Cryosphere*, 7(2):499–510, 2013. doi: 10.5194/tc-7-499-2013.

J. L. Bamber, A. J. Tedstone, M. D. King, I. M. Howat, E. M. Enderlin, M. R. van den Broeke, and B. Noel. Land Ice Freshwater Budget of the Arctic and North Atlantic Oceans: 1. Data, Methods, and Results. *Journal of Geophysical Research: Oceans*, 123(3):1827–1837, 2018a. doi: 10.1002/2017JC013605.

J. L. Bamber, R. M. Westaway, B. Marzeion, and B. Wouters. The land ice contribution to sea level during the satellite era. *Environmental Research Letters*, 13(6):063008, 2018b. doi: 10.1088/1748-9326/aac2f0.

E. A. Barnes. Revisiting the evidence linking Arctic amplification to extreme weather in midlatitudes. *Geophysical Research Letters*, 40(17): 4734–4739, 2013. doi: 10.1002/grl.50880.

E. A. Barnes and L. M. Polvani. CMIP5 Projections of Arctic Amplification, of the North American/North Atlantic Circulation, and of Their Relationship. *Journal of Climate*, 28(13):5254–5271, 2015b. doi: 10.1175/JCLI-D-14-00589.1.

E. A. Barnes and J. A. Screen. The impact of Arctic warming on the midlatitude jet-stream: Can it? Has it? Will it? *WIREs Climate Change*, 6(3):277–286, 2015a. doi: 10.1002/wcc.337.

E. A. Barnes, J. W. Hurrell, I. Ebert-Uphoff, C. Anderson, and D. Anderson. Viewing forced climate patterns through an AI lens. *Geophysical Research Letters*, 46(22):13389–13398, 2019. doi: 10.1029/2019GL084944.

P. Barros, S. Magg, C. Weber, and S. Wermter. A multichannel convolutional neural network for hand posture recognition. In S. Wermter, C. Weber, W. Duch, T. Honkela, P. Koprinkova-Hristova, S. Magg, G. Palm, and A. E. P. Villa, editors, *Artificial Neural Networks and Machine Learning – ICANN 2014*, pages 403–410. Springer International Publishing, 2014.

E. Bauer and A. Ganopolski. Comparison of surface mass balance of ice sheets simulated by positive-degree-day method and energy balance approach. *Climate of the Past*, 13(7):819–832, 2017. doi: 10.5194/cp-13-819-2017.

A. C. M. Beljaars, A. R. Brown, and N. Wood. A new parametrization of turbulent orographic form drag. *Quarterly Journal of the Royal Meteorological Society*, 130(599):1327–1347, 2004. doi: 10.1256/qj.03.73.

R. Bennartz, M. Shupe, D. D. Turner, V. P. Walden, K. Steffen, C. J. Cox, M. S. Kulie, N. B. Miller, and C. Pettersen. July 2012 Greenland melt extent enhanced by low-level liquid clouds. *Nature*, 496:83–86, 2013. doi: 10.1038/nature12002.

M. Berdahl, A. Rennermalm, A. Hammann, J. Mioduszweski, S. Hameed, M. Tedesco, J. Stroeve, T. Mote, T. Koyama, and J. R. McConnell. Southeast Greenland winter precipitation strongly linked to the Icelandic Low position. *Journal of Climate*, 31(11):4483–4500, 2018. doi: 10.1175/JCLI-D-17-0622.1.

M. Bevis, C. Harig, S. A. Khan, A. Brown, F. J. Simons, M. Willis, X. Fettweis, M. R. Van Den Broeke, F. B. Madsen, E. Kendrick, et al. Accelerating changes in ice mass within Greenland, and the ice sheet's sen-

sitivity to atmospheric forcing. *Proceedings of the National Academy of Sciences*, 116(6):1934–1939, 2019.

R. Bintanja and M. R. van den Broeke. The influence of clouds on the radiation budget of ice and snow surfaces in Antarctica and Greenland in summer. *International Journal of Climatology*, 16(11): 1281–1296, 1996. doi: 10.1002/(SICI)1097-0088(199611)16:11<1281::AID-JOC83>3.0.CO;2-A.

R. Blackport and P. J. Kushner. Isolating the atmospheric circulation response to Arctic sea ice loss in the coupled climate system. *Journal of Climate*, 30(6):2163–2185, 2017. doi: 10.1175/JCLI-D-16-0257.1.

P. A. Bogenschutz and S. K. Krueger. A simplified PDF parameterization of subgrid-scale clouds and turbulence for cloud-resolving models. *Journal of Advances in Modeling Earth Systems*, 5(2):195–211, 2013. doi: 10.1002/jame.20018.

S. Bony, B. Stevens, D. M. Frierson, C. Jakob, M. Kageyama, R. Pincus, T. G. Shepherd, S. C. Sherwood, A. P. Siebesma, A. H. Sobel, et al. Clouds, circulation and climate sensitivity. *Nature Geoscience*, 8(4): 261–268, 2015.

M. Bougamont, J. L. Bamber, J. K. Ridley, R. M. Gladstone, W. Greuell, E. Hanna, A. J. Payne, and I. Rutt. Impact of model physics on estimating the surface mass balance of the Greenland ice sheet. *Geophysical Research Letters*, 34(17), 2007. doi: 10.1029/2007GL030700.

J. E. Box and A. Rinke. Evaluation of Greenland ice sheet surface climate in the HIRHAM regional climate model using automatic weather station data. *Journal of Climate*, 16(9):1302–1319, 2003. doi: 10.1175/1520-0442-16.9.1302.

J. E. Box and K. Steffen. Sublimation on the Greenland Ice Sheet from automated weather station observations. *Journal of Geophysical Research: Atmospheres*, 106(D24), 2001. doi: 10.1029/2001JD900219.

J. E. Box, X. Fettweis, J. C. Stroeve, M. Tedesco, D. K. Hall, and K. Steffen. Greenland ice sheet albedo feedback: thermodynamics and atmospheric drivers. *The Cryosphere*, 6(4):821–839, 2012. doi: 10.5194/tc-6-821-2012.

R. J. Braithwaite. Positive degree-day factors for ablation on the Greenland ice sheet studied by energy-balance modelling. *Journal of Glaciology*, 41(137):153–160, 1995. doi: 10.3189/S0022143000017846.

D. H. Bromwich, Q.-S. Chen, L.-S. Bai, E. N. Cassano, and Y. Li. Modeled precipitation variability over the greenland ice sheet. *Journal of Geophysical Research: Atmospheres*, 106(D24):33891–33908, 2001. doi: 10.1029/2001JD900251.

H. L. Bryden, W. E. Johns, B. A. King, G. McCarthy, E. L. McDonagh, B. I. Moat, and D. A. Smeed. Reduction in ocean heat transport at 26N since 2008 cools the Eastern Subpolar Gyre of the North Atlantic Ocean. *Journal of Climate*, 33(5):1677–1689, 2020. doi: 10.1175/JCLI-D-19-0323.1.

F. G. L. Cawkwell and J. L. Bamber. The impact of cloud cover on the net radiation budget of the Greenland ice sheet. *Annals of Glaciology*, 34:141–149, 2002. doi: 10.3189/172756402781817789.

C. Charalampidis, D. Van As, W. T. Colgan, R. S. Fausto, M. Macferrin, and H. Machguth. Thermal tracing of retained meltwater in the lower accumulation area of the Southwestern Greenland ice sheet. *Annals of Glaciology*, 57(72):1–10, 2016. doi: 10.1017/aog.2016.2.

J. A. Church, P. U. Clark, A. Cazenave, J. M. Gregory, S. Jevrejeva, A. Levermann, M. A. Merrifield, G. A. Milne, R. S. Nerem, P. D. Nunn, et al. Sea level change. *PM Cambridge University Press*, 2013.

J. Cohen, J. A. Screen, J. C. Furtado, M. Barlow, D. Whittleston, D. Coumou, J. Francis, K. Dethloff, D. Entekhabi, J. Overland, and J. Jones. Recent Arctic amplification and extreme mid-latitude weather. *Nature Geoscience*, 7(9):627–637, 2014. doi: 10.1038/ngeo2234.

W. Colgan, H. Rajaram, R. S. Anderson, K. Steffen, H. J. Zwally, T. Phillips, and W. Abdalati. The annual glaciohydrology cycle in the ablation zone of the greenland ice sheet: Part 2. observed and modeled ice flow. *Journal of Glaciology*, 58(207):51–64, 2012. doi: 10.3189/2012JoG11J081.

D. Coumou, G. Di Capua, S. Vavrus, L. Wang, and S. Wang. The influence of Arctic amplification on mid-latitude summer circulation. *Nature Communications*, 9(1):2959, 2018. doi: 10.1038/s41467-018-05256-8.

C. Cox, N. Humphrey, and J. Harper. Quantifying meltwater refreezing along a transect of sites on the Greenland ice sheet. *The Cryosphere*, 9(2):691–701, 2015. doi: 10.5194/tc-9-691-2015.

R. I. Cullather, S. M. J. Nowicki, B. Zhao, and M. J. Suarez. Evaluation of the Surface Representation of the Greenland Ice Sheet in a General Circulation Model. *Journal of Climate*, 27(13):4835–4856, 2014. doi: 10.1175/JCLI-D-13-00635.1.

G. Danabasoglu. NCAR CESM2 model output prepared for CMIP6 CMIP 1pctCO2. Version 20190128, 2019b.

G. Danabasoglu. Ncar cesm2 model output prepared for cmip6 pamip pdsst-piarcsic. version 20200205., 2019e.

G. Danabasoglu. Ncar cesm2 model output prepared for cmip6 pamip pdsst-futarcsic. version 20200205., 2019f.

G. Danabasoglu, S. G. Yeager, Y.-O. Kwon, J. J. Tribbia, A. S. Phillips, and J. W. Hurrell. Variability of the Atlantic meridional overturning circulation in CCSM4. *Journal of Climate*, 25(15):5153–5172, 2012. doi: 10.1175/JCLI-D-11-00463.1.

G. Danabasoglu, D. Lawrence, K. Lindsay, W. Lipscomb, and G. Strand. NCAR CESM2 model output prepared for CMIP6 CMIP piControl. Version 20190128, 2019a.

G. Danabasoglu, J.-F. Lamarque, J. Bacmeister, D. A. Bailey, A. K. DuVivier, J. Edwards, L. K. Emmons, J. Fasullo, R. Garcia, A. Gettelman, C. Hannay, M. M. Holland, W. G. Large, P. H. Lauritzen, D. M. Lawrence, J. T. M. Lenaerts, K. Lindsay, W. H. Lipscomb, M. J. Mills, R. Neale, K. W. Oleson, B. Otto-Bliesner, A. S. Phillips, W. Sacks, S. Tilmes, L. van Kampenhout, M. Vertenstein, A. Bertini, J. Dennis, C. Deser, C. Fischer, B. Fox-Kemper, J. E. Kay, D. Kinnison, P. J. Kushner, V. E. Larson, M. C. Long, S. Mickelson, J. K. Moore, E. Nienhouse, L. Polvani, P. J. Rasch, and W. G. Strand. The Community Earth System Model version 2 (CESM2). *Journal of Advances in Modeling Earth Systems*, 12(2):e2019MS001916, 2020. doi: 10.1029/2019MS001916.

P. Davini, C. Cagnazzo, R. Neale, and J. Tribbia. Coupling between Greenland blocking and the North Atlantic Oscillation pattern. *Geophysical Research Letters*, 39(14), 2012. doi: 10.1029/2012GL052315.

D. P. Dee, S. M. Uppala, A. J. Simmons, P. Berrisford, P. Poli, S. Kobayashi, U. Andrae, M. A. Balmaseda, G. Balsamo, P. Bauer, P. Bechtold, A. C. M. Beljaars, L. van de Berg, J. Bidlot, N. Bormann, C. Delsol, R. Dragani, M. Fuentes, A. J. Geer, L. Haimberger, S. B. Healy, H. Hersbach, E. V. Hólm, L. Isaksen, P. Kållberg, M. Köhler, M. Matricardi, A. P. McNally, B. M. Monge-Sanz, J.-J. Morcrette, B.-K. Park, C. Peubey, P. de Rosnay, C. Tavolato, J.-N. Thépaut, and F. Vitart. The era-interim reanalysis: configuration and performance of the data assimilation system. *Quarterly Journal of the Royal Meteorological Society*, 137(656):553–597, 2011. doi: 10.1002/qj.828.

A. Delhasse, X. Fettweis, C. Kittel, C. Amory, and C. Agosta. Brief communication: Impact of the recent atmospheric circulation change in

summer on the future surface mass balance of the Greenland Ice Sheet. *The Cryosphere*, 12(11):3409–3418, 2018. doi: 10.5194/tc-12-3409-2018.

A. Delhasse, C. Kittel, C. Amory, S. Hofer, D. van As, R. S. Fausto, and X. Fettweis. Brief communication: Evaluation of the near-surface climate in ERA5 over the Greenland Ice Sheet. *The Cryosphere*, 14(3): 957–965, 2020. doi: 10.5194/tc-14-957-2020.

A. Delhasse, E. Hanna, C. Kittel, and X. Fettweis. Brief communication: CMIP6 does not suggest any atmospheric blocking increase in summer over Greenland by 2100. *International Journal of Climatology*, n/a (n/a), 2021. doi: 10.1002/joc.6977.

C. Deser, R. Tomas, M. Alexander, and D. Lawrence. The seasonal atmospheric response to projected Arctic sea ice loss in the late twenty-first century. *Journal of Climate*, 23(2):333–351, 2010. doi: 10.1175/2009JCLI3053.1.

E. Driesschaert, T. Fichefet, H. Goosse, P. Huybrechts, I. Janssens, A. Mouchet, G. Munhoven, V. Brovkin, and S. L. Weber. Modeling the influence of Greenland ice sheet melting on the Atlantic meridional overturning circulation during the next millennia. *Geophysical Research Letters*, 34(10):1–5, 2007. doi: 10.1029/2007GL029516.

S. Drijfhout, G. J. van Oldenborgh, and A. Cimatoribus. Is a decline of AMOC causing the warming hole above the North Atlantic in observed and modeled warming patterns? *Journal of Climate*, 25(24):8373–8379, 2012. doi: 10.1175/JCLI-D-12-00490.1.

T. L. Edwards, X. Fettweis, O. Gagliardini, F. Gillet-Chaulet, H. Goelzer, J. M. Gregory, M. Hoffman, P. Huybrechts, A. J. Payne, M. Perego, S. Price, A. Quiquet, and C. Ritz. Effect of uncertainty in surface mass balance-elevation feedback on projections of the future sea level contribution of the Greenland ice sheet. *The Cryosphere*, 8:195–208, 2014. doi: 10.5194/tc-8-195-2014.

K. Emanuel. Global Warming Effects on U.S. Hurricane Damage. *Weather, Climate, and Society*, 3(4):261–268, 2011. doi: 10.1175/WCAS-D-11-00007.1.

E. M. Enderlin, I. M. Howat, S. Jeong, M.-J. Noh, J. H. van Angelen, and M. R. van den Broeke. An improved mass budget for the Greenland ice sheet. *Geophysical Research Letters*, 41(3):866–872, 2014. doi: 10.1002/2013GL059010.

J. Ettema, M. R. van den Broeke, E. van Meijgaard, W. J. van de Berg, J. L. Bamber, J. E. Box, and R. C. Bales. Higher surface mass

balance of the Greenland ice sheet revealed by high-resolution climate modeling. *Geophysical Research Letters*, 36(12), 2009. doi: 10.1029/2009GL038110.

J. Ettema, M. R. van den Broeke, E. van Meijgaard, and W. J. van de Berg. Climate of the Greenland ice sheet using a high-resolution climate model – Part 2: Near-surface climate and energy balance. *The Cryosphere*, 4(4):529–544, 2010. doi: 10.5194/tc-4-529-2010.

V. Eyring, S. Bony, G. A. Meehl, C. A. Senior, B. Stevens, R. J. Stouffer, and K. E. Taylor. Overview of the Coupled Model Intercomparison Project phase 6 (CMIP6) experimental design and organization. *Geoscientific Model Development*, 9(5):1937–1958, 2016. doi: 10.5194/gmd-9-1937-2016.

R. S. Fausto, A. P. Ahlstrøm, D. Van As, C. E. Bøggild, and S. J. Johnsen. A new present-day temperature parameterization for Greenland. *Journal of Glaciology*, 55(189):95–105, 2009. doi: 10.3189/002214309788608985.

X. Fettweis. The smb model intercomparison (smbmip) over greenland: first results. 2018. URL http://hdl.handle.net/2268/232923.

X. Fettweis, B. Franco, M. Tedesco, J. H. van Angelen, J. T. M. Lenaerts, M. R. van den Broeke, and H. Gallée. Estimating the Greenland ice sheet surface mass balance contribution to future sea level rise using the regional atmospheric climate model MAR. *The Cryosphere*, 7(2): 469–489, 2013a. doi: 10.5194/tc-7-469-2013.

X. Fettweis, E. Hanna, C. Lang, A. Belleflamme, M. Erpicum, and H. Gallée. Brief communication: "Important role of the mid-tropospheric atmospheric circulation in the recent surface melt increase over the Greenland ice sheet". *The Cryosphere*, 7(1):241–248, 2013b. doi: 10.5194/tc-7-241-2013.

X. Fettweis, J. E. Box, C. Agosta, C. Amory, C. Kittel, C. Lang, D. van As, H. Machguth, and H. Gallée. Reconstructions of the 1900–2015 Greenland ice sheet surface mass balance using the regional climate MAR model. *The Cryosphere*, 11(2):1015–1033, 2017. doi: 10.5194/tc-11-1015-2017.

X. Fettweis, S. Hofer, U. Krebs-Kanzow, C. Amory, T. Aoki, C. J. Berends, A. Born, J. E. Box, A. Delhasse, K. Fujita, P. Gierz, H. Goelzer, E. Hanna, A. Hashimoto, P. Huybrechts, M.-L. Kapsch, M. D. King, C. Kittel, C. Lang, P. L. Langen, J. T. M. Lenaerts, G. E. Liston, G. Lohmann, S. H. Mernild, U. Mikolajewicz, K. Modali, R. H. Mottram, M. Niwano, B. Noël, J. C. Ryan, A. Smith, J. Streffing, M. Tedesco, W. J. van de Berg, M. van den Broeke, R. S. W. van de Wal, L. van Kampenhout,

D. Wilton, B. Wouters, F. Ziemen, and T. Zolles. GrSMBMIP: Intercomparison of the modelled 1980–2012 surface mass balance over the Greenland ice sheet. *The Cryosphere*, 14(11):3935–3958, 2020. doi: 10.5194/tc-14-3935-2020.

R. Fischer, S. Nowicki, M. Kelley, and G. A. Schmidt. A system of conservative regridding for iceâ€"atmosphere coupling in a general circulation model (gcm). *Geoscientific Model Development*, 7(3): 883–907, 2014. doi: 10.5194/gmd-7-883-2014. URL https://www.geosci-model-dev.net/7/883/2014/.

M. G. Flanner and C. S. Zender. Linking snowpack microphysics and albedo evolution. *Journal of Geophysical Research: Atmospheres*, 111 (D12), 2006. doi: 10.1029/2005JD006834.

G. M. Flato. Earth system models: an overview. *Wiley Interdisciplinary Reviews: Climate Change*, 2(6):783–800, 2011. doi: 10.1002/wcc.148.

J. A. Francis and S. J. Vavrus. Evidence linking Arctic amplification to extreme weather in mid-latitudes. *Geophysical Research Letters*, 39 (6), 2012. doi: 10.1029/2012GL051000.

B. Franco, X. Fettweis, C. Lang, and M. Erpicum. Impact of spatial resolution on the modelling of the greenland ice sheet surface mass balance between 1990-2010, using the regional climate model mar. *The Cryosphere*, 6(3):695–711, 2012. doi: 10.5194/tc-6-695-2012.

B. Franco, X. Fettweis, and M. Erpicum. Future projections of the Greenland ice sheet energy balance driving the surface melt. *The Cryosphere*, 7(1):1–18, 2013. doi: 10.5194/tc-7-1-2013.

J. Fyke, O. Sergienko, M. Löfverström, S. Price, and J. T. M. Lenaerts. An Overview of Interactions and Feedbacks Between Ice Sheets and the Earth System. *Reviews of Geophysics*, 56(2):361–408, 2018. doi: 10.1029/2018RG000600.

J. G. Fyke, A. J. Weaver, D. Pollard, M. Eby, L. Carter, and A. Mackintosh. A new coupled ice sheet/climate model: description and sensitivity to model physics under eemian, last glacial maximum, late holocene and modern climate conditions. *Geoscientific Model Development*, 4(1): 117–136, 2011. doi: 10.5194/gmd-4-117-2011.

J. G. Fyke, M. Vizcaíno, and W. H. Lipscomb. The pattern of anthropogenic signal emergence in Greenland ice sheet surface mass balance. *Geophysical Research Letters*, 41(16):6002–6008, 2014a. doi: 10.1002/2014GL060735.

J. G. Fyke, M. Vizcaíno, W. Lipscomb, and S. Price. Future climate warming increases greenland ice sheet surface mass balance variability. *Geophysical Research Letters*, 41(2):470–475, 2014b. doi: 10.1002/2013GL058172.

A. Gettelman and H. Morrison. Advanced two-moment bulk microphysics for global models. Part I: Off-line tests and comparison with other schemes. *Journal of Climate*, 28(3):1268–1287, 2015. doi: 10.1175/JCLI-D-14-00102.1.

A. Gettelman, C. Hannay, J. T. Bacmeister, R. B. Neale, A. G. Pendergrass, G. Danabasoglu, J.-F. Lamarque, J. T. Fasullo, D. A. Bailey, D. M. Lawrence, and M. J. Mills. High climate sensitivity in the Community Earth System Model version 2 (CESM2). *Geophysical Research Letters*, 46(14):8329–8337, 2019a. doi: 10.1029/2019GL083978.

A. Gettelman, M. J. Mills, D. E. Kinnison, R. R. Garcia, A. K. Smith, D. R. Marsh, S. Tilmes, F. Vitt, C. G. Bardeen, J. McInerny, H.-L. Liu, S. C. Solomon, L. M. Polvani, L. K. Emmons, J.-F. Lamarque, J. H. Richter, A. S. Glanville, J. T. Bacmeister, A. S. Phillips, R. B. Neale, I. R. Simpson, A. K. DuVivier, A. Hodzic, and W. J. Randel. The whole atmosphere community climate model version 6 (WACCM6). *Journal of Geophysical Research: Atmospheres*, 124(23):12380–12403, 2019b. doi: 10.1029/2019JD030943.

N. P. Gillett and J. C. Fyfe. Annular mode changes in the CMIP5 simulations. *Geophysical Research Letters*, 40(6):1189–1193, 2013. doi: 10.1002/grl.50249.

X. Glorot and Y. Bengio. Understanding the difficulty of training deep feedforward neural networks. In *Proceedings of the Thirteenth International Conference on Artificial Intelligence and Statistics*, volume 9 of *Proceedings of Machine Learning Research*, pages 249–256. PMLR, 2010.

H. Goelzer, P. Huybrechts, J. Furst, F. Nick, M. Andersen, T. Edwards, X. Fettweis, A. Payne, and S. Shannon. Sensitivity of Greenland ice sheet projections to model formulations. *Journal of Glaciology*, 59 (216):733–749, 2013. doi: 10.3189/2013JoG12J182.

D. N. Goldberg. A variationally derived, depth-integrated approximation to a higher-order glaciological flow model. *Journal of Glaciology*, 57 (201):157–170, 2011. doi: 10.3189/002214311795306763.

N. R. Golledge, E. D. Keller, N. Gomez, K. A. Naughten, J. Bernales, L. D. Trusel, and T. L. Edwards. Global environmental consequences of twenty-first-century ice-sheet melt. *Nature*, 566(7742):65, 2019. doi: 10.1038/s41586-019-0889-9.

J. Gregory and P. Huybrechts. Ice-sheet contributions to future sea-level change. *Philosophical Transactions of the Royal Society A: Mathematical, Physical and Engineering Sciences*, 364(1844):1709–1732, 2006.

J. M. Gregory, P. Huybrechts, and S. C. B. Raper. Threatened loss of the greenland ice-sheet. *Nature*, 428(6983):616–616, 2004.

J. M. Gregory, S. E. George, and R. S. Smith. Large and irreversible future decline of the Greenland ice-sheet. *The Cryosphere Discussions*, 2020: 1–28, 2020. doi: 10.5194/tc-2020-89.

L. Hahn, C. C. Ummenhofer, and Y.-O. Kwon. North Atlantic natural variability modulates emergence of widespread Greenland melt in a warming climate. *Geophysical Research Letters*, 45(17):9171–9178, 2018. doi: 10.1029/2018GL079682.

E. Hanna, P. Huybrechts, I. Janssens, J. Cappelen, K. Steffen, and A. Stephens. Runoff and mass balance of the greenland ice sheet: 1958–2003. *Journal of Geophysical Research: Atmospheres*, 110 (D13), 2005. doi: 10.1029/2004JD005641.

E. Hanna, P. Huybrechts, J. Cappelen, K. Steffen, R. C. Bales, E. Burgess, J. R. McConnell, J. Peder Steffensen, M. Van den Broeke, L. Wake, G. Bigg, M. Griffiths, and D. Savas. Greenland ice sheet surface mass balance 1870 to 2010 based on twentieth century reanalysis, and links with global climate forcing. *Journal of Geophysical Research: Atmospheres*, 116(D24), 2011. doi: 10.1029/2011JD016387.

E. Hanna, F. J. Navarro, F. Pattyn, C. M. Domingues, X. Fettweis, E. R. Ivins, R. J. Nicholls, C. Ritz, B. Smith, S. Tulaczyk, et al. Ice-sheet mass balance and climate change. *Nature*, 498(7452):51, 2013a. doi: 10.1038/nature12238.

E. Hanna, T. E. Cropper, P. D. Jones, A. A. Scaife, and R. Allan. Recent seasonal asymmetric changes in the NAO (a marked summer decline and increased winter variability) and associated changes in the AO and Greenland Blocking Index. *International Journal of Climatology*, 35(9): 2540–2554, 2015. doi: 10.1002/joc.4157.

E. Hanna, T. E. Cropper, R. J. Hall, and J. Cappelen. Greenland Blocking Index 1851–2015: a regional climate change signal. *International Journal of Climatology*, 36(15):4847–4861, 2016. doi: 10.1002/joc.4673.

E. Hanna, X. Fettweis, and R. J. Hall. Brief communication: Recent changes in summer Greenland blocking captured by none of the CMIP5 models. *The Cryosphere*, 12(10):3287–3292, 2018. doi: 10.5194/tc-12-3287-2018.

E. Hanna, J. Cappelen, X. Fettweis, S. H. Mernild, T. L. Mote, R. Mottram, K. Steffen, T. J. Ballinger, and R. J. Hall. Greenland surface air temperature changes from 1981 to 2019 and implications for ice-sheet melt and mass-balance change. *International Journal of Climatology*, n/a(n/a), 2020. doi: 10.1002/joc.6771.

D. L. Hartmann, A. M. Klein Tank, M. Rusticucci, L. V. Alexander, S. Brönnimann, Y. A. R. Charabi, F. J. Dentener, E. J. Dlugokencky, D. R. Easterling, A. Kaplan, B. J. Soden, P. W. Thorne, M. Wild, and P. Zhai. Observations: Atmosphere and surface. *Climate Change 2013 the Physical Science Basis: Working Group I Contribution to the Fifth Assessment Report of the Intergovernmental Panel on Climate Change*, 9781107057:159–254, 2013. doi: 10.1017/CBO9781107415324.008.

M. M. Helsen, R. S. Van De Wal, M. R. Van Den Broeke, W. J. Van De Berg, and J. Oerlemans. Coupling of climate models and ice sheet models by surface mass balance gradients: Application to the Greenland Ice Sheet. *Cryosphere*, 6(2):255–272, 2012. doi: 10.5194/tc-6-255-2012.

H. Hersbach, B. Bell, P. Berrisford, S. Hirahara, A. Horányi, J. Muñoz-Sabater, J. Nicolas, C. Peubey, R. Radu, D. Schepers, A. Simmons, C. Soci, S. Abdalla, X. Abellan, G. Balsamo, P. Bechtold, G. Biavati, J. Bidlot, M. Bonavita, G. De Chiara, P. Dahlgren, D. Dee, M. Diamantakis, R. Dragani, J. Flemming, R. Forbes, M. Fuentes, A. Geer, L. Haimberger, S. Healy, R. J. Hogan, E. Hólm, M. Janisková, S. Keeley, P. Laloyaux, P. Lopez, C. Lupu, G. Radnoti, P. de Rosnay, I. Rozum, F. Vamborg, S. Villaume, and J.-N. Thépaut. The era5 global reanalysis. *Quarterly Journal of the Royal Meteorological Society*, n/a(n/a), 2020. doi: 10.1002/qj.3803.

S. Hofer, A. J. Tedstone, X. Fettweis, and J. L. Bamber. Decreasing cloud cover drives the recent mass loss on the Greenland Ice Sheet. *Science Advances*, 3(6):e1700584, 2017.

S. Hofer, C. Lang, C. Amory, C. Kittel, A. Delhasse, A. Tedstone, and X. Fettweis. Greater Greenland ice sheet contribution to global sea level rise in CMIP6. *Nature Communications*, 11(1):6289, 2020. doi: 10.1038/s41467-020-20011-8.

M. M. Holland and C. M. Bitz. Polar amplification of climate change in coupled models. *Climate Dynamics*, 21(3):221–232, 2003. doi: 10.1007/s00382-003-0332-6.

F. Hourdin, T. Mauritsen, A. Gettelman, J.-C. Golaz, V. Balaji, Q. Duan, D. Folini, D. Ji, D. Klocke, Y. Qian, F. Rauser, C. Rio, L. Tomassini, M. Watanabe, and D. Williamson. The art and science of climate model

tuning. *Bulletin of the American Meteorological Society*, 98(3):589–602, 2017. doi: 10.1175/BAMS-D-15-00135.1.

E. Hunke, W. Lipscomb, P. Jones, A. Turner, N. Jeffery, and S. Elliott. CICE, the Los Alamos Sea Ice Model, version 00, 2017.

E. C. Hunke, W. H. Lipscomb, A. K. Turner, N. Jeffery, and S. Elliott. CICE: the Los Alamos Sea Ice Model Documentation and Software User's Manual Version 4.1 LA-CC-06-012. *T-3 Fluid Dynamics Group, Los Alamos National Laboratory*, 675, 2010.

J. W. Hurrell. Decadal trends in the North Atlantic oscillation: Regional temperatures and precipitation. *Science*, 269(5224):676–679, 1995. doi: 10.1126/science.269.5224.676.

J. W. Hurrell and C. Deser. North Atlantic climate variability: The role of the North Atlantic oscillation. *Journal of Marine Systems*, 79(3):231 – 244, 2010. doi: 10.1016/j.jmarsys.2009.11.002.

J. W. Hurrell, M. M. Holland, P. R. Gent, S. Ghan, J. E. Kay, P. J. Kushner, J. F. Lamarque, W. G. Large, D. Lawrence, K. Lindsay, W. H. Lipscomb, M. C. Long, N. Mahowald, D. R. Marsh, R. B. Neale, P. Rasch, S. Vavrus, M. Vertenstein, D. Bader, W. D. Collins, J. J. Hack, J. Kiehl, and S. Marshall. The community earth system model: A framework for collaborative research. *Bulletin of the American Meteorological Society*, 94(9):1339–1360, 2013. doi: 10.1175/BAMS-D-12-00121.1.

M. Izeboud, S. Lhermitte, K. Van Tricht, J. T. M. Lenaerts, N. P. M. Van Lipzig, and N. Wever. The spatiotemporal variability of cloud radiative effects on the Greenland ice sheet surface mass balance. *Geophysical Research Letters*, 47(12):e2020GL087315, 2020. doi: 10.1029/2020GL087315.

A. Jahn, K. Sterling, M. M. Holland, J. E. Kay, J. A. Maslanik, C. M. Bitz, D. A. Bailey, J. Stroeve, E. C. Hunke, and W. H. Lipscomb. Late-twentieth-century simulation of Arctic sea ice and ocean properties in the CCSM4. *Journal of Climate*, 25(5):1431–1452, 2012.

D. Kennedy, T. Parker, T. Woollings, B. Harvey, and L. Shaffrey. The response of high-impact blocking weather systems to climate change. *Geophysical Research Letters*, 43(13):7250–7258, 2016. doi: 10.1002/2016GL069725.

A. Khazendar, I. G. Fenty, D. Carroll, A. Gardner, C. M. Lee, I. Fukumori, O. Wang, H. Zhang, H. Seroussi, D. Moller, et al. Interruption of two decades of Jakobshavn Isbrae acceleration and thinning as regional ocean cools. *Nature Geoscience*, 12(4):277–283, 2019.

M. D. King, I. M. Howat, S. Jeong, M. J. Noh, B. Wouters, B. Noël, and M. R. van den Broeke. Seasonal to decadal variability in ice discharge from the Greenland ice sheet. *The Cryosphere*, 12(12):3813–3825, 2018. doi: 10.5194/tc-12-3813-2018.

D. P. Kingma and J. Ba. Adam: A method for stochastic optimization, 2014.

K. K. Kjeldsen, N. J. Korsgaard, A. A. Bjørk, S. A. Khan, J. E. Box, S. Funder, N. K. Larsen, J. L. Bamber, W. Colgan, M. Van Den Broeke, et al. Spatial and temporal distribution of mass loss from the greenland ice sheet since ad 1900. *Nature*, 528(7582):396, 2015.

D. M. Lawrence, K. W. Oleson, M. G. Flanner, P. E. Thornton, S. C. Swenson, P. J. Lawrence, X. Zeng, Z.-L. Yang, S. Levis, K. Sakaguchi, G. B. Bonan, and A. G. Slater. Parameterization improvements and functional and structural advances in version 4 of the community land model. *Journal of Advances in Modeling Earth Systems*, 3(1), 2011. doi: 10.1029/2011MS00045.

D. M. Lawrence, R. A. Fisher, C. D. Koven, K. W. Oleson, S. C. Swenson, G. Bonan, N. Collier, B. Ghimire, L. van Kampenhout, D. Kennedy, E. Kluzek, P. J. Lawrence, F. Li, H. Li, D. Lombardozzi, W. J. Riley, W. J. Sacks, M. Shi, M. Vertenstein, W. R. Wieder, C. Xu, A. A. Ali, A. M. Badger, G. Bisht, M. van den Broeke, M. A. Brunke, S. P. Burns, J. Buzan, M. Clark, A. Craig, K. Dahlin, B. Drewniak, J. B. Fisher, M. Flanner, A. M. Fox, P. Gentine, F. Hoffman, G. Keppel-Aleks, R. Knox, S. Kumar, J. Lenaerts, L. R. Leung, W. H. Lipscomb, Y. Lu, A. Pandey, J. D. Pelletier, J. Perket, J. T. Randerson, D. M. Ricciuto, B. M. Sanderson, A. Slater, Z. M. Subin, J. Tang, R. Q. Thomas, M. Val Martin, and X. Zeng. The Community Land Model version 5: Description of new features, benchmarking, and impact of forcing uncertainty. *Journal of Advances in Modeling Earth Systems*, 11(12):4245–4287, 2019. doi: 10.1029/2018MS001583.

S. Le clec'h, S. Charbit, A. Quiquet, X. Fettweis, C. Dumas, M. Kageyama, C. Wyard, and C. Ritz. Assessment of the Greenland ice sheet–atmosphere feedbacks for the next century with a regional atmospheric model coupled to an ice sheet model. *The Cryosphere*, 13 (1):373–395, 2019. doi: 10.5194/tc-13-373-2019.

J. T. M. Lenaerts, B. Medley, M. R. van den Broeke, and B. Wouters. Observing and modeling ice sheet surface mass balance. *Reviews of Geophysics*, 57(2):376–420, 2019. doi: 10.1029/2018RG000622.

N. J. L. Lenssen, G. A. Schmidt, J. E. Hansen, M. J. Menne, A. Persin, R. Ruedy, and D. Zyss. Improvements in the GISTEMP Uncertainty Model. *Journal of Geophysical Research: Atmospheres*, 124(12): 6307–6326, 2019. doi: 10.1029/2018JD029522.

S.-J. Lin and R. B. Rood. An explicit flux-form semi-lagrangian shallow-water model on the sphere. *Quarterly Journal of the Royal Meteorological Society*, 123(544):2477–2498, 1997. doi: 10.1002/qj.49712354416.

W. H. Lipscomb, J. G. Fyke, M. Vizcaíno, W. J. Sacks, J. Wolfe, M. Vertenstein, A. Craig, E. Kluzek, and D. M. Lawrence. Implementation and Initial Evaluation of the Glimmer Community Ice Sheet Model in the Community Earth System Model. *Journal of Climate*, 26(19):7352–7371, 2013. doi: 10.1175/JCLI-D-12-00557.1.

W. H. Lipscomb, S. F. Price, M. J. Hoffman, G. R. Leguy, A. R. Bennett, S. L. Bradley, K. J. Evans, J. G. Fyke, J. H. Kennedy, M. Perego, D. M. Ranken, W. J. Sacks, A. G. Salinger, L. J. Vargo, and P. H. Worley. Description and evaluation of the Community Ice Sheet Model (CISM) v2.1. *Geoscientific Model Development*, 12(1):387–424, 2019. doi: 10.5194/gmd-12-387-2019.

J. Liu, Z. Chen, J. Francis, M. Song, T. Mote, and Y. Hu. Has Arctic sea ice loss contributed to increased surface melting of the Greenland ice sheet? *Journal of Climate*, 29(9):3373–3386, 2016. doi: 10.1175/JCLI-D-15-0391.1.

M. Lofverstrom, J. G. Fyke, K. Thayer-Calder, L. Muntjewerf, M. Vizcaino, W. J. Sacks, W. H. Lipscomb, B. L. Otto-Bliesner, and S. L. Bradley. An efficient ice sheet/Earth system model spin-up procedure for CESM2-CISM2: Description, evaluation, and broader applicability. *Journal of Advances in Modeling Earth Systems*, 12(8):e2019MS001984, 2020. doi: 10.1029/2019MS001984.

G. A. Meehl, C. A. Senior, V. Eyring, G. Flato, J.-F. Lamarque, R. J. Stouffer, K. E. Taylor, and M. Schlund. Context for interpreting equilibrium climate sensitivity and transient climate response from the CMIP6 Earth system models. *Science Advances*, 6(26), 2020.

M. Monirul Qader Mirza. Global warming and changes in the probability of occurrence of floods in Bangladesh and implications. *Global Environmental Change*, 12(2):127 – 138, 2002. doi: https://doi.org/10.1016/S0959-3780(02)00002-X.

M. Morlighem, C. N. Williams, E. Rignot, L. An, J. E. Arndt, J. L. Bamber, G. Catania, N. Chauché, J. A. Dowdeswell, B. Dorschel, I. Fenty, K. Hogan, I. Howat, A. Hubbard, M. Jakobsson, T. M. Jordan, K. K. Kjeldsen, R. Millan, L. Mayer, J. Mouginot, B. P. Y. Noël, C. O'Cofaigh, S. Palmer, S. Rysgaard, H. Seroussi, M. J. Siegert, P. Slabon, F. Straneo, M. R. van den Broeke, W. Weinrebe, M. Wood, and K. B. Zinglersen. BedMachine v3: Complete Bed Topography and Ocean Bathymetry Mapping of Greenland From Multibeam Echo Sounding

Combined With Mass Conservation. *Geophysical Research Letters*, 44 (21):11,051–11,061, 2017. doi: 10.1002/2017GL074954.

R. Mottram, F. Boberg, P. Langen, S. Yang, C. Rodehacke, J. H. Christensen, and M. S. Madsen. Surface mass balance of the Greenland ice sheet in the regional climate model HIRHAM5: Present state and future prospects. *Low Temperature Science*, 75:105–115, 2017. doi: 10.14943/lowtemsci.75.105.

J. Mouginot, E. Rignot, A. A. Bjørk, M. van den Broeke, R. Millan, M. Morlighem, B. Noël, B. Scheuchl, and M. Wood. Forty-six years of Greenland Ice Sheet mass balance from 1972 to 2018. *Proceedings of the National Academy of Sciences*, 116(19):9239–9244, 2019. doi: 10.1073/pnas.1904242116.

L. Muntjewerf, M. Petrini, M. Vizcaino, R. Ernani da Silva, Carolina and, M. D. W. Scherrenberg, K. Thayer-Calder, S. L. Bradley, J. T. M. Lenaerts, W. H. Lipscomb, and M. Lofverstrom. Greenland ice sheet contribution to 21st century sea level rise as simulated by the coupled CESM2.1-CISM2.1. *Geophysical Research Letters*, 47(9): e2019GL086836, 2020a. doi: 10.1029/2019GL086836.

L. Muntjewerf, R. Sellevold, M. Vizcaino, C. Ernani da Silva, M. Petrini, K. Thayer-Calder, M. D. W. Scherrenberg, S. L. Bradley, C. A. Katsman, J. Fyke, W. H. Lipscomb, M. Lofverstrom, and W. J. Sacks. Accelerated Greenland ice sheet mass loss under high greenhouse gas forcing as simulated by the coupled CESM2.1-CISM2.1. *Journal of Advances in Modeling Earth Systems*, 12(10):e2019MS002031, 2020b. doi: https://doi.org/10.1029/2019MS002031.

L. Muntjewerf, W. J. Sacks, M. Lofverstrom, J. Fyke, W. H. Lipscomb, C. Ernani da Silva, M. Vizcaino, K. Thayer-Calder, and J. T. M. Lenaerts. Description and demonstration of the coupled Community Earth System Model v2.1 - Community Ice Sheet Model v2.1 (CESM2.1-CISM2.1). *Journal of Advances in Modeling Earth Systems*, submitted.

R. B. Neale. The NCAR Community Atmosphere Model version 6 (CAM6): Scientific configuration and simulation fidelity. *J. Adv. Model. Earth Syst.*, in review.

R. B. Neale, J. Richter, S. Park, P. H. Lauritzen, S. J. Vavrus, P. J. Rasch, and M. Zhang. The Mean Climate of the Community Atmosphere Model (CAM4) in Forced SST and Fully Coupled Experiments. *Journal of Climate*, 26(14):5150–5168, 2013. doi: 10.1175/JCLI-D-12-00236.1.

U. Neu, M. G. Akperov, N. Bellenbaum, R. Benestad, R. Blender, R. Caballero, A. Cocozza, H. F. Dacre, Y. Feng, K. Fraedrich, J. Grieger,

S. Gulev, J. Hanley, T. Hewson, M. Inatsu, K. Keay, S. F. Kew, I. Kindem, G. C. Leckebusch, M. L. R. Liberato, P. Lionello, I. I. Mokhov, J. G. Pinto, C. C. Raible, M. Reale, I. Rudeva, M. Schuster, I. Simmonds, M. Sinclair, M. Sprenger, N. D. Tilinina, I. F. Trigo, S. Ulbrich, U. Ulbrich, X. L. Wang, and H. Wernli. IMILAST: A community effort to intercompare extratropical cyclone detection and tracking algorithms. *Bulletin of the American Meteorological Society*, 94(4):529–547, 2013. doi: 10.1175/BAMS-D-11-00154.1.

S. V. Nghiem, D. K. Hall, T. L. Mote, M. Tedesco, M. R. Albert, K. Keegan, C. A. Shuman, N. E. DiGirolamo, and G. Neumann. The extreme melt across the Greenland ice sheet in 2012. *Geophysical Research Letters*, 39(20), 2012. doi: 10.1029/2012GL053611.

B. Noël, X. Fettweis, W. J. Van De Berg, M. R. Van Den Broeke, and M. Erpicum. Sensitivity of Greenland Ice Sheet surface mass balance to perturbations in sea surface temperature and sea ice cover: A study with the regional climate model MAR. *Cryosphere*, 8(5):1871–1883, 2014. doi: 10.5194/tc-8-1871-2014.

B. Noël, W. J. van de Berg, E. van Meijgaard, P. Kuipers Munneke, R. S. W. van de Wal, and M. R. van den Broeke. Evaluation of the updated regional climate model RACMO2.3: summer snowfall impact on the Greenland Ice Sheet. *The Cryosphere*, 9(5):1831–1844, 2015. doi: 10.5194/tc-9-1831-2015.

B. Noël, W. J. van de Berg, H. Machguth, S. Lhermitte, I. Howat, X. Fettweis, and M. R. van den Broeke. A daily, 1 km resolution data set of downscaled Greenland ice sheet surface mass balance (1958–2015). *The Cryosphere*, 10(5):2361–2377, 2016. doi: 10.5194/tc-10-2361-2016.

B. Noël, W. van De Berg, S. Lhermitte, B. Wouters, H. Machguth, I. Howat, M. Citterio, G. Moholdt, J. Lenaerts, and M. R. van den Broeke. A tipping point in refreezing accelerates mass loss of Greenland's glaciers and ice caps. *Nature communications*, 8:14730, 2017.

B. Noël, W. J. van de Berg, J. M. van Wessem, E. van Meijgaard, D. van As, J. T. M. Lenaerts, S. Lhermitte, P. Kuipers Munneke, C. J. P. P. Smeets, L. H. van Ulft, R. S. W. van de Wal, and M. R. van den Broeke. Modelling the climate and surface mass balance of polar ice sheets using racmo2 – part 1: Greenland (1958–2016). *The Cryosphere*, 12 (3):811–831, 2018. doi: 10.5194/tc-12-811-2018.

B. Noël, W. J. van de Berg, S. Lhermitte, and M. R. van den Broeke. Rapid ablation zone expansion amplifies north Greenland mass loss. *Science advances*, 5(9):eaaw0123, 2019. doi: 10.1126/sciadv.aaw0123.

B. Noël, L. van Kampenhout, W. J. van de Berg, J. T. M. Lenaerts, B. Wouters, and M. R. van den Broeke. Brief communication: CESM2 climate forcing (1950–2014) yields realistic Greenland ice sheet surface mass balance. *The Cryosphere*, 14(4):1425–1435, 2020a. doi: 10.5194/tc-14-1425-2020.

B. Noël, L. van Kampenhout, W. J. van de Berg, J. T. M. Lenaerts, B. Wouters, and M. R. van den Broeke. Brief communication: CESM2 climate forcing (1950–2014) yields realistic Greenland ice sheet surface mass balance. *The Cryosphere*, 14(4):1425–1435, 2020b. doi: 10.5194/tc-14-1425-2020.

S. M. J. Nowicki, A. Payne, E. Larour, H. Seroussi, H. Goelzer, W. Lipscomb, J. Gregory, A. Abe-Ouchi, and A. Shepherd. Ice Sheet Model Intercomparison Project (ISMIP6) contribution to CMIP6. *Geoscientific Model Development*, 9(12):4521–4545, 2016. doi: 10.5194/gmd-9-4521-2016.

M. Oltmanns, F. Straneo, and M. Tedesco. Increased Greenland melt triggered by large-scale, year-round cyclonic moisture intrusions. *The Cryosphere*, 13(3):815–825, 2019. doi: 10.5194/tc-13-815-2019.

B. C. O'Neill, C. Tebaldi, D. P. van Vuuren, V. Eyring, P. Friedlingstein, G. Hurtt, R. Knutti, E. Kriegler, J.-F. Lamarque, J. Lowe, G. A. Meehl, R. Moss, K. Riahi, and B. M. Sanderson. The scenario model intercomparison project (scenariomip) for cmip6. *Geoscientific Model Development*, 9(9):3461–3482, 2016. doi: 10.5194/gmd-9-3461-2016.

M. Oppenheimer, B. Glavovic, J. Hinkel, R. van de Wal, A. Magnan, A. Abd-Elgawad, R. Cai, M. CifuentesJara, R. DeConto, T. Ghosh, J. Hay, F. Isla, B. Marzeion, B. Meyssignac, and Z. Sebesvari. Sea level rise and implications for low-lying islands, coasts and communities. Technical report, IPCC Special Report on the Ocean and Cryosphere in a Changing Climate [H.-O. Pörtner, D.C. Roberts, V. Masson-Delmotte, P. Zhai, M. Tignor, E. Poloczanska, K. Mintenbeck, A. Alegría, M. Nicolai, A. Okem, J. Petzold, B. Rama, N.M. Weyer (eds.)], 2019.

J. Overland, J. A. Francis, R. Hall, E. Hanna, S.-J. Kim, and T. Vihma. The melting Arctic and midlatitude weather patterns: Are they connected? *Journal of Climate*, 28(20):7917–7932, 2015. doi: 10.1175/JCLI-D-14-00822.1.

J. Overland, E. Hanna, I. Hanssen-Bauer, S.-J. Kim, J. Walsh, M. Wang, U. Bhatt, R. Thoman, et al. Surface air temperature. *Arctic report card*, 2018.

V. Parry, P. Nienow, D. Mair, J. Scott, B. Hubbard, K. Steffen, and D. Wingham. Investigations of meltwater refreezing and density variations in the snowpack and firn within the percolation zone of the

Greenland ice sheet. *Annals of Glaciology*, 46:61–68, 2007. doi: 10.3189/172756407782871332.

F. Pattyn, C. Ritz, E. Hanna, X. Asay-Davis, R. DeConto, G. Durand, L. Favier, X. Fettweis, H. Goelzer, N. R. Golledge, et al. The Greenland and Antarctic ice sheets under 1.5 C global warming. *Nature Climate Change*, 8(12):1053–1061, 2018.

R. A. Pedersen and J. H. Christensen. Attributing Greenland warming patterns to regional Arctic sea ice loss. *Geophysical Research Letters*, 46(17-18):10495–10503, 2019. doi: 10.1029/2019GL083828.

Y. Peings and G. Magnusdottir. Forcing of the wintertime atmospheric circulation by the multidecadal fluctuations of the North Atlantic ocean. *Environmental Research Letters*, 9(3):034018, 2014a. doi: 10.1088/1748-9326/9/3/034018.

Y. Peings and G. Magnusdottir. Response of the wintertime northern hemisphere atmospheric circulation to current and projected Arctic sea ice decline: A numerical study with CAM5. *Journal of Climate*, 27(1):244–264, 2014b. doi: 10.1175/JCLI-D-13-00272.1.

F. Pithan and T. Mauritsen. Arctic amplification dominated by temperature feedbacks in contemporary climate models. *Nature Geosci*, 7(3):181–184, mar 2014.

J. G. L. Rae, G. Adalgeirsdottir, T. L. Edwards, X. Fettweis, J. M. Gregory, H. T. Hewitt, J. A. Lowe, P. Lucas-Picher, R. H. Mottram, A. J. Payne, J. K. Ridley, S. R. Shannon, W. J. van de Berg, R. S. W. van de Wal, and M. R. van den Broeke. Greenland ice sheet surface mass balance: Evaluating simulations and making projections with regional climate models. *The Cryosphere*, 6(6):1275–1294, 2012. doi: 10.5194/tc-6-1275-2012.

J. Ran, M. Vizcaino, P. Ditmar, M. R. van den Broeke, T. Moon, C. R. Steger, E. M. Enderlin, B. Wouters, B. Noël, C. H. Reijmer, R. Klees, M. Zhong, L. Liu, and X. Fettweis. Seasonal mass variations show timing and magnitude of meltwater storage in the greenland ice sheet. *The Cryosphere*, 12(9):2981–2999, 2018. doi: 10.5194/tc-12-2981-2018. URL https://www.the-cryosphere.net/12/2981/2018/.

N. A. Rayner, D. E. Parker, E. B. Horton, C. K. Folland, L. V. Alexander, D. P. Rowell, E. C. Kent, and A. Kaplan. Global analyses of sea surface temperature, sea ice, and night marine air temperature since the late nineteenth century. *Journal of Geophysical Research: Atmospheres*, 108(D14), 2003. doi: 10.1029/2002JD002670.

A. K. Rennermalm, L. C. Smith, J. C. Stroeve, and V. W. Chu. Does sea ice influence Greenland ice sheet surface-melt? *Environmental Research Letters*, 4(2):024011, 2009. doi: 10.1088/1748-9326/4/2/024011.

A. M. Rhoades, X. Huang, P. A. Ullrich, and C. M. Zarzycki. Characterizing Sierra Nevada snowpack using variable-resolution CESM. *Journal of Applied Meteorology and Climatology*, 55(1):173–196, 2016. doi: 10.1175/JAMC-D-15-0156.1.

A. M. Rhoades, P. A. Ullrich, and C. M. Zarzycki. Projecting 21st century snowpack trends in western USA mountains using variable-resolution CESM. *Climate Dynamics*, 50(1-2):261–288, 2018. doi: 10.1007/s00382-017-3606-0.

J. K. Ridley, P. Huybrechts, J. M. Gregory, and J. A. Lowe. Elimination of the Greenland Ice Sheet in a high CO_2 climate. *Journal of Climate*, 18 (17):3409–3427, 2005. doi: 10.1175/JCLI3482.1.

A. Robinson, R. Calov, and A. Ganopolski. Multistability and critical thresholds of the Greenland ice sheet. *Nature Climate Change*, 2(6): 429–432, 2012.

I. C. Rutt, M. Hagdorn, N. R. J. Hulton, and A. J. Payne. The Glimmer community ice sheet model. *Journal of Geophysical Research: Earth Surface*, 114(F2), 2009.

J. C. Ryan, A. Hubbard, M. Stibal, T. D. Irvine-Fynn, J. Cook, L. C. Smith, K. Cameron, and J. Box. Dark zone of the greenland ice sheet controlled by distributed biologically-active impurities. *Nature communications*, 9(1):1065, 2018.

G. A. Schmidt, D. Bader, L. J. Donner, G. S. Elsaesser, J.-C. Golaz, C. Hannay, A. Molod, R. B. Neale, and S. Saha. Practice and philosophy of climate model tuning across six us modeling centers. *Geoscientific Model Development*, 10(9):3207–3223, 2017. doi: 10.5194/gmd-10-3207-2017.

J. A. Screen and I. Simmonds. The central role of diminishing sea ice in recent Arctic temperature amplification. *Nature*, 464(7293):1334–1337, 2010. doi: 10.1038/nature09051.

J. A. Screen and I. Simmonds. Exploring links between Arctic amplification and mid-latitude weather. *Geophysical Research Letters*, 40(5): 959–964, 2013b. doi: 10.1002/grl.50174.

J. A. Screen, C. Deser, and I. Simmonds. Local and remote controls on observed arctic warming. *Geophysical Research Letters*, 39(10), 2012. doi: 10.1029/2012GL051598.

J. A. Screen, I. Simmonds, C. Deser, and R. Tomas. The atmospheric response to three decades of observed Arctic sea ice loss. *Journal of Climate*, 26(4):1230–1248, 2013a. doi: 10.1175/JCLI-D-12-00063.1.

R. Sellevold and M. Vizcaino. Global warming threshold and mechanisms for accelerated Greenland ice sheet surface mass loss. *Journal of Advances in Modeling Earth Systems*, 12(9):e2019MS002029, 2020. doi: 10.1029/2019MS002029.

R. Sellevold and M. Vizcaino. Projecting 21st century Greenland ice sheet surface melt using artificial neural networks. *Geophysical Research Letters*, n/a(n/a):n/a, in review.

R. Sellevold, S. Sobolowski, and C. Li. Investigating possible Arctic–midlatitude teleconnections in a linear framework. *Journal of Climate*, 29(20):7329–7343, 2016. doi: 10.1175/JCLI-D-15-0902.1.

R. Sellevold, L. van Kampenhout, J. T. M. Lenaerts, B. Noël, W. H. Lipscomb, and M. Vizcaino. Surface mass balance downscaling through elevation classes in an Earth system model: application to the Greenland ice sheet. *The Cryosphere*, 13(12):3193–3208, 2019. doi: 10.5194/tc-13-3193-2019.

R. Sellevold, J. T. M. Lenaerts, and M. Vizcaino. Influence of Arctic sea-ice loss on the Greenland ice sheet climate. *Climate Dynamics*, n/a (n/a):n/a, in review.

M. C. Serreze and R. G. Barry. Processes and impacts of Arctic amplification: A research synthesis. *Global and Planetary Change*, 77(1):85 – 96, 2011. doi: https://doi.org/10.1016/j.gloplacha.2011.03.004.

M. C. Serreze and J. A. Francis. The Arctic amplification debate. *Climatic change*, 76(3-4):241–264, 2006.

M. C. Serreze and J. Stroeve. Arctic sea ice trends , variability and implications for seasonal ice forecasting Subject Areas : Author for correspondence :. *Phil. Trans. R. Soc.*, 373(figure 1):1–16, 2015.

M. C. Serreze, F. Carse, R. G. Barry, and J. C. Rogers. Icelandic Low cyclone activity: Climatological features, linkages with the NAO, and relationships with recent changes in the Northern Hemisphere circulation. *Journal of Climate*, 10(3):453–464, 1997. doi: 10.1175/1520-0442(1997)010<0453:ILCACF>2.0.CO;2.

M. C. Serreze, A. P. Barrett, J. C. Stroeve, D. N. Kindig, and M. M. Holland. The emergence of surface-based Arctic amplification. *The Cryosphere*, 3(1):11–19, 2009. doi: 10.5194/tc-3-11-2009.

G. Sgubin, D. Swingedouw, S. Drijfhout, Y. Mary, and A. Bennabi. Abrupt cooling over the North Atlantic in modern climate models. *Nature Communications*, 8:14375, 2017.

A. Shepherd, E. R. Ivins, G. A, V. R. Barletta, M. J. Bentley, S. Bettadpur, K. H. Briggs, D. H. Bromwich, R. Forsberg, N. Galin, M. Horwath, S. Jacobs, I. Joughin, M. A. King, J. T. M. Lenaerts, J. Li, S. R. M. Ligtenberg, A. Luckman, S. B. Luthcke, M. McMillan, R. Meister, G. Milne, J. Mouginot, A. Muir, J. P. Nicolas, J. Paden, A. J. Payne, H. Pritchard, E. Rignot, H. Rott, L. S. Sørensen, T. A. Scambos, B. Scheuchl, E. J. O. Schrama, B. Smith, A. V. Sundal, J. H. van Angelen, W. J. van de Berg, M. R. van den Broeke, D. G. Vaughan, I. Velicogna, J. Wahr, P. L. Whitehouse, D. J. Wingham, D. Yi, D. Young, and H. J. Zwally. A reconciled estimate of ice-sheet mass balance. *Science*, 338(6111): 1183–1189, 2012. doi: 10.1126/science.1228102.

A. Shepherd, E. Ivins, E. Rignot, B. Smith, M. van den Broeke, I. Velicogna, P. Whitehouse, K. Briggs, I. Joughin, G. Krinner, S. Nowicki, T. Payne, T. Scambos, N. Schlegel, A. Geruo, C. Agosta, A. Ahlstrøm, G. Babonis, V. R. Barletta, A. A. Bjørk, A. Blazquez, J. Bonin, W. Colgan, B. Csatho, R. Cullather, M. E. Engdahl, D. Felikson, X. Fettweis, R. Forsberg, A. E. Hogg, H. Gallee, A. Gardner, L. Gilbert, N. Gourmelen, A. Groh, B. Gunter, E. Hanna, C. Harig, V. Helm, A. Horvath, M. Horwath, S. Khan, K. K. Kjeldsen, H. Konrad, P. L. Langen, B. Lecavalier, B. Loomis, S. Luthcke, M. McMillan, D. Melini, S. Mernild, Y. Mohajerani, P. Moore, R. Mottram, J. Mouginot, G. Moyano, A. Muir, T. Nagler, G. Nield, J. Nilsson, B. Noël, I. Otosaka, M. E. Pattle, W. R. Peltier, N. Pie, R. Rietbroek, H. Rott, L. S. Sørensen, I. Sasgen, H. Save, B. Scheuchl, E. Schrama, L. Schröder, K.-W. Seo, S. B. Simonsen, T. Slater, G. Spada, T. Sutterley, M. Talpe, L. Tarasov, W. Jan van de Berg, W. van der Wal, M. van Wessem, B. D. Vishwakarma, D. Wiese, D. Wilton, T. Wagner, B. Wouters, J. Wuite, and T. I. Team. Mass balance of the Greenland Ice Sheet from 1992 to 2018. *Nature*, 579(7798):233–239, 2019.

D. M. Smith, J. A. Screen, C. Deser, J. Cohen, J. C. Fyfe, J. García-Serrano, T. Jung, V. Kattsov, D. Matei, R. Msadek, Y. Peings, M. Sigmond, J. Ukita, J.-H. Yoon, and X. Zhang. The polar amplification model intercomparison project (PAMIP) contribution to CMIP6: Investigating the causes and consequences of polar amplification. *Geoscientific Model Development*, 12(3):1139–1164, 2019. doi: 10.5194/gmd-12-1139-2019.

R. Smith, P. Jones, B. Briegleb, F. Bryan, G. Danabasoglu, J. Dennis, J. Dukowicz, C. Eden, B. Fox-Kemper, and P. Gent. The Parallel Ocean Program (POP) reference manual ocean component of the Community

Climate System Model (CCSM) and Community Earth System Model (CESM). *Rep. LAUR-01853*, 141:1–140, 2010.

R. S. Smith, S. George, and J. M. Gregory. FAMOUS version xotzb (FAMOUS-ice): a GCM capable of energy- and water- conserving coupling to an ice sheet model. *Geoscientific Model Development Discussions*, 2020:1–25, 2020. doi: 10.5194/gmd-2020-207.

T. J. Snape and P. M. Forster. Decline of Arctic sea ice: Evaluation and weighting of CMIP5 projections. *Journal of Geophysical Research: Atmospheres*, 119(2):546–554, 2014. doi: 10.1002/2013JD020593.

C. R. Steger, C. H. Reijmer, and M. R. van den Broeke. The modelled liquid water balance of the Greenland Ice Sheet. *The Cryosphere*, 11 (6):2507–2526, 2017. doi: 10.5194/tc-11-2507-2017.

J. C. Stroeve, J. R. Mioduszewski, A. Rennermalm, L. N. Boisvert, M. Tedesco, and D. Robinson. Investigating the local-scale influence of sea ice on Greenland surface melt. *The Cryosphere*, 11(5):2363–2381, 2017. doi: 10.5194/tc-11-2363-2017.

Q. Sun, M. M. Whitney, F. O. Bryan, and Y. heng Tseng. A box model for representing estuarine physical processes in Earth system models. *Ocean Modelling*, 112:139 – 153, 2017. doi: https://doi.org/10.1016/j.ocemod.2017.03.004.

K. E. Taylor, R. J. Stouffer, and G. A. Meehl. An Overview of CMIP5 and the Experiment Design. *Bulletin of the American Meteorological Society*, 93(4):485–498, 2012. doi: 10.1175/BAMS-D-11-00094.1.

M. Tedesco and X. Fettweis. Unprecedented atmospheric conditions (1948–2019) drive the 2019 exceptional melting season over the Greenland ice sheet. *The Cryosphere*, 14(4):1209–1223, 2020. doi: 10.5194/tc-14-1209-2020.

L. D. Trusel, S. B. Das, M. B. Osman, M. J. Evans, B. E. Smith, X. Fettweis, J. R. McConnell, B. P. Noël, and M. R. van den Broeke. Nonlinear rise in Greenland runoff in response to post-industrial Arctic warming. *Nature*, 564(7734):104–108, 2018. doi: 10.1038/s41586-018-0752-4.

M. Tsukernik, D. N. Kindig, and M. C. Serreze. Characteristics of winter cyclone activity in the northern North Atlantic: Insights from observations and regional modeling. *Journal of Geophysical Research: Atmospheres*, 112(D3), 2007. doi: 10.1029/2006JD007184.

J. H. van Angelen, J. T. M. Lenaerts, M. R. van den Broeke, X. Fettweis, and E. van Meijgaard. Rapid loss of firn pore space accelerates 21st century Greenland mass loss. *Geophysical Research Letters*, 40(10): 2109–2113, 2013. doi: 10.1002/grl.50490.

J. H. van Angelen, M. R. van den Broeke, B. Wouters, and J. T. Lenaerts. Contemporary (1960–2012) Evolution of the Climate and Surface Mass Balance of the Greenland Ice Sheet. *Surveys in Geophysics*, 35(5): 1155–1174, 2014. doi: 10.1007/s10712-013-9261-z.

D. van As, A. Bech Mikkelsen, M. Holtegaard Nielsen, J. E. Box, L. Claesson Liljedahl, K. Lindbäck, L. Pitcher, and B. Hasholt. Hypsometric amplification and routing moderation of Greenland ice sheet meltwater release. *The Cryosphere*, 11(3):1371–1386, 2017. doi: 10.5194/tc-11-1371-2017.

R. S. W. van de Wal. Mass-balance modelling of the Greenland ice sheet: a comparison of an energy-balance and a degree-day model. *Annals of Glaciology*, 23:36–45, 1996. doi: 10.3189/S0260305500013239.

M. van den Broeke, P. Smeets, J. Ettema, and P. K. Munneke. Surface radiation balance in the ablation zone of the west Greenland ice sheet. *Journal of Geophysical Research: Atmospheres*, 113(D13), 2008. doi: 10.1029/2007JD009283.

M. R. van den Broeke and H. Gallée. Observation and simulation of barrier winds at the western margin of the Greenland ice sheet. *Quarterly Journal of the Royal Meteorological Society*, 122(534):1365–1383, 1996. doi: 10.1002/qj.49712253407.

M. R. van den Broeke, E. M. Enderlin, I. M. Howat, P. Kuipers Munneke, B. P. Y. Noël, W. J. van de Berg, E. van Meijgaard, and B. Wouters. On the recent contribution of the Greenland ice sheet to sea level change. *The Cryosphere*, 10(5):1933–1946, 2016. doi: 10.5194/tc-10-1933-2016.

L. van Kampenhout, J. T. M. Lenaerts, W. H. Lipscomb, W. J. Sacks, D. M. Lawrence, A. G. Slater, and M. R. van den Broeke. Improving the representation of polar snow and firn in the Community Earth System Model. *Journal of Advances in Modeling Earth Systems*, 9(7):2583–2600, 2017. doi: 10.1002/2017MS000988.

L. van Kampenhout, A. M. Rhoades, A. R. Herrington, C. M. Zarzycki, J. T. M. Lenaerts, W. J. Sacks, and M. R. van den Broeke. Regional grid refinement in an Earth system model: impacts on the simulated Greenland surface mass balance. *The Cryosphere*, 13(6):1547–1564, 2019. doi: 10.5194/tc-13-1547-2019.

L. van Kampenhout, J. T. M. Lenaerts, W. H. Lipscomb, S. Lhermitte, B. Noël, M. Vizcaíno, W. J. Sacks, and M. R. van den Broeke. Present-Day Greenland Ice Sheet Climate and Surface Mass Balance in CESM2. *Journal of Geophysical Research: Earth Surface*, 125(2): e2019JF005318, 2020. doi: 10.1029/2019JF005318.

K. Van Tricht, S. Lhermitte, I. V. Gorodetskaya, and N. P. M. van Lipzig. Improving satellite-retrieved surface radiative fluxes in polar regions using a smart sampling approach. *The Cryosphere*, 10(5):2379–2397, 2016a. doi: 10.5194/tc-10-2379-2016.

B. Vandecrux, M. MacFerrin, H. Machguth, W. T. Colgan, D. van As, A. Heilig, C. M. Stevens, C. Charalampidis, R. S. Fausto, E. M. Morris, E. Mosley-Thompson, L. Koenig, L. N. Montgomery, C. Miège, S. B. Simonsen, T. Ingeman-Nielsen, and J. E. Box. Firn data compilation reveals widespread decrease of firn air content in western Greenland. *The Cryosphere*, 13(3):845–859, 2019. doi: 10.5194/tc-13-845-2019.

M. Vizcaíno, U. Mikolajewicz, J. Jungclaus, and G. Schurgers. Climate modification by future ice sheet changes and consequences for ice sheet mass balance. *Climate Dynamics*, 34(2):301–324, 2010. doi: 10.1007/s00382-009-0591-y.

M. Vizcaino, U. Mikolajewicz, F. Ziemen, C. B. Rodehacke, R. Greve, and M. R. van den Broeke. Coupled simulations of Greenland Ice Sheet and climate change up to A.D. 2300. *Geophysical Research Letters*, 42(10):3927–3935, 2015. doi: 10.1002/2014GL061142.

M. Vizcaíno, W. H. Lipscomb, W. J. Sacks, J. H. van Angelen, B. Wouters, and M. R. van den Broeke. Greenland Surface Mass Balance as Simulated by the Community Earth System Model. Part I: Model Evaluation and 1850–2005 Results. *Journal of Climate*, 26(20):7793–7812, 2013. doi: 10.1175/JCLI-D-12-00615.1.

M. Vizcaíno, W. H. Lipscomb, W. J. Sacks, and M. van den Broeke. Greenland Surface Mass Balance as Simulated by the Community Earth System Model. Part II: Twenty-First-Century Changes. *Journal of Climate*, 27(1):215–226, 2014a. doi: 10.1175/JCLI-D-12-00588.1.

L. Wake and S. Marshall. Assessment of current methods of positive degree-day calculation using in situ observations from glaciated regions. *Journal of Glaciology*, 61(226):329–344, 2015. doi: 10.3189/2015JoG14J116.

E. Waldmann. Quantile regression: A short story on how and why. *Statistical Modelling*, 18(3-4):203–218, 2018. doi: 10.1177/1471082X18759142.

M. Wang and J. E. Overland. A sea ice free summer Arctic within 30 years: An update from CMIP5 models. *Geophysical Research Letters*, 39(18), 2012. doi: 10.1029/2012GL052868.

W. Wang, C. S. Zender, D. van As, and N. B. Miller. Spatial distribution of melt season cloud radiative effects over Greenland: Evaluating satellite observations, reanalyses, and model Simulations Against In Situ Measurements. *Journal of Geophysical Research: Atmospheres*, 124 (1):57–71, 2019. doi: 10.1029/2018JD028919.

P. L. Whitehouse. Glacial isostatic adjustment modelling: Historical perspectives, recent advances, and future directions. *Earth Surface Dynamics*, 6(2):401–429, 2018. doi: 10.5194/esurf-6-401-2018.

I. Wientjes, R. Van de Wal, G.-J. Reichart, A. Sluijs, and J. Oerlemans. Dust from the dark region in the western ablation zone of the greenland ice sheet. *The Cryosphere*, 5(3):589–601, 2011.

D. J. Wilton, A. Jowett, E. Hanna, G. R. Bigg, M. R. van den Broeke, X. Fettweis, and P. Huybrechts. High resolution (1 km) positive degree-day modelling of Greenland ice sheet surface mass balance, 1870–2012 using reanalysis data. *Journal of Glaciology*, 63(237):176–193, 2017. doi: 10.1017/jog.2016.133.

T. Woollings, A. Hannachi, and B. Hoskins. Variability of the North Atlantic eddy-driven jet stream. *Quarterly Journal of the Royal Meteorological Society*, 136(649):856–868, 2010. doi: 10.1002/qj.625.

B. Xu, N. Wang, T. Chen, and M. Li. Empirical evaluation of rectified activations in convolutional network, 2015.

M. Yoshimori and A. Abe-Ouchi. Sources of spread in multimodel projections of the Greenland ice sheet surface mass balance. *Journal of Climate*, 25(4):1157–1175, 2012. doi: 10.1175/2011JCLI4011.1.

M. D. Zelinka, T. A. Myers, D. T. McCoy, S. Po-Chedley, P. M. Caldwell, P. Ceppi, S. A. Klein, and K. E. Taylor. Causes of Higher Climate Sensitivity in CMIP6 Models. *Geophysical Research Letters*, 47 (1):e2019GL085782, 2020. doi: 10.1029/2019GL085782.

X. Zhang, J. E. Walsh, J. Zhang, U. S. Bhatt, and M. Ikeda. Climatology and interannual variability of Arctic cyclone activity: 1948–2002. *Journal of Climate*, 17(12):2300–2317, 2004. doi: 10.1175/1520-0442(2004)017<2300:CAIVOA>2.0.CO;2.

Curriculum Vitæ

Raymond Sellevold

09-06-1989	Born in Bergen, Norway
2005–2008	**Tanks Videregående Skole** Bergen, Norway
2008–2009	**Military Service** Kirkenes, Norway
2009–2010	**Year Study in Law** University of Bergen, Norway
2010–2013	**Bachelor of Science in Meteorology and Oceanography** University of Bergen, Norway
2013–2015	**Master of Science in Meteorology and Oceanography** University of Bergen, Norway Specialzation in climate dynamics Thesis: ”The linear stationary wave response to Arctic amplification related heating.” Supervisor: Prof. Camille Li
2015–2016	**Meteorology Consultant** Meteorologisk institutt, Bjørnøya, Norway
2016–present	**Doctoral Candidate** Delft University of Technology, the Netherlands

List of Publications

v. **R. Sellevold**, M. Vizcaino: *Global warming threshold and mechanisms for accelerated Greenland ice sheet surface mass loss*, Journal of Advances in Modeling Earth Systems **12**, 9 (2020).

iv. L. Muntjewerf, **R. Sellevold**, M.Vizcaino, C.E. da Silva, M. Petrini, K. Thayer-Calder, M.D.W. Scherrenberg, S.L. Bradley, J. Fyke, W.H. Lipscomb, M. Lofverstrom, W.J. Sacks: *Accelerated Greenland ice sheet mass loss under high greenhouse gas forcing as simulated by the coupled CESM2.1-CISM2.1*, Journal of Advances in Modeling Earth Systems (accepted).

iii. L. Muntjewerf, M. Petrini, M. Vizcaino, C.E. da Silva, **R. Sellevold**, M.D.W. Scherrenberg, K. Thayer-Calder, S.L. Bradley, J.T.M. Lenaerts, W.H. Lipscomb, M. Lofverstrom: *Greenland ice sheet contribution to 21st century sea level rise as simulated by the coupled CESM2.1-CISM2.1*, Geophysical Research Letters **47**, 9 (2020).

ii. **R. Sellevold**, L. van Kampenhout, J.T.M. Lenaerts, B. Noël, W.H. Lipscomb, M. Vizcaino: *Surface mass balance downscaling through elevation classes in an Earth system model: Application to the Greenland ice sheet*, The Cryosphere **13**, 12 (2019).

i. **R. Sellevold**, S. Sobolowski, C. Li: *Investigating possible Arctic-midlatitude teleconnections in a linear framework*, Journal of Climate **29**, 20 (2016).